UNIVERSITÀ DEGLI STUDI DI FERRARA

FACOLTÀ DI SCIENZE MM.FF.NN.

XV CICLO DI DOTTORATO
2000-2003

PhD Thesis

Hard Exclusive Electroproduction of Two Pions at HERMES

THESIS ADVISOR:
Prof.ssa PAOLA FERRETTI DALPIAZ
Università di Ferrara

JOINT THESIS ADVISOR:
dott. PASQUALE DI NEZZA
INFN-Laboratori Nazionali di Frascati

CANDIDATE:
RICCARDO FABBRI

When we consider and reflect upon nature at large or the history of mankind or our own intellectual activity, at first we see the picture of an endless entanglement of relations and reactions in which nothing remains what, where and as it was, but everything moves, changes, comes into being and passes away. This primitive, naive but intrinsically correct conception of the world is that of ancient Greek philosophy, and was first clearly formulated by Heraclitus: everything is and is not, for everything is fluid, is constantly changing, constantly coming into being and passing away. (Engels, Anti-Duhring)

Contents

Chapter 1

Introduction

In 1930s it was realized that the forces binding together nucleons in nuclei are different from the electromagnetic forces, which are much weaker. The gradual progress in our understanding of the dynamics of nucleons and of their internal structure gave rise in the 70's to the birth of the Quantum Chromodynamics (QCD) as the fundamental theory of the strong interactions.

Historically, in the late 1960s a series of experiments at the Stanford Linear Accelerator (SLAC) on deep inelastic scattering off hydrogen and deuterium targets showed that the nucleon is made of point-like objects, interpreted as the Feynman's partons, several further experiments were performed in the second half of the last century. By the results provided by experiments, it became possible to understand more and more the inner structure of nucleons. Partons were proved to be actually of two types: quarks and gluons. Quarks were found to be 1/2 spin objects with fractional electrical charge, sharing only $\sim$ 50% of the overall nucleon momentum and continuously interacting with gluons, the quanta of the strong interaction, which carry the remaining $\sim$ 50% of the nucleon momentum.

As typical in science, unexpected new results can sway our knowledge about some phenomena. In the 1980s it was experimentally found by the EMC Collaboration at CERN, that quarks seemed not to account for the whole spin content of the nucleon. After a strong theoretical effort it became clear that what was named 'The Spin Crisis', actually was the spin crisis in the "Quark Parton Model". This model, able to explain some of the parton properties inside nucleons, failed in accounting for the more recent results given by experiments. Instead, in the framework of QCD, with quarks interacting with gluons, the explanation of many puzzles that arose in the last decade, started to merge. In the picture that emerges, gluons share with quarks the overall nucleon helicity. In 2000 the HERMES Collaboration published the first indication of positive gluon helicity, and more precise results are expected from current dedicated experiments as COMPASS at CERN and STAR and PHENIX at BNL.

Moreover, it is now evident that the nucleon spin can not be decomposed only into the spin carried by its constituent quarks and gluons. Partons, with non zero transverse momentum have orbital angular momentum which must be taken into account to understand the whole spin nucleon structure. As theoretically demonstrated recently, an efficient way to access the quark orbital angular momentum is through hard exclusive processes, that is through exclusive processes probed with wave lengths smaller then the nucleon size. This condition is obtained at large $Q^2 = -q^2$, q^2 being the four-momentum squared of the probe.

These reactions can be described in terms of Generalized Parton Distributions (*GPD*) which essentially describe the correlation between parton states with different momenta in the nucleon. These distributions were shown to be strongly correlated with fundamental parton properties. In particular they obey certain sum rules that in the forward limit, i.e. at zero transfer momentum from the probe to the nucleon, are related to elastic form factors and to the total angular momentum carried by partons. The 'asymptotic regime' at large Q^2 allows *GPD*s to naturally appear in a factorized convolution in the amplitude of the exclusive process. At the moment these reactions are being studied by the HERMES, H1, ZEUS Collaborations and at JLAB, which started to give data on Deeply Virtual Compton Scattering and on Hard Exclusive Meson Production. Collecting data from hard exclusive processes, (where all the event tracks are reconstructed) at different kinematic regimes has now become a challenge to help the modeling of these parton correlations strongly linked to the inner structure of nucleons.

In order to give more and new information on *GPD*s, the analysis of hard exclusive processes $e^+p \longrightarrow e^+p\pi^+\pi^-$ and $e^+d \longrightarrow e^+d\pi^+\pi^-$ at *HERMES* is presented. The data have been accumulated with the HERMES forward spectrometer [84] during the running period 1996-2000. The 27.6 GeV positron beam was scattered off hydrogen and deuterium targets, and events with both unpolarized and polarized targets were considered in this analysis, since it is not sensitive to the spin target.

In particular, some angular distributions of the π^+ in the $\pi^+\pi^-$ rest frame have been studied in the invariant mass range $0.3 < m_{\pi\pi} < 1.35$ GeV. Theoretical models show that these angular distributions receive only contribution from the interference between the odd and even l $\pi^+\pi^-$ states, l being the π^+ orbital angular momentum in the 2π rest frame.

Chapter 2 is devoted to an overview of the GPDs, introducing their formalism and presenting some model. In this chapter the link of GPDs with the total angular momentum carried by partons is debated. Chapter 3 deals with an overview of the theory associated with hard exclusive $\pi^+\pi^-$ leptoproduction. The experimental set up is described in chapter 4. The whole data analysis to study the process is shown in details in chapter 5. In this chapter the comparison of current experimental results with the theoretical predictions so far available is shown. The conclusions which summarize the results of this work are reported in chapter 6.

The results from this analysis, together with results from different exclusive channels are meant to lead to a better modeling of *GPD*s in order to reach a better understanding of the spin structure of nucleons.

Chapter 2

Generalized Parton Distributions

Experimental results of the last decades showed that the nucleon spin can not be decomposed only into the spin carried by its constituents quarks and gluons, see Appendix A. Furthermore from the Uncertainty Principle, partons inside a $\sim 1fm^3$ box must have a non zero transverse momentum, and this provides them with orbital angular momentum which has to be taken into account to understand the helicity structure of the nucleon.

A way to access the quark orbital angular momentum is through hard exclusive processes, studied with a high resolving probe. These reactions may be described in term of Generalized Parton Distributions (*GPD*s) which essentially describe the correlation between parton states with different momenta and same flavors in the nucleon. In a more enlarged interpretation of *GPD*s, they can also describe the correlation between parton states with different flavors, as in the case of a transition between different nucleons [1].

2.1 *GPD*s and Hard Exclusive Reactions

*GPD*s are related to off-diagonal matrix elements of bilocal operators of quarks or gluons[1] between nucleon states of different momentum. They are generalizations of the usual parton distributions which parameterize the diagonal matrix elements of the corresponding operators. Keeping in mind the optical theorem [2]

$$\sigma_t \propto Im\ T_e(0)\ , \tag{2.1}$$

where the sum of the cross-sections of all processes is denoted by σ_t and the forward ($\theta = 0$) elastic scattering amplitude is $T_e(0)$, one can relate the *DIS* cross section to the deeply virtual Compton scattering amplitude on nucleon, described at quark level in

[1] Field bilinears are the product of two field operators.

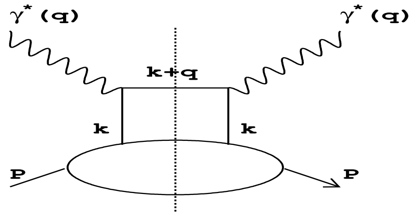

Figure 2.1: The optical theorem relates the elastic cross section of virtual photons off quarks to the imaginary part of the forward virtual Compton scattering.

Fig.2.1. The dotted line in the picture means diagrammatically the imaginary part of the amplitude. The hadronic blob that describes the nucleon transition between equal states $N(P_\mu, S_\mu)$ can be formally decomposed in the most general way (Appendix. B):

$$\sum_q \int < P|\bar{\psi}\Gamma\psi|P > , \tag{2.2}$$

where Γ is an element of the basis of Dirac matrices

$$\Gamma = \{1, \gamma^\mu, \gamma^\mu\gamma^5, i\gamma^5, i\sigma^{\mu\nu}\gamma^5\} . \tag{2.3}$$

These expectation values of quark-field bilinears are also known as *forward* parton distributions, due to the fact that, in this Compton scattering, the four-momentum squared t transferred by the electromagnetic probe to the target is null. In this case, when $t = 0$ (zero transfer momentum), the virtual photon is scattered in the forward direction. Furthermore, describing the transition between two equal nucleon states they are also called *diagonal* distributions.

They have a natural generalization when non-null t momentum is transferred to the target by the probe, and in this case they are known as generalized (*or off-diagonal*) parton distributions, *GPD*. These new distributions are not accessed by inclusive *DIS* processes whose cross section probes the transition between equal nucleon states, due to the optical theorem as shown in Fig.2.1. Instead they are accessed only through in the hard exclusive ones. As an example, the amplitude of the hard exclusive meson lepto-production at large virtuality Q^2 of the electromagnetic probe (hard regime) and large virtual photon-nucleon center of mass energy $\sqrt{W}$ can be factorized into the convolution

$$\sum_{i,j} \int dz dx_1 f_{i/N}^{N'}(x_1, x_1 - x_{Bj}, t)\ H_{ij}\Big(\frac{x_1}{x_{Bj}}, Q^2, z\Big)\, \Phi_j^F(z)$$
$$+\text{power-suppressed corrections} \tag{2.4}$$

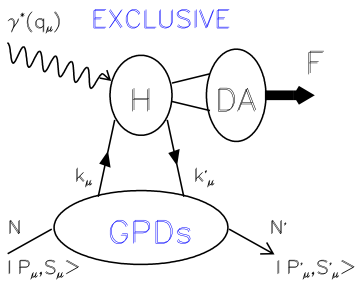

Figure 2.2: The typical factorized amplitude of the meson leptoproduction is shown. The amplitude is factorized into a perturbative factor H with two non perturbative amplitudes which describe the nucleon transition (*GPD*) and the meson formation (*DA*).

where H_{ij} is the hard part computable in perturbative QCD as a series in α_s, $\Phi_j^F(z)$ is the distribution amplitude (DA) of the hadronic state [3] describing the non-perturbative transition from partons, produced in the hard scattering, to the final hadronic state, and $f_{i/N}^{N'}$ is the Generalized Parton Distribution related to the nucleon transition $N \rightarrow N'$ [4], Fig. 2.2. Due to the above factorization, *GPD*s naturally enter this kind of process. The hard part H of the interaction of the probe with a constituent parton has a time-scale evaluated to be much smaller then the interaction time-scale among partons, and sometimes it is referred as the short range part of the overall interaction. Instead the nucleon transition, which is parameterized in terms of generalized structure functions, describes the strong correlation between partons inside the nucleon with time-scale larger then the interaction length with the incoming probe.

There are different formalisms to describe these generalized matrix elements, as an example *off-forward* parton distributions (OFPD) [5] and *non-forward* parton distributions (NFPD) [3]. The two examples are described by different variables as the *skewedness* parameter and the parton momentum k^+ involved in the hard perturbative sector of the amplitude. In the OFPD and NFPD formalisms these variables are measured in units of the average $\bar{P}^+ = \frac{1}{2}(p^+ + p^{'+})$ and the initial nucleon momenta p^+, respectively. The skewedness parameter is an important parameter for non-diagonal matrix elements, defined as:

$$
\begin{aligned}
\xi &= -\frac{\Delta^+}{2\bar{P}^+} \; (OFPD) \\
\zeta &= -\frac{\Delta^+}{p^+} \; (NFPD) \\
\xi &= \frac{\zeta}{2-\zeta} \; , \qquad (2.5)
\end{aligned}
$$

where $\Delta_\mu = p_\mu - p'_\mu$ is the momentum transferred to the nucleon. Whatever is the choice of formalism, there are one-to-one relations between OFPDs and NFDPs [3].

In the following we will adopt the formalism of OFPDs. At leading twist–2 level [2] with the constrains of time-reversal and parity invariance, the nucleon transition can be therefore parameterized in terms of eight quark OFPDs, denoted by $H_q, \tilde{H}_q, E_q, \tilde{E}_q, H_{T_q}, E_{T_q}, \tilde{H}_{T_q}, \tilde{E}_{T_q}$, and eight gluon OFPDs, denoted by $H_g, \tilde{H}_g, E_g, \tilde{E}_g$, $H_{T_g}, E_{T_g}, \tilde{H}_{T_g}, \tilde{E}_{T_g}$. As an example, the complete set of off-forward twist–2 quark distributions is given below [6, 7]:

$$\begin{aligned}
\int \frac{d\lambda}{2\pi} e^{i\lambda x} \langle P'S'|\bar{\psi}_q(-\frac{1}{2}\lambda n)\gamma^\mu \psi_q(\frac{1}{2}\lambda n)|PS\rangle &= H_q(x,\xi)\bar{N}(P'S')\gamma^\mu N(PS) \\
&\quad + E_q(x,\xi)\bar{N}(P'S')\frac{i\sigma^{\mu\nu}\Delta_\nu}{2m_N}N(PS) + \ldots\,, \\
\int \frac{d\lambda}{2\pi} e^{i\lambda x} \langle P'S'|\bar{\psi}_q(-\frac{1}{2}\lambda n)\gamma^\mu\gamma_5 \psi_q(\frac{1}{2}\lambda n)|PS\rangle &= \tilde{H}_q(x,\xi)\bar{N}(P'S')\gamma^\mu\gamma_5 N(PS) \\
&\quad + \tilde{E}_q(x,\xi)\bar{N}(P'S')\frac{\gamma_5\Delta^\mu}{2m_N}N(PS) + \ldots\,, \\
\int \frac{d\lambda}{2\pi} e^{i\lambda x} \langle P'S'|\bar{\psi}_q(-\frac{1}{2}\lambda n)\sigma^{\mu\nu} \psi_q(\frac{1}{2}\lambda n)|PS\rangle &= H_{Tq}(x,\xi)\bar{N}(P'S')\sigma^{\mu\nu} N(PS) \\
&\quad + E_{Tq}(x,\xi)\bar{N}(P'S')\frac{i\gamma^{[\mu}\Delta^{\nu]}}{m_N}N(PS) \\
&\quad + \tilde{H}_T(x,\xi)\bar{N}(P'S')\frac{2i\ P^{[\mu}\Delta^{\nu]}}{m_N^2}N(PS) \\
&\quad + \tilde{E}_T(x,\xi)\bar{N}(P'S')\frac{2i\ \gamma^{[\mu}P^{\nu]}}{m_N}N(PS) + \ldots\,,
\end{aligned} \tag{2.6}$$

where ψ is the quark field of flavor q, N the nucleon spinor, m_N the nucleon mass, $n = (1,0,0,-1)$ is a light cone vector, $\gamma^{[\mu}\Delta^{\nu]} = \gamma^\mu\Delta^\nu - \gamma^\nu\Delta^\mu$ and the ellipses denote higher twist structures present when the virtuality Q^2 is finite.

The light-cone momentum fraction x is defined (see Fig. 2.3) by $\bar{k}^+ = x\bar{P}^+$, where $\bar{k}$ is the quark loop momentum $\bar{k} = (k + k\,')/2$ (average quark momentum), $\bar{P}$ is the average nucleon momentum $\bar{P} = (p + p\,')/2$, and $p, p\,'$ are the initial and final nucleon momenta respectively. The variable x refers to the average of the longitudinal momentum fractions of the struck parton in its initial and final state. The skewedness variable ξ is $\Delta^+ = -2\xi\,\bar{P}^+$, and $2\xi \to x_B/(1 - x_B/2)$ in the Bjorken limit $Q^2 \to \infty$.

[2] twist–2 amplitudes are the terms describing the nucleon transition at large virtuality of the photon $Q^2 \to \infty$. Terms scaling with powers of $1/Q$ are called higher twist terms and their contribution may become sizable at lower Q^2.

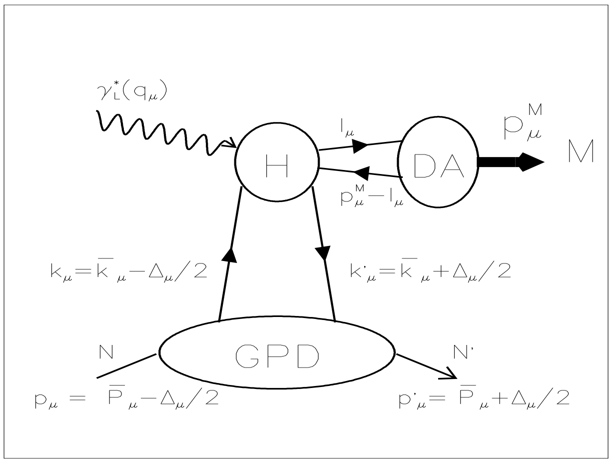

Figure 2.3: Amplitude of the hard exclusive electroproduction of mesons in the *OFPD* formalism. The hadronic blob, describing the transition from nucleon states at different momentum, is parameterized in terms of GPDs.

Furthermore, the third variable entering the GPDs is given by the Mandelstam invariant $t = \Delta^2$. The virtual photon momentum q^μ and the average nucleon momentum $\bar{P}^\mu$ are collinear along the z-axis and in opposite versus. In order to ensure the color gauge invariance of all the quantities defined in Eq. 2.6, the *path ordered* gauge link $Pe^{ig\int dy^\mu A_\mu}$ is always assumed, A_μ being the color field and $g^2 = 2\pi\alpha_s$ the coupling constant.

The left hand side of Eq. 2.6 can be interpreted as a Fourier integral along the light-cone distance y^- of a quark-quark correlation function, representing the process where a quark is taken out of the initial nucleon (having momentum p) at the space-time point $y/2$, and is put back in the final nucleon (having momentum $p\,'$) at the space-time point $-y/2$, e.g.

$$\int dy\ e^{iky} \langle P'S'|\bar{\psi}_q(-\frac{y}{2})\gamma^\mu \psi_q(\frac{y}{2})|PS\rangle\ . \tag{2.7}$$

This picture can be understood if in the quark correlation matrix of Eq. 2.7 the term $\int\int dk\ d(\frac{\lambda}{2\pi})e^{i\lambda(x-k\cdot n)} = 1$ is introduced and the integration on k_μ is performed [8]. This process takes place at equal light-cone time ($y^+ = 0$) and at zero transverse separation ($\vec{y}_\perp = 0$) between the quarks. The resulting one-dimensional Fourier integral along the light-cone distance y^- is with respect to the quark light-cone momentum $x\bar{P}^+$.

The right hand side of Eq. 2.6 parameterizes this non-perturbative object in terms of OFPDs, which satisfy particular symmetries; for example they are real and, due to time-reversal and hermiticity they are even functions of ξ [5]. The GPDs $H, \tilde{H}, E, \tilde{E}$

describe the helicity non flip (parton helicity conserving distributions) of the outgoing parton with respect to that of the incoming parton, while $H_T, \tilde{H}_T, E_T, \tilde{E}_T$ describe the helicity flip of partons exchanged with the nucleon. In terms of chirality, the two sets can also be referred to as *chirally-even* and *chirally-odd*, respectively. In case of gluons, which have no definite chirality, the above chiral classification is not true at all. Moreover, the nucleon helicity is conserved by the H-distributions, but not by the E-ones.

The variable x runs from -1 to 1, therefore the momentum fractions $x+\xi$ or $x-\xi$ of the active quarks can either be positive or negative. Since positive and negative momentum fractions correspond to quarks and antiquarks respectively [3], one can identify two regions for the GPDs: when $x > \xi$ both partons represent quarks, whereas for $x < -\xi$ both partons represent antiquarks. In these regions, the GPDs are the generalization of the usual parton distributions from DIS. Actually, in the forward direction, the GPDs H and $\tilde{H}$ reduce to the quark density distribution $q(x)$ and quark helicity distribution $\Delta q(x)$ respectively, obtained from DIS:

$$H_q(x,0,0) = \begin{cases} q(x), & x > 0 \\ -\bar{q}(-x), & x < 0 \,, \end{cases} \tag{2.8}$$

$$\tilde{H}_q(x,0,0) = \begin{cases} \Delta q(x), & x > 0 \\ \Delta\bar{q}(-x), & x < 0 \,. \end{cases} \tag{2.9}$$

The functions E, $\tilde{E}$, E_T and $\tilde{H}_T$ are not measurable through inclusive DIS because the associated tensors in Eq. 2.6 vanish in the forward limit ($\Delta \to 0$). Therefore, E, $\tilde{E}$, E_T and $\tilde{H}_T$ are new leading twist functions, which are accessible through the hard exclusive electroproduction only.

In the region $-\xi < x < \xi$, one parton connected to the lower blob in Fig. 2.3 represents a quark and the other one an antiquark. In this region, the GPDs behave like a meson distribution amplitude describing the hadron formation from two partons. It contains completely new information about nucleon structure, because the region $-\xi < x < \xi$ is absent in DIS, which corresponds to the limit $\xi \to 0$.

Besides coinciding with the quark distributions at vanishing momentum transfer, the generalized parton distributions have interesting links with other nucleon structure quantities. The first moments of the GPDs are related to the elastic form factors of the nucleon through model independent sum rules. By integrating Eq. 2.6 over x, one obtains for any ξ the following relations to the Dirac, Pauli, axial and pseudo-scalar elastic nucleon form factors [9] :

$$\begin{aligned}
\int_{-1}^{+1} dx\, H^q(x,\xi,t) &= F_1^q(t) \ , \quad (2.10)\\
\int_{-1}^{+1} dx\, E^q(x,\xi,t) &= F_2^q(t) \ , \quad (2.11)\\
\int_{-1}^{+1} dx\, \tilde{H}^q(x,\xi,t) &= g_A^q(t) \ , \quad (2.12)\\
\int_{-1}^{+1} dx\, \tilde{E}^q(x,\xi,t) &= h_A^q(t) \ . \quad (2.13)
\end{aligned}$$

Given the fact that one can associate the Fourier transform of form factors with charge distributions in position space, recently some information about the distributions in parton space have been investigated [12]. Whereas x and ξ characterize the longitudinal momenta of the partons involved, the t-dependence of the GPDs is related to their transverse momentum. By Fourier transform, the longitudinal momentum fraction of quarks and their position in the transverse plane may be accessed simultaneously. For example, the GPD distributions $H(x,\xi,t)$ and $E(x,\xi,t)$ can be written as

$$\begin{aligned}
H_q(x,\xi=0,t=\Delta_\perp^2) &= \int d^2b_\perp\, exp^{-i\ \Delta_\perp\cdot b_\perp} f(x,b_\perp)\\
E_q(x,\xi=0,t=\Delta_\perp^2) &= \int d^2b_\perp\, exp^{-i\ \Delta_\perp\cdot b_\perp} f(x,b_\perp)\ . \quad (2.14)
\end{aligned}$$

where $f(x,b_\perp)$ is the probability to find a quark with momentum fraction x at a distance $b_\perp$ in the plane perpendicular to the center of mass momentum. This would open the way to a *femto-photography* of the nucleon [13,14].

An interesting connection of GPDs to light-cone wave functions of the nucleon was considered in Refs. [11, 15]. In these papers an exact representation of generalized parton distributions for unpolarized and polarized quarks and gluons as an overlap of the nucleon light-cone wave functions has been constructed.

In 1995 [16] it was demonstrated the following *Ji* Sum Rule

$$J_{q/g} = \lim_{\xi=t\to 0} \int_{-1}^{1} dx x[H_{q/g}(x,\xi,t) + E_{q/g}(x,\xi,t)] \ , \quad (2.15)$$

which relates the $H(x,\xi,t)$ and $E(x,\xi,t)$ moment on x to the total angular momentum carried by partons. This sum rule provides a further way to investigate the nucleon spin structure, as the knowledge of GPDs may allow one to isolate the contribution of the parton total angular momentum J_q and J_g to the helicity 1/2 of the nucleon. When protons are considered, their helicity can be decomposed in the different parton contributions as:

$$\frac{1}{2} = J_q + J_g = (\frac{1}{2}\Delta\Sigma + L_q) + (\Delta G + L_g) \ , \tag{2.16}$$

$\frac{1}{2}\Delta\Sigma$, ΔG being the helicity contributions and L_q, L_g the orbital angular momentum z-projected contributions of quarks and gluons respectively.

2.2 *GPDs* and the Parton Total Angular Momentum

A satisfactory understanding of the spin structure would defined as knowing how much spin of the nucleon is carried by the quark and gluon helicities and orbital angular momenta individually, in the same way as one now understands how the mass of the nucleon is partitioned among contributions from the quark and gluon kinetic energies, quark masses, and the trace anomaly [17].

The angular momentum operator in QCD is defined according to the generators of Lorentz transformation,

$$J^i = \frac{1}{2}\epsilon^{ijk} \int d^3x J^{jk} \ , \tag{2.17}$$

J^{jk} being the generators of Lorentz transformations [18],

$$J^{\mu\nu} = \int d^3x M^{0\mu\nu} \ . \tag{2.18}$$

$M^{\alpha\mu\nu}$ is the angular momentum density defined as:

$$\begin{aligned} M^{\alpha\mu\nu} = \quad & i\bar{\psi}\gamma^\alpha(x^\mu\partial^\nu - x^\nu\partial^\mu)\psi + \frac{i}{4}\bar{\psi}\gamma^\alpha[\gamma^\mu, \gamma^\nu]\psi \\ & -F^{\alpha\sigma}(x^\mu\partial^\nu - x^\nu\partial^\mu)A_\sigma - F^{\alpha\mu}A^\nu + F^{\alpha\nu}A^\mu \ , \end{aligned} \tag{2.19}$$

where A_μ is the color field, $F_{\mu\nu}$ is the corresponding Yang-Mills field, and color indices are implicit. Furthermore $M^{\alpha\mu\nu}$ is expressible in terms of the energy-momentum tensor $T^{\mu\nu}$ through

$$M^{\alpha\mu\nu} = T^{\alpha\nu}x^\mu - T^{\alpha\mu}x^\nu \ . \tag{2.20}$$

The tensor $T^{\mu\nu}$ has the *Belinfante-improved* form and is symmetric, gauge-invariant, and conserved [96]. It can be separated into gauge-invariant quark and gluon contributions,

$$T^{\mu\nu} = T_q^{\mu\nu} + T_g^{\mu\nu} \ , \tag{2.21}$$

where the quark part is

$$T_q^{\mu\nu} = \frac{1}{2}[\bar{\psi} i\gamma^{(\mu} \overrightarrow{D}^{\nu)}\psi + \bar{\psi} i\gamma^{(\mu}\overleftarrow{D}^{\nu)}\psi] \ , \tag{2.22}$$

and the gluon part is

$$T_g^{\mu\nu} = \frac{1}{4} g^{\mu\nu} F^2 - F^{\mu\alpha} F^{\nu}_{\ \alpha} \ , \tag{2.23}$$

with $\gamma^{(\mu}\overleftarrow{D}^{\nu)} = \gamma^{\mu}\overleftarrow{D}^{\nu} + \gamma^{\mu}\overleftarrow{D}^{\nu}$ denoting symmetrization with respect to μ, ν indices.

For the above equations, one sees that $\vec{J}$ can be written as a gauge invariant sum, $\vec{J}_{\rm QCD} = \vec{J}_q + \vec{J}_g$, where

$$J^i_{q,g} = \frac{1}{2}\epsilon^{ijk} \int d^3x (T^{0k}_{q,g} x^j - T^{0j}_{q,g} x^k) \ . \tag{2.24}$$

To understand the physical content of the gauge invariant $\vec{J}_q$ and $\vec{J}_g$, after some algebra [9] one can re-express them:

$$\begin{aligned} \vec{J}_q &= \int d^3x \ \psi^\dagger [\vec{\gamma}\gamma_5 + (\vec{x} \times i\vec{D})]\psi = \int d^3x \ \psi^\dagger \left[\frac{1}{2}\vec{\Sigma} + (\vec{x} \times i\vec{D})\right]\psi \ , \\ \vec{J}_g &= \int d^3x \ (\vec{x} \times (\vec{E} \times \vec{B})) \ . \end{aligned} \tag{2.25}$$

The two terms entering the quark total angular momentum $\vec{J}_q$ have the direct interpretation of gauge-independent intrinsic $\left(\frac{1}{2}\int d^3x \ \psi^\dagger \vec{\Sigma}\psi\right)$ and gauge-dependent orbital $\left(\int d^3x \ \psi^\dagger (\vec{x} \times i\vec{D})\psi\right)$ angular momentum. Instead, the gluon angular momentum $\vec{J}_g$ does not admit further gauge-invariant decomposition as spin and orbital contributions, contrary to the quark case.

Using Lorentz covariance and invariance under the discrete symmetries, one can expand the matrix elements of $T^{\mu\nu}_{q,g}$ in terms of four form factors:

$$\begin{aligned} \langle P'|T^{\mu\nu}_{q,g}|P\rangle &= \overline{u}(P')\Big[A_{q,g}(t) \ \gamma^{\{\mu}\overline{P}^{\nu\}} \ + \ B_{q,g}(t) \ \overline{P}^{\{\mu} i\sigma^{\nu\}\alpha}\Delta_\alpha/2M \\ &\quad + C_{q,g}(t) \ (\Delta^\mu\Delta^\nu - g^{\mu\nu}t)/M \ + \ \overline{C}_{q,g}(t) \ g^{\mu\nu}M\Big]u(P) \ , \end{aligned} \tag{2.26}$$

where the braces $\{\cdots\}$ on the superscripts denote symmetrization. Taking the forward limit $\Delta = 0$ and integrating over 3-space, one finds that $A_{q,g}(0)$ give the momentum fraction of the nucleon carried by quarks and gluons ($A_q(0) + A_g(0) = 1$). On the other hand, substituting the above into the nucleon matrix element of $\vec{J}_{q,g}$, one finds fractions of the nucleon spin z-component carried by quarks, J_q, and gluons, J_g [9],

$$J_{q,g} \;=\; \frac{1}{2}\Big(A_{q,g}(0) + B_{q,g}(0)\Big)\ . \tag{2.27}$$

Measuring the form factors of the energy-momentum tensor in practice is very difficult, partly because there is no fundamental probe which couples to them (the graviton does, but only to the total tensor). Because of asymptotic freedom (factorization of the process amplitude), the form factors can be measured through deep-inelastic sum rules. Now, an important sum rule relevant to the nucleon helicity is the following which relates GPDs H, E to energy-momentum form factors A, B:

$$\int_{-1}^{1} dx\ x\Big(H(x,\xi,t) + E(x,\xi,t)\Big) \;=\; A(t) + B(t)\ , \tag{2.28}$$

where the ξ dependence drops out. Extrapolating this sum rule to $t = 0$ and taking into account the result of Eq. 2.27, the total quark (gluon) angular momentum contribution to the nucleon spin is obtained:

$$J_{q/g} = \frac{1}{2} \lim_{\xi=t\to 0} \int_{-1}^{1} dx x[H_{q/g}(x,\xi,t) + E_{q/g}(x,\xi,t)]\ , \tag{2.29}$$

where J_q (J_g) is the fraction of the nucleon angular momentum carried by a quark of flavor q (gluon). Thus a deep understanding of the spin structure of the nucleon may be achieved by measuring *GPD*s from high-energy experiments.

The result by *Ji* seems to be the experimental favorite since the GPDs involved, in principle, are measurable and related to energy-momentum factor forms A and B in hard exclusive processes. Nevertheless, the decomposition $\vec{J}_g = \int d^3x\ (\vec{x} \times (\vec{E} \times \vec{B}))$ is not able to describe Δg and L_g separately. Theoretical debates [20–22] are currently going on about how defining proper angular momentum observables related to physical quantities measurable in *DIS* experiments and able to disentangle the intrinsic and orbital angular momentum. At present, there is few amount of experimental data to constrain these distributions. The only strong constraint is given by their forward limit to ordinary distributions and their link to elastic nucleon form factors. Most of these data have recently acquired a satisfactory precision. However, the knowledge of these limits, or projections, does not imply a complete knowledge of the GPDs themselves. Compared with the ordinary parton distributions, GPDs depend on two additional variables: the *skewedness* ξ and transverse momentum squared t. Because of these, they contain much more information and are more difficult to model in practice. Furthermore, for the spin structure of the nucleon only small values of t are relevant but, reaching small t in real experiments is difficult. Models are currently being developed for a complete representation, and some results are presented in the next section with some parametrization included.

To better model *GPD*s, much more experimental data are needed, thus hard exclusive processes have started to be investigated [23–25]. New experimental data coming from these processes, with results from future measurements in hard exclusive processes, are therefore meant to give stronger and stronger constrains to universal *GPD*s, leading a deeper understanding of the nucleon spin structure. A deeper insight into this topic may be found in [1].

2.3 Modeling of GPDs

A quantitative description of GPDs requires not only knowledge of their perturbative evolution, but also non-perturbative information in the form of the OFPD's at some initial normalization point. Thus, a computation of the OFPD's at a low normalization point in a realistic model of the nucleon is of great importance. While the usual parton distributions have been measured in a variety of different experiments and can be confronted with model calculations *a posteriori*, in the case of the off–forward distributions the situation is rather opposite: here, model calculations of the distributions at a low normalization point are required to determine the very feasibility of measuring the OFPD's, say, in DVCS at experimental energies.

QCD inspired models are very useful to understand how non-perturbative mechanisms generate various structures in GPDs. There are many nucleon models on the market in which the OFPDs could be calculated. Anyway, only bag models and quark-soliton models have been extensively used to model GPDs, mainly because they managed to describe quite well standard hadron features.

In the simple MIT bag model [26, 27], GPDs have but a weak dependence on ξ, and show no structure for $|x| < \xi$. A number of calculations in different constituent quark models are being developed. The choice of the MIT bag is based on the fact that it has quark degrees of freedom and gives reasonable results for the electromagnetic form factors [28, 29], as well as for polarized and unpolarized parton distributions [28, 30]. However, being a model, it has a number of unwanted artifacts, such as a sharp boundary, absence of gluons, and the breaking of translational invariance and chiral symmetry. Nonetheless, results are thought to provide a reasonable first guess of the unknown distributions at a low energy scale, $\mathcal{O}(10^{-1}\ \mathrm{GeV}^2)$.

The coordinate space wave function of a quark in the rest frame of the MIT bag is given by:

$$\psi(\vec{r}) = \sqrt{4\pi} N R^3 \left(\begin{array}{c} j_0(\epsilon_0 r) \\ i\overrightarrow{\sigma} \cdot \widehat{r}\, j_1(\epsilon_0 r) \end{array} \right) \chi \ , \tag{2.30}$$

where R is the bag radius, $\epsilon_0 = \omega_0/R$ is the quark energy, and $\omega_0 = 2.04$ is lowest frequency solution of the bag eigenequation, $\tan\omega_0 = \omega_0/(1-\omega_0)$. The functions $j_{0,1}$ are the spherical Bessel functions and χ is the quark spinor. The radius in the basic version of the bag model is given by the relation: $RM_P = 4\omega_0$.

Calculation of the OFPDs requires wave functions of a moving nucleon. Therefore boosting the rest frame wave function (2.30) to a frame moving with velocity $\vec{v}$. The effect of a Lorentz boost on the wave function can be represented by:

$$\begin{aligned}
\psi_{\vec{v}}\left(t,\vec{r}\right) &= S\left(\Lambda_{\vec{v}}\right) \;\; \psi\left(\left(t-\vec{v}\cdot\vec{r}\right)\cosh\omega;\;\; \vec{r}+\widehat{v}\cdot\vec{r}\,\left(\cosh\omega-1\right)-\vec{v}t\;\cosh\omega\right) \\
&= \exp\left(-i\epsilon_0(t-\vec{v}\cdot\vec{r})\cosh\omega\right) \\
&\quad \times S\left(\Lambda_{\vec{v}}\right)\;\psi\left(\vec{r}+\widehat{v}\cdot\vec{r}\,\left(\cosh\omega-1\right)-\vec{v}t\;\cosh\omega\right), \qquad (2.31)
\end{aligned}$$

where

$$S\left(\Lambda_{\vec{v}}\right) = \exp\left(\frac{\omega\hat{v}\cdot\vec{\alpha}}{2}\right) \;=\; \cosh\frac{\omega}{2} \;+\; \hat{v}\cdot\vec{\alpha}\;\sinh\frac{\omega}{2} \quad \textit{and} \quad \omega = \tanh^{-1}v \;. \qquad (2.32)$$

In practical calculations, it will be more convenient to use a momentum space wave function, $\varphi(k)$, which is related to the coordinate space wave function $\psi_{\vec{v}}(t,\vec{r})$ by a Fourier transformation,

$$\varphi(\vec{k}) \;=\; \sqrt{4\pi}NR^3 \begin{pmatrix} t_0(k) \\ \overrightarrow{\sigma}\cdot\widehat{k}\;t_1(k) \end{pmatrix}\chi\,, \qquad (2.33)$$

where

$$\begin{aligned}
t_0(k) &= \frac{j_0(\omega_0)\;\cos(kR) - j_0(kR)\;\cos\omega_0}{\omega_0^2 - \vec{k}^2R^2}\,, \\
t_1(k) &= \frac{j_0(kR)\;j_1(\omega_0)\;kR - j_0(\omega_0)\;j_1(kR)\;\omega_0}{\omega_0^2 - \vec{k}^2R^2}\,. \qquad (2.34)
\end{aligned}$$

Furthermore the following important assumption is made. Even though a momentum transfer Δ is given to the active quark, nevertheless after the interaction the nucleon still moves as a whole, meaning that in the realistic situation the nucleon wave function contains correlations. The moment transfer injected to a single quark is in turn transferred through correlations to the other constituents, and asymptotically is equally shared among them. These correlations are actually needed to compute GPDs, and in the simple MIT Bag model they are taken into account parameterizing the effective momentum transfer through the active quark as $\tilde{\Delta} = \eta\Delta$. In the unboosted quark calculation $\eta = 1 - \epsilon_0/M$. Ultimately, in calculations η is determined by fitting the electromagnetic form factors of the nucleon, expecting η to be around 1/3.

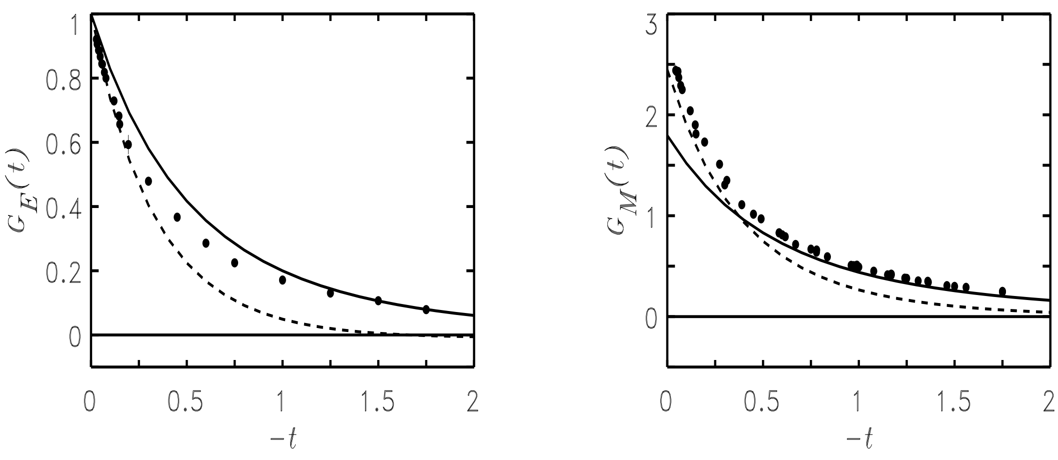

Figure 2.4: Left(right) panel: t dependence of the proton electric (magnetic) form factor for $\eta = 0.35$ (solid) and $\eta = 0.55$ (dashed). The data are from [31, 32].

In Fig. 2.4 experimental data on the electric and magnetic form factors are compared with model predictions at values of $\eta = 0.35$ and 0.55. Because at the small $|t|$ form factors are better described with $\eta = 0.55$, this value is chosen to parameterize OFPDs. Having fixed the model parameter η, the individual OFPDs as a function of x and ξ, for different values of t can be computed. The matrix elements in Eq. 2.6 are thus calculated using the boosted wave function of the active quark and the effective momentum transfer $\tilde{\Delta}$. Some results are shown in Fig. 2.5 and Fig. 2.6 for the OFPDs H and E respectively.

The dependence of quark OFPDs on ξ is quite weak, without a simple explanation for this. The t dependence however, is rather strong, as expected from the form factor behavior, Fig 2.4 [26]. In Fig. 2.7 the energy-momentum quark form factors combination $A(t) + B(t)$ is evaluated at different values of the parameter η. To estimate its limit at zero momentum transfer momentum $t = 0$ to the total parton angular momentum (see Eq. 2.29), the value $\eta = 0.55$ is chosen to model OFPDs. This value gives $2J_q = A(0) + B(0) \sim 0.7$.

Using models with no exact translational invariance, a different choice of frame for calculations could, in principle, give different results. Nevertheless, it is likely that the main features of these results will be weakly frame dependent, due to the agreement found with other experimental observables such as unpolarized and polarized forward quark distributions, and form factors G_E and G_M.

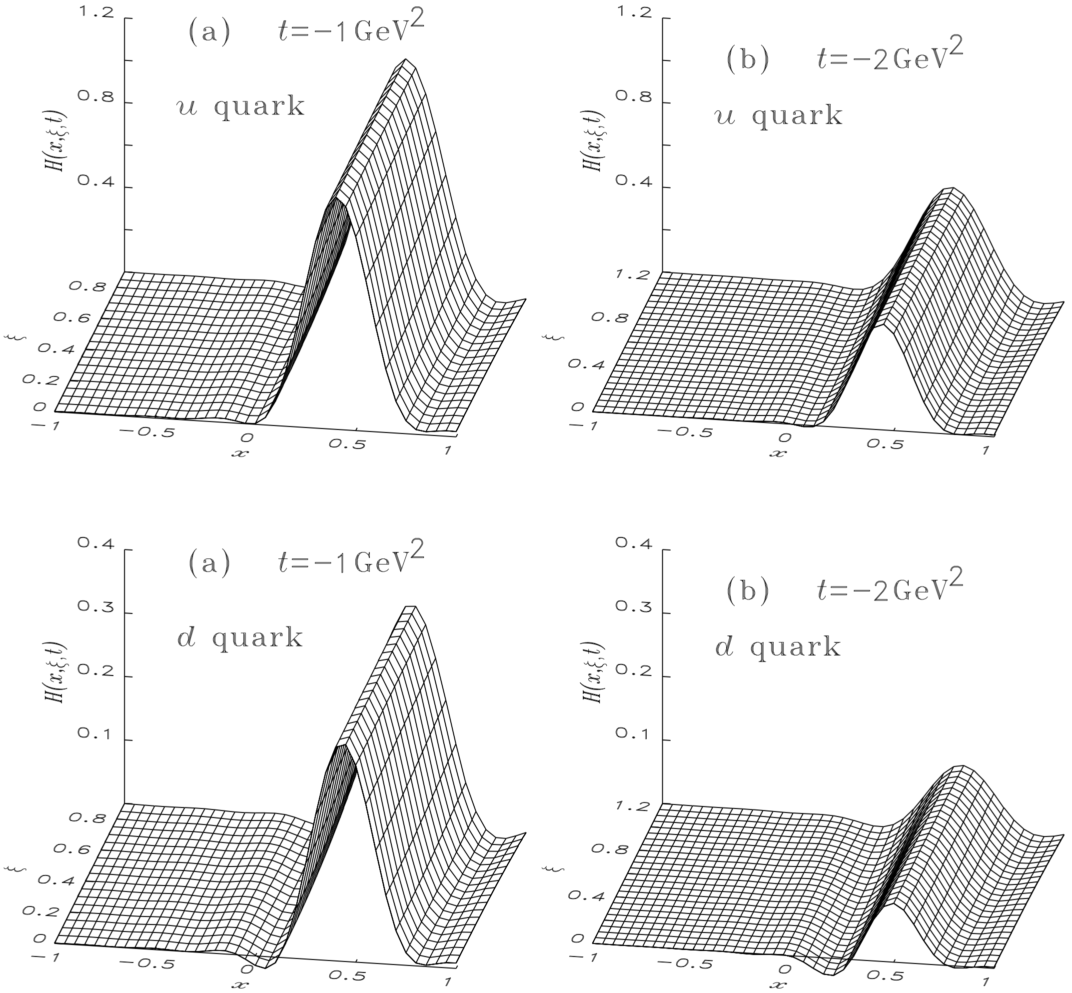

Figure 2.5: **Top (bottom) panels:** OFPDs $H(x, \xi, t)$ for the quark $u(d)$ as a function of x and ξ, for $t = -1$ GeV^2 (a) and $t = -2$ GeV^2 (b). The ξ dependence is extremely weak, while the t dependence is much stronger. The theoretical curves are calculated within the bag model [26].

Recently a new approach to the calculation of quark distribution functions has been developed [33] within the context of the chiral quark-soliton model (χQSM) of the nucleon [34]. This approach is essentially based on the $1/N_c$ expansion. Although in reality the number of colors is $N_c = 3$, the academic limit of large N_c is known to be a useful guideline. In this effective low-energy theory the nucleon is regarded as a state of N_c quarks and at large N_c is heavy and can be viewed as a classical soliton of the pion field [35, 36] using the *mean field theory*. Quarks are bound by a chiral field

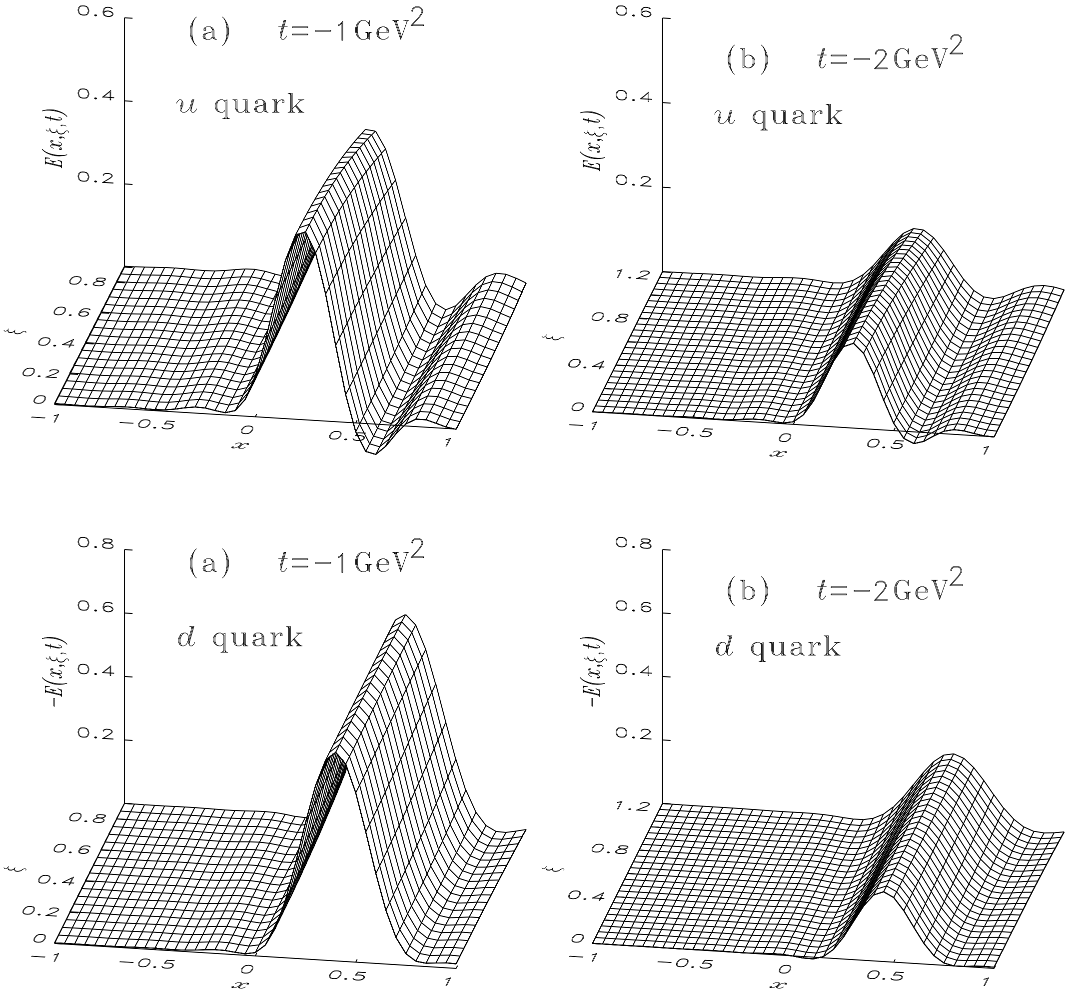

Figure 2.6: **Top (bottom) panels:** OFPDs $E(x, \xi, t)$ for the quark $u(d)$ as a function of x and ξ, for $t = -1$ GeV^2 (a) and $t = -2$ GeV^2 (b). The ξ dependence is extremely weak, while the t dependence is much stronger. The theoretical curves are calculated within the bag model [26].

configuration, namely a Goldston pions field (the 'soliton') whose energy coincides with the whole energy of quarks of the negative-energy Dirac continuum. The spectrum of the Dirac Hamiltonian is given by

$$H\Phi_n = E_n\Phi_n \ , \tag{2.35}$$

where $H(U) = -i\gamma^0\gamma^k\partial_k + M\gamma^0 U^{\gamma_5}$, M is the quark mass, due to spontaneous break-

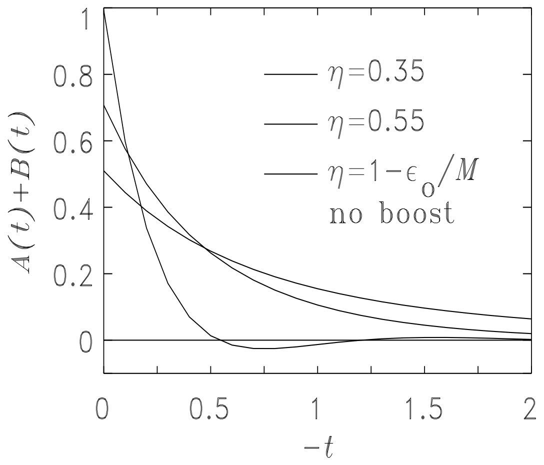

Figure 2.7: t dependence of the form factor $A(t){+}B(t)$ of the nucleon energy-momentum tensor at different values of the parameter η. The form factors are more accurately described at low t with $\eta = 0.55$ (dashed) which gives $A(0) + B(0) \sim 0.7$.

down of chiral symmetry,

$$U^{\gamma_5} \;=\; \exp\left[i\pi^a(x)\tau^a\gamma_5\right] \;=\; \frac{1+\gamma_5}{2}U + \frac{1-\gamma_5}{2}U^\dagger \quad ; \quad U \;=\; \exp\left[i\pi^a(x)\tau^a\right], \tag{2.36}$$

U being the $SU(2)$ chiral pion field. This Hamiltonian contains the free positive and sea Dirac continuum energy levels (distorted by the presence of the external pion field), and in principle, also discrete bound-state levels, if the pion field is strong enough. Supposing one bound level state, since the pion field is color blind, one can put N_c quarks on that level with energy $E_{\rm lev}$ in the color charge antisymmetric state. To get the nucleon mass one has to add $N_c E_{\rm lev}$ and the energy of the pion field [37]. The χQSM is a quantum field theoretical description of the nucleon, with explicit quark degrees of freedom, which allows an unambiguous identification of the quark as well as antiquark forward distributions in the nucleon. The general properties of these distributions (positivity, sum rules, Soffer inequalities, *etc.*) are nicely reproduced in this description. As an example, in Fig. 2.8 the results of calculations of $\Delta u(x) + \Delta d$, $\Delta\bar{u}(x){+}\Delta\bar{d}(x)$ [38] are compared with the $GRSV$ parametrization at leading order [39]. At the same time, the χQSM gives a good account of a variety of static properties of the nucleon and other baryons, such as masses and form factors G_E, G_M. Given the success in describing the above nucleon properties, this approach was used for a theoretical investigation of the nucleon OFPDs at a low normalization point [40].

The calculation of these distributions proceeds in the same way as that of the usual parton distributions [33]. In general one expands the quark fields, Eq. 2.6, in the basis of quark single–particle wave functions in the background pion field, Eq. 2.35, and obtains the nucleon OFPD matrix element by summing over all occupied single–particle states, i.e. the bound–state level and the negative–energy continuum. Fig. 2.9 shows the predicted dependence of $H(x, \xi, \Delta^2)$ on ξ and Δ^2 at fixed momentum transfer

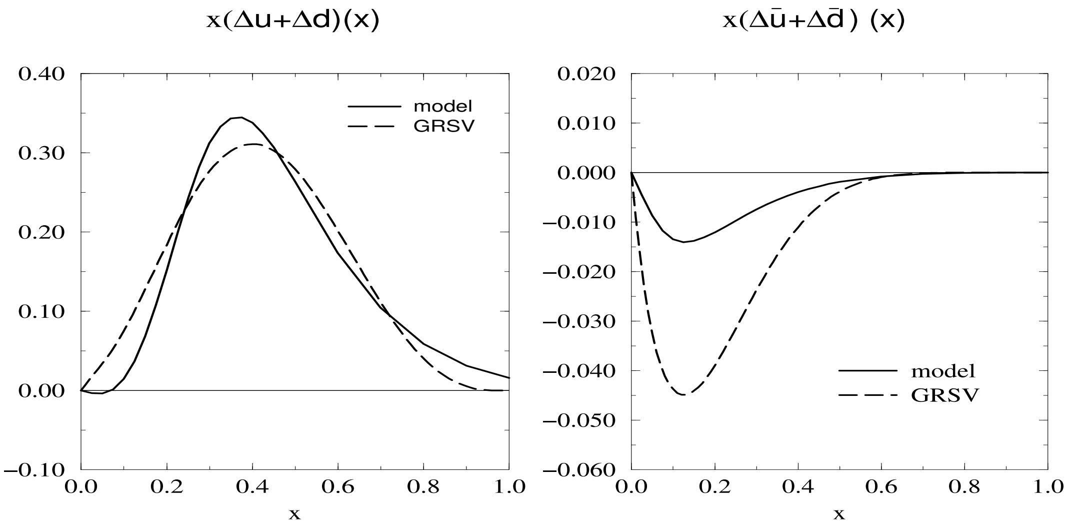

Figure 2.8: The quark soliton model results for $x[\Delta u(x) + \Delta d]$ and $x[\Delta\bar{u}(x) + \Delta\bar{d}(x)]$ are compared with the *GRSV*-LO parametrization versus x at the scale $\mu \sim 600\ MeV$.

of $\Delta^2 = -0.5$ GeV^2 for various values of ξ is plotted in the upper panel, and at fixed $\xi = 0.3$ for various values of momentum transfer in the bottom panel. The contribution of the Dirac continuum changes drastically the picture compared to the bag model predictions: the function $H(x, \xi, \Delta^2)$ shows a fast crossover around the points $x = \pm\xi/2$.

In the large N_c limit the nucleon OFPDs do not automatically go to zero at $x = 1$. However, at $x \gg 1/N_c$ the distributions behave as $\sim \exp(-\text{const}\cdot N_c x)$ and numerically, even for $N_c = 3$ all distributions computed are very small at $x \approx 1$.

In the χQSM, where the quarks interact through a highly non-linear pion field, the OFPDs exhibit a rich structure for $|x| < \xi$. The same model leads also to a t-dependence which can be approximated by $H(x, 0, t) \sim x^{-at} q(x)$ and deviates significantly from the commonly used factorized *ansatz* $H(x, 0, t) \sim F(t)q(x)$.

A simple method to estimate the OFPDs is their parameterization assuming physical ansatzes. The procedure is mainly based on the factorization of their dependence on x, ξ, t into functions each one depending on one of the three variables respectively. In the following some examples of OFPD parameterizations are shown [41].

The simplest ansatz is to write H and $\tilde{H}$ as a product of a form factor and a quark

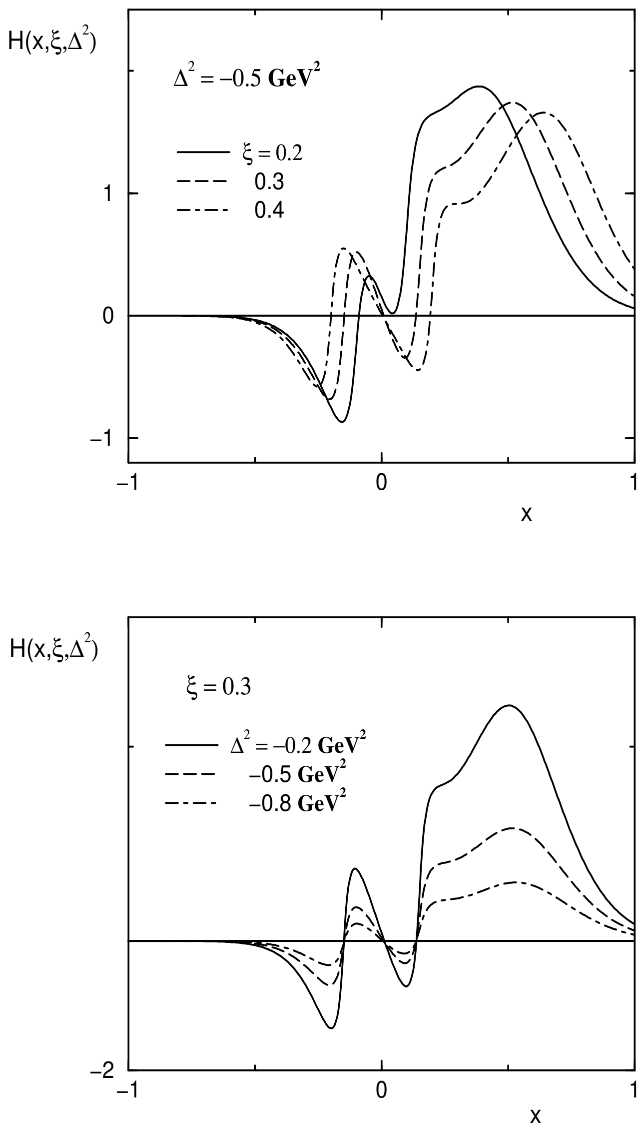

Figure 2.9: **Top panel:** isosinglet distribution $H(x, \xi, \Delta^2)$ for fixed $\Delta^2 = -0.5$ GeV^2 and various values of ξ. **Bottom panel:** isosinglet distribution $H(x, \xi, \Delta^2)$ for fixed $\xi = 0.3$ and various values of Δ^2. The predicted curves are from [40].

distribution function, neglecting any ξ dependence,

$$\begin{aligned} H^{u/p}(x,\xi,t) &= \frac{1}{2}u(x)F_1^{u/p}(t) , \\ H^{d/p}(x,\xi,t) &= d(x)F_1^{d/p}(t) , \\ H^{s/p}(x,\xi,t) &= 0 , \end{aligned} \tag{2.37}$$

where $u(x)$ and $d(x)$ and are the unpolarized quark distributions. This ansatz satisfies both

$$H^q(x,0,0) = q(x) , \tag{2.38}$$

and the sum rule

$$\int_{-1}^{+1} dx\ H^q(x,\xi,t) = F_1^q(t) . \tag{2.39}$$

To model $\tilde{H}^q$, one needs the corresponding polarized quark distributions. Following [42], where a next to leading order QCD analysis of inclusive polarized deep-inelastic lepton-nucleon scattering was performed and which yields an excellent fit of the world data, the input polarized densities (at a scale $Q_0^2 = 1$ GeV^2) are given by:

$$\begin{aligned} \Delta u_V(x,Q_0^2) &= \eta_u\, A_u\, x^{0.250}\ u_V(x,Q_0^2) , \\ \Delta d_V(x,Q_0^2) &= \eta_d\, A_d\, x^{0.231}\ d_V(x,Q_0^2) , \\ \Delta\bar{q}(x,Q_0^2) &= \eta_{\bar{q}}\, A_S\, x^{0.576}\ S(x,Q_0^2) , \end{aligned} \tag{2.40}$$

where a SU(3) symmetric sea is assumed (i.e. $\Delta\bar{q} \equiv \Delta\bar{u} = \Delta\bar{d} = \Delta\bar{s}$ and S represents the total sea distributions. The parameters are experimentally fixed as

$$\eta_u \approx 0.918 , \qquad \eta_d \approx -0.339 , \qquad \eta_{\bar{q}} \approx -0.054 . \tag{2.41}$$

The ansatz for $\tilde{H}^q$ is to multiply the polarized quark distributions by the axial form factor, neglecting any ξ-dependence and sea contribution, the last assumption being motivated by results in [117]:

$$\begin{aligned} \tilde{H}^{u/p}(x,\xi,t) &= \Delta u_v(x) g_A^{u/p}(t)/g_A^{u/p}(0) , \\ \tilde{H}^{d/p}(x,\xi,t) &= \Delta d_v(x) g_A^{d/p}(t)/g_A^{d/p}(0) , \end{aligned} \tag{2.42}$$

verifying by construction the forward limit

$$\tilde{H}^q(x,0,0) = \Delta q(x) , \tag{2.43}$$

axial form factors $g_A^{u/p}$ and $g_A^{d/p}$, and the sum rule

$$\int_{-1}^{+1} dx\ \tilde{H}^q(x, \xi, t) \ = \ g_A^q(t) \tag{2.44}$$

is satisfied within 10 %.

The dependence on ξ can be parameterized considering the *double distributions* formalism of GPDs introduced by Radyushkin [44]. These new distributions are F^q, K^q for quarks, $F^{\bar{q}}$, $K^{\bar{q}}$ for the anti-quarks, and are related to the *NFPD*s, which have a one to one relation with the *OFPD*. A guess for the helicity independent double distribution $F(\tilde{x}, y, t)$ was proposed in Ref. [45], as a product of a quark distribution function $q(\tilde{x})$, describing the momentum flow along p, and an asymptotic "meson-like" distribution amplitude $\sim y(1-\tilde{x}-y)$, describing the momentum flow along Δ. In the double distribution formalism the active quark with momentum k^+ is assumed to carry a fraction $\tilde{x}$ of the initial nucleon momentum p^+ plus a fraction y of the momentum transfer Δ^+:

$$k^+ = \tilde{x}p^+ - y\Delta^+. \tag{2.45}$$

From comparison with the formalism of *NFPD*s, one obtains the actual fraction of the nucleon momentum $X = k^+/p^+$

$$X \ = \ \tilde{x} + \zeta y\ . \tag{2.46}$$

Following the above assumptions, the parameterization of F is obtained:

$$F^q(\tilde{x}, y, t) \ = \ F_1^q(t)/F_1^q(0)\ q(\tilde{x})\ 6\,\frac{y(1-\tilde{x}-y)}{(1-\tilde{x})^3}\ , \tag{2.47}$$

where the t-dependent part is given by the form factor F_1. Similarly for the helicity dependent double distribution, this ansatz yields :

$$\tilde{F}^q(\tilde{x}, y, t) \ = \ g_A^q(t)/g_A^q(0)\ \Delta q(\tilde{x})\ 6\,\frac{y(1-\tilde{x}-y)}{(1-\tilde{x})^3}\ . \tag{2.48}$$

Considering the relations between the different GPDs formalisms, the OFPD H^q and $\tilde{H}^q$ are then constructed. As an example, in Fig. 2.10 the dependence on ξ, predicted by this model for the valence d-quark and total d-quark OFPDs, is shown.

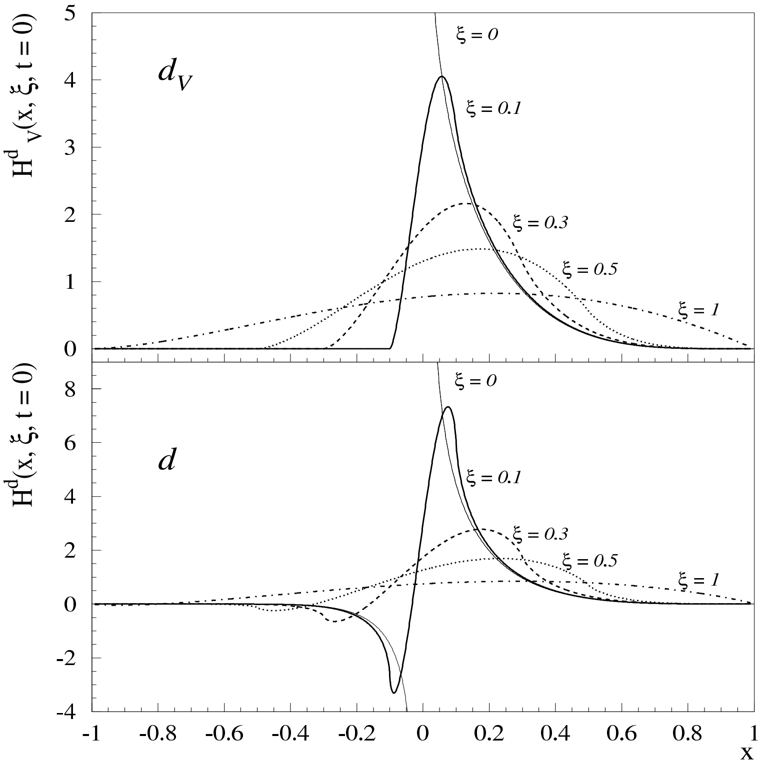

Figure 2.10: ξ dependence of the OFPD H^d at $t = 0$ using the parameterization described in the text and based on the MRST98 quark distributions [46]. **Upper panel:** valence d-quark OFPD. **Lower panel:** total d-quark OFPD. The thin lines ($\xi = 0$) correspond with the ordinary d-quark distributions (MRST98 parameterization at $Q^2 = 2$ GeV^2).

Chapter 3

$\pi^+\pi^-$ Hard Exclusive Electroproduction

The subject of this analysis is the hard exclusive leptoproduction of $\pi^+\pi^-$ pairs at *HERMES* off unpolarized proton and deuteron, and in the following the theoretical description of the process off protons is described. At the moment, no theoretical reference is available on the scattering off deuterons. The leptoproduction $e^+p \longrightarrow e^+p\pi^+\pi^-$ amplitude can be expressed in terms of the amplitude of virtual photons scattering:

$$\gamma^* p \longrightarrow \pi^+\pi^- p \ . \tag{3.1}$$

The process depends on three kinematic variables: the photon virtuality Q^2 [1], the square of the center of mass energy for the photon-proton system W, and the squared momentum transfer t to the target. Due to the factorization theorem [4], at large collision energy $W \to \infty$, at large virtuality of the photon $Q^2 \to \infty$, at fixed Bjorken variable x, and assuming the $\pi^+\pi^-$ invariant mass $m_{\pi\pi} \ll Q$, the amplitude of the reaction can be factorized as in the convolution of Eq. 2.4 (Fig. 2.2), and may be interpreted in the framework of GPDs. This general factorization theorem works with longitudinally polarized photons only, while in case of transverse polarized photon it is not possible to demonstrate its general validity. This amplitude is shown to be suppressed of $1/Q$ relative to the case of a longitudinal photon. In experimental data, as at *HERMES*, where events have Q^2 of few GeV, both contributions from longitudinal and transverse polarized photons are present.

In this analysis some angular distributions of the π^+ in the $\pi^+\pi^-$ rest system have been studied in the invariant mass range $0.3 < m_{\pi\pi} < 1.35$ GeV. Theoretical models derived in terms of GPDs show that these angular distributions receive only contri-

[1] Q^2 is defined as $Q^2 = -q^2$, q_μ being the four-momentum of the virtual photon.

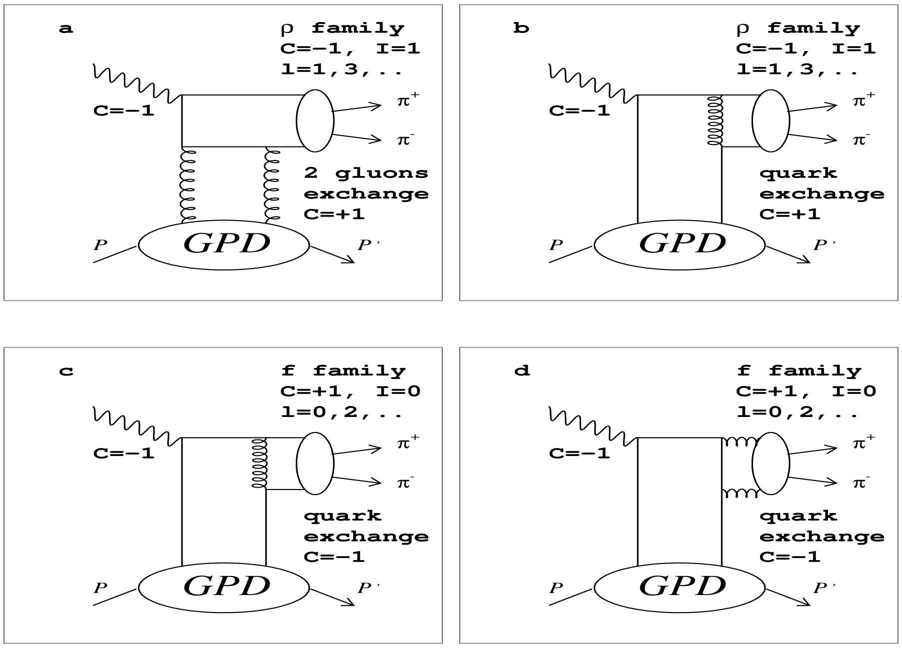

Figure 3.1: Leading twist diagrams for the hard exclusive reaction $e^+p \to e^+p\ \pi^+\pi^-$. The gluon exchange (*a)* gives rise to pions in the isovector state only, while the quark exchange (*b,c,d*) gives rise to pions both in the isoscalar and in the isovector state.

butions from the interference between the isoscalar channel $I = 0$ and the isovector channel $I = 1$.

3.1 Amplitude of the Process

In the asymptotic limit $Q^2 \to \infty$, when the reaction is switched on by longitudinal polarized photons only, the $\pi^+\pi^-$ exclusive production has been theoretically studied in [48,49]. The relevant diagrams for this reaction at leading twist are shown in Fig. 3.1. The pion pairs may be produced through gluon or quark exchange with the target, either from quark (Fig. 3.1a,b,c) or gluon fragmentation (Fig. 3.1d). The particular state describing the $\pi^+\pi^-$ pair, with the angular momentum quantum number l being odd or even, also defines unequivocally the quantum numbers C-Parity (C) and Strong Isospin (I) of this state. This feature can be understood if the hard and the DA sectors of the amplitude in Fig. 2.2 are considered as a whole amplitude, Fig. 3.2. Through the crossing relation [96], this new amplitude describes a process involving the incoming $q\bar{q}$ pair, the virtual photon $\gamma^\star$ and the outcoming produced $\pi^+\pi^-$ pair. The same description can be performed in the case of gluon exchange between the

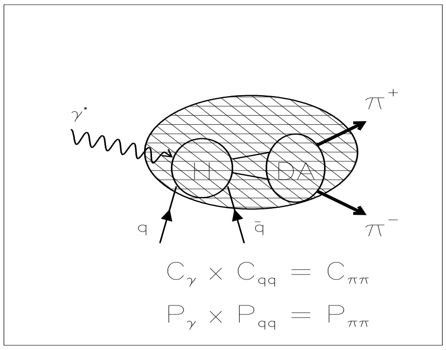

Figure 3.2: The hard and the meson sub-sectors of the $\pi^+\pi^-$ exclusive leptoproduction off a proton are considered as a whole amplitude which describes the photon scattering off a $q\bar{q}$ pair producing the pion pair. Quark and pion pairs have P-parity and C-parity of equal and opposite sign respectively.

photon with the nucleon target. The amplitude of 2π production is described through electromagnetic and strong forces which do conserve the C-parity. In this case the following C-parity conservation rule must be satisfied in the above sub-process:

$$C_\gamma \;\cdot C_{q\bar{q}\ (gg)} \;=\; C_{\pi^+\pi^-}\ , \tag{3.2}$$

where for the photon $C_\gamma = -1$ [50]. Therefore this quantum number for the $q\bar{q}$ pair and for the 2π system must have opposite sign. Defining the orbital angular momentum of one quark (pion) on respect to the $q\bar{q}$ (2π) center of mass system as $l_{q\bar{q}}$ ($l_{\pi\pi}$), and the total spin of the quark pair as $s_{q\bar{q}}$, the C-parity for the $q\bar{q}$ and the 2π system is found to be $(-1)^{l_{q\bar{q}}+s_{q\bar{q}}}$ and $(-1)^{l_{\pi\pi}}$ respectively. When pions are in the $C = 1$ state their quantum number l is even, while the negative C-parity $C = -1$ implies l odd. Furthermore, since the parity is conserved,

$$P_\gamma \;\cdot P_{q\bar{q}\ (gg)} \;=\; P_{\pi^+\pi^-}\ , \tag{3.3}$$

and $P_\gamma = 1$, the exchanged quark pair parity $(-1)^{l_{q\bar{q}}+1}$ and the pions parity $(-1)^{l_{\pi\pi}}$ must be equal. In principle, the pions can be produced in the isospin state $I = 0, 1, 2$ but, as shown in Fig. 3.3 the state $I = 2$ is not allowed due to isospin conservation in

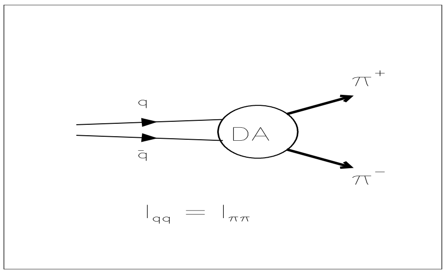

Figure 3.3: Quark and gluons produced from the hard scattering of photon with the nucleon, hadronize into a $\pi^+\pi^-$ pair through strong interaction, which conserves the isospin quantum number. Quarks may have $I = 0, 1$, implying that pions can not be produced in a $I = 2$ state.

strong interactions, which describe the pion' formation from hadronization of partons that may have $I = 1, 0$ only.

The choice of a particular isospin state is a consequence of the total symmetrization of the pions wave function,

$$\psi(2\pi) = \phi(\vec{r}) \cdot \chi(I) \ , \tag{3.4}$$

where the wave function has been factorized into its space and isospin dependences, which have symmetry $(-1)^{l_{\pi\pi}}$ and $(-1)^{I_{\pi\pi}}$ under particle interchange, respectively. This feature implies that the isospin is unequivocally determined by the orbital angular momentum of the pion state. From the above considerations, which may be extended to the two-gluon exchange amplitude, the $\pi^+\pi^-$ quantum numbers are therefore found to be the same as the f-meson's $(I, J^{PC} = 0, l^{++}_{even})$ or ρ-meson's $(I, J^{PC} = 1, l^{--}_{odd})$ ones, and due to this reason are called f-type or ρ-type respectively. The possible combinations of quantum numbers in the process are list in Tab. 3.1.

	$\pi^+\pi^-$ pair			$q\bar{q}$ (gg) exchanged pair			
$l_{\pi\pi}$	$C_{\pi\pi}$	$P_{\pi\pi}$	$I_{\pi\pi}$	C_{qq}	P_{qq}	C_{gg}	P_{gg}
odd $\Rightarrow$	-1	-1	1	+1	+1	+1	+1
even $\Rightarrow$	+1	+1	0	-1	+1	-	-

Table 3.1: The quantum number $l_{\pi\pi}$ of the pion system determines univocally the C-parity and P-parity of the exchanged quark (gluon) pairs and of the produced pion pairs. Due to parity conservation, an isoscalar $\pi^+\pi^-$ pair can not be produced through the two-gluon exchange mechanism, being $C_g = -1$.

The leading order amplitude for the reaction (3.1) corresponds to diagrams of the type shown in Fig. 3.1 and can be expressed in the form [49]

$$\begin{aligned}
T^{\pi^+\pi^-} &= \langle P', \pi^+\pi^- | J^{\mathrm{e.m.}} \cdot \varepsilon_L | P \rangle \\
&= -(4\pi e \alpha_s) \frac{1}{2Q} \int_{-1}^{1} dx \int_0^1 dz \\
&\times \Bigg\{ \frac{C_F}{N_c} \sum_f F_{ff}(x,\xi,t) \Phi_{ff}^{\pi^+\pi^-}(z,\zeta,m_{\pi\pi}) \Bigg[\frac{e_f}{z(x+\xi-i\epsilon)} + \frac{e_f}{(1-z)(x-\xi+i\epsilon)} \Bigg] \\
&- \frac{1}{N_c} \sum_f e_f F_{ff}(x,\xi,t) \Phi_G^{\pi^+\pi^-}(z,\zeta,m_{\pi\pi}) \Bigg[\frac{1}{z(1-z)} \Big(\frac{1}{x+\xi-i\epsilon} - \frac{1}{x-\xi+i\epsilon} \Big) \Bigg] \\
&+ \frac{1}{2N_c} \sum_f e_f F_G(x,\xi,t) \Phi_{ff}^{\pi^+\pi^-}(z,\zeta,m_{\pi\pi}) \Bigg[\frac{1}{z(1-z)} \Big(\frac{1}{x+\xi-i\epsilon} + \frac{1}{x-\xi+i\epsilon} \Big) \Bigg] \Bigg\} ,
\end{aligned} \tag{3.5}$$

where e_f is the electric charge of a quark of flavor f and ε_L^μ is the longitudinal photon polarization vector

$$\varepsilon_L^\mu = \frac{2\tilde{\xi}}{Q} \tilde{n}^\mu + \frac{Q}{4\tilde{\xi}} n^\mu , \tag{3.6}$$

being $\varepsilon_L^\mu = \frac{1}{Q}(q^3, 0, 0, q^0)$ in a frame with $n^\mu \propto (1,0,0,1)$ and $\tilde{n}^\mu \propto (1,0,0,-1)$. Terms inside the squared brackets in Eq. 3.5 refers to propagators of quark and/or gluons involved in the perturbative sector of the amplitude. The functions $F_{ff}(x,\xi,t)$ and $F_G(x,\xi,t)$ are OFPDs for quarks or gluons in the proton respectively defined as

$$\begin{aligned}
F_{ff}(x,\xi,t) &= \int \frac{d\lambda}{2\pi} e^{i\lambda x} \langle P' | T \Big[\bar{\psi}_f \Big(-\frac{\lambda n}{2} \Big) \not{n} \psi_f \Big(\frac{\lambda n}{2} \Big) \Big] | P \rangle , \\
F_G(x,\xi,t) &= \frac{1}{x} \int \frac{d\lambda}{2\pi} e^{i\lambda x} n^\mu n^\nu \langle P' | T \Big[F_\mu^{A\alpha} \Big(-\frac{\lambda n}{2} \Big) F_{\alpha\nu}^{A} \Big(\frac{\lambda n}{2} \Big) \Big] | P \rangle .
\end{aligned} \tag{3.7}$$

The gluon color index A is understood to be summed over. The two-pion distribution amplitudes

$$\begin{aligned}
\Phi_{ff}^{\pi^+\pi^-}(z,\zeta,m_{\pi\pi}) &\equiv \int \frac{d\lambda}{2\pi} e^{-i\lambda z (q'\cdot\tilde{n})} \langle \pi^+\pi^- | T \big[\bar{\psi}_f(\lambda\tilde{n}) \not{\tilde{n}} \psi_f(0) \big] | 0 \rangle , \\
\Phi_G^{\pi^+\pi^-}(z,\zeta,m_{\pi\pi}) &\equiv \frac{1}{\tilde{n}\cdot q'} \int \frac{d\lambda}{2\pi} e^{-i\lambda z (q'\cdot\tilde{n})} \tilde{n}^\mu \tilde{n}^\nu \langle \pi^+\pi^- | T \big[F_\mu^{A\alpha}(\lambda\tilde{n}) F_{\alpha\nu}^{A}(0) \big] | 0 \rangle
\end{aligned} \tag{3.8}$$

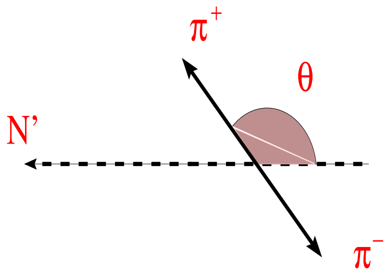

Figure 3.4: Scattering angle θ of π^+ in the $\pi^+\pi^-$ rest frame.

describe how a pion pair is produced by two quarks (Φ_{ff}) or gluons respectively (Φ_G). In Eq. 3.7-3.8 it is implied that the gauge link $\mathcal{P}[e^{(ig\int_{z_2}^{z_1} A_\mu dz^\mu)}]$ with $A_\mu = \sum_A t^A A_\mu^A$ is inserted between the two operators at different space-time coordinates, being t^A and A_μ^A the Gell-Mann $SU(3)$ matrices and the color fields respectively. The variable z is the fraction of the longitudinal (along the vector n) meson pair momentum $q' = q - \Delta$ [2] carried by one of the two partons produced in the hard interaction. The variable ζ characterizes the distribution of the longitudinal component of q' between the two pions and is given in terms of the momentum $k^{(+)}$ of the pion π^+ and the total momentum of the pion pair q' by

$$\zeta = \frac{k^{(+)} \cdot \tilde{n}}{q' \cdot \tilde{n}} \ . \tag{3.9}$$

This quantity is related to the scattering angle θ of the π^+ in the $\pi^+\pi^-$ center of mass system according to the direction and opposite versus of recoiled proton as in Fig 3.4 [51], by

$$\beta \cos\theta = 2\zeta - 1 \quad with \quad \beta \equiv \sqrt{1 - \frac{4m_\pi^2}{m_{\pi\pi}^2}} \ . \tag{3.10}$$

The pion pairs can be produced either through a resonance or a non-resonant channel. Their DA in Eq. 3.8 can be isospin decomposed and expressed in terms of only two independent quark 2πDA's corresponding to isospin $I = 0$ and $I = 1$ pair production respectively and one single gluon 2πDA with $I = 0$,

$$\begin{aligned} \Phi_{ff}^{\pi^+\pi^-}(z,\zeta,m_{\pi\pi}) &= \Phi^{I=0}(z,\zeta,m_{\pi\pi}) + \tau_3 \Phi^{I=1}(z,\zeta,m_{\pi\pi}) \ , \\ \Phi_G^{\pi^+\pi^-}(z,\zeta,m_{\pi\pi}) &= \Phi^G(z,\zeta,m_{\pi\pi}) \ . \end{aligned} \tag{3.11}$$

Taking into account the C-invariance of the underlying theory, the following symmetry

[2] The variable Δ is the four-momentum transferred to the target by the virtual photon.

properties for the three 2πDA's can be derived:

$$\begin{aligned}
\Phi^{I=0}(z,\zeta,m_{\pi\pi}) &= -\Phi^{I=0}(1-z,\zeta,m_{\pi\pi}) = \Phi^{I=0}(z,1-\zeta,m_{\pi\pi})\ ,\\
\Phi^{I=1}(z,\zeta,m_{\pi\pi}) &= \Phi^{I=1}(1-z,\zeta,m_{\pi\pi}) = -\Phi^{I=1}(z,1-\zeta,m_{\pi\pi})\ ,\\
\Phi^{G}(z,\zeta,m_{\pi\pi}) &= \Phi^{G}(1-z,\zeta,m_{\pi\pi}) = \Phi^{G}(z,1-\zeta,m_{\pi\pi})\ . \qquad (3.12)
\end{aligned}$$

Using the decompositions (3.11) and the symmetry relations (3.12) the transition amplitude for $\pi^+\pi^-$ exclusive production can be written in the form

$$T^{\pi^+\pi^-} = T^{I=0} + T^{I=1} \qquad (3.13)$$

with

$$\begin{aligned}
T^{I=0} &= -(4\pi e\alpha_s)\frac{C_F}{N_c}\frac{1}{12Q}\,\tilde{\Phi}^{I=0}\Big(2I_u^- - I_d^-\Big)\ ,\\
T^{I=1} &= -(4\pi e\alpha_s)\frac{C_F}{N_c}\frac{1}{12Q}\,\tilde{\Phi}^{I=1}\Big(2I_u^+ + I_d^+ + \frac{3}{C_F}I_G\Big)\ , \qquad (3.14)
\end{aligned}$$

where $C_F = 4/3$. Here $\tilde{\Phi}^{I=0}$ and $\tilde{\Phi}^{I=1}$ are functions of $m_{\pi\pi}$ and $\cos\theta$ defined as

$$\begin{aligned}
\tilde{\Phi}^{I=0} &= \int_0^1 dz \frac{(1-2z)\Phi^{I=0}(z,\zeta,m_{\pi\pi}) - \frac{2}{C_F}\Phi^G(z,\zeta,m_{\pi\pi})}{z(1-z)}\ ,\\
\tilde{\Phi}^{I=1} &= \int_0^1 dz \frac{\Phi^{I=1}(z,\zeta,m_{\pi\pi})}{z(1-z)}\ , \qquad (3.15)
\end{aligned}$$

and $I_f^\pm$, I_G are the following integrals over OFPD's depending on $\xi = x_{Bj}/(2-x_{Bj})$ and t:

$$\begin{aligned}
I_f^\pm &= \int_{-1}^1 dx F_{ff}(x,\xi,t)\left[\frac{1}{x+\xi-i\epsilon} \pm \frac{1}{x-\xi+i\epsilon}\right]\ ,\\
I_G &= \int_{-1}^1 dx F_G(x,\xi,t)\left[\frac{1}{x+\xi-i\epsilon} + \frac{1}{x-\xi+i\epsilon}\right]\ . \qquad (3.16)
\end{aligned}$$

The differential cross section of the electroproduction process is given in terms of its T-matrix element $\tilde{T}^{\pi^+\pi^-}$ by

$$\frac{d\sigma^{\pi^+\pi^-}}{dx_{Bj}dy\,dt\,dm_{\pi\pi}\,d\cos\theta} = \frac{m_{\pi\pi}\beta}{8(4\pi)^5 p\cdot l}\sum_{S',s'}|\tilde{T}^{\pi^+\pi^-}|^2\,, \qquad (3.17)$$

where l is the initial positron four-momentum, y is defined by $y = (p\cdot q)/(p\cdot l)$ and corresponds to the energy loss of the scattered lepton in the proton rest frame, and the sum is understood to run over the spin polarizations of the scattered nucleon and lepton. The T-matrix element of the electroproduction reaction $e^-(l) + P(p) \to \pi\pi(q') + e^-(l-q) + P'(p+\Delta)$ is related to the amplitude of the sub-process (3.1) calculated above by

$$\tilde{T}^{\pi\pi} = \bar{u}(l-q,s')\gamma_\mu u(l,s)\varepsilon_L^\mu \frac{-e}{Q^2} T^{\pi\pi} \,. \tag{3.18}$$

Summing over all the spin states one gets

$$\sum_{S's'} |\tilde{T}^{\pi\pi}|^2 = \frac{2e^2(1-y)}{p\cdot l\, x_{Bj} y^3} \sum_{S'} |T^{\pi\pi}|^2 \,. \tag{3.19}$$

This analysis is valid only up to $1/Q$ power corrections, which are not necessarily negligible at realistic scales in experiments like *HERMES*. In any case, these higher twist contributions, not theoretically evaluated yet, usually cancel out in cross-section ratios and in asymmetries of the cross-section [52]. In this analysis, particular asymmetries of the cross-section have been measured, which are supposed to be weakly sensitive to higher twist effects.

3.2 $2\pi DA$'s and GPD's Parameterization

The two-pion distribution amplitudes defined in Eq.3.8 describe the fragmentation of a pair of collinear partons (quarks or gluons) into the final pion pair. In this section some constraints for these functions are discussed in order to construct realistic models for them.

Following [53] both quark and gluon 2πDAs can be decomposed in eigenfunctions of the ERBL [54,55] evolution equation (i.e the Gegenbauer polynomials[3] $C_n^{3/2}(2z-1)$), and in partial waves of produced pions (i.e the Gegenbauer polynomials $C_l^{1/2}(\beta^{-1}(2\zeta-1))$). It is worth to mention that Gegenbauer polynomials $C_l^{1/2}$ corresponds to Legendre polynomials P_l. In Tab. 3.2 Gegenbauer polynomials $C_n^\lambda(x)$ of the first four orders are listed. Generically, the decomposition for both isoscalar and isovector $2\pi DA$s has the form:

$$\Phi(z,\zeta,m_{\pi\pi}^2) = 6z(1-z)\sum_{n=0}^{\infty}\sum_{l=0}^{n+1} B_{nl}(m_{\pi\pi}^2) C_n^{3/2}(2z-1) C_l^{1/2}(\beta^{-1}(2\zeta-1)). \tag{3.20}$$

The evolution equation for the coefficient B_{nl} is

$$B_{nl}(m_{\pi\pi}^2;Q^2) = B_{nl}(m_{\pi\pi}^2;Q_0^2)\left(\frac{\alpha_s(Q^2)}{\alpha_s(Q_0^2)}\right)^{(\gamma_n-\gamma_0)/(2\beta_0)} \,, \tag{3.21}$$

[3]Gegenbauer polynomials or ultraspheric polynomials consists in a orthogonal complete basis for the space $[-1,+1]$ [56].

n	$P_n^\lambda(x)$
0	1
1	$2\lambda x$
2	$-\lambda + 2\lambda(1+\lambda)x^2$
3	$-2\lambda(1+\lambda)x + 4/3\lambda)(1+\lambda)(2+\lambda)x^3$

Table 3.2: First four orders of Gegenbauer polynomials of fractional index λ. They correspond to Legendre polynomials when $\lambda = 1/2$.

where $\beta_0 = 11 - 2/3N_f$ and

$$\gamma_n = \frac{8}{3}\Big(1 - \frac{2}{(1+n)(2+n)} + 4\sum_{k=2}^{n+1}\frac{1}{k}\Big) \quad , \quad \gamma_n > \gamma_{n-1} \ .$$

Due to the decomposition of Eq. 3.20 and to Eq. 3.21 a simple prediction for the ratio of the amplitude for the the hard $\pi^+\pi^-$ production in $P-$ and $F-$ waves, at large virtuality of the incident photon, fixed $m^2_{\pi\pi}$ and x_{Bj} can be made:

$$\frac{F\text{−wave amplitude}}{P\text{−wave amplitude}} \sim \frac{1}{\log(Q^2)^{50/(99-6N_f)}} \ , \tag{3.22}$$

or generically for the $2k+1$ wave:

$$\frac{(2k+1)\text{−wave amplitude}}{P\text{−wave amplitude}} \sim \frac{1}{\log(Q^2)^{\gamma_{2k}/(2\beta_0)}} \ . \tag{3.23}$$

From the above ratio, in this kinematic regime, the 2π production in states with $l > 2$ is strongly suppressed, and therefore its contribution is neglected.

Using the symmetry properties of Eq. 3.12 one obtains that the index n goes over even and the index l goes over odd numbers for isovector 2πDAs. On the contrary, for the isoscalar 2πDAs the index n goes over odd and the index l goes over even numbers.

The quark and gluon 2πDA decomposition reads

$$
\begin{aligned}
\Phi^{I=0}(z,\zeta,m_{\pi\pi}) &= 6z(1-z)\sum_{\substack{n=1\\ \text{odd}}}^{\infty}\sum_{\substack{l=0\\ \text{even}}}^{n+1} B_{nl}^{I=0}(m_{\pi\pi})C_n^{3/2}(2z-1)P_l(\beta^{-1}(2\zeta-1)) \\
\Phi^{I=1}(z,\zeta,m_{\pi\pi}) &= 6z(1-z)\sum_{\substack{n=0\\ \text{even}}}^{\infty}\sum_{\substack{l=1\\ \text{odd}}}^{n+1} B_{nl}^{I=1}(m_{\pi\pi})C_n^{3/2}(2z-1)P_l(\beta^{-1}(2\zeta-1)) \\
\Phi^{G}(z,\zeta,m_{\pi\pi}) &= 30z^2(1-z)^2\sum_{\substack{n=0\\ \text{even}}}^{\infty}\sum_{\substack{l=0\\ \text{even}}}^{n+2} A_{nl}^{G}(m_{\pi\pi})C_n^{5/2}(2z-1)P_l(\beta^{-1}(2\zeta-1)).
\end{aligned}
\tag{3.24}
$$

With the choice of Legendre polynomials for the ζ-expansion the above decomposition is directly related to the partial wave expansion of the resulting production amplitude for pion pairs.

Soft pion theorems provide pions properties in the zero mass limit $m_{\pi\pi}^2 \to 0$, and in the studied kinematic regime, the above condition can be satisfied when the four-momentum of one of the two pions goes to zero. In this limit, the 2πDAs can be related to the distribution amplitude of a single pion $\varphi_\pi(z)$ [53],

$$
\begin{aligned}
\Phi^{I=0}(z,\zeta=1,m_{\pi\pi}=0) &= \Phi^{I=0}(z,\zeta=0,m_{\pi\pi}=0)=0 \\
\Phi^{I=1}(z,\zeta=1,m_{\pi\pi}=0) &= -\Phi^{I=1}(z,\zeta=0,m_{\pi\pi}=0)=\varphi(z) \\
\Phi^{G}(z,\zeta=1,m_{\pi\pi}=0) &= \Phi^{G}(z,\zeta=0,m_{\pi\pi}=0)=0\,.
\end{aligned}
\tag{3.25}
$$

Additional constrains are provided by the crossing relations between the quark and gluon 2πDA's and the corresponding forward and off-forward parton distributions in the pion [53, 57], Fig. 3.5. Expressed in terms of the coefficients B_{nl}^I and A_{nl}^G, in the limit of zero transferred momentum $t=0$ they take the form

$$
\begin{aligned}
B_{n-1,n}^{I=0}(0) &= \frac{2}{3}\frac{2n+1}{n+1}\int_0^1 dx\, x^{n-1}\frac{1}{N_f}\sum_f (q_\pi^f(x)+q_\pi^{\bar f}(x)) \\
B_{n-1,n}^{I=1}(0) &= \frac{2}{3}\frac{2n+1}{n+1}\int_0^1 dx\, x^{n-1}(q_{\pi^+}^u(x)-\bar{q}_{\pi^+}^{\bar u}(x)) \\
A_{n-2,n}^{G}(0) &= \frac{4}{5}\frac{2n+1}{(n+1)(n+2)}\int_0^1 dx\, x^{n-1}g_\pi(x)\,,
\end{aligned}
\tag{3.26}
$$

where $q_\pi^f(x)$, and $g_\pi(x)$ are the usual quark and gluon distributions in the pion. Using these relations one obtains the normalization of the 2πDA's $\Phi^{I=0}$ and Φ^G at $m_{\pi\pi}=0$,

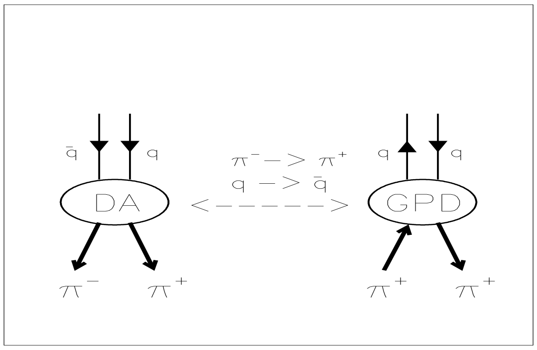

Figure 3.5: Crossing relation provides a relation between $2\pi DA$ and pion GPD.

and $\Phi^{I=1}$ for arbitrary values of $m_{\pi\pi}$ expressed in terms of the electromagnetic pion form factor $F_\pi(m_{\pi\pi})$:

$$\begin{aligned}
\int_0^1 dz(2z-1)\Phi^{I=0}(z,\zeta,m_{\pi\pi}=0) &= -\frac{4}{N_f}\, M_2^Q\zeta(1-\zeta) \\
\int_0^1 dz\Phi^{G}(z,\zeta,m_{\pi\pi}=0) &= -2M_2^G\zeta(1-\zeta) \\
\int_0^1 dz\Phi^{I=1}(z,\zeta,m_{\pi\pi}) &= (2\zeta-1)F_\pi(m_{\pi\pi})\ , \qquad (3.27)
\end{aligned}$$

where M_2^Q and $M_2^G = 1 - M_2^Q$ are the momentum fractions carried by quarks or gluons respectively in the pion. The Q^2-evolution of coefficients B_{nl} in Eq. 3.21 allows one to determine the asymptotic shape at large Q^2 of 2πDA's. In the asymptotic limit only the coefficients $B_{10}^{I=0}$, $B_{12}^{I=0}$, $B_{01}^{I=1}$, A_{00}^G, and A_{02}^G do not vanish. Therefore the asymptotic expression for the isovector 2πDA has the form

$$\begin{aligned}
\Phi^{I=1}(z,\zeta,m_{\pi\pi}) &= 6z(1-z)(2\zeta-1)F_\pi(m_{\pi\pi})\,, \\
\Phi^{I=0}(z,\zeta,m_{\pi\pi}=0) &= -\frac{120M_2^Q}{N_f}z(1-z)(2z-1)\zeta(1-\zeta) \\
\Phi^{G}(z,\zeta,m_{\pi\pi}=0) &= -60M_2^G z^2(1-z)^2\zeta(1-\zeta)\,. \qquad (3.28)
\end{aligned}$$

The $m_{\pi\pi}$-dependence of the 2πDA's can be analyzed by means of dispersion relations [53]. In the region $m_{\pi\pi}^2 < 16m_\pi^2$ the imaginary part of a 2πDA is related to the elastic pion-pion scattering amplitude by Watson's theorem [58]. As an example, for the coefficients of $\Phi^{I=0}$ this relation can be written in the following dispersion relation form

$$B_{nl}^{I=0}(m_{\pi\pi}) = \sum_{k=0}^{N-1}\frac{m_{\pi\pi}^{2k}}{k!}\frac{d^k}{d(m_{\pi\pi}^2)^k}B_{nl}^{I=0}(0) + \frac{m_{\pi\pi}^{2N}}{\pi}\int_{4m_\pi^2}^{\infty} ds\frac{\tan(\delta_l^0(s))\mathrm{Re}\{B_{nl}^{I=0}(\sqrt{s})\}}{s^N(s-m_{\pi\pi}^2-i\epsilon)} \qquad (3.29)$$

where δ_l^I are the two pion phase shifts. Solutions of the above dispersion can be written in the form

$$\frac{B_{nl}^{I=0}(m_{\pi\pi})}{B_{nl}^{I=0}(0)} = f_l(m_{\pi\pi}) = \exp\left[i\delta_l^0(m_{\pi\pi}^2) + \frac{m_{\pi\pi}^2}{\pi}\mathrm{Re}\left\{ \int_{4m_\pi^2}^{\infty} ds \frac{\delta_l^0(s)}{s(s-m_{\pi\pi}^2 - i\epsilon)} \right\} \right] \tag{3.30}$$

where $f_l(m_{\pi\pi})$ are called Omnès functions [59]. In principle, the solution of Eq. 3.30 is valid only below the two-pions threshold $m_{\pi\pi}^2 < 16m_\pi^2$, however, the deviations due to inelastic pion-pion scattering are expected to be small up to rather high energies. In terms of the Omnès functions $f_l(m_{\pi\pi})$, the asymptotic 2πDA's $\Phi^{I=0}$ and Φ^G take the form

$$\begin{aligned} \Phi^{I=0}(z,\zeta,m_{\pi\pi}) &= -\frac{120M_2^Q}{N_f} z(1-z)(2z-1) \\ &\cdot \left[\frac{3C-\beta^2}{12} f_0(m_{\pi\pi})P_0(\cos\theta) - \frac{\beta^2}{6} f_2(m_{\pi\pi})P_2(\cos\theta) \right] \\ \Phi^G(z,\zeta,m_{\pi\pi}) &= -60M_2^G z^2(1-z)^2 \\ &\cdot \left[\frac{3C-\beta^2}{12} f_0(m_{\pi\pi})P_0(\cos\theta) - \frac{\beta^2}{6} f_2(m_{\pi\pi})P_2(\cos\theta) \right] . \end{aligned} \tag{3.31}$$

The constant C in Eqs. 3.31 plays the role of an integration constant in the Omnès solution of the corresponding dispersion relation. Using the χQSM for calculations of $B_{nl}(m_{\pi\pi})$ at low energies [53] one finds the constant C to be equal to:

$$C = 1 + bm_\pi^2 + \mathcal{O}(m_\pi^4) \quad with \quad b \approx -1.7\,\mathrm{Ge}V^{-2} . \tag{3.32}$$

Using the above expressions the integrals in Eq. 3.15 can be evaluated:

$$\begin{aligned} \tilde{\Phi}^{I=0} &= \left(\frac{40M_2^Q}{N_f} + \frac{20M_2^G}{C_F} \right) \left[\frac{3C-\beta^2}{12} f_0(m_{\pi\pi})P_0(\cos\theta) - \frac{\beta^2}{6} f_2(m_{\pi\pi})P_2(\cos\theta) \right] \\ \tilde{\Phi}^{I=1} &= 6\beta F_\pi(m_{\pi\pi})P_1(\cos\theta) . \end{aligned} \tag{3.33}$$

The GPDs defined in Eq. 3.7 are decomposed into different Lorentz structures adopting the OFPD formalism:

$$\begin{aligned} F_{ff}(x,\xi,t) &= H_f(x,\xi,t)\,\bar{u}(p',S')\not{n}u(p,S) + E_f(x,\xi,t)\,\bar{u}(p',S')\frac{i\sigma_{\mu\nu}n^\mu\Delta^\nu}{2m_N}u(p,S) \\ F_G(x,\xi,t) &= H_G(x,\xi,t)\,\bar{u}(p',S')\not{n}u(p,S) + E_G(x,\xi,t)\,\bar{u}(p',S')\frac{i\sigma_{\mu\nu}n^\mu\Delta^\nu}{2m_N}u(p,S) . \end{aligned} \tag{3.34}$$

The functions $H_f(x,\xi,t)$ and $H_G(x,\xi,t)$ are modeled using Radyushkin's double distributions F, K [45] introduced in Section 2.3, adopting the ansatz $F(\tilde{x},y;t=0) = q(\tilde{x})\,\pi(\tilde{x},y)$ (for quark distributions) and $F(\tilde{x},y;t=0) = \tilde{x}\,G(\tilde{x})\,\pi(\tilde{x},y)$ (for gluon distributions), where $q(\tilde{x})$, $G(\tilde{x})$ are the ordinary quark and gluon parton distributions in the nucleon and $\pi(\tilde{x},y)$ is a profile function chosen to be $\pi(\tilde{x},y) = 6\,y(1-\tilde{x}-y)(1-\tilde{x})^{-3}$ for quarks and $\pi(\tilde{x},y) = 30\,y^2(1-\tilde{x}-y)^2(1-\tilde{x})^{-5}$ for gluons. The forward parton distributions are modeled using the MRSA parameterizations of the reference [60] at $Q^2 = 4\,\mathrm{Ge}V^2$. For the t-dependence of the OFPDs the factorized ansatz [61, 62] is used, motivated by sum rules that relate their first moments to form factors. The quark distributions are constrained by

$$\int_{-1}^{1} dx H_f(x,\xi,t) = F_1^{f/p}(t) \;, \tag{3.35}$$

with the Pauli form factor F_1 of the proton with respect to the flavor f. Nucleon form factors are parameterized as in [63] taking into account the relations

$$F_1^{u/p} = 2F_1^p + F_1^n \,, \quad F_1^{d/p} = 2F_1^n + F_1^p \;, \tag{3.36}$$

which are valid if the contribution of strange (and heavier) quarks to the nucleon form factor is neglected. The same factorization ansatz is applied for $H_G(x,\xi,t)$:

$$H_G(x,\xi,t) = H_G(x,\xi,0)\frac{F_\theta(t)}{F_\theta(0)} \;, \tag{3.37}$$

with the gluon form factor F_θ of the proton defined by

$$\langle p'|G_{\mu\lambda}(0)G^{\lambda}_{\ \nu}(0)|p\rangle = (2p_\mu p_\nu - \frac{1}{2}g_{\mu\nu}m_N^2)F_\theta(t) \;, \tag{3.38}$$

and parameterized as in [64].

In [47] it is shown that the GPDs in the double distributions formalisms are not complete and that an additional term has to be added, the Polyakov-Weiss *D-term*. This term is taken into account and estimated from the χQSM [40], obtaining for the function $D(x)$ the following numerical estimate:

$$D(x) = -4\;(1-x^2)\Big[C_1^{3/2}(x) + 0.3\;C_3^{3/2}(x) + 0.1\;C_5^{3/2}(x)\Big] \;, \tag{3.39}$$

The OFPDs $E_f(x,\xi,t)$ are less constrained compared to $H_f(x,\xi,t)$ because they have no forward limit to standard parton distributions, and therefore are modeled using the sum rule

$$\int_{-1}^{1} dx\, x \sum_f \Big[H_f(x,\xi,t) + E_f(x,\xi,t)\Big] = \;\textit{independent of}\;\xi\,. \tag{3.40}$$

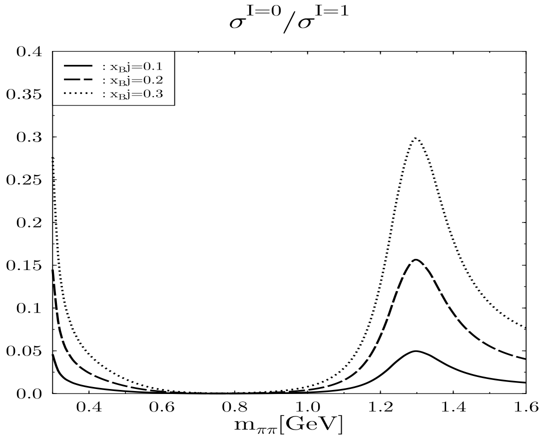

Figure 3.6: The ratio of the cross sections for the isoscalar and isovector $\pi^+\pi^-$ exclusive electroproduction as a function of $m_{\pi\pi}$ at different x_{Bj} values.

3.3 Theoretical Predictions for the Cross Section

In the previous section the analytical expressions for the cross sections were determined in the framework of GPDs of the nucleon and $2\pi DA$s. The distribution amplitudes have been parameterized in terms of the electromagnetic pion form factor, the Omnès functions $f_0(m_{\pi\pi})$ and $f_2(m_{\pi\pi})$, and the momentum fraction M_2^Q carried by the quarks in the pion.

If the number of flavors is chosen to be $N_f = 3$ the number of parameters can be reduced. In fact, from Eq. 3.33, M_2^Q is found to enter the expression for the cross sections in the combination

$$40M_2^Q/N_f + 20M_2^G/C_F \;=\; 20/C_F + (40/N_f - 20/C_F)M_2^Q \;, \tag{3.41}$$

which is weakly dependent on the value of M_2^Q when $N_f = 3$.

The pion form factor $F_\pi(m_{\pi\pi})$ entering the isovector 2πDA is modeled using its parameterization given in [65]. The Omnès functions may contain information about the $\pi\pi$ resonances and the non-resonant background. The function $f_2(m_{\pi\pi})$ is dominated by the $f_2(1270)$ resonance and, in the expression of Eq. 3.30 for $f_2(m_{\pi\pi})$, the D-wave pion scattering phase shift δ_2^0 given by the Breit–Wigner contribution of the $f_2(1270)$ resonance is chosen. For the the Omnès function $f_0(m_{\pi\pi})$ the approximation in [66], where the contribution from the f_0 meson decay is not considered, is used. With all the above assumptions, in Fig. 3.6, for different $x_{Bj} = 0.1, 0.2, 0.3$ the ratio of the differential cross sections for the production of pion pairs with isospin $I = 0$ and $I = 1$ as a function of the $m_{\pi\pi}$ invariant mass of the two pions is shown. The squared momentum transfer t has been integrated from $-0.6\,\mathrm{Ge}V^2$ to $-t_{\min} = -m_N^2 x_{Bj}^2/(1 - x_{Bj})$. The

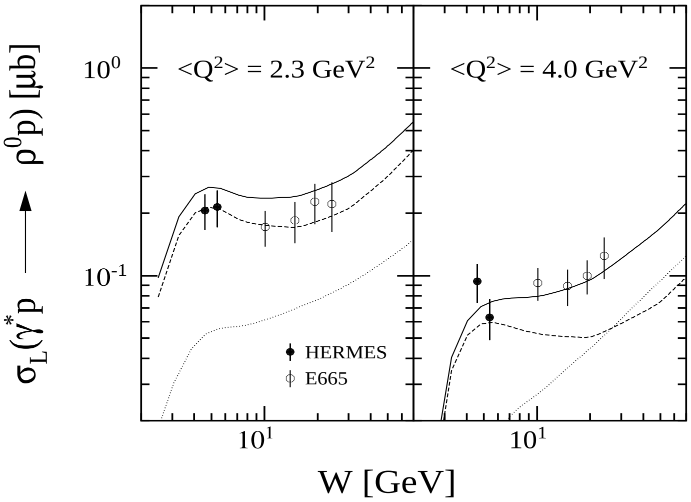

Figure 3.7: The longitudinal component of the virtual-photoproduction cross section for ρ^0 production versus W at average Q^2 values of 2.3 (left) and 4.0 GeV^2 (right). The dashed (dotted) curves represent the quark (two-gluon) exchange contributions. The solid lines represent the results of the calculations of Refs. [62, 68].

plot shows that, for $I = 0$, relatively large contribution to the cross section is expected at small $m_{\pi\pi}$, i.e. close to the threshold due to the S-wave $\pi^+\pi^-$ non-resonant production, and around $1.3\,GeV$ due to D-wave $\pi^+\pi^-$ production which is dominated by the $f_2(1270)$ resonance. However, near the ρ^0 resonance, i.e. around $0.770\,GeV$, the isoscalar contribution is negligible compared to the production of isovector pion pairs. Results in Fig. 3.6 show that the most favorable kinematic region for observables which involve the isoscalar channel is in the two $m_{\pi\pi}$ regions above or below the ρ^0 resonance and at relatively large values of x_{Bj}. In fact, at small values of x_{Bj}, pions are produced mostly in the isovector state, because the dominant mechanism is the two-gluon exchange with positive C-parity (Fig. 3.1a). Instead at large x_{Bj} the production of pion pairs is dominated by $q\bar{q}$ exchange (Fig. 3.1b,c,d) which leads to a sizable admixture of pion pairs with isospin zero. The above conclusions may be explained considering that at large x_{Bj}, mainly valence quarks may be probed inside the nucleon, Fig. A.3 bottom left panel, which favorites the $q\bar{q}$ exchange mechanism in the studied process, while at small x_{Bj} the inner nucleon structure is described by sea quarks and gluons. In particular the gluon distribution dominates the quark one in this Bjorken regime and, as consequence, the $\pi^+\pi^-$ pairs are mainly produced through the two-gluon exchange mechanism with the nucleon target.

Recently, data about the process $\gamma_L^\star p \longrightarrow \rho_L^0 p$, with $\gamma_L^\star$ and ρ_L^0 both longitudinally polarized, have been reported by the *HERMES* Collaboration [67] for Q^2 up to 5 GeV^2 and around $W \sim 5$ GeV. The comparison of the theoretical predictions [62] with data is shown in Fig. 3.7, where calculations are performed with quark exchange mechanism (dashed curves), with the two-gluon exchange (dotted curves), and with the sum of both (full curves). Results in the figure confirm a clear dominance of the quark exchange mechanism in this intermediate W range, which corresponds to a medium value of x_{Bj}, being $< x_{Bj} > \sim Q^2/W^2 \ \sim 0.1$.

The $\pi^+\pi^-$ production with $C = +1$ at small x_{Bj} requires at least three gluons in the t-channel, which gives an amplitude that is power suppressed relative to the leading quark-antiquark or two-gluon exchange in the GPD framework. In the *Regge* framework, this contribution has been considered in [69, 70].

3.4 Intensity Densities

In the *HERMES* kinematics the $\pi^+\pi^-$ cross section is dominated by the P-wave isovector channel, i.e. the ρ^0 resonant production. The less copious isoscalar, resonant and not resonant $\pi^+\pi^-$ production, can be investigated by studying its interference with the isovector channel, i.e. studying the interference between the odd and even l wave production. An observable suitable to probe this interference appears to be the *intensity density* [48, 49], defined as the l^{th} Legendre Polynomial $P_l(cos\theta)$ moment

$$\langle P_l(cos\theta)\rangle^{\pi^+\pi^-} = \frac{\int_{-1}^{1} dcos\theta \, P_l(cos\theta) \, \frac{d\sigma^{\pi^+\pi^-}}{dcos\theta}}{\int_{-1}^{1} dcos\theta \, \frac{d\sigma^{\pi^+\pi^-}}{dcos\theta}}, \tag{3.42}$$

where θ is the scattering angle of π^+ meson in the $\pi^+\pi^-$ rest frame with respect to the direction of the recoiled system, Fig. 3.4. Some of the above defined quantities are non-zero only if the interference between the isoscalar and the isovector channels is present. In a general way this can be shown with the following consideration. The differential cross section may be decomposed into contributions from $\pi^+\pi^-$ production in l-odd, l-even states and from the interference of the two channels:

$$\frac{d\sigma}{dcos\theta} \propto \mid T_{m\ odd} \mid^2 + \mid T_{n\ even} \mid^2 + 2\,\mathrm{Re}\ T_{m\ odd} T^{\star}_{n\ even}\ , \tag{3.43}$$

m, n being the quantum number l which characterizes the amplitude T. Due to the $2\pi DA$ composition of Eq. 3.24, Legendre Polynomials with index $l = m(n)$ enter the corresponding amplitude $T_{m(n)}$ and the cross section. The intensity density $\langle P_l(cos\theta)\rangle^{\pi^+\pi^-}$ is proportional to the integrals

$$\begin{aligned} I_1 &= \int_{-1}^{1} dcos\theta \, P_l(cos\theta) \mid T_{m(n)} \mid^2 \\ I_2 &= \int_{-1}^{1} dcos\theta \, P_l(cos\theta) \, \mathrm{Re}\ T_{m\ odd} T^{\star}_{n\ even}, \end{aligned} \tag{3.44}$$

where $\mid T_{m(n)} \mid^2$ gives only even powers of $cos\theta$, therefore intensity densities with index l odd get contributions only from interference integral, since in this case the integral

I_1 is null:

$$\langle P_l(cos\theta)\rangle_{l\ odd}^{\pi^+\pi^-} = 0 \iff interference\ term\ null\ . \tag{3.45}$$

As discussed in section 3.2, at large virtuality Q^2, the contribution from 2π production in states with $l > 2$ is negligible, and $\langle P_{l\ odd}(cos\theta)\rangle^{\pi^+\pi^-}$ can get contribution from the interference of P-wave with S-wave and D-wave $\pi^+\pi^-$ production. An important feature of $\langle P_3(cos\theta)\rangle^{\pi^+\pi^-}$ is that it is sensitive to the interference between S-wave and D-wave only. In fact

$$\begin{aligned}
\langle P_3(cos\theta)\rangle^{\pi^+\pi^-} &\propto \int_{-1}^{1} dcos\theta\, P_3(cos\theta)\,\mathrm{Re}\ T_{m=1}T^{\star}_{n=0,2} \\
&\approx \int_{-1}^{1} dcos\theta\, P_3(cos\theta)[P_1(cos\theta)(a_0P_0(cos\theta) + a_2P_2(cos\theta))] \\
&= \int_{-1}^{1} dcos\theta\, a_2P_3[P_1P_2] \\
&= \int_{-1}^{1} dcos\theta \sum_{k=0,2,4,6} b_k cos^k\theta\ .
\end{aligned} \tag{3.46}$$

The S-wave enters the above expression with the term P_0 only which contributes the integral $\int_{-1}^{1} dcos\theta\, a_2P_3P_1P_0$ that is null. Therefore, the only contribution to this intensity density may come from a pure $\Big(P\text{-}D\Big)$-wave interference. No particular Legendre polynomial can be chosen to probe the interference of 2π in P-wave only with 2π in the S-wave state.

Decomposing $2\pi DA$s as in section 3.2, the full analytic expressions for the $cos\theta$-integrated absolute squares of the T-matrix elements, weighted with Legendre polynomials $P_l(\cos\theta)$, as they enter the intensity densities, can be shown:

$$\int_{-1}^{1} d\cos\theta \sum_{S'} |T^{\pi^+\pi^-}|^2 = \int_{-1}^{1} d\cos\theta \sum_{S'} \Big(|T^{I=0}|^2 + |T^{I=1}|^2\Big)\ , \tag{3.47}$$

with

$$
\begin{aligned}
\int_{-1}^{1} d\cos\theta \sum_{S'} |T^{I=0}|^2 &= \frac{(e\pi\alpha_s)^2 C_F^2}{18N_c^2}\frac{1}{p\cdot l\, x_{Bj} y}\sum_{S'}\Big|2I_u^- - I_d^-\Big|^2\left(\frac{40M_2^Q}{N_f}+\frac{20M_2^G}{C_F}\right)^2 \\
&\times\left[\frac{(3C-\beta^2)^2}{72}|f_0(m_{\pi\pi})|^2+\frac{\beta^4}{90}|f_2(m_{\pi\pi})|^2\right] , \\
\int_{-1}^{1} d\cos\theta \sum_{S'} |T^{I=1}|^2 &= \frac{(e\pi\alpha_s)^2 C_F^2}{18N_c^2}\frac{1}{p\cdot l\, x_{Bj} y} \\
&\times\sum_{S'}\Big|2I_u^+ + I_d^+ + \frac{3}{C_F}I_G\Big|^2 24\beta^2|F_\pi(m_{\pi\pi})|^2 , \qquad (3.48)
\end{aligned}
$$

where the sum is performed over the nucleon polarization states S'. Other non-vanishing integrals are:

$$
\begin{aligned}
\int_{-1}^{1} d\cos\theta \sum_{S'} |T^{\pi^+\pi^-}|^2 P_1(\cos\theta) &= \frac{(e\pi\alpha_s)^2 C_F^2}{18N_c^2}\frac{1}{p\cdot l\, x_{Bj} y}\left(\frac{40M_2^Q}{N_f}+\frac{20M_2^G}{C_F}\right) \\
&\times 2\mathrm{Re}\Bigg\{\sum_{S'}\Big(2I_u^- - I_d^-\Big)^*\Big(2I_u^+ + I_d^+ + \frac{3}{C_F}I_G\Big) \\
&\quad\times\left[\frac{3C-\beta^2}{3}f_0(m_{\pi\pi})^* - \frac{4\beta^2}{15}f_2(m_{\pi\pi})^*\right]\beta F_\pi(m_{\pi\pi})\Bigg\} , \\
\int_{-1}^{1} d\cos\theta \sum_{S'} |T^{\pi^+\pi^-}|^2 P_3(\cos\theta) &= -\frac{(e\pi\alpha_s)^2 C_F^2}{18N_c^2}\frac{1}{p\cdot l\, x_{Bj} y}\left(\frac{40M_2^Q}{N_f}+\frac{20M_2^G}{C_F}\right) \\
&\times 2\mathrm{Re}\Bigg\{\sum_{S'}\Big(2I_u^- - I_d^-\Big)^*\Big(2I_u^+ + I_d^+ + \frac{3}{C_F}I_G\Big) \\
&\times\frac{6\beta^3}{35}f_2(m_{\pi\pi})^* F_\pi(m_{\pi\pi})\Bigg\} . \qquad (3.49)
\end{aligned}
$$

From the above expressions the relation between *GPD*s and the intensity densities $\langle P_{1(3)}(cos\theta)\rangle^{\pi^+\pi^-}$ can be seen, using the following estimation

$$
\langle P_{1(3)}(cos\theta)\rangle \;\propto\; 2\mathrm{Re}\sum_{S'}\Big(2I_u^- - I_d^-\Big)^*\Big(2I_u^+ + I_d^+ + \frac{3}{C_F}I_G\Big)A_{1(3)} , \qquad (3.50)
$$

with

$$A_1 = \left[\frac{3C-\beta^2}{3} f_0(m_{\pi\pi})^* - \frac{4\beta^2}{15} f_2(m_{\pi\pi})^*\right] \beta F_\pi(m_{\pi\pi})$$
$$A_3 = \frac{6\beta^3}{35} f_2(m_{\pi\pi})^* F_\pi(m_{\pi\pi}) \; . \qquad (3.51)$$

By the *GPD*s modeling as described in section 3.2 [48], the intensity density $\langle P_1(cos\theta)\rangle$ has been computed neglecting the two-gluon exchange mechanism. The predicted values at $m_{\pi\pi} = 0.770$ GeV and at $m_{\pi\pi} = 0.5$ GeV with different x_{Bj} values are reported in Tab. 3.3. Using the same GPDs parameterization, in Ref. [49] the $m_{\pi\pi}$- and x_{Bj}-dependence of $\langle P_1(cos\theta)\rangle$ have been computed including the contribution from the two-gluon exchange mechanism. Graphical results are shown in Fig. 3.8. Figure 3.9 reports the invariant mass dependence of $\langle P_1(cos\theta)\rangle^{\pi^+\pi^-}$ at different x_{Bj} values.

Results predict $\langle P_{1(3)}(cos\theta)\rangle^{\pi^+\pi^-}$ to be strongly sensitive to the interference showing an angular production asymmetry of π^+ that depends on the invariant mass $m_{\pi^+\pi^-}$ of the $\pi^+\pi^-$ system. The size of these signals increases with x_{bj} due to the increasing interference effects between the isovector and isoscalar $\pi^+\pi^-$ production channels.

The comparison of experimental data on these distributions with theoretical predictions separately with and without the inclusion of the nucleon gluon *GPD*, could in principle lead to a better modeling of this non-perturbative variable. Furthermore, the analysis of $\langle P_{1(3)}(cos\theta)\rangle^{\pi^+\pi^-}$ could highlights the very elusive f_0 and f_2 isoscalar states in the upper tail of the ρ^0 meson resonance, and the continuum $m_{\pi\pi}$-spectrum of the non-resonant $\pi^+\pi^-$ production.

$m_{\pi\pi} = 0.770$ GeV			
x_{Bj}	0.1	0.2	0.3
$\langle cos\theta\rangle$	-0.04	-0.07	-0.1
$m_{\pi\pi} = 0.5$ GeV			
x_{Bj}	0.1	0.2	0.3
$\langle cos\theta\rangle$	-0.18	-0.27	-0.33

Table 3.3: Theoretical predictions for the intensity density $\langle P_1(cos\theta)\rangle$ at $m_{\pi\pi} = 0.770$ GeV and at $m_{\pi\pi} = 0.5$ GeV with increasing x_{Bj} values. Data come from [48], where the two-gluon exchange mechanism contribution to the process amplitude is neglected.

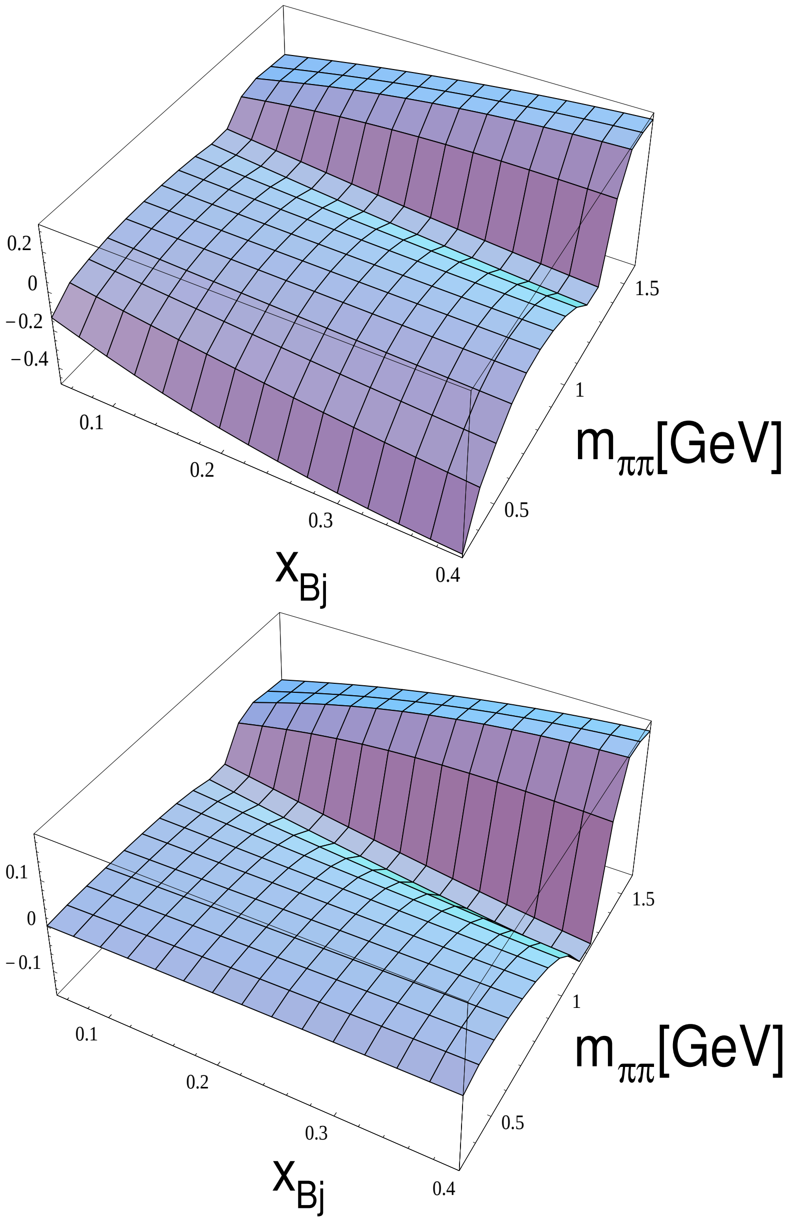

Figure 3.8: x_{bj}- and $m_{\pi^+\pi^-}$-dependence theoretical calculations for $\langle P_1(cos\theta)\rangle^{\pi^+\pi^-}$ (**upper panel**) and for $\langle P_3(cos\theta)\rangle^{\pi^+\pi^-}$ (**bottom panel**) [49].

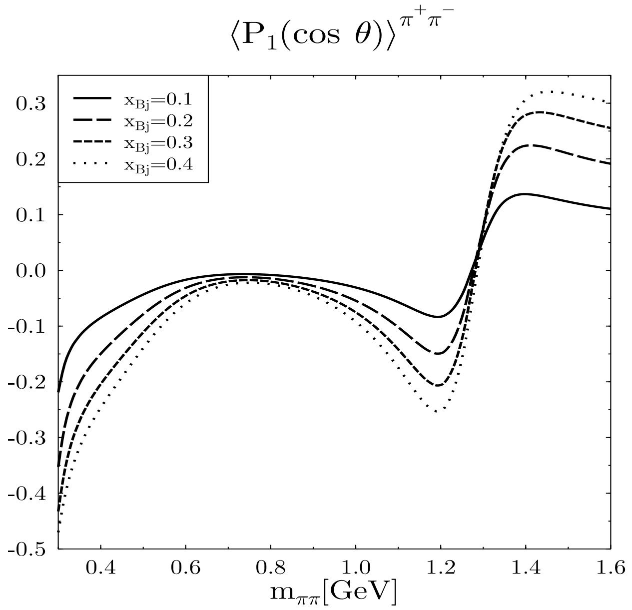

Figure 3.9: The intensity density $\langle P_1(cos\theta)\rangle^{\pi^+\pi^-}$ for different values of x_{bj}. Data comes from [71] using the same modeling of GPDs and $2\pi DA$s as in [49].

Chapter 4

The *HERMES* Experiment

The main goal of the *HERMES* (HERa MEasurement of Spin) experiment is to investigate the spin structure of nucleons. The original proposal involved the use of the technology of polarized gaseous targets located along the positron storage ring at the DESY laboratory in Hamburg, for the measurement of DIS processes with high statistic and systematic precision. The innovative feature of this technology is the zero dilution of the target and its fast spin inversion ($\sim$ 1 sec). After the proposal submission to DESY in 1990, with full approval in 1992, data taking started with ^3He target in 1995. In the following years, the study of DIS processes was performed with different targets, e.g. H e D.

In addition to the determination of the polarized nucleon structure functions via inclusive measurements of DIS, *HERMES* may perform semi-inclusive measurements taking advantage of its capability of reconstruct and identify final state hadrons, and therefore investigating in a wide kinematic plane the dynamic processes of hadrons formation through the fragmentation and hadronization of the struck quark. A relevant aspect of the experiment is its capability to perform measurements of processes of exclusive physics, even though it was originally conceived as an experiment of inclusive and semi-inclusive physics.

4.1 The *HERA* Storage Ring Facility

The *HERMES* experiment [72] is located along the *HERA* storage ring of the *DESY* (Deutches Elektronen SYnchrotron) accelerator laboratory in Hamburg (Germany). The underground storage ring facility *HERA* is located in a 6.3 Km tunnel and consists of two beam lines, respectively for the 27.57 GeV electron/positron and the 820 (920 from 1998) GeV proton beams. An experimental hall, in each of the four straight sections along the *HERA* tunnel, houses a different experiment. In particular the

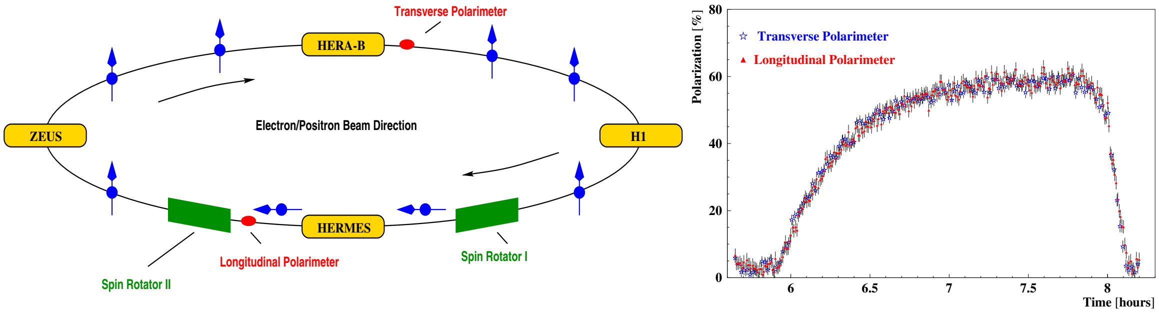

Figure 4.1: **Left panel:** sketch of the *HERA* positron ring showing the positions of the spin rotators and of the beam polarimeters. **Right panel:** rise time profile of the *HERA* positron beam polarization as measured by both the transverse and longitudinal Compton polarimeters.

fixed-target *HERMES* experiment is located in the East Hall and uses the positron beam only. Positrons in the *HERA* lepton beam are stored in 189 individual bunches which had a 96 ns (29 m) separation, and are arranged in three bunch trains. Each lepton bunch is 27 ps (8mm) long and contains $2 \cdot 10^{10}$ particles. The average lifetime of the positron beam is around 10 hours.

The positron beam is polarized by the self polarizing *Sokolov-Ternov* effect [73]. A small asymmetry spin-flip amplitude enhances the polarization state where the spin of the positron is parallel to the magnetic field of the ring. This gives rise to a natural build-up of transverse polarization in storage rings. The spin dynamics in magnetic fields in storage rings is described by the *Thomas-Bargmann-Michel-Telegdi* (T-BMT) equation [74, 75].

Most of the analysis at *HERMES* requires longitudinal polarization of the positron beam, therefore before and after the interaction region a pair of 90^o spin rotators has been installed to turn the spin into the beam direction and then back into the vertical again, Fig. 4.1 left panel. The design of these spin rotators derives from the *Siberian snake* concept [76, 77] which enables to change the original spin direction of a beam. In the particular case of *HERA*, they consist of a succession of horizontal and vertical normal conductor magnets. In Fig. 4.1, right panel, the rise time of the *HERA* lepton beam transverse and longitudinal polarization is shown. The measurement is performed by using transverse and longitudinal Compton polarimeters.

4.2 The *HERMES* Storage Gaseous Target

The *HERA* running conditions are not compatible with the use of a liquid or solid target upon the positron beam; furthermore the use of low dilution targets was requested for the *HERMES* experiment. Due to the above conditions an internal gas target was chosen. The target complex consists mainly of the polarized ABS-type source, the unpolarized source UGFS, the internal storage cell and the target monitor system TGA/BRP.

The *Stern-Gerlach* Atomic Beam Source (ABS), Fig. 4.2 [79], consists of a dissociator to form atoms, a skimmer and a collimator for the formation of the atomic beam, a sextuple magnet system to bend away from the beam the sample with unwanted electron polarization, and high frequency units to transfer the polarization of electrons to nucleons [80].

The unpolarized gas is injected into the target using the thermo-valve and diaphram system UGFS, through a different tube then the feed tube from the ABS, Fig. 4.3. The density of unpolarized gas is two order of magnitude larger then the density of polarized gas.

Polarized atomic gas targets offer many advantages over solid polarized targets for spin experiments. The target figure of merit is given by the factor $(fP)^2N$ [82], where f is the dilution factor, P the target polarization and N the areal density. Solid targets provide a high density ($\leq 10^{25}$ atoms/cm^2) but, as an example for deuterium, suffer from dilution ($f < 0.3$) and lower polarization ($P < 0.5$). The gas targets are free of dilution ($f = 1$), highly polarized ($P > 0.8$), and the spin of the atoms can be inverted in few milliseconds, instead of hours, significantly reducing the systematic errors. The low areal density of gas atomic polarized jets ($\leq 2 \cdot 10^{11}$ atoms/cm^2) has been improved with the introduction of gas storage cells as target.

The *HERMES* target storage cell is an open-ended 400 mm long tube with an elliptical cross section of 21 x 8.9 mm^2, Fig. 4.3. The numerous collisions of the atoms with the cell walls may depolarize the nucleons and/or facilitate the recombination of atoms into molecules, reducing the target polarization. These processes are inhibited by the use of $75 \mu m$ thin aluminum foil coated with *Drifilm*. A layer of solid H_2O or D_2O forms on the interior cell surface. The presence of water is a result of the small admixture of oxygen in the hydrogen or deuterium gas flow into the ABS dissociator, which increases the atomic fraction of the exiting gas. This ice layer was found to

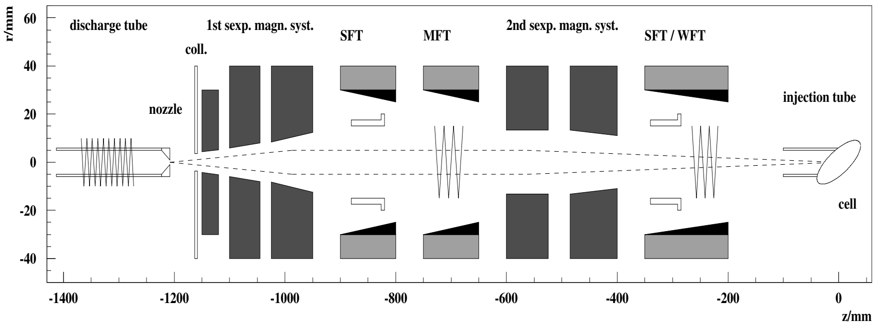

Figure 4.2: Schematic of the ABS setup.

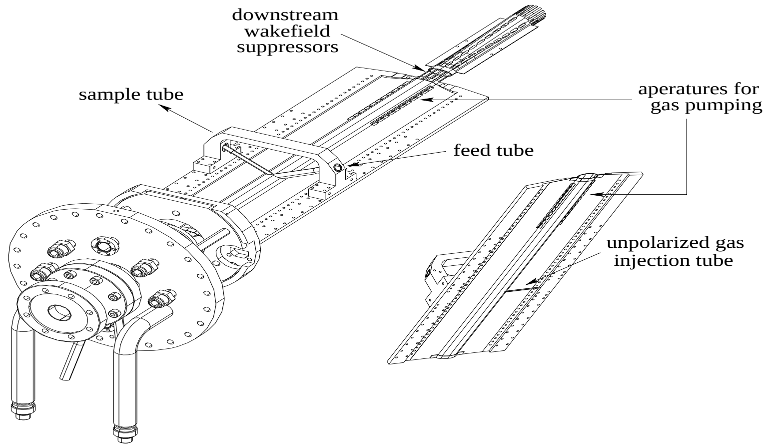

Figure 4.3: The storage cell and its support structure

improve the surface quality inside the cell [82]. A conduction-cooled, super-conductive magnet produces a longitudinal uniform magnetic field in the target region to both decouple the electron and the nucleon spins, reducing the depolarization of the nucleons in the target gas [83], and to provide the proper nuclear target spin orientation.

The target monitor apparatus consists of the Target Gas Analyzer (TGA) and the Breit Rabi Polarimeter (BRP). The TGA is used to evaluate the fraction of nucleons in the atomic state in the target cell. The BRP is devoted to monitor the nuclear target polarization.

4.3 The *HERMES* Spectrometer

The *HERMES* spectrometer [84] is a forward angle detector, symmetric about a central horizontal shielding plate in the magnet. In Fig. 4.4 a diagram of the spectrometer is shown. The *HERMES* coordinate system has the z-axis along the beam momentum, the y-axis vertical upwards and the x-axis horizontal, pointing towards the outside of the ring.

Charged particles tracks are reconstructed using the 6 microstrip gas chamber (MSGC) planes and 57 wire planes of the tracking chambers, namely the vertex chambers VC and the drift chambers DVC, FC, MC and BC.

Particle identification (PID) is provided by a lead-glass calorimeter, a preshower (H2) consisting of two radiation length of a lead followed by a plastic scintillator hodoscope, a transition radiation detector (TRD) and a threshold Cherenkov detector (C). From 1998, an upgrade to a Ring Imaging CHerenkov detector (RICH) has been performed. The calorimeter and the pre-shower detector are included in the trigger along with a second hodoscope (H1) placed in front of the TRD. An additional trigger

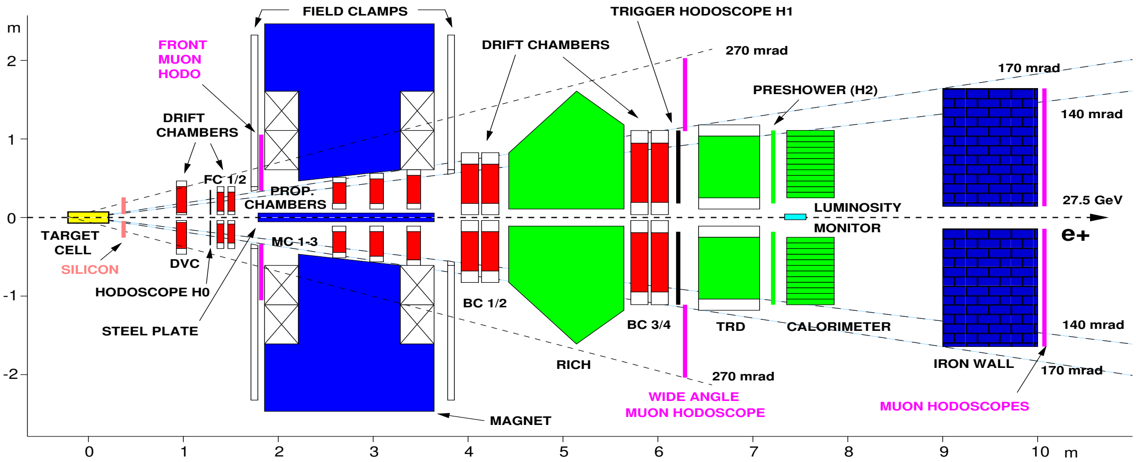

Figure 4.4: Schematic side view of *HERMES* spectrometer. The incoming positron beam enters the spectrometer from the left side of the picture.

hodoscope (H0) was included in 1996 in front of FC1 to reduce the trigger rate from background caused by the *HERA* proton beam.

The acceptance is limited at small values of the polar θ scattering angle ($40 < \theta < 220$ mrad) by an iron plate in the beam plane which shields the *HERA* positron and proton beams (separated by 72 cm) from the magnetic field of the spectrometer magnet. The kinematic plane for the experiment (Q^2 vs. ν) is shown in Fig. 4.5, where y is the fractional energy of the photon relative to the beam energy.

4.3.1 The Tracking System

The kinematic of charged particles inside the spectrometer is reconstructed by the tracking system, which consists of different chambers whose location is shown in Fig. 4.4. The microstrip gas chambers (MSGC) VC1/2, the drift vertex chambers DVC, and the front drift chambers FC1/2 provide the *front tracking* which relies in both the vertex reconstruction and the determination of θ and of the azimuthal scattering angle ϕ. The VCs resolution was excellent at the design value of $45\mu m$, but the chambers suffered in efficiency, generally inadequate and spatially non-uniform, ranging from to zero to near 90%. In 1998 they have been removed from the *HERMES* detector. In conjunction with the front tracking, the back drift chambers BC1/2 and BC3/4 measure the charged track bending due to the spectrometer magnet, and hence the track momentum. The proportional chambers inside the magnet MC1/3 ensure that multi-track ambiguities could be resolved. Moreover they are useful for the momentum analysis of low energy tracks which are strongly deflected and do not reach the downstream track-

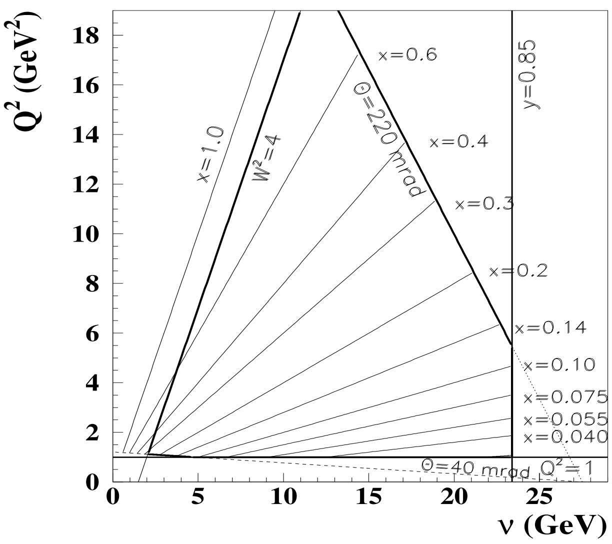

Figure 4.5: Kinematic plane for the *HERMES* experiment

ing detectors. All the drift chambers consist of six planar planes with the same gas composition $Ar/CO_2/CF_4$ but with different proportions. The track reconstruction methods are performed considering the information from different combinations of the above sets of chambers. The performance of the tracking system has been studied using a Monte Carlo simulation, obtaining the resolution $\Delta p/p < 1.25\%$, $\Delta\theta < 0.6$ mrad, and for the longitudinal and transverse vertex position $\Delta z \sim 1.7$ mm and $\Delta r \sim 0.1$ mm respectively, being $r = \sqrt{x^2 + y^2}$.

4.3.2 The Particle Identification

Particle identification relies on the basic fact that different particle types cause different signals in PID detectors, and is performed asking for the largest *hadron rejection factor* (HRF) possible for the same *positron efficiency*. The HRF is defined as the number of all hadrons in the acceptance divided by the number of hadrons misidentified as leptons. The *positron efficiency* is the ratio of the identified positrons to all positrons in the sample. In order to satisfy the above requirements, a combination of four particle identification detectors is used to separate positrons and electrons from hadrons. Particles are identified using a probability based procedure which relies mainly on comparing the probability $P(A_i/E)$ that the measured detector signal E is caused by the particle type A_i with the probability $P(E/A_i)$ that a particle of a given type A_i causes a detector response E. These are typical *conditional probabilities* and are related to each other through the *Bayes's theorem* [94]:

$$P(A_i/E) = \frac{P(A_i) \cdot P(E/A_i)}{\sum_{k=1}^{n} P(A_k) \cdot P(E/A_k)} \ , \tag{4.1}$$

where the sum runs over all particle types A_k, $P(A_i) = \phi_i(p, \theta)$ is the probability that a particle of type A_i is present in the detector and is given by the normalized flux ϕ_i which depends on the momentum p and the scattering angle θ. The probability $P(E/A_i)$ for a given detector D is equivalent to the *parent distribution* $L_D^i = L_D^i(E, p)$ which is the typical response from different particle types in the detector depending on the particle type A_i, particle momentum p and the detector response E. At *HERMES*, parent distributions have been determined from collected data, and through Bayes' theorem the conditional probability $P^i = P(A_i/E)$ was extracted, once the particle fluxes were known.

The probability that the detector response is due by the positron or by the hadron respectively is indicated as P_D^e or P_D^h. The Beyes' theorem gives its expression as:

$$P_D^e = \frac{L_D^e}{\Phi L_D^h + L_D^e} \qquad P_D^h = \frac{L_D^h}{L_D^h + \Phi^{-1} L_D^e} \ \ ,$$

where $\Phi = \phi^h/\phi^e$ is the flux of hadrons over the positrons one. Positrons are separated from hadrons according to the value of the quantity $PID_D = log_{10}\frac{P_D^e}{P_D^h} = log_{10}\frac{L_D^e}{\Phi L_D^h}$. A positive value of the PID indicates a likely positron, a negative value a proton. To avoid the PID spectrum to be momentum dependent, the Φ term is neglected imposing cuts on PIDs: for values smaller than zero for hadrons and larger than the minimum in the PID spectrum for leptons the small $log_{10}\Phi$ contribution can be ignored. Using all the PID detectors, an overall PID value is defined:

$$PID = log_{10} \prod_D \frac{L_D^e}{L_D^h} = \sum_D log_{10} \frac{L_D^e}{L_D^h} \ , \tag{4.2}$$

with the sum running over the detectors considered. Fig. 4.6 shows a comparison between different PID parameters, where the $PID4$ considers the four detectors, in $PID3$ the response from TRD (which is referred to as $PID5$) is non considered, and in $PID2$ only the response from calorimeter and preshower are considered. The figure shows a clean separation between the hadrons and positrons when the four particle identification detectors are used. The system provides a hadron rejection factor of at least 10^4 in offline analysis to keep the contamination of the positron sample by hadrons below 1% for the whole kinematic range.

The preshower (hodoscope H2) consists of 11 mm of Pb, accomplished of vertical scintillator modules which are 1 cm thick and 9.3 x 91 cm^2 in area. Each scintillator is coupled to a photomultiplier via a light guide. The lead sheet initiates electromagnetic

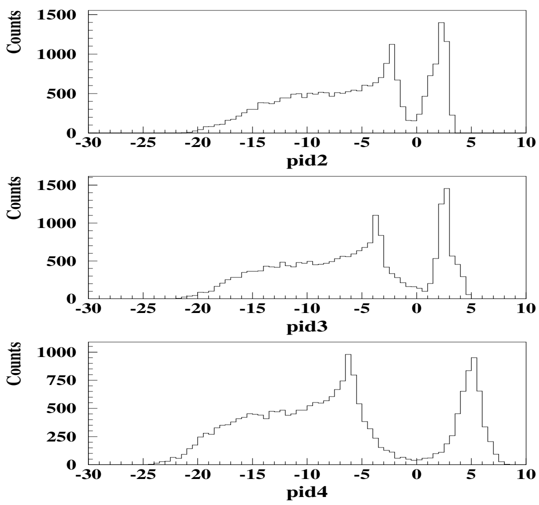

Figure 4.6: Comparison between different PID parameters for the 1995 data set. Positrons have positive values of PIDs, while hadrons have negative values for these quantities.

showers which deposits energy in the scintillator with average values of $20 - 40$ GeV for positrons and few MeV for hadrons.

The electromagnetic calorimeter [85] consists of 840 horizontal lead-glass blocks. The blocks have an area of 9x9 cm^2, a lenght of 50 cm ($\sim$ 18 radiation lengths), and are stacked in two walls each having a 42x10 array of blocks. In combination with the preshower, the performance of a 3x3 array of counters showed a HRF of $\sim 10^3$, with a 95% positron efficiency. Radiation damage of the lead glass is prevented moving the calorimeter walls away vertically from the beam pipe during the beams injection in the storage ring.

The main purpose of Cherenkov detector is to separate pions, kaons and protons using the Cherenkov effect to get information on the track parent particle. If the particle's speed v exceeds the speed of light in the medium, that is $v > \frac{c}{n}$, c being the light speed in the vacuum and n the refractive index of the traversed material, it is possible for the particle to radiate electromagnetic waves, the Cherenkov radiation [86]. For a particle with mass m and momentum p, the opening angle of the Cherenkov radiation cone satisfies the relation $cos\theta_C = \frac{1}{n}\sqrt{1 - \frac{m^2c^2}{p^2}}$. This feature provides a lower threshold momentum for the particle to radiate, allowing to separate pions from hadrons in the momentum range $(4-14)GeV$. From 1998 the Cherenkov detector was upgraded to a dual *Ring Imaging CHerenkov* detector (RICH), which is made of two Cherenkov detectors filled with gases at different refractive index. The information given by both radiators allows for a discrimination between hadrons over the whole kinematic range. The Cherenkov counter uses a gas mixture at atmospheric pressure of nitrogen and perfluorobutane, C_4F_{10}, in a (30:70) ratio. The emitted Cherenkov light is focused by spherical mirrors and collected by phototubes.

The TRD relies on the property that radiation is emitted when a relativistic charged particle crosses a boundary between media of different dielectric constants. The radiation is emitted in the forward direction at an angle $\theta \propto 1/\gamma$ with the particle trajectory, γ being the Lorentz factor. In the *HERMES* energy regime only positrons ($\gamma > 6000$) produce transition radiation, and the detection of X-rays in coincidence with the charged particle can be used to discriminate between positrons and hadrons ($\gamma < 200$). The emitted photons have energy of typically $2 - 15$ KeV. The TRD consists of six modules each having a radiator followed by an X-ray detector. The radiator consists of a 6.5 cm thick matrix of randomly oriented propylene fibers with $17 - 20\mu m$ diameter. The X-ray detector is a planar wire chamber containing a high Z gas (Xenon) for efficient X-ray absorption which produces clusters of electrons in the gas.

4.3.3 The Trigger System

The function of the trigger system is to distinguish interesting events from background, and initiate digitization and readout of detector signals. At *HERMES* different trigger schemes are implemented. corresponding to DIS of a positron, photoproduction processes (when no positron is detected), and additional triggers for detector monitoring and calibration. In particular, the DIS trigger used in this analysis selects events with positrons by requiring coincidence of the *HERA clock* and hits in the three hodoscopes, H0, H1 and H2, together with an energy deposit in two adjacent columns of the calorimeter of at least 3.5 GeV and 1.4 GeV with unpolarized and polarized targets, respectively. When a positive trigger signal is obtained, the Data AcQuisition system (DAQ) initializes the readout of all detectors information relative to the event. During the time needed for the digitization and readout of the detectors components, no new trigger can be accepted, leading to a *dead time* $\sim 2\%$ of the data acquisition.

Chapter 5

Data analysis

5.1 Introduction

In this work the hard exclusive processes $e^+p \to e^+p\ \pi^+\pi^-$ and $e^+d \to e^+d\ \pi^+\pi^-$ were studied, with the aim to measure, for the first time, the *intensity densities* $\langle P_1(cos\theta)\rangle$ and $\langle P_3(cos\theta)\rangle$ (see chapter 3) to evaluate the interference between the $\pi^+\pi^-$ production in P-wave with $(S+D)$-wave state. Experimentally the above quantities are measured as the average values of the Legendre Polynomials P_1 and P_3, calculated as function of $m_{\pi\pi}$ and x_{Bj}.

The data have been accumulated with the HERMES forward spectrometer [84] during the running period 1996-2000. The 27.6 GeV positron beam was scattered off hydrogen and deuterium targets, and events with both unpolarized and polarized targets were considered in this analysis.

Events have been selected with one positron track and two oppositely charged hadron tracks without additional neutral clusters in the calorimeter. Moreover, in order to enter the *hard* regime of the process, the constraints $Q^2 > 1$ GeV^2 and $W > 2$ GeV were imposed, where W is the invariant mass of the virtual-photon nucleon system. Since the recoil proton is not detected in the present *HERMES* apparatus, exclusive events were selected performing studies on the invariant mass M_X of the undetected system. The exclusivity of the events was ensured by imposing a cut on the elasticity $\Delta E = \frac{M_X^2 - M_{targ}^2}{2M_{targ}}$, M_{targ} being the target mass. For scattering off composite nuclei one can have either incoherent scattering from individual nucleons inside the target nucleus ($M_{targ} = M_p$) or coherent scattering from the entire nucleus N ($M_{targ} = M_N$). Due to the experimental difficulty to distinguish the two different types of scattering processes off deuteron, throughout the entire analysis M_{targ} was chosen to be the proton mass.

For the measured exclusive process, the background source from target resonance decays is negligible due to the cut $W > 2$ GeV. Instaed, kaons from the ϕ decays gives a large contribution to the background at $m_{\pi\pi} \sim 0.4$ GeV. This kind of background is avoided as described in section 5.4.

Due to the instrumental resolution and smearing, the most important source of background to the exclusive channel comes from current and target fragmentation in semi-inclusive Deep Inelastic Scattering (*DIS*) at low ΔE. The contamination of this kind of events was evaluated (section 5.6.1, 5.7.1) reproducing the shape of the *DIS* background by the *Monte Carlo* package *GMC*, used by the *HERMES* Collaboration, and which is based on the *LEPTO* generator [87] and the *LUND* model [88]. The detector response was simulated by the *GEANT* Monte Carlo code [89]. Monte Carlo events (*MC*) were normalized to experimental data at $\Delta E > 2$ GeV. The above cut has been chosen to ensure an event sample mainly populated by this kind of background, as it will shown in section 5.5.

In this analysis, it is important to maximize the ratio of the exclusive signal over the background (Sg/Bg) and minimize its relative statistical error, with hydrogen and deuterium target respectively. Exclusive events have been selected choosing an appropriate ΔE cut optimized analyzing the ratio (Sg/Bg) in several bins of the $m_{\pi\pi}$ and x_{Bj} spectrum.

For the analysis of the invariant mass dependence of intensity densities, in order to observe the enhancing of the isoscalar $\pi^+\pi^-$ production and consequently the interference between the isovector and isoscalar channel, the cut $x_{Bj} > 0.1$ was required. On the contrary, the analysis of the x_{Bj} dependence of intensity densities was performed in the whole *HERMES* x_{Bj} spectrum.

The *intensity density* of the background, $\langle P_l(cos\theta)\rangle_{Bg}$, was evaluated using data for $\Delta E > 2$ GeV, assuming its ΔE independence. This hypothesis was tested checking the stability of $\langle P_l(cos\theta)\rangle_{Bg}$ in different ΔE bins. In every bin of the spectrum studied, the value of $\langle P_l(cos\theta)\rangle_{Bg}$, weighted by the ratio Sg/Bg for the chosen ΔE cut, was subtracted to the distribution of data events within the selected exclusive ΔE region. Results of the *intensity densities* were proved to be stable measuring those distributions at different exclusive ΔE cuts, section 5.6.3, 5.7.3.

5.2 Data Aquisition and Event Selection

Events have been selected with one positron track and two oppositely charged hadron tracks ($E_h > 1.0$ GeV) with no additional neutral clusters ($E_\gamma > 0.8$ GeV) in the calorimeter. In particular the unpolarized data and polarized data with different polarization states were used from the following productions: 96c1, 97b4, 98c1, 99b2 and 00b1. This analysis has been performed separately for hydrogen and deuterium targets.

The data storing is defined according to bursts and runs. A *burst* represents the smallest time division of the data taking, $\sim 10sec$. The *HERMES* Data Acquisition

PARAMETER	**DATA QUALITY SELECTION CRITERIUM**
run level	
stable operational conditions of the Cerenkov (only for 96,97)	*OK*
stable operational conditions of the TRD	*OK*
Run analyzable according to shift logbook	*OK*
burst level	
first and last burst in each run	removed
good *Data Quality* at burst level	OK
discards data with unreasonable values of the burst length	$\Delta t < 11$ sec
charged track level	
z-component of the vertex inside the target region	$\lvert Z_{vertex}\rvert < 20\ cm$
transverse component of the vertex inside the target region	$\lvert D_{vertex}\rvert < 0.75\ cm$
geometrical acceptance	$\begin{cases} 0.04 < \lvert\theta_y\rvert < 0.14\ rad \\ \lvert\theta_x\rvert < 0.17\ rad \end{cases}$
reconstruction method of the track	without vertex chambers (*NOVC*)
cuts on the positron track	
positron identification	$\begin{cases} PID3 + PID5 > 1\ (96, 97) \\ PID2 + PID5 > 1\ (98, 99, 00) \end{cases}$
DIS regime	$Q^2 > 1\, GeV^2$
non-resonance target region	$W > 2\, GeV$
small radiative corrections	$y \equiv \frac{E-E'}{E} < 0.85$
cuts on hadronic tracks	
hadron identification	$\begin{cases} PID3 + PID5 < -1\ (96, 97) \\ -100 < PID2 + PID5 < -1\ (98, 99, 00) \end{cases}$

Table 5.1: Data quality conditions chosen in this analysis.

(DAQ) organizes bursts information into runs: a *run* is just another convenient block of information corresponding to one file of data. The DAQ automatically ends a run whenever 560 Mb of information are collected. The *HERMES* database is written around the *ADAMO* concept whose databases are organized into records, each of them containing the full set of all the tables which group together information of a particular type.

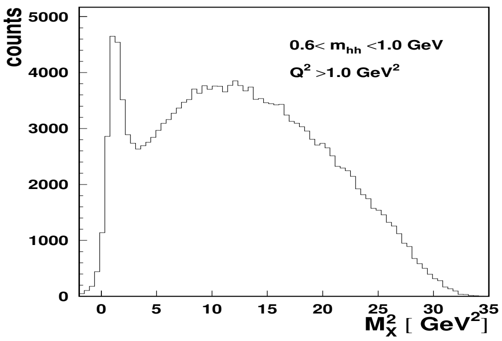

Figure 5.1: Typical distribution of the variable M_X^2 that is defined from kinematics of the undetected system X. The hadronic shower X from the target fragmentation can in principle contain several hadrons. The peak of its invariant mass M_X around the target mass corresponds to $\Delta E = 0$ and means the exclusive production and that the target has not fragmented.

The quality of data have been ensured by asking for stable operational conditions of the spectrometer detectors, and a good data acquisition at run and burst level was required. This information, encoded in bits, is stored in the ADAMO tables. The whole chosen data quality (*DQ*) cuts are shown in Tab. 5.1.

The scattered positrons and charged hadrons were identified using the PID parameters, described in section 4.3.2. For the DIS-positron and the charged hadrons, tracks were required to originate in the target cell, applying a cut on the vertex coordinate, and on the horizontal θ_x and vertical θ_y scattering angles. The used track reconstruction method neglected the information from the vertex chambers (*NOVC*).

To select events in *hard* regime, the cut $Q^2 > 1$ GeV was imposed. After the above kinematic cuts, the whole sample of $\sim 12 \cdot 10^6$ DIS events is reduced to $\sim 7 \cdot 10^5$. To analyze the $m_{\pi\pi}$ dependence of the *intensity densities*, the cut $x_{Bj} > 0.1$ was applied, in order to enhance the isoscalar $\pi^+\pi^-$production and consequently the interference between the isovector and isoscalar channel, as explained in chapter 3. In the *HERMES* kinematics, it is not possible to apply a larger cut on x_{Bj} without a strong reduction of the statistics.

Since the recoil proton is not detected in the present *HERMES* apparatus, the exclusivity of these events was ensured applying the further cut on the elasticity $\Delta E = \frac{M_X^2 - M_p^2}{2M_p}$, where M_X is the missing mass, shown in Fig. 5.1, and M_p is the proton mass. In principle, also the fractional energy $z = \frac{E_{\pi^+} + E_{\pi^-}}{E_{\gamma^\star}}$ carried by the 2π system may be used, but in the current work ΔE was chosen mainly because its direct link to the exclusivity of the process. The peak of the invariant mass M_X around the proton mass, corresponding to $\Delta E = 0$, is a strong signal of the exclusive production.

5.3 Experimental Resolution

The experimental resolution was evaluated using the Monte Carlo. In this case the *DIPSI* generator [90] was used in order to simulate the diffractive exclusive $\pi^+\pi^-$

leptoproduction off protons and is based on the Ryskin model [91]. In this model the virtual photon exchanged by the incoming positron, fluctuates into a $q\bar{q}$ pair interacting with a gluon ladder emitted by the proton target in the approximation LLA, Fig. 5.2.

The crossing of generated tracks through the *HERMES* spectrometer is simulated by the *GEANT* Monte Carlo. Its output is processed by the *HERMES* ReConstruction Software (*HRC*) which basically collects all the simulated hits on the wire chambers and reconstructs the crossing track. For each track, the output by the *HRC* processing, which takes into account the experimental smearing, can be compared with the output by DIPSI, the generated tracks in the *HERMES* acceptance. The comparison of the two outputs gives the experimental resolution. In Fig. 5.3 the resolution of Q^2, tx_{Bj}, W and $m_{\pi\pi}$ is shown. The resolution is evaluated for the spectrometer 1998 geometry setup. Fitting a gaussian shape to the relative deviation between the generated and the reconstructed variables gives absolute resolutions on Q^2, x_{Bj}, W and $m_{\pi\pi}$ of about 60 MeV^2 (3%), $4 \cdot 10^{-3}$ (5%), 60 MeV (1.4%) and 10 MeV (1.4%) respectively. The comparison with the same relative resolutions obtained with the 1997 set up [92], shows that the resolution got worse after 1998. Fig. 5.4 shows the resolution of the exclusive variable ΔE with the geometry set up of 1997 (left panel) and the geometry set up in 1998 (right panel). Still, the 1998 geometry set up led to a worst resolution. Monte Carlo studies have shown that the worst experimental resolution from the current geometry set up is due to the introduction of the RICH detector which substituted the threshold Cerenkov from 1998.

5.4 Contamination Sources

A contamination to the studied process may come from the target resonances. As an example, the proton target can be excited into a delta baryon which decays into a proton emitting a pion. This meson can be produced in coincidence with an oppositely charged exclusive pion produced in the current fragmentation. The observed $\pi^+\pi^-$ pair is therefore, in principle, indistinguishable from the exclusive pion pair coming

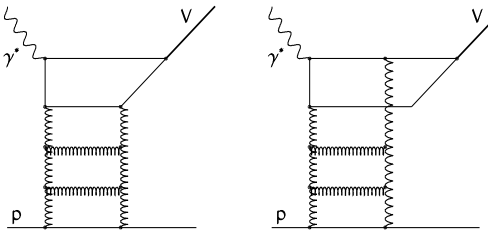

Figure 5.2: Exclusive vector meson production according to the Ryskin model used in the *DIPSI* Monte Carlo. The exchanged virtual photon fluctuates into a $q\bar{q}$ pair which then interacts with the proton target.

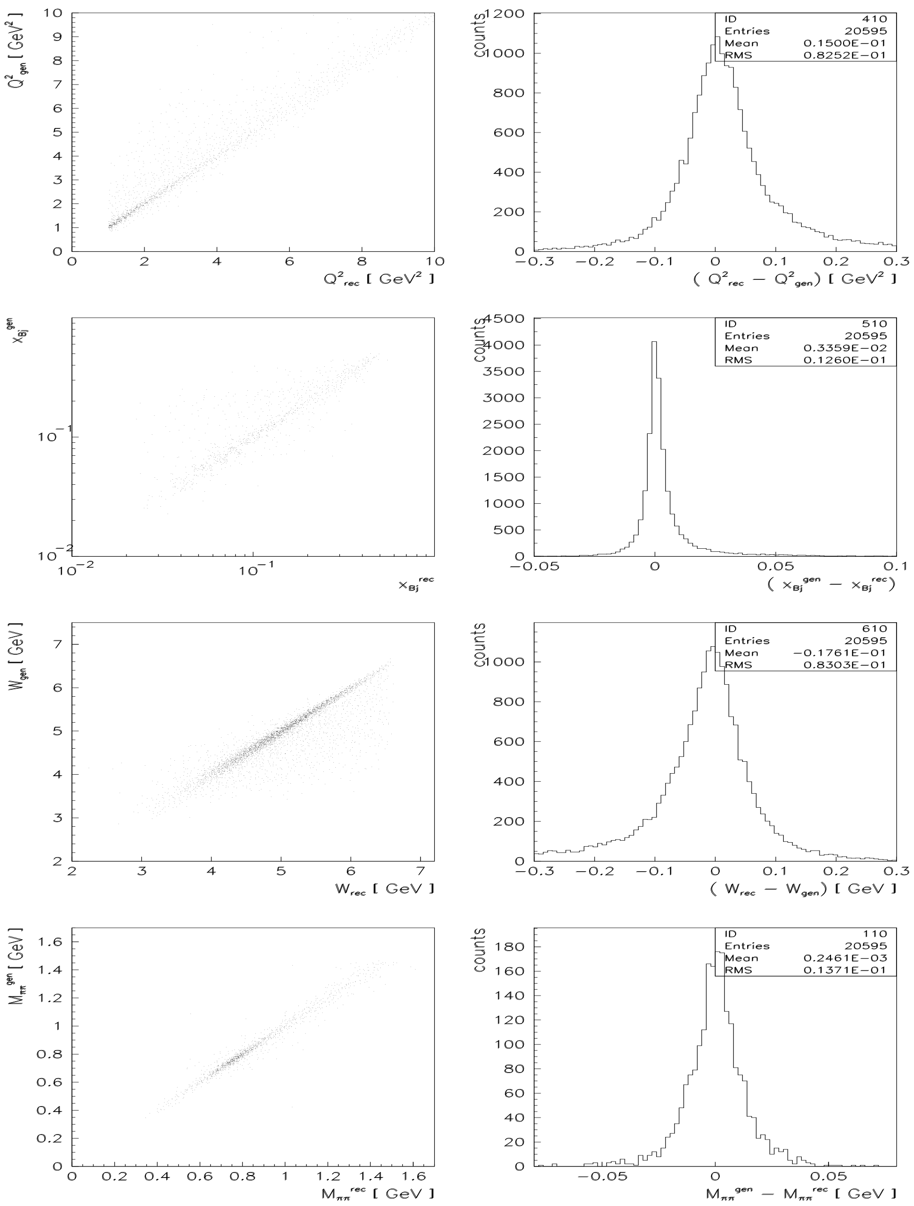

Figure 5.3: The resolution of the variables Q^2, x_{Bj} W and $m_{\pi\pi}$ is evaluated fitting a gaussian to the relative deviation between the generated and reconstructed ones. The resolution is evaluated for the 1998 spectrometer geometry setup. Radiative corrections were not considered.

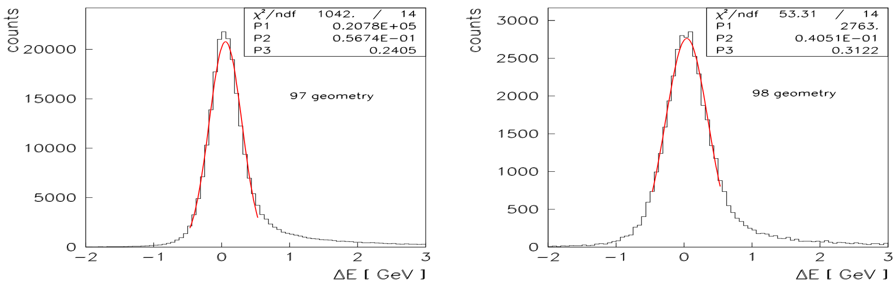

Figure 5.4: The experimental resolution of the exclusive variable ΔE with the geometry set up of 1997 (1998) is shown in the left (right) panel.

only from the current fragmentation and represents a source of background. Target resonances (e.g. Δ^{++}, Δ^0) were suppressed requiring the virtual-photon target-nucleon center of mass energy to be larger then the proton resonances mass ($W > 2\, GeV$).

A study via Dalitz plots has confirmed this assumption. In Fig. 5.5 left (right) panel, the exclusive $\pi^+\pi^-$ contribution from the target excitation and its following

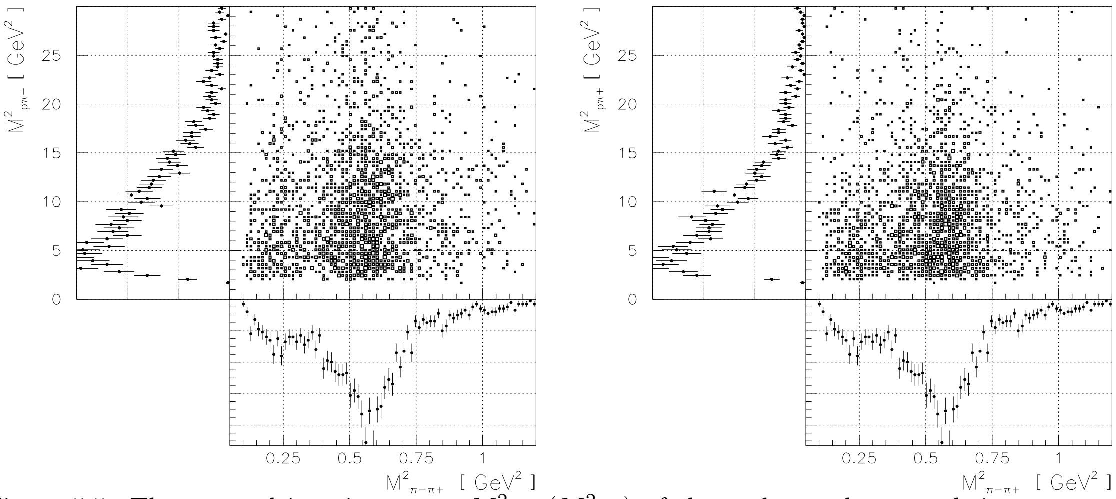

Figure 5.5: The squared invariant mass $M^2_{p\pi^-}$ ($M^2_{p\pi^+}$) of the undetected system being supposed a proton ($M_X = M_p$) and of π^- (π^+), is plotted versus the squared invariant mass $M^2_{\pi^+\pi^-}$ with the exclusive cut $\Delta E < 0.625\, GeV$, center plot of the left (right) panel. In each panel, the left and bottom corner plots refer to the $M^2_{p\pi}$ and $M^2_{\pi\pi}$ distributions respectively. The yields of $M^2_{p\pi^-}$ ($M^2_{p\pi^+}$) does not show any clear peak out the phase space shape, which is due to the kinematic distribution of the proton and the π^- (π^+) only. That is a clear indication of the absence of the Δ^0 (Δ^{++}) resonance in our sample.

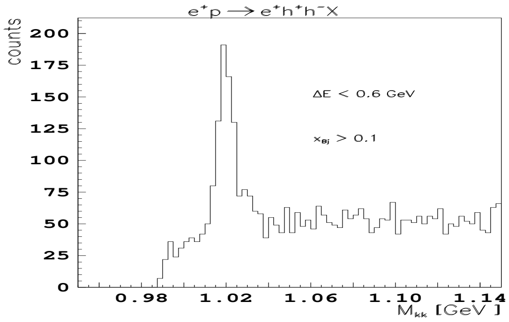

Figure 5.6: Distribution of the invariant mass m_{kk} with the exclusive cut $\Delta E <$ 0.6 GeV and $x_{Bj} > 0.1$. All hadrons are considered as kaons. The ϕ meson decay peak is clearly superimposed to the kinematic phase space kaon pairs distribution.

decay $e^+p \rightarrow e^+\Delta^0\pi^+ \rightarrow e^+p\pi^+\pi^-$ ($e^+p \rightarrow e^+\Delta^{++}\pi^- \rightarrow e^+p\pi^+\pi^-$) is found to be negligible. The invariant mass $m^2_{p\pi^-}$ ($m^2_{p\pi^+}$) of the undetected system, being supposed a proton ($M_X = M_p$) and of π^- (π^+), is plotted versus the $\pi^-\pi^-$ invariant mass with the exclusive cut $\Delta E < 0.625\ GeV$, center plot of the left (right) panel. In each panel, the left and bottom corner plots refer to the $m^2_{p\pi}$ and $m^2_{\pi\pi}$ distributions respectively. The yield of $m^2_{p\pi^-}$ ($m^2_{p\pi^+}$) distributions does not show any peak around the Δ^0 (Δ^{++}) mass. This is a clear indication of the absence of the Δ^0 (Δ^{++}) resonance in our sample.

The sample is contaminated by exclusive and semi-inclusive non $\pi^+\pi^-$ pairs. In the *HERMES* kinematic range and with the kinematic cuts used in this analysis, the main huge background source of this type is the ϕ meson decay into a K^+K^- pair. In Fig. 5.6 the invariant mass m_{kk} spectrum, hadrons being considered as kaons, is

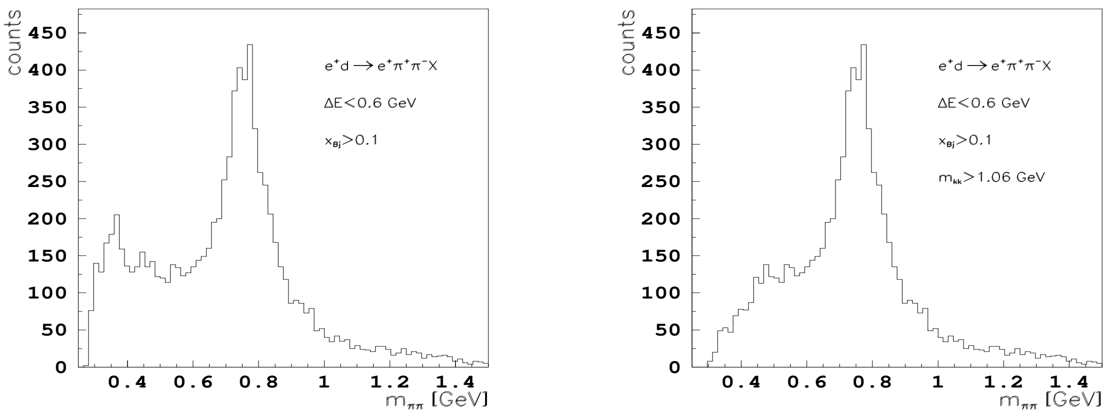

Figure 5.7: Distribution of the $\pi^+\pi^-$ invariant mass $m_{\pi\pi}$ for $x_{Bj} > 0.1$ and the exclusive cut $\Delta E < 0.6$ GeV on deuterium target, without (**left panel**) and with (**right panel**) the cut $m_{kk} > 1.06\ GeV$. The peak at low $m_{\pi\pi}$, in the left panel, is the reflection of the ϕ mesons decay into K^+K^-.

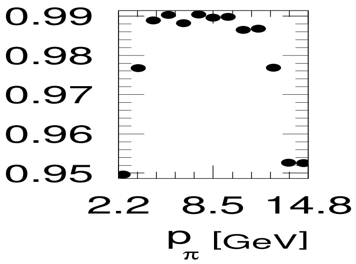

Figure 5.8: Momentum dependence of the probability that a particle identified as pion by the RICH is truly a pion, when only one hadron is detected in one halve of the RICH. This probability was obtained with a Monte Carlo simulation.

shown. Above the phase space distribution, a peak at $m_{kk} \sim 1.020\ GeV$ is clearly observed and is identified as the ϕ meson. This contamination is strongly peaked at $m_{\pi\pi} \sim 0.4\ GeV$. Fig. 5.7, left panel, shows the spectrum of the $\pi^+\pi^-$ invariant mass $m_{\pi\pi}$ after the cut $x_{Bj} > 0.1$ and the exclusive cut $\Delta E < 0.6$ GeV were applied. The peak at low $m_{\pi\pi}$ is the reflection of the ϕ mesons decay into K^+K^- and was avoided applying the cut $m_{kk} > 1.06$ GeV, Fig. 5.7 right panel.

The remaining contamination is spread over the whole spectrum, and is evaluated in few percent to the whole sample. This can be verified using the information from the *RICH* detector. Pions are identified among the whole hadron sample in a very large energy range $2 < E_\pi < 15\ GeV$ with no *unfolding*, which is a procedure to extract the true particle spectrum from the measured one. Previous Monte Carlo analysis showed that the probability that a particle identified as pion by RICH is truly a pion is bigger then 99% in most of the energy range $2 < E_\pi < 15\ GeV$, Fig. 5.8. In Fig. 5.9, the $m_{\pi\pi}$ and m_{hh} invariant mass spectra are compared. The analyzed sample is a subsample of the whole deuterium one with cuts $x_{Bj} > 0.1, \Delta E < 0.625\ GeV$ and $m_{kk} > 1.06\ GeV$ in the energy window $2 < E_{\pi(h)} < 15\ GeV$. A few percent contamination of non $\pi^+\pi^-$ pairs is found. Moreover, it is estimated to be dominated by the contribution from semi-inclusive pairs, as can be found considering, for instance, the exclusive channel $\phi \rightarrow \rho\pi$ with *Branching Ratio* $\frac{\sigma_{\phi\rightarrow\rho\pi}}{\sigma_{\rho^0\rightarrow\pi^+\pi^-}} < 1\%$. The contamination from exclusive non $\pi^+\pi^-$ pairs was taken into account within the systematic uncertainties.

The above few percent contamination is also confirmed by *MC* simulation. In Fig. 5.10 a sample of semi-inclusive $\pi^+\pi^-$ and K^+K^- pairs generated by the Monte Carlo *Pythia* in the *HERMES* geometrical acceptance is plotted versus the positive hadron energy. Even if the sample is small, it can be assumed that the kaon contamination is few percent. Also the contribution from other type of hadrons is negligible.

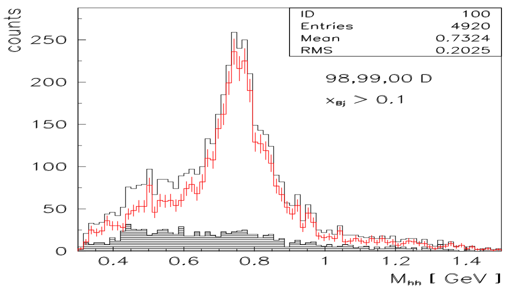

Figure 5.9: The $m_{\pi\pi}$ invariant mass spectrum (crosses) is subtracted to m_{hh} one (solid line) with deuterium target for $\Delta E < 0.625$ GeV and $m_{kk} > 1.06$ GeV. Dashed area represents the non $\pi^+\pi^-$ sample. The energy window of the hadronic tracks is $2 < E_{\pi(h)} < 15$ GeV.

5.5 Background Subtraction and Statistical Error Propagation

From the above considerations, it is clear that the most important source of background to the exclusive channel comes from fragmentation of partons in semi-inclusive deep inelastic scattering at low ΔE. The study on the experimental resolution in the exclusive variable ΔE shows that those events may contaminate the exclusive sample. In Fig. 5.11 a typical ΔE spectrum of data in the invariant mass region around the strong ρ^0 peak $0.6 < \Delta E < 1.0$ GeV is shown. Even though the DIS background is spread at larger ΔE, it may contaminate the exclusive sample at low ΔE, due to the experimental resolution and smearing.

The shape of the *DIS* background for h^+h^- pairs is reproduced by a Monte Carlo *GMC*. During summer 2001, the *GMC* package was run on an ALPHA station equipped with Tru64 UNIX (Digital UNIX). About $2.3 \cdot 10^6$ DIS simulated events were generated and reconstructed in the *HERMES* acceptance. The main chosen parameters of the

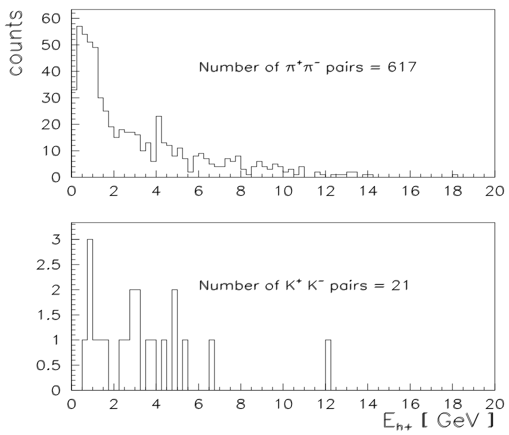

Figure 5.10: $\pi^+\pi^-$ and K^+K^- pairs generated by the Monte Carlo *Pythia* are plotted versus the positive hadron energy in the *HERMES* geometrical acceptance.

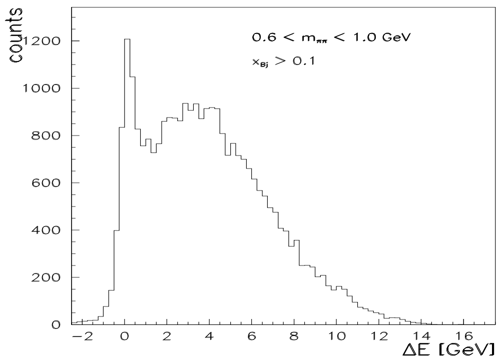

Figure 5.11: Typical ΔE spectrum in the invariant mass region around the ρ^0 peak, $0.6 < m_{\pi\pi} < 1.0$ GeV. The exclusive ρ^0 sample is peaked at $\Delta E = 0$. The background shape is spread at larger ΔE and contaminates the exclusive sample at low ΔE due to experimental resolution and smearing.

simulation are listed in Appendix C. The parton distribution functions parameterization chosen for the LEPTO generation was *CTEQ4* [93].

Events simulated by Monte Carlo, due to parton fragmentation in DIS, are supposed to reproduce the shape of the main source of background.

MC data were normalized to experimental data at $\Delta E > 2$ GeV, in the fragmentation region where the signal from exclusivity is assumed negligible, and then subtracted to obtain the exclusive sample. The following procedure was performed in different bins of the $m_{\pi\pi}$ and x_{Bj} spectrum, according to the specific analysis done. As an example, the analysis of the $m_{\pi\pi}$ dependence of intensity densities was performed dividing the $m_{\pi\pi}$ spectrum in 12 bins.

Exclusive events were selected choosing the ΔE cut in order to maximize the ratio of the exclusive signal (Sg) over the background (Bg) and minimize its relative statistical error $\sigma(Sg)/Sg$. Sg and Bg are, in practice, the numerical sum of yields N_i bin per bin versus ΔE, the sum starting from $\Delta E = -0.5$ GeV:

$$\begin{aligned} Sg &= \sum_{bins}(N^i_{data} - N^i_{MC}) \\ Bg &= \sum_{bins} N^i_{MC} \ , \end{aligned} \tag{5.1}$$

where the chosen ΔE bin width is 250 GeV. The relative statistical error $\sigma(Sg)/Sg$ is computed using the error propagation law [94]. With two independent samples, experimental data and *MC*, one can compute it in the following way:

$$\sigma(Sg)/Sg = \frac{\sqrt{\sum_{bin}(N^i_{data} + N^i_{MC})}}{\sum_{bin}(N^i_{data} - N^i_{MC})} \ . \tag{5.2}$$

In each of the studied bins, the *intensity density* for raw data $\langle P_l(cos\theta)\rangle_{data}$ was measured in the selected ΔE cut. The *intensity density* of the background, $\langle P_l(cos\theta)\rangle_{Bg}$, was evaluated using data for $\Delta E > 2$ GeV, assuming its ΔE independence. This assumption was tested checking the stability of $\langle P_l(cos\theta)\rangle_{Bg}$ in different ΔE bins. A lower ΔE cut was not used, due to the contamination from the exclusive channels in that fragmentation region.

In the selected ΔE cut the *intensity density* of data is actually the sum of the contributions from the exclusive $\pi^+\pi^-$ channel $\langle P_l(cos\theta)\rangle_{Sg}$ and from the *DIS* background $\langle P_l(cos\theta)\rangle_{Bg}$ respectively,

$$\langle P_l(cos\theta)\rangle_{data} = \alpha \cdot \langle P_l(cos\theta)\rangle_{Sg} + \beta \cdot \langle P_l(cos\theta)\rangle_{Bg} \ , \tag{5.3}$$

where α and β are the fraction of the two contributions:

$$\frac{\alpha}{\beta} = Sg/Bg \quad , \quad \alpha + \beta = 1 \ . \tag{5.4}$$

In every bin of the studied variable ($m_{\pi\pi} or x_{BJ}$), the value of $\langle P_l(cos\theta)\rangle_{Bg}$, weighted by the ratio Sg/Bg for the chosen ΔE cut, was therefore subtracted. Within the above bins, the statistical error on $\langle P_l(cos\theta)\rangle$ was computed as in [94]:

$$s = \sigma_i/\sqrt{(}N_i) \ , \tag{5.5}$$

where σ_i is the unknown variance of the $\langle P_l(cos\theta)\rangle$ distribution. In the analysis its estimation *Root Mean Squared* was used. Practically, the number N_i in (eq. 5.5), when referring to $\langle P_l(cos\theta)\rangle_{data}$ is the bin yield in the exclusive ΔE cut, and when referring to $\langle P_l(cos\theta)\rangle_{Bg}$ is the bin yield at $\Delta E > 2$ GeV.

These statistical errors were propagated into the statistical error of $\langle P_l(cos\theta)\rangle_{Sg}$ from the exclusive channel as:

$$\sigma_{Sg} = \sqrt{\frac{1}{\alpha^2}\sigma^2_{data} + \frac{\beta^2}{\alpha^2}\sigma^2_{Bg}} \ , \tag{5.6}$$

with σ_{data} being the statistical error of *intensity density* inside the selected exclusive region, and σ_{Bg} the statistical error of *intensity density* from the DIS background.

5.6 $m_{\pi\pi}$-dependence of Intensity Densities

The analysis of the $m_{\pi\pi}$ dependence of intensity densities $\langle P_l(cos\theta)\rangle$ is interesting because some of them are sensitive to the interference between different l-wave channels $\pi^+\pi^-$ exclusive production, as discussed in chapter 3. In particular $\langle P_1(cos\theta)\rangle$ and $\langle P_3(cos\theta)\rangle$ were measured. These quantities are non zero if the interference between $\pi^+\pi^-$ production in (S, D)-waves and in P-wave states is present. Therefore, they can be used to highlight the presence of channels superimposed to the ρ^0 resonance (P-wave) over the studied invariant mass spectrum $0.3 < m_{\pi\pi} < 1.35$ GeV.

For this kind of analysis, in order to observe the enhancing of the isoscalar $\pi^+\pi^-$ production and consequently the interference between the isovector and isoscalar channel, the cut $x_{Bj} > 0.1$ was required, as discussed in section 3.3.

5.6.1 Background Subtraction

The $m_{\pi\pi}$ spectrum was divided in twelve bins. In each $m_{\pi\pi}$ bin Monte Carlo was normalized to experimental data at $\Delta E > 2$ GeV, Fig. 5.12-5.13, and then subtracted to them as a function of ΔE, Fig. 5.14-5.15, for hydrogen and deuterium targets respectively. The simulated background shape is in agreement with data at large ΔE, while at small ΔE there is an eccess of data due to the exclusive process $e^+p(d) \longrightarrow e^+p(d)\pi^+\pi^-$, not simulated in the Monte Carlo. In particular, in the invariant mass $0.6 < m_{\pi\pi} < 0.95$ GeV the huge eccess of data is mainly due by the meson decay $\rho^0 \longrightarrow \pi^+\pi^-$.

The dependence of the ratio of the exclusive signal over the background (Sg/Bg) on ΔE is shown in Fig. 5.16-5.17. In order to maximize Sg/Bg and minimize its relative statistical error in most of the bins, the exclusive cuts $\Delta E < 0.625$ GeV for hydrogen target and $\Delta E < 0.125$ GeV for deuterium target were chosen. Tab. 5.2 shows the measured ratio Sg/Bg corresponding to the chosen exclusive cuts.

$m_{\pi\pi}$ $[GeV]$	Sg/Bg (H) $\Delta E < 0.625$ GeV	Sg/Bg (D) $\Delta E < 0.125$ GeV
$0.30 - 0.43$	0.74	1.36
$0.43 - 0.60$	0.88	2.57
$0.60 - 0.70$	1.35	3.98
$0.70 - 0.80$	2.39	7.21
$0.80 - 0.95$	2.35	6.34
$0.95 - 0.98$	1.44	5.41
$0.98 - 1.00$	2.65	17.01
$1.00 - 1.05$	0.91	3.98
$1.05 - 1.10$	0.92	1.63
$1.10 - 1.21$	0.24	1.66
$1.21 - 1.27$	0.74	0.56
$1.27 - 1.35$	0.54	0.75

Table 5.2: Ratio Sg/Bg chosen for different $m_{\pi\pi}$ bins at $x_{Bj} > 0.1$ with hydrogen and deuterium targets.

Hydrogen target: *MC* normalization to experimental data.

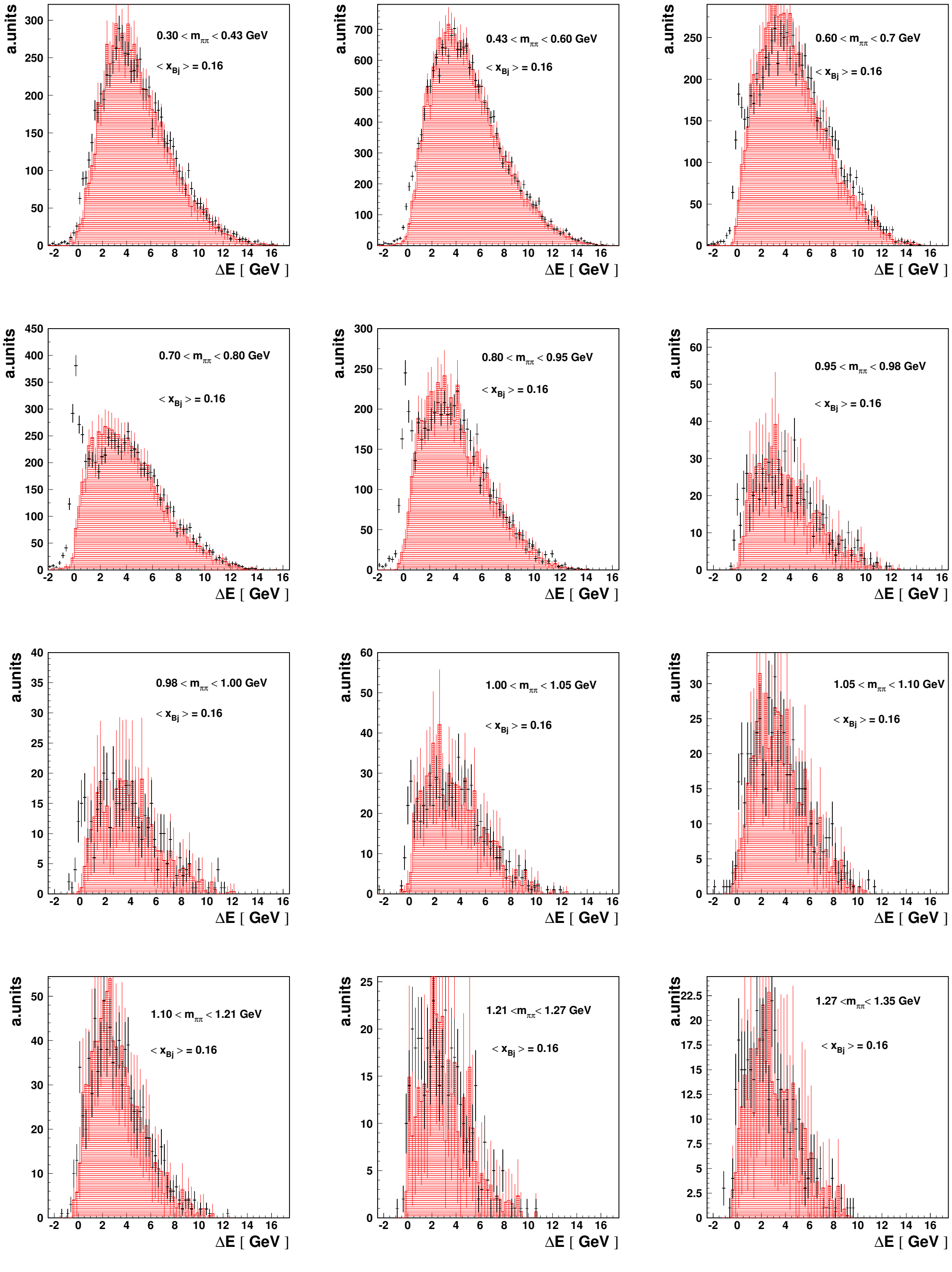

Figure 5.12: ΔE distribution in the 12 invariant mass bins for hydrogen target. *MC* data (shadowed) are normalized to the experimental one (crosses) for $\Delta E > 2$ GeV.

Deuterium target: *MC* normalization to experimental data.

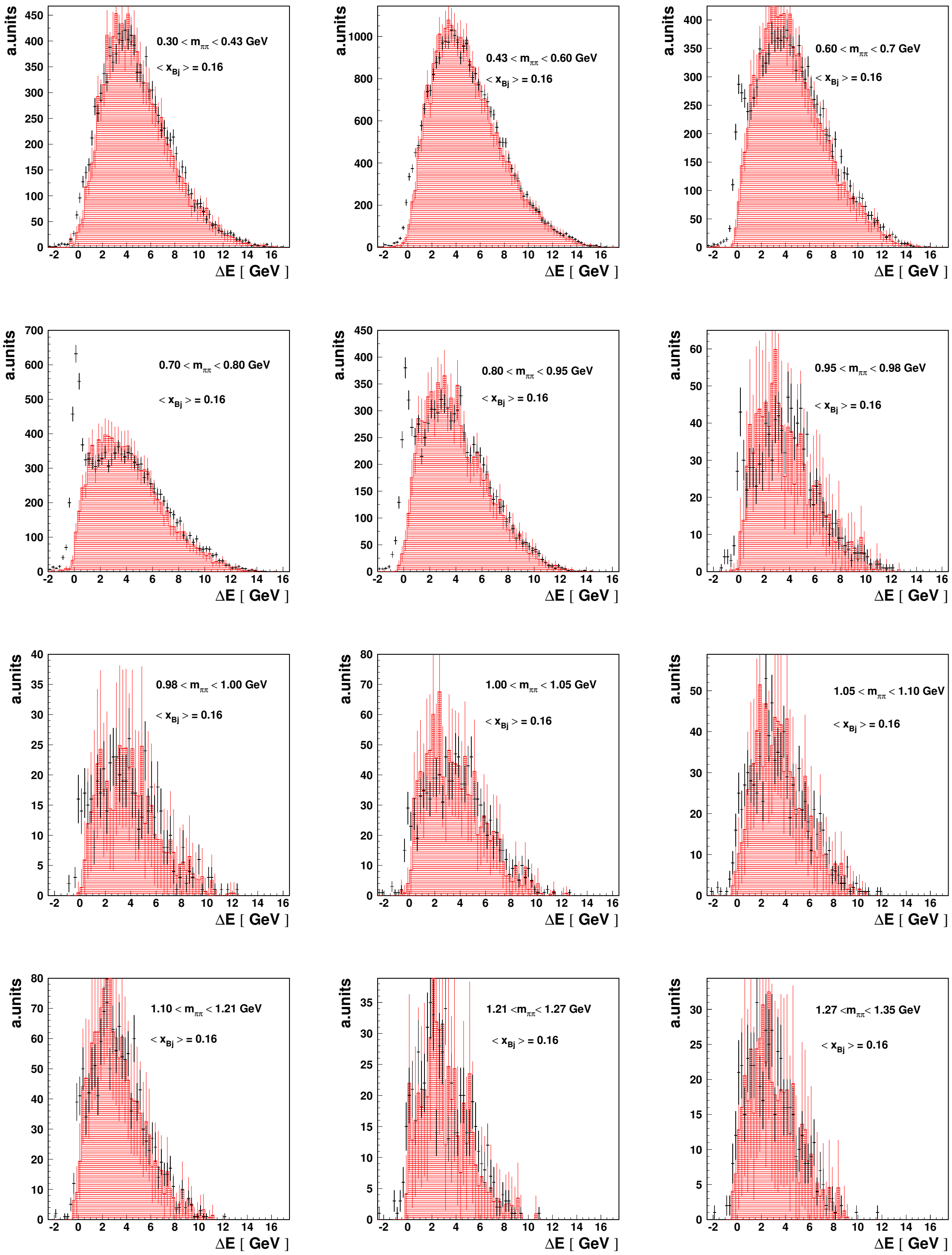

Figure 5.13: ΔE distribution in the 12 invariant mass bins for deuterium target. *MC* data (shadowed) are normalized to the experimental one (crosses) for $\Delta E > 2$ GeV.

Hydrogen target: extraction of the exclusive signal (Sg).

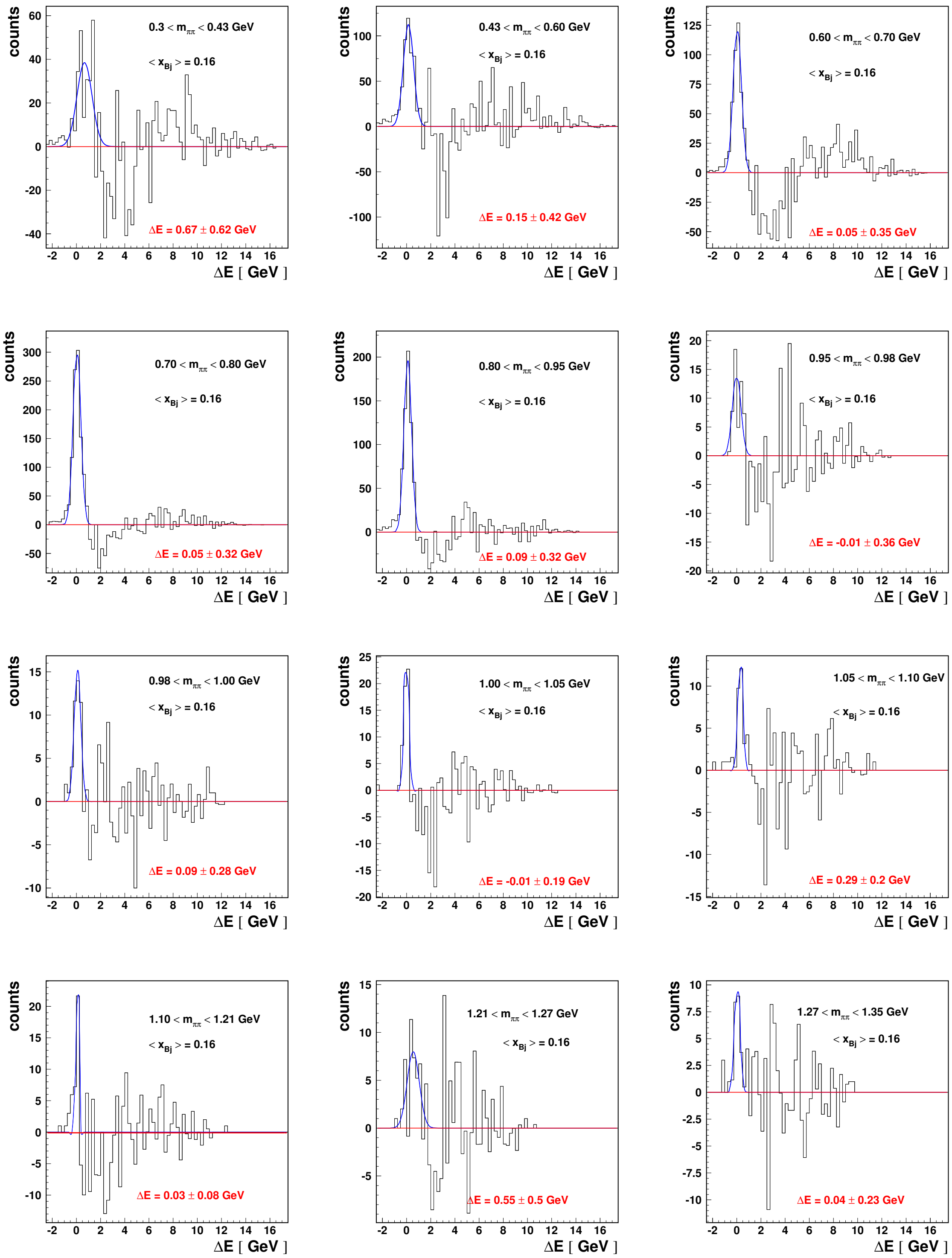

Figure 5.14: Yield of the $\pi^+\pi^-$ exclusive channel versus ΔE in the 12 invariant mass bins for hydrogen target. The exclusive peak is fitted with a gaussian whose expectation value and width values are shown in the bottom left side of each plot.

Deuterium target: extraction of the exclusive signal (Sg).

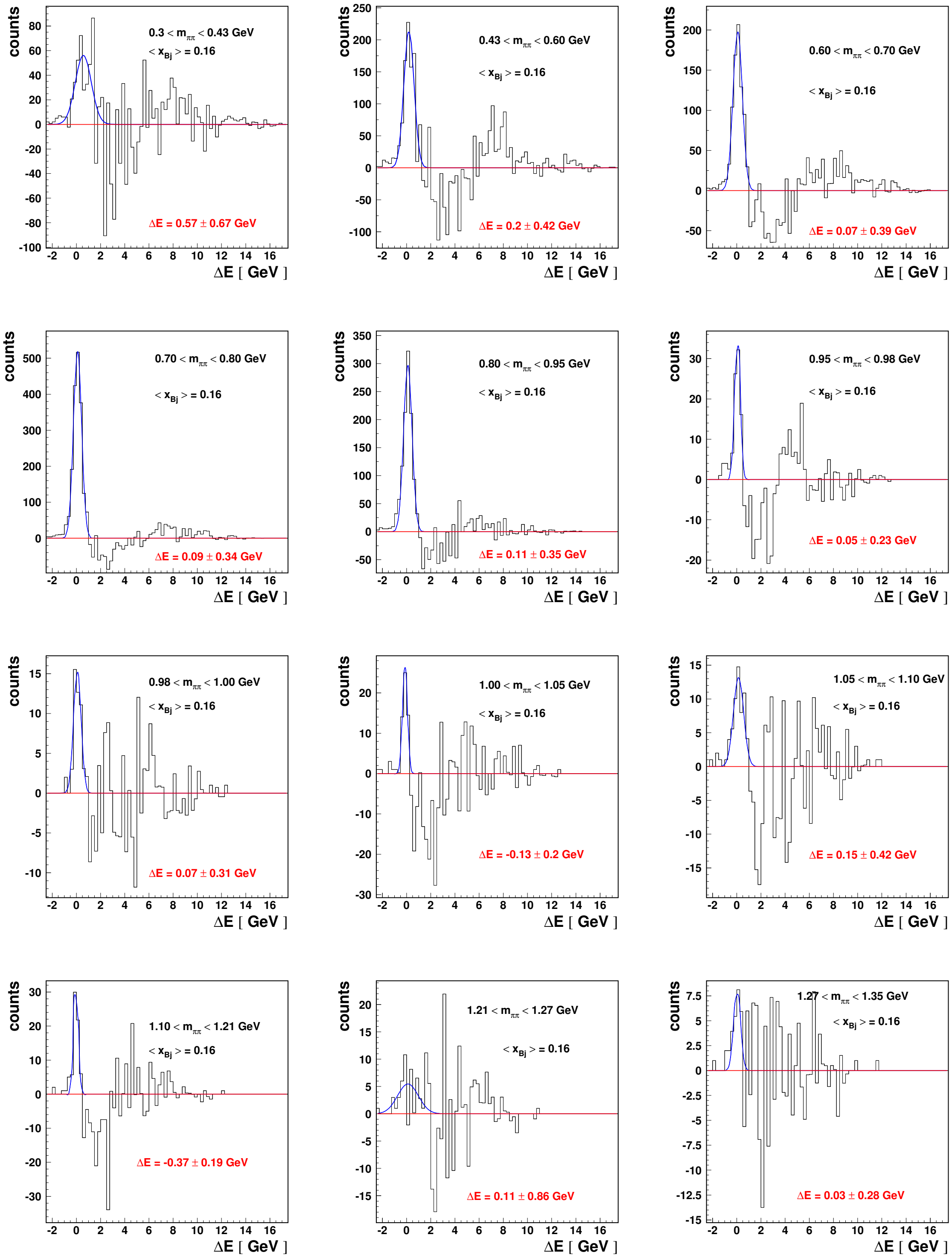

Figure 5.15: Yield of the $\pi^+\pi^-$ exclusive channel versus ΔE in the 12 invariant mass bins for deuterium target. The exclusive peak is fitted with a gaussian whose expectation value and width values are shown in the bottom left side of each plot.

Hydrogen target: ratio Sg/Bg versus ΔE.

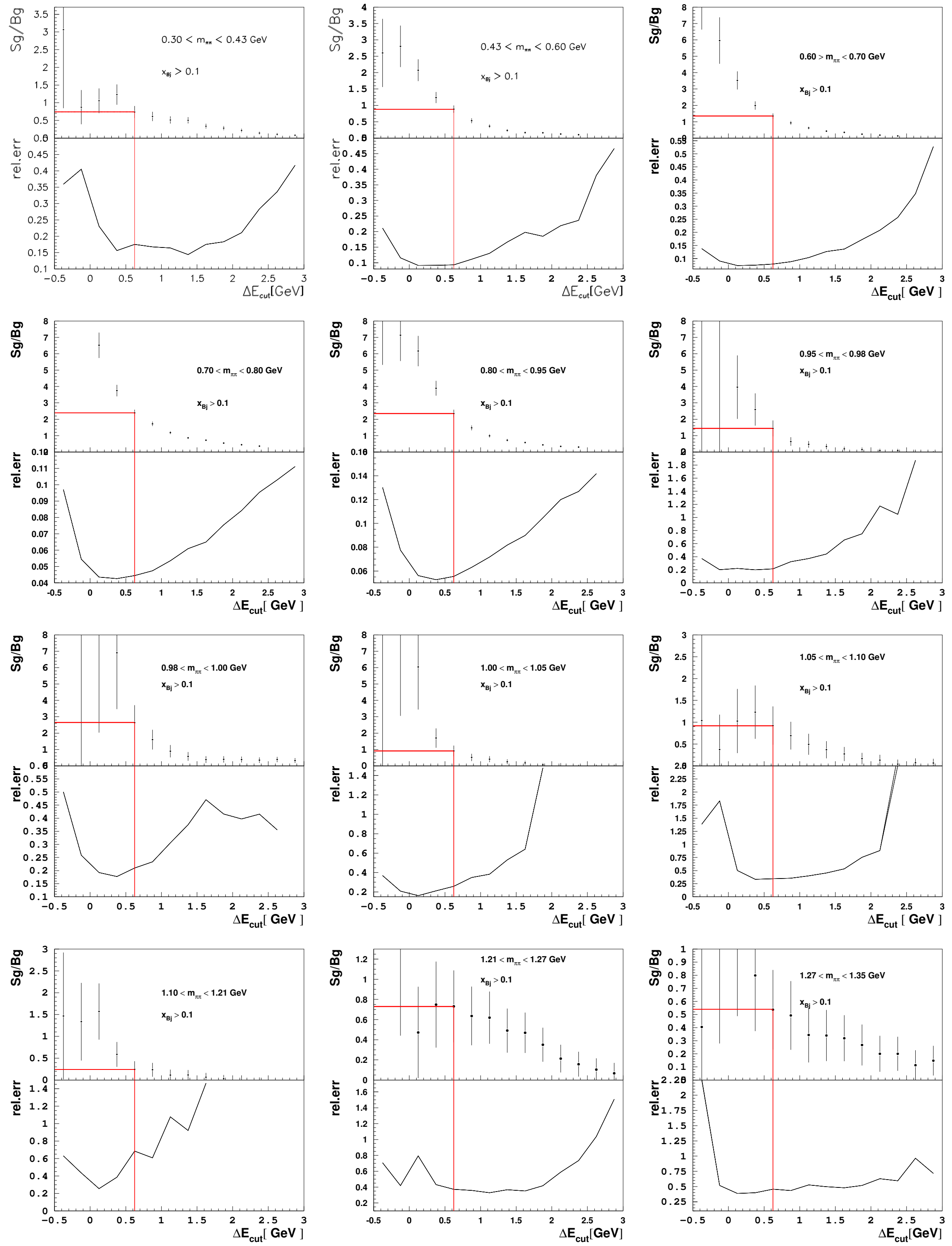

Figure 5.16: In each plot, the behavior of the ratio Sg/Bg (top panel) and its relative statistical error (bottom panel) versus ΔE in each of the 12 invariant mass bins for hydrogen target is shown. The vertical line shows the chosen ΔE_{cut} and the horizontal one shows the corresponding ratio Sg/Bg.

Deuterium target: ratio Sg/Bg versus ΔE.

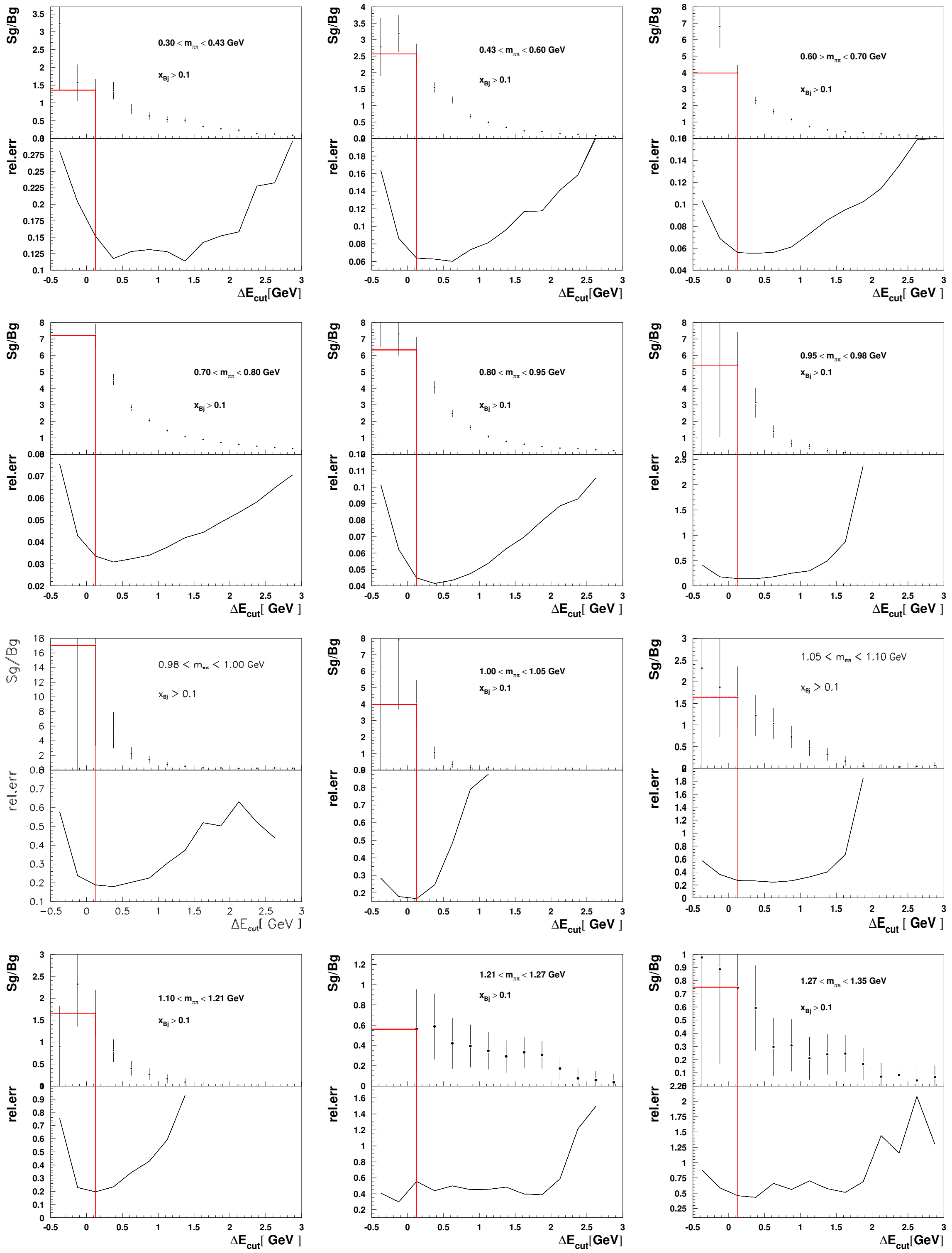

Figure 5.17: In each plot, the behavior of the ratio Sg/Bg (top panel) and its relative statistical error (bottom panel) versus ΔE in each of the 12 invariant mass bins for deuterium target is shown. The vertical line shows the chosen ΔE_{cut} and the horizontal one shows the corresponding ratio Sg/Bg.

target	Number of events at $x_{Bj} > 0.1$
H	$4.4 \cdot 10^3$ ($\Delta E < 0.625$ GeV)
D	$3.7 \cdot 10^3$ ($\Delta E < 0.125$ GeV)

Table 5.3: The total statistics of the data sample with hydrogen (deuterium) target for the exclusive chosen cut $\Delta E < 0.625$ GeV ($\Delta E < 0.125$ GeV), and $x_{Bj} > 0.1$.

In Tab. 5.3 the number of events in the chosen ΔE cuts are reported for both hydrogen and deuterium targets. Within the above exclusive cuts, the intensity densities $\langle P_1(cos\theta)\rangle$ and $\langle P_3(cos\theta)\rangle$ were calculated in the twelve $m_{\pi\pi}$ bins, Fig 5.18. The distributions for the background, $\langle P_{1,3}(cos\theta)\rangle_{Bg}$, were evaluated using data for $\Delta E > 2$ GeV Fig. 5.19-5.20 left panels, supposing its ΔE independence, as described in section 5.5. This hypotheses was tested checking the stability of $\langle P_{1,3}(cos\theta)\rangle_{Bg}$ in different ΔE bins, Fig. 5.19-5.20 right panels. In each bin of $m_{\pi\pi}$, the value of $\langle P_{1,3}(cos\theta)\rangle_{Bg}$, weighted by the ratio Sg/Bg for the selected ΔE cut, was subtracted. The background corrections range between $10-70\%$ in the various bins. This procedure was performed with both hydrogen and deuterium targets respectively.

Fig. 5.21,5.22 show the $m_{\pi\pi}$ dependence of the intensity densities $\langle P_{1(3)}(cos\theta)\rangle$ after background subtraction. Results on $\langle P_1(cos\theta)\rangle$ report an angular production asymmetry of π^+ which depends on the invariant mass $m_{\pi^+\pi^-}$ of the $\pi^+\pi^-$ system at fixed x_{Bj}. At small invariant mass, i.e. close to the threshold $m^2_{\pi^+\pi^-} = 2m_\pi$, this non zero intensity density may be interpreted as originating from the interference of the ρ^0 lower tail with the S-wave non-resonant $\pi^+\pi^-$ production. The absolute value of this quantity shows a minimum at $m_{\pi^+\pi^-} = m_{\rho^0}$. At larger invariant mass the size of the distribution increases due to the interference of the ρ^0 upper tail (P-wave) with the S-wave non-resonant $\pi^+\pi^-$ production. In the f_2 meson region, data indicates a change of sign interpreted as due to the interference of the ρ^0 upper tail with $\pi^+\pi^-$ production from the f_2 (D-wave). At $m_{\pi^+\pi^-} \sim 1$ GeV, the observed asymmetry suggests an interference between the ρ^0 tail and the $\pi^+\pi^-$ production from the f_0 (S-wave).

Results on $\langle P_3(cos\theta)\rangle$ are sensitive only to the interference between the $\pi^+\pi^-$ production channels in P-wave and D-wave. Data clearly show that no pion pair in D-wave is produced in the region $m_{\pi^+\pi^-} \leq 1$ GeV. The distribution $\langle P_3(cos\theta)\rangle$ for deuterium target increases in size and changes sign in the f_2 meson region, and this behavior may be explained as due to the interference of the P-wave and D-wave resonant $\pi^+\pi^-$ channels. On the contrary, data for hydrogen target are compatible with zero in the whole studied $m_{\pi\pi}$ spectrum.

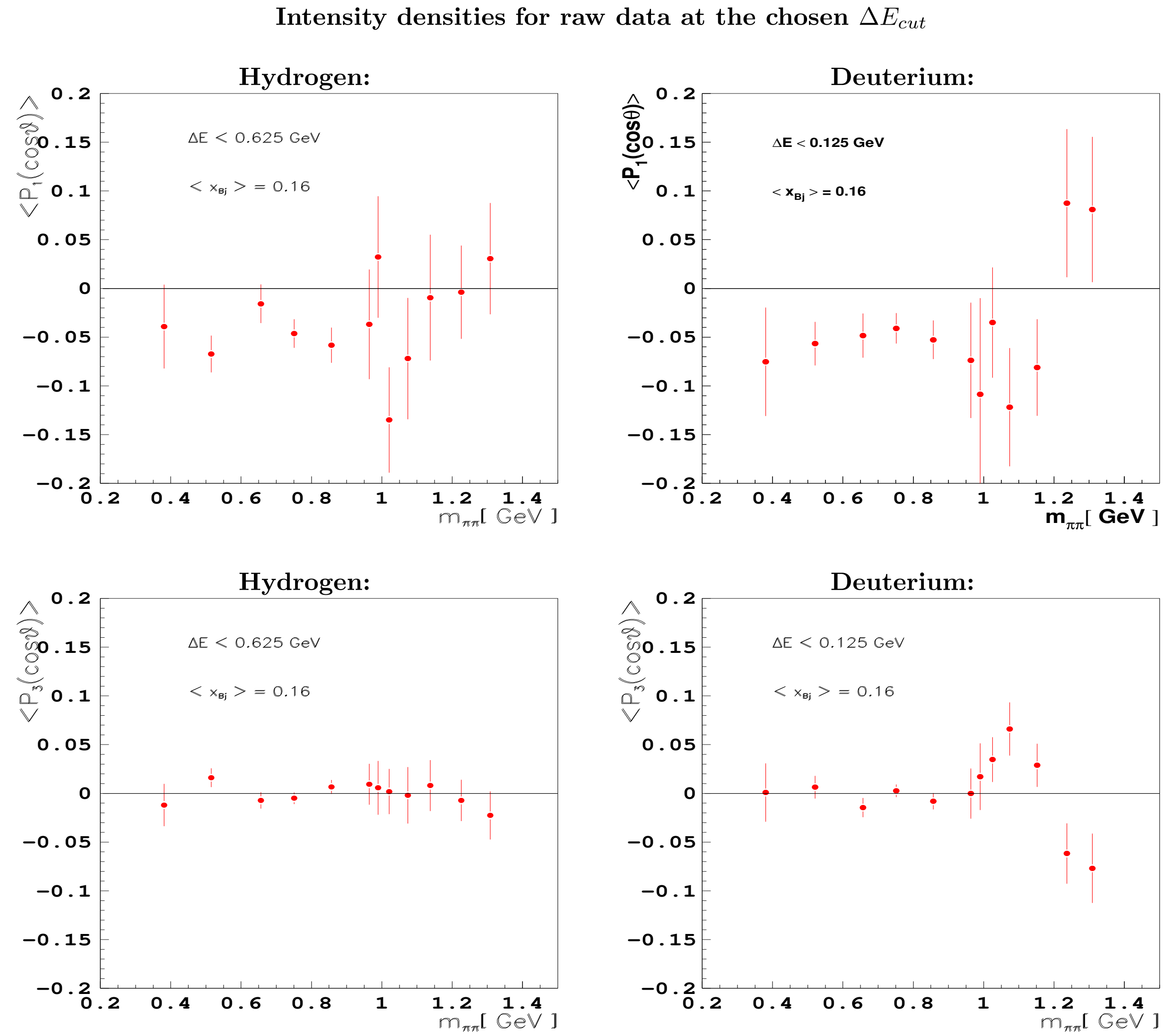

Figure 5.18: $m_{\pi\pi}$ dependence of $\langle P_1(cos\theta)\rangle$ (**upper panels**) and $\langle P_3(cos\theta)\rangle$ (**bottom panels**) distribution for raw data at the chosen exclusive cut $\Delta E < 0.625$ GeV ($\Delta E < 0.125$ GeV) for hydrogen (deuterium) target. The DIS background contribution is not subtracted yet. The distributions have $< m_{\pi\pi} >= 0.78$ GeV.

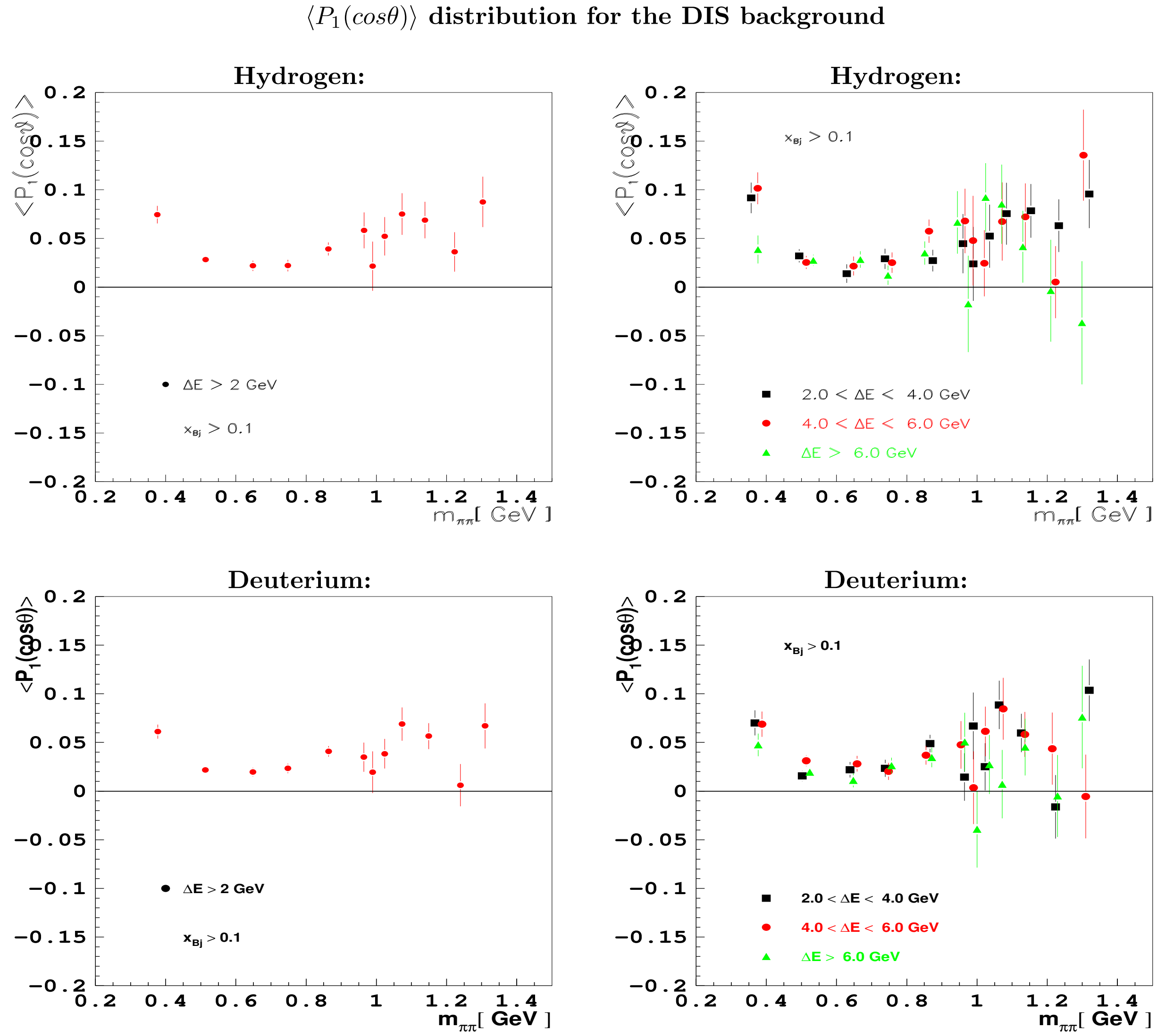

Figure 5.19: $m_{\pi\pi}$ dependence of $\langle P_1(cos\theta)\rangle$ for DIS background (**left panels**) for hydrogen and deuterium targets. The ΔE independence of the distribution has been tested measuring it in different ΔE bins (**right panels**).

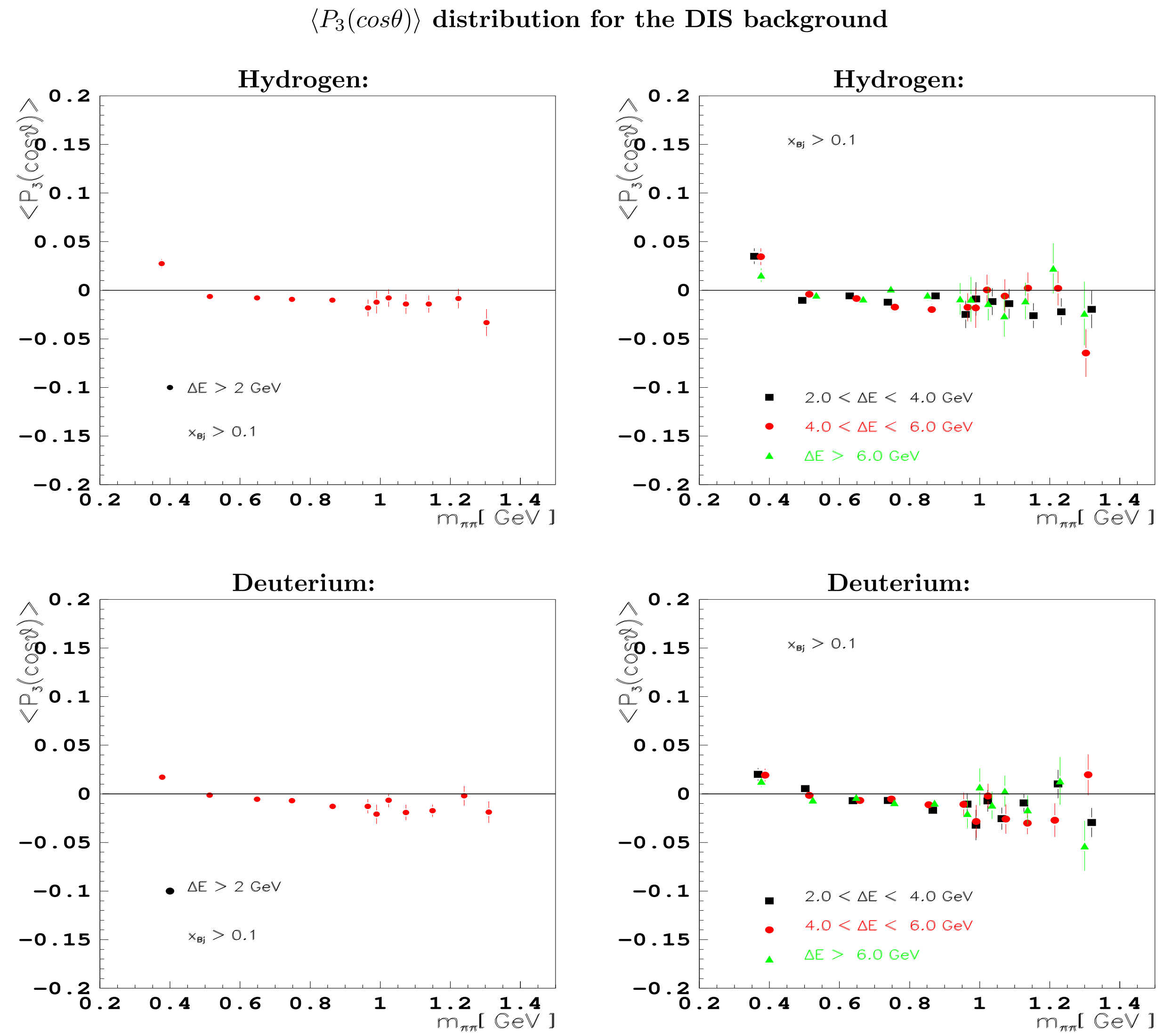

Figure 5.20: $m_{\pi\pi}$ dependence of $\langle P_3(cos\theta)\rangle$ distribution for DIS background (**left panels**) for hydrogen and deuterium targets. The ΔE independence of the distribution has been tested measuring it in different ΔE bins (**right panels**).

$\langle P_1(cos\theta)\rangle$ distributions after DIS background subtraction:

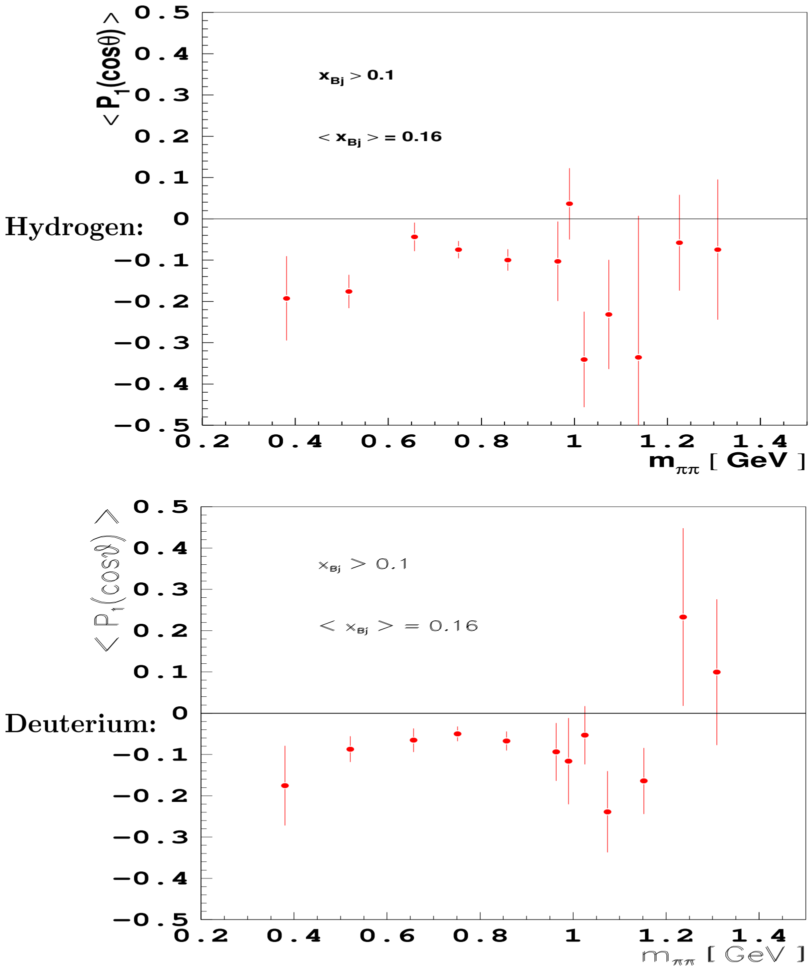

Figure 5.21: Invariant mass dependence of the $\langle P_1(cos\theta)\rangle$ distribution for the exclusive channel $e^+p \rightarrow e^+p\ \pi^+\pi^-$ (**upper panel**) and $e^+d \rightarrow e^+d\ \pi^+\pi^-$ (**bottom panel**) after DIS background subtraction.

$\langle P_3(cos\theta)\rangle$ distributions after DIS background subtraction:

Hydrogen:

Deuterium:

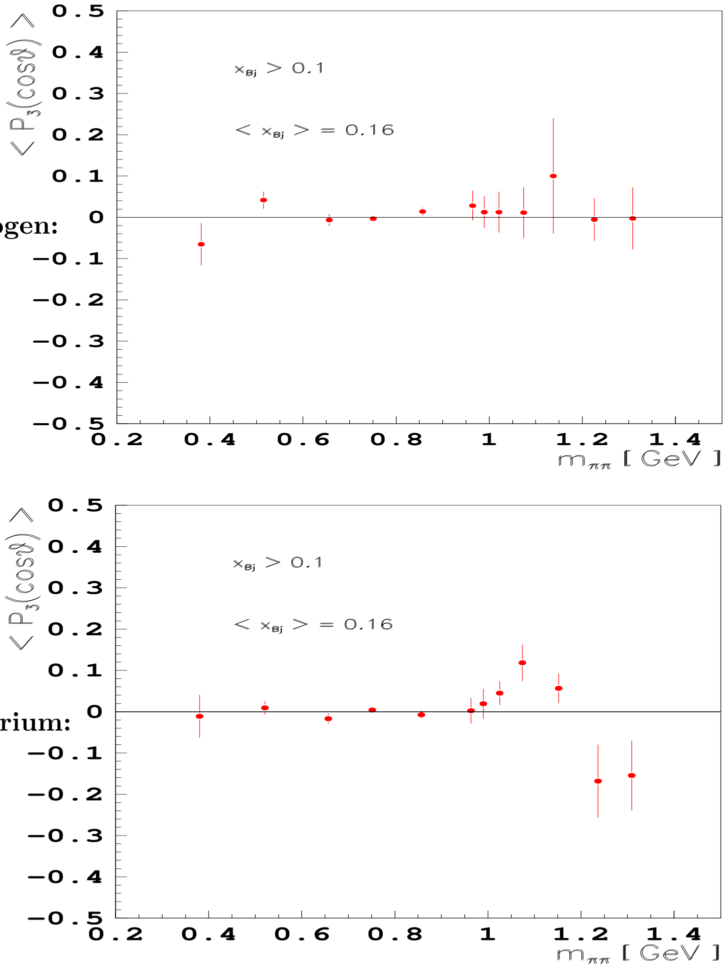

Figure 5.22: Invariant mass dependence of the $\langle P_3(cos\theta)\rangle$ distribution for the exclusive channel $e^+p \rightarrow e^+p\ \pi^+\pi^-$ (**upper panel**) and $e^+d \rightarrow e^+d\ \pi^+\pi^-$ (**bottom panel**) after DIS background subtraction.

5.6.2 Acceptance Effects and Radiative Corrections

To evaluate any effect due to the forward geometrical acceptance, a Monte Carlo simulation was used. Nowadays no Monte Carlo dedicated for the $\pi^+\pi^-$ hard exclusive production exists. Instead several generators have been developed for the $\pi^+\pi^-$ exclusive production which is ruled by different mechanisms from the studied process in this work, and in this analysis acceptance effects have been studied using the Monte Carlo *DIPSI* described in section 5.3. Table 5.4 shows the total number of both the events generated in the solid angle 4π [1] and the events reconstructed in the *HERMES* acceptance for hydrogen target, and within the cut $x_{Bj} > 0.1$. In Fig. 5.23 both the

target	Generated events in the solid angle 4π	Reconstructed events in the *HERMES* acceptance
H	$50 \cdot 10^3$	$30 \cdot 10^3$

Table 5.4: The total statistics of both the generated events and the reconstructed events in the *HERMES* acceptance produced by the Monte Carlo *DIPSI* generator for hydrogen target and within the cut $x_{Bj} > 0.1$.

geometrical acceptance and smearing, for $\langle P_1(cos\theta)\rangle$ (upper panel) and $\langle P_3(cos\theta)\rangle$ (bottom panel) versus the invariant mass with hydrogen target are shown. The evaluation of smearing effects was performed chaining the *DIPSI* simulation with the *HERMES* spectrometer simulator and the reconstruction program. From the above results, the effects due to acceptance are clearly negligible.

To estimate the radiative corrections of the intensity densities, reference [95] was taken into account. In this reference it is studied how radiative corrections can modify the angular distributions of decay products of ρ^0 mesons. It is finally claimed that this kind of corrections is less than 1% in the H1 and ZEUS kinematics where events have an average x_{Bj} lower then one order of magnitude on respect to the *HERMES* kinematics. That means that for the current analysis, and in particular for the analysis of the $m_{\pi\pi}$ dependence of $\langle P_{1(3)}(cos\theta)\rangle$ where the cut $x_{Bj} > 0.1$ is applied, radiative corrections effects can be considered negligible.

[1] All particles are generated in the solid angle 4π except the scattered positron which is generated in the *HERMES* acceptance.

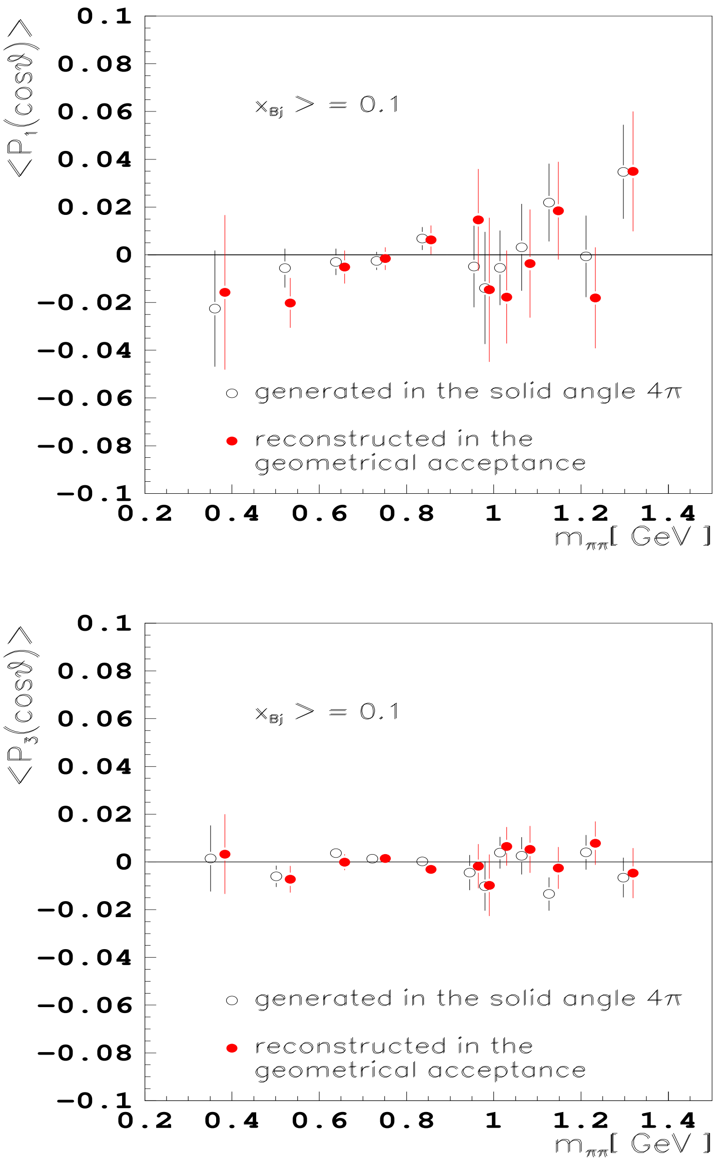

Figure 5.23: Instrumental smearing and geometrical acceptance effects evaluated for $\langle P_1(cos\theta)\rangle$, **upper panel**, and for $\langle P_3(cos\theta)\rangle$ **bottom panel**, using the Monte Carlo *DIPSI* generator for hydrogen target.

5.6.3 Systematic Uncertainties

To evaluate the significativity of the results, studies on the systematic uncertainties have been performed. In particular, the systematic uncertainties have been evaluated considering a different choice of the ratio Sg/Bg, a different normalization cut of *DIS MC* sample to data, and taking into account the initial assumption to consider all hadrons as pions. Each of the systematic uncertainties are given as absolute values.

Figure 5.24 shows the $m_{\pi\pi}$ dependence of $\langle P_{1(3)}(cos\theta)\rangle$ measured using different exclusive ΔE cuts for hydrogen and deuterium targets respectively. The maximum difference, bin by bin, of the measured distributions is considered as the uncertainty given by the particular ΔE cut chosen in the analysis. Table 5.5 reports the maximum factor change of the ratio Sg/Bg in each $m_{\pi\pi}$ bin. It is worth to note that, even though the ratio Sg/Bg changes up to an average factor 3, the systematic uncertainties are less then few percent in most of the bins. This means that the *DIS* background subtraction was good and reliable. Numerical values of this kind of uncertainty are reported in Tab. 5.6.

	Factor change of Sg/Bg	
$m_{\pi\pi}$ $[GeV]$	**Hydrogen**	**Deuterium**
$0.30 - 0.43$	2.02	1.64
$0.43 - 0.60$	2.34	2.20
$0.60 - 0.70$	2.14	2.44
$0.70 - 0.80$	2.18	2.54
$0.80 - 0.95$	2.65	2.57
$0.95 - 0.98$	4.05	3.95
$0.98 - 1.00$	4.32	7.40
$1.00 - 1.05$	3.33	11.71
$1.05 - 1.10$	1.77	1.03
$1.10 - 1.21$	2.57	4.15
$1.21 - 1.27$	1.19	1.33
$1.27 - 1.35$	1.63	2.50

Table 5.5: Maximum factor change of the ratio Sg/Bg due to the choice of different exclusive ΔE cuts for hydrogen and deuterium target respectively.

Intensity densities $\langle P_{1(3)}(cos\theta)\rangle$ measured using different ΔE cuts.

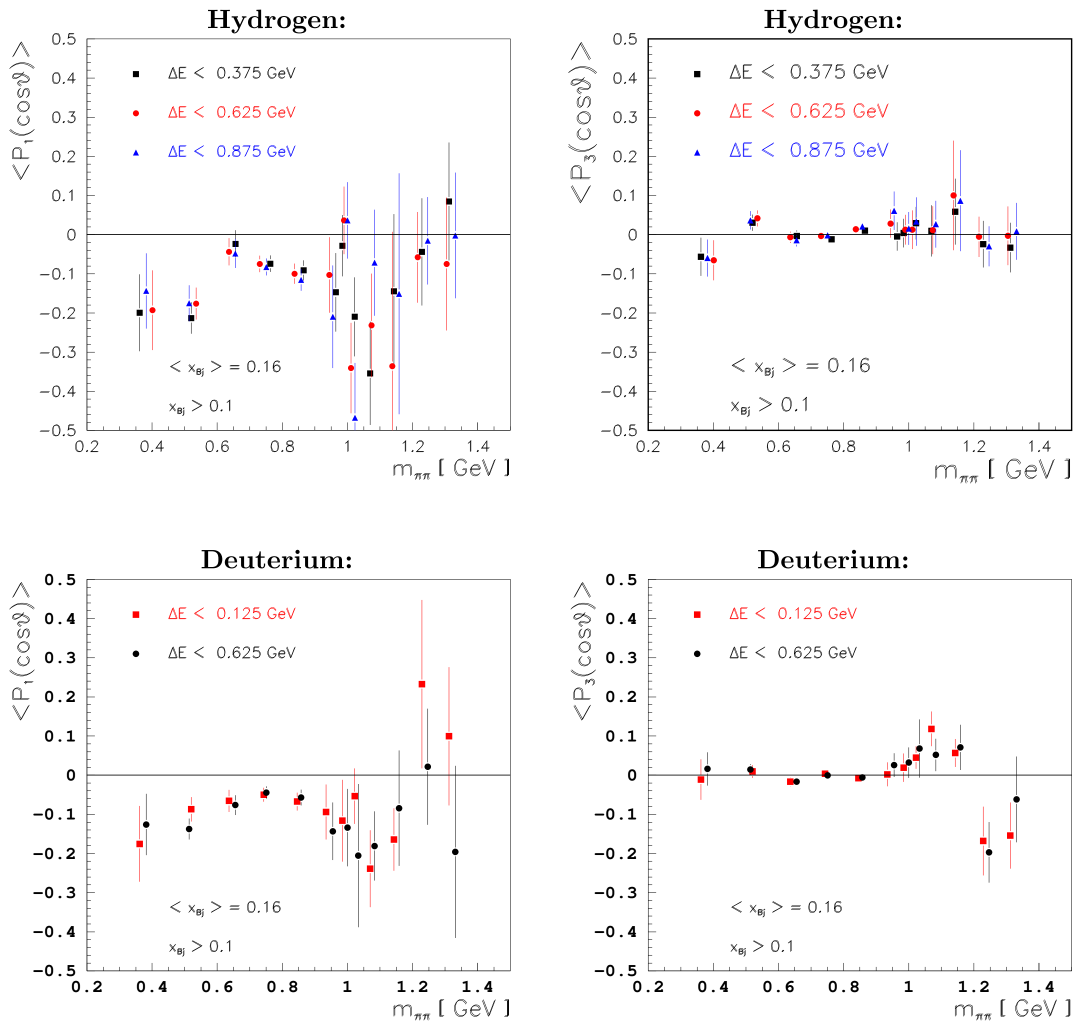

Figure 5.24: $\langle P_{1(3)}(cos\theta)\rangle$ distributions versus $m_{\pi\pi}$ at $x_{Bj} > 0.1$ obtained using different exclusive ΔE cuts for hydrogen (**upper panels**) and deuterium (**bottom panels**) targets respectively.

Systematic uncertainty due to different ΔE cuts				
	Hydrogen		**Deuterium**	
$m_{\pi\pi}$ $[GeV]$	$\langle P_1(cos\theta)\rangle$	$\langle P_3(cos\theta)\rangle$	$\langle P_1(cos\theta)\rangle$	$\langle P_3(cos\theta)\rangle$
0.30 – 0.43	0.049	0.009	0.050	0.027
0.43 – 0.60	0.037	0.011	0.050	0.005
0.60 – 0.70	0.020	0.008	0.011	0.000
0.70 – 0.80	0.008	0.008	0.006	0.005
0.80 – 0.95	0.016	0.007	0.010	0.001
0.95 – 0.98	0.107	0.033	0.050	0.024
0.98 – 1.00	0.065	0.008	0.018	0.013
1.00 – 1.05	0.131	0.021	0.152	0.023
1.05 – 1.10	0.160	0.016	0.058	0.066
1.10 – 1.21	0.191	0.042	0.080	0.014
1.21 – 1.27	0.042	0.024	0.211	0.029
1.27 – 1.35	0.160	0.030	0.295	0.093

Table 5.6: Absolute systematic uncertainties in the determination of $\langle P_{1(3)}(cos\theta)\rangle$ versus $m_{\pi\pi}$, due to the choice of different ΔE cuts for both hydrogen and deuterium targets.

The choice of a normalization cut for *DIS* background to data at a chosen ΔE is a contribution to the systematic uncertainty. This uncertainty depends on how well the generated montecarlo sample reproduces the shape of background in the studied kinematic region, and in particular at very low values of the variable ΔE. To estimate this uncertainty, the montecarlo has been normalized at $2.0 < \Delta E < 4.0$ GeV, i.e in the region close the exclusive peak for the process $e^+p(d) \longrightarrow e^+p(d)\pi^+\pi^-$ characterized by ΔE peaked around zero.

This systematic uncertainty is evaluated as the difference of values bin by bin of $\langle P_{1(3)}(cos\theta)\rangle$ measured for a background normalization at $\Delta E > 2$ GeV and $2 < \Delta E < 4$ GeV respectively, Fig. 5.25. Numerical results of this measured systematic uncertainty are reported in Tab. 5.7.

Intensity densities $\langle P_{1(3)}(cos\theta)\rangle$ measured using different MC normalization cuts to data.

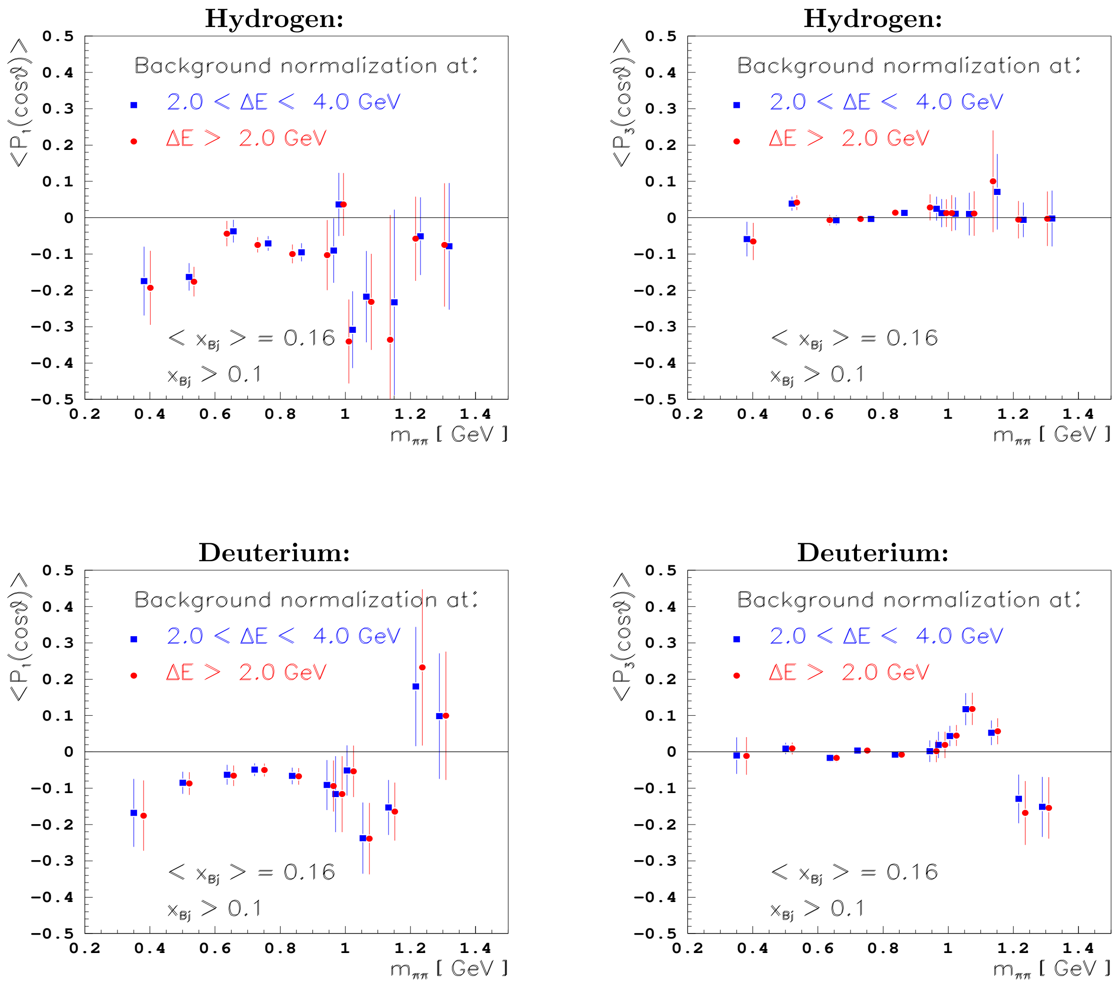

Figure 5.25: $\langle P_{1(3)}(cos\theta)\rangle$ distributions versus $m_{\pi\pi}$ at $x_{Bj} > 0.1$ obtained using different cuts for the *DIS* Monte Carlo normalization to data for both hydrogen (**upper panels**) and deuterium (**bottom panels**) targets.

Systematic uncertainty due to different normalization cuts				
	Hydrogen		**Deuterium**	
$m_{\pi\pi}$ $[GeV]$	$\langle P_1(cos\theta)\rangle$	$\langle P_3(cos\theta)\rangle$	$\langle P_1(cos\theta)\rangle$	$\langle P_3(cos\theta)\rangle$
$0.30 - 0.43$	0.018	0.006	0.007	0.001
$0.43 - 0.60$	0.013	0.003	0.002	0.000
$0.60 - 0.70$	0.006	0.000	0.003	0.000
$0.70 - 0.80$	0.004	0.000	0.001	0.000
$0.80 - 0.95$	0.004	0.001	0.001	0.000
$0.95 - 0.98$	0.012	0.003	0.003	0.000
$0.98 - 1.00$	0.000	0.000	0.000	0.000
$1.00 - 1.05$	0.032	0.002	0.002	0.001
$1.05 - 1.10$	0.014	0.001	0.001	0.001
$1.10 - 1.21$	0.102	0.029	0.011	0.004
$1.21 - 1.27$	0.007	0.000	0.053	0.039
$1.27 - 1.35$	0.004	0.001	0.001	0.003

Table 5.7: Absolute systematic uncertainty in the determination of $\langle P_{1(3)}(cos\theta)\rangle$ versus $m_{\pi\pi}$ at $x_{Bj} > 0.1$, due to different cuts to normalize DIS background to data for both hydrogen and deuterium targets.

In this analysis, the exclusive and semi-inclusive non $\pi^+\pi^-$ pairs contamination was evaluated in few percent of the whole hadron sample, therefore all hadrons were considered as pions. The semi-inclusive contamination was subtructed using the Monte Carlo *GMC*, as described in 5.5. Instead, the above exclusive contamination (e.g. from $\phi \rightarrow \rho\pi$) was taken into account in the systematic uncertainty and determined with the following procedure.

Using the information by the RICH detecror (section 4.3), pions are identified in the energy range $2 - 15$ GeV. Since the RICH was intalled in 1998, this identification was performed only with data of the 1998, 1999 and 2000 productions. Within this energy cut, for all hadrons and separately the identified pions, the ratio Sg/Bg was measured at the exclusive ΔE cut used in this analysis, and the background contribution to $\langle P_{1(3)}(cos\theta)\rangle$ was subtracted.

This systematic uncertainty is evaluated as the difference of values bin by bin of the intensity densities measured for the above selected hadron and pion pairs respectively, Fig. 5.26. Numerical values are reported in Tab. 5.8. The uncertainty due to this contamination was assumed to be the same for data collected in 1996 and 1997.

Systematic uncertainty due to assumption of considering all hadrons as pions

	Hydrogen		**Deuterium**	
$m_{\pi\pi}$ $[GeV]$	$\langle P_1(cos\theta)\rangle$	$\langle P_3(cos\theta)\rangle$	$\langle P_1(cos\theta)\rangle$	$\langle P_3(cos\theta)\rangle$
$0.30 - 0.43$	0.200	0.098	0.007	0.023
$0.43 - 0.60$	0.018	0.026	0.002	0.004
$0.60 - 0.70$	0.023	0.006	0.004	0.001
$0.70 - 0.80$	0.003	0.001	0.005	0.002
$0.80 - 0.95$	0.008	0.006	0.002	0.002
$0.95 - 0.98$	0.032	0.020	0.009	0.027
$0.98 - 1.00$	0.031	0.023	0.093	0.043
$1.00 - 1.05$	0.049	0.027	0.036	0.010
$1.05 - 1.10$	0.104	0.064	0.030	0.006
$1.10 - 1.21$	0.051	0.053	0.039	0.018
$1.21 - 1.27$	0.076	0.012	0.084	0.011
$1.27 - 1.35$	0.055	0.082	0.368	0.169

Table 5.8: Absolute systematic uncertainty in the determination of $\langle P_{1(3)}(cos\theta)\rangle$ versus $m_{\pi\pi}$ at $x_{Bj} > 0.1$, due to assumption to consider all hadrons as pions, for hydrogen and deuterium target, respectively.

Comparison of intensity densities $\langle P_{1(3)}(cos\theta)\rangle$ measured using pions and hadrons at $2 < E < 15$ GeV, respectively

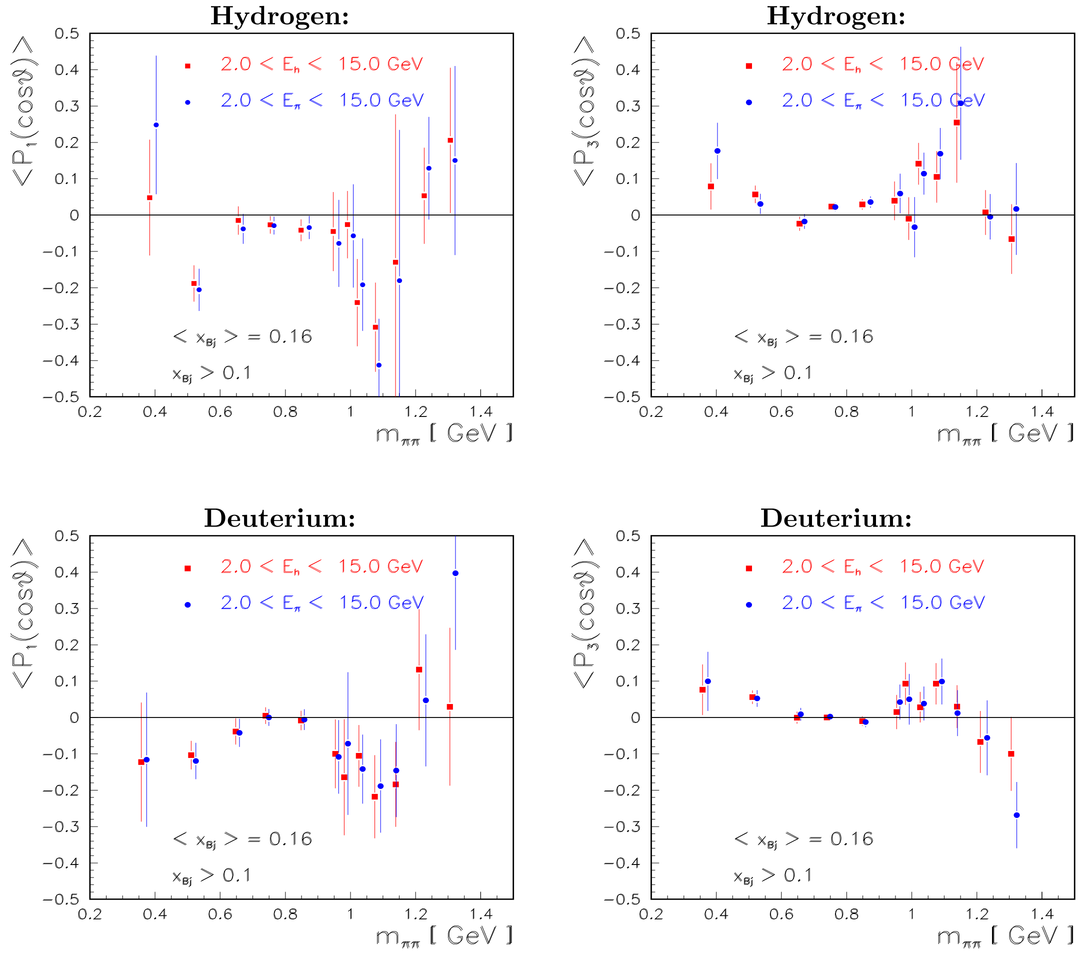

Figure 5.26: $m_{\pi\pi}$ dependence of $\langle P_{1(3)}(cos\theta)\rangle$ in the invariant mass region $0.6 < m_{\pi\pi(hh)} < 1.0$ GeV, obtained using pion (squares) and hadron (circles) pairs with particles having energy $2 < E < 15$ GeV, for hydrogen (**upper panels**) and deuterium (**bottom panels**) target respectively.

In the whole invariant mass region, the total systematic uncertainty, reported in Tab. 5.9 has been computed bin by bin as follows:

$$\sigma_{syst\_tot} = \sqrt{\sum_{k=1,3} \sigma^2_{syst\_k}} \ , \tag{5.7}$$

considering the different uncertainties σ_{syst_k} as due to independent sources. From the comparison of all the uncertainties, the change of the ratio Sg/Bg results to be the main source of systematic uncertainty.

Total systematic uncertainty				
	Hydrogen		**Deuterium**	
$m_{\pi\pi}$ $[GeV]$	$\langle P_1(cos\theta)\rangle$	$\langle P_3(cos\theta)\rangle$	$\langle P_1(cos\theta)\rangle$	$\langle P_3(cos\theta)\rangle$
$0.30 - 0.43$	0.207	0.099	0.051	0.035
$0.43 - 0.60$	0.043	0.028	0.050	0.006
$0.60 - 0.70$	0.031	0.010	0.012	0.001
$0.70 - 0.80$	0.009	0.008	0.008	0.005
$0.80 - 0.95$	0.018	0.009	0.010	0.002
$0.95 - 0.98$	0.112	0.039	0.051	0.036
$0.98 - 1.00$	0.072	0.024	0.095	0.045
$1.00 - 1.05$	0.143	0.034	0.156	0.025
$1.05 - 1.10$	0.191	0.066	0.065	0.066
$1.10 - 1.21$	0.222	0.074	0.090	0.023
$1.21 - 1.27$	0.087	0.027	0.233	0.050
$1.27 - 1.35$	0.169	0.087	0.472	0.193

Table 5.9: Absolute total systematic uncertainty in the determination of $\langle P_{1(3)}(cos\theta)\rangle$ versus $m_{\pi\pi}$ at $x_{Bj} > 0.1$, for hydrogen and deuterium target, respectively.

5.6.4 Results

The invariant mass dependence of the intensity densities has been analyzed with the *HERMES* experiment. The average values of the relevant variables x_{Bj}, Q^2 and t are reported in Tab. 5.10.

Hydrogen			**Deuterium**		
$\langle x_{Bj}\rangle$	$\langle Q^2\rangle$ $[GeV^2]$	$\langle -t\rangle$ $[GeV^2]$	$\langle x_{Bj}\rangle$	$\langle Q^2\rangle$ $[GeV^2]$	$\langle -t\rangle$ $[GeV^2]$
0.16	3.3	0.43	0.16	3.2	0.29

Table 5.10: Average values of the relevant variables x_{Bj}, Q^2 and t in the analysis of the $m_{\pi\pi}$ dependence of $\langle P_1(cos\theta)\rangle$ and $\langle P_3(cos\theta)\rangle$.

Results on $\langle P_1(cos\theta)\rangle$ report an asymmetry of the angular production of π^+ which depends on the invariant mass $m_{\pi\pi}$ of the $\pi^+\pi^-$ system at fixed x_{Bj}. At small invariant mass, i.e. close to the threshold $m^2_{\pi\pi} = 2m_\pi$, this non zero intensity density may be interpreted as originating from the interference of the ρ^0 lower tail with the S-wave non-resonant $\pi^+\pi^-$ production. At $m_{\pi\pi} = m_{\rho^0}$, the absolute value of this quantity shows a minimum which can be explained as due to a smaller interference between the isovector and isoscalar $\pi^+\pi^-$ exclusive chanels. The increasing of the size of $\langle P_1(cos\theta)\rangle$ at larger invariant mass may be interpreted as due to the interference of the ρ^0 upper tail (P-wave) with the S-wave non-resonant $\pi^+\pi^-$ production. Moreover, in the f_2 meson region, the data indicate a change of sign explained as due to the superimposion of the interference between the ρ^0 upper tail and the the f_2 (D-wave). It is worth mentioning that at $m_{\pi\pi} \sim 1$ GeV, the observed asymmetry suggests the interference with the ρ^0 tail and the $\pi^+\pi^-$ production from the f_0 (S-wave). This fact by itself is interesting due to the importance of the scalar meson physics.

Results on $\langle P_3(cos\theta)\rangle$ are sensitive only to the interference between the $\pi^+\pi^-$ production channels in P-wave and D-wave. Data clearly show that no pion pair in D-wave are produced in the region $m_{\pi\pi} \leq 1$ GeV, in agreement with the fact the no resonance decay into $\pi^+\pi^-$ is expected in this invariant mass region. The distribution $\langle P_3(cos\theta)\rangle$ for deuterium target increases in size and changes sign in the f_2 meson region, as expected due to the interference of the P-wave and D-wave resonant $\pi^+\pi^-$ channels. With respect to data for deuterium target, inside the statistical and systematical uncertainty for hydrogen, results do not show evidence of the D-wave channel.

A consequence of the results on the $m_{\pi\pi}$ dependence of the studied intensity densities is that the angular distribution of the $\pi^+\pi^-$ pair is not the one of a pure P-wave. It is essential to know how important contributions from other partial waves are for analyses of the helicity density matrix in ρ^0 production, which describes the transfer of virtual photon helicity to the vector meson. In fact the usual extraction methods for ρ^0 helicity density matrix assume a pure P-wave.

$m_{\pi\pi}$**-dependence of** $\langle P_1(cos\theta)\rangle$**:**

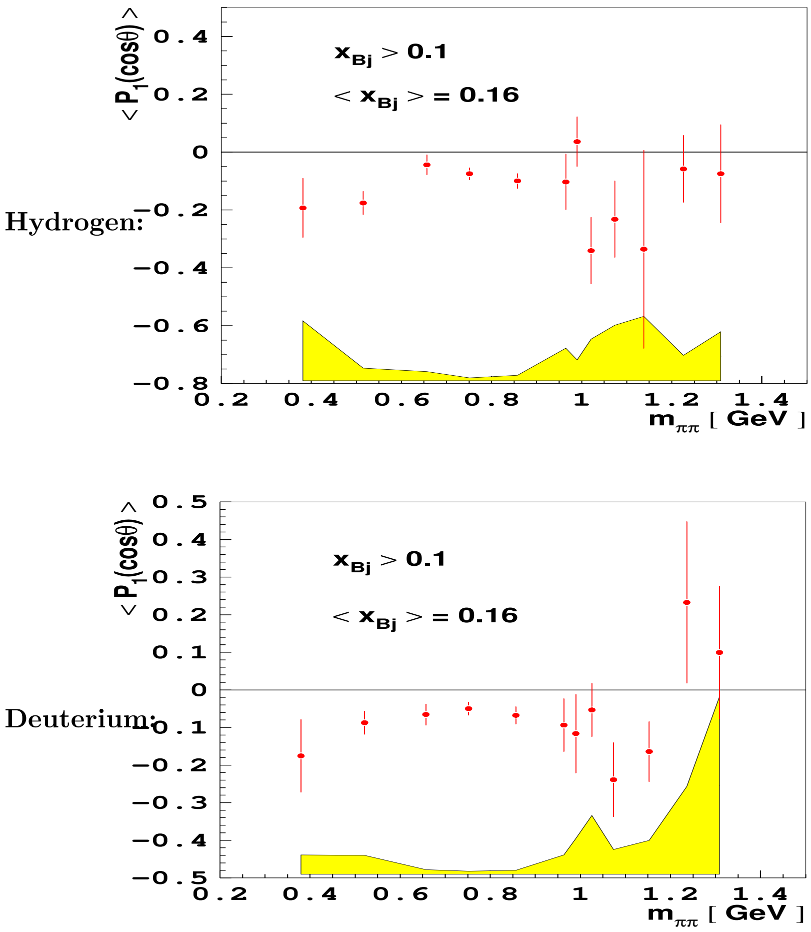

Figure 5.27: Invariant mass dependence of the $\langle P_1(cos\theta)\rangle$ distribution for the exclusive channel $e^+p \rightarrow e^+p\ \pi^+\pi^-$ (**upper panel**) and $e^+d \rightarrow e^+d\ \pi^+\pi^-$ (**bottom panel**) after DIS background subtraction.

$m_{\pi\pi}$**-dependence of** $\langle P_3(cos\theta)\rangle$**:**

Hydrogen:

Deuterium:

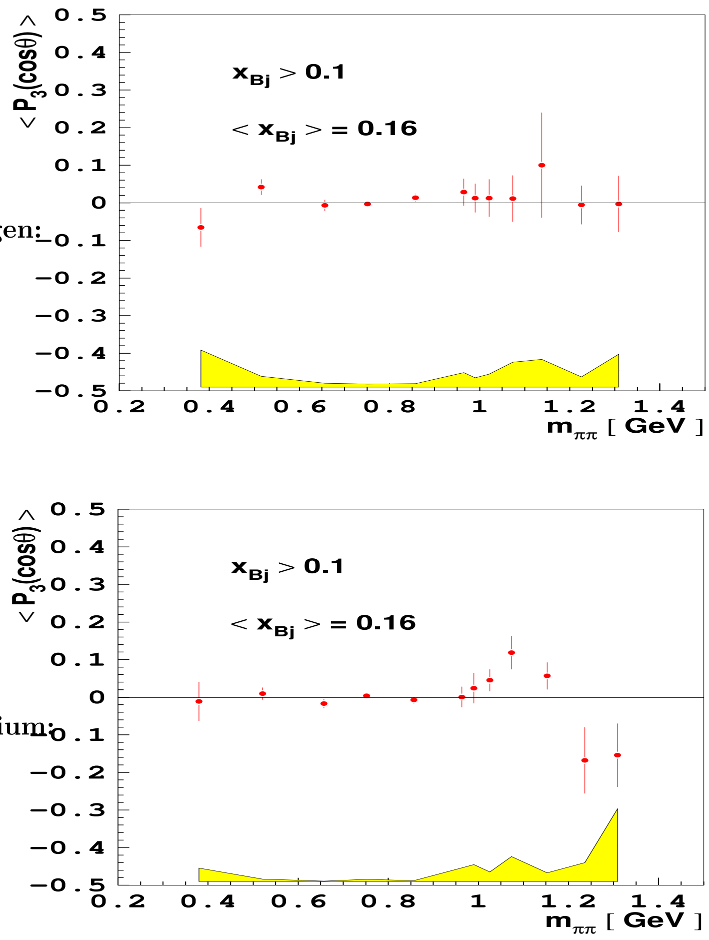

Figure 5.28: Invariant mass dependence of the $\langle P_3(cos\theta)\rangle$ distribution for the exclusive channel $e^+p \rightarrow e^+p\ \pi^+\pi^-$ (**upper panel**) and $e^+d \rightarrow e^+d\ \pi^+\pi^-$ (**bottom panel**) after DIS background subtraction.

5.7 x_{Bj}-dependence of Intensity Densities

An interesting feature of $\langle P_1(cos\theta)\rangle$ and $\langle P_3(cos\theta)\rangle$ is that they are predicted to depend strongly on x_{Bj}. This is mainly due to the different mechanism that take place at different x_{Bj} regions. In section 3.3 it was shown that at large x_{Bj} the pion pairs production is dominated by $q\bar{q}$ exchange, which leads to a sizable admixture of pion pairs with isospin zero [48]. Therefore at large x_{Bj} the interference between the isovector and the isoscalar channel is predicted to increase, resulting in the increasing size of the intensity densities which depend linearly on the interference term of the amplitude. Consequently the x_{Bj}-dependence of the intensity densities $\langle P_1(cos\theta)\rangle$ and $\langle P_3(cos\theta)\rangle$ was analyzed to measure the above interference and highlight the weak isoscalar $\pi^+\pi^-$ production. The hydrogen and deuterium targets have been analyzed separately.

The analysis was performed in two different $m_{\pi\pi}$ regions, $0.3 < m_{\pi\pi} < 0.6$ GeV and $0.6 < m_{\pi\pi} < 1.0$ GeV with average values $< m_{\pi\pi} > = 0.48$ GeV and $< m_{\pi\pi} > = 0.78$ GeV respectively. In the invariant mass region $m_{\pi\pi} > 1$ GeV the statistics is very small, and for this reason this analysis was not performed.

5.7.1 Background Subtraction

The *DIS* background contribution to the exclusive channel was subtracted following the same procedure applied when the $m_{\pi\pi}$ dependence of $\langle P_{1(3)}(cos\theta)\rangle$ distributions was studied, 5.6.1. In the studied $m_{\pi\pi}$ regions, the x_{Bj} spectrum was divided in six bins: $x_{Bj} \leq 0.053$, $0.053 < x_{Bj} \leq 0.072$, $0.072 < x_{Bj} \leq 0.100$, $0.100 < x_{Bj} \leq 0.125$, $0.125 < x_{Bj} \leq 0.145$, $x_{Bj} > 0.145$. In each bin, the Monte Carlo was normalized to the experimental data at $\Delta E > 2$ GeV. Fig. 5.29-5.30 show that the Monte Carlo well reproduces the background shape at large ΔE, while at small ΔE there is an eccess of data which is due to the exclusive process $e^+p(d) \longrightarrow e^+p(d)\pi^+\pi^-$, mainly through the ρ^0 meson decay, not simulated in the Monte Carlo. After the background normalization, the exclusive sample was extracted (Fig. 5.31-5.32) and the ratio Sg/Bg was measured (Fig. 5.33-5.34).

In the $0.6 < m_{\pi\pi} < 1.0$ GeV region the exclusive cuts $\Delta E < 0.625$ and $\Delta E < 0.375$ GeV for hydrogen and deuterium targets respectively were chosen to maximize the ratio of the exclusive signal over the background and to minimize its relative statistical error.

$0.6 < m_{\pi\pi} < 1.0$ GeV
Hydrogen target: *MC* normalization to experimental data.

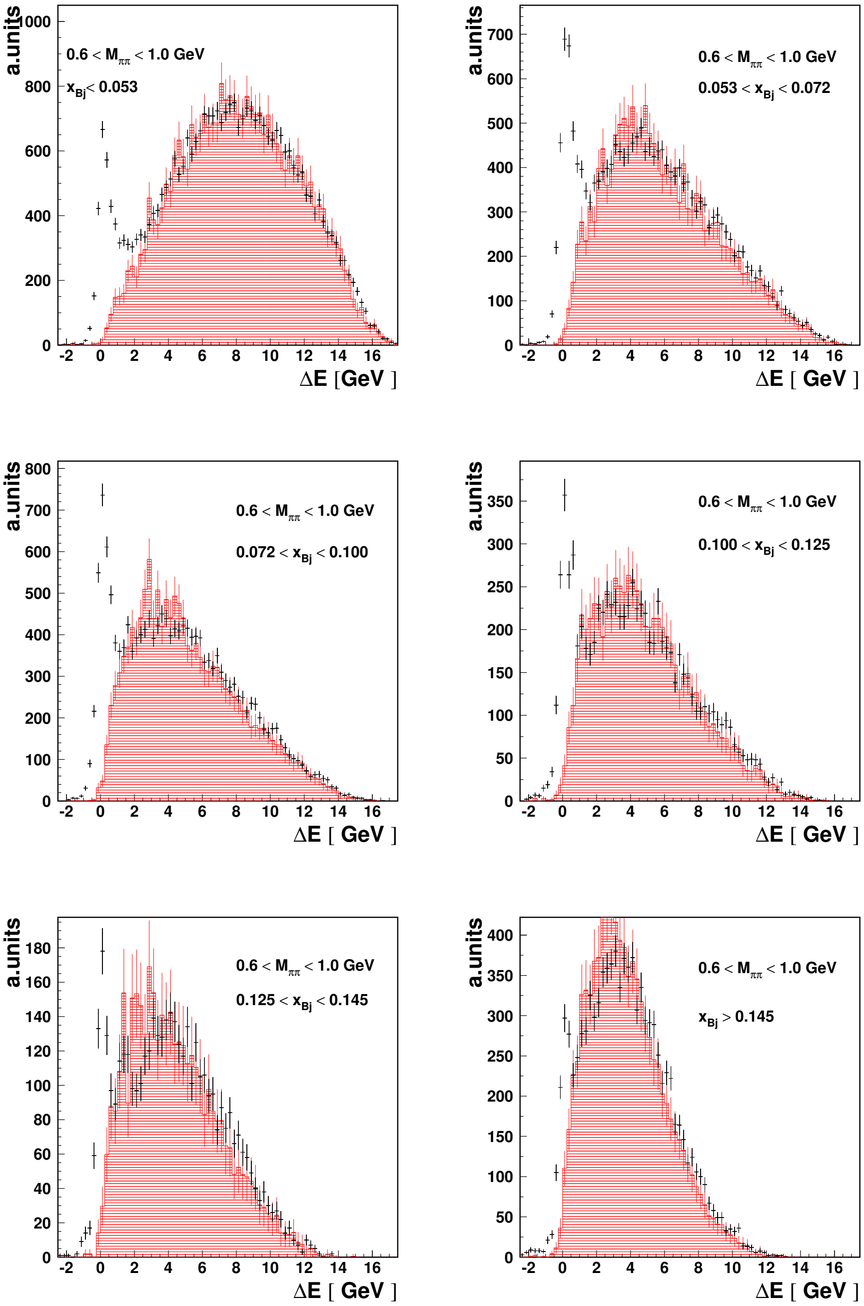

Figure 5.29: ΔE distribution in the six x_{Bj} bins inside the invariant mass region $0.6 < m_{\pi\pi} < 1.0$ GeV for hydrogen target. *MC* data (shadowed) are normalized to the experimental one (crosses) for $\Delta E > 2$ GeV.

$0.6 < m_{\pi\pi} < 1.0$ GeV

Deuterium target: *MC* normalization to experimental data.

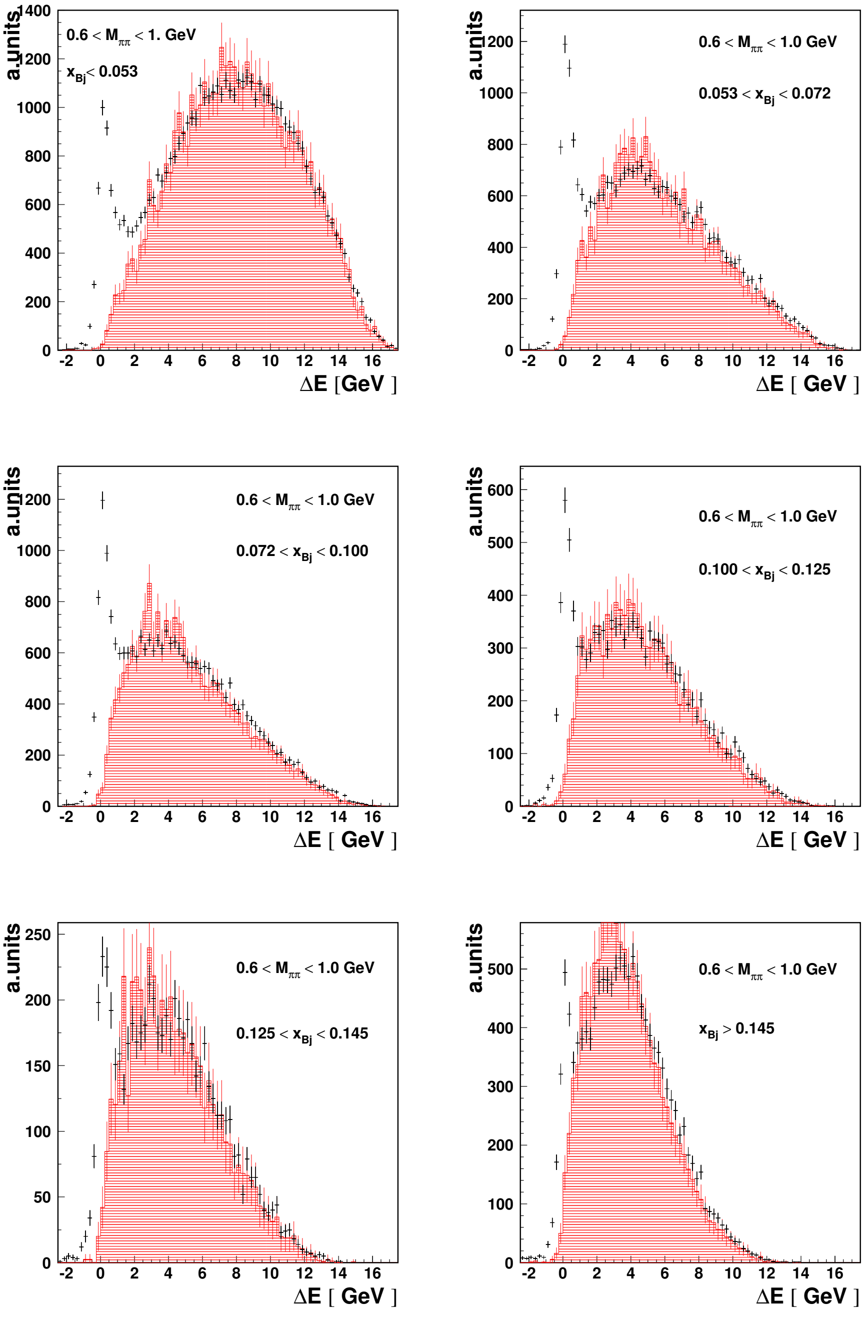

Figure 5.30: ΔE distribution in the six x_{Bj} bins inside the invariant mass region $0.6 < m_{\pi\pi} < 1.0$ GeV for deuterium target. *MC* data (shadowed) are normalized to the experimental one (crosses) for $\Delta E > 2$ GeV.

$0.6 < m_{\pi\pi} < 1.0$ **GeV**
Hydrogen target: extraction of the exclusive signal (Sg)

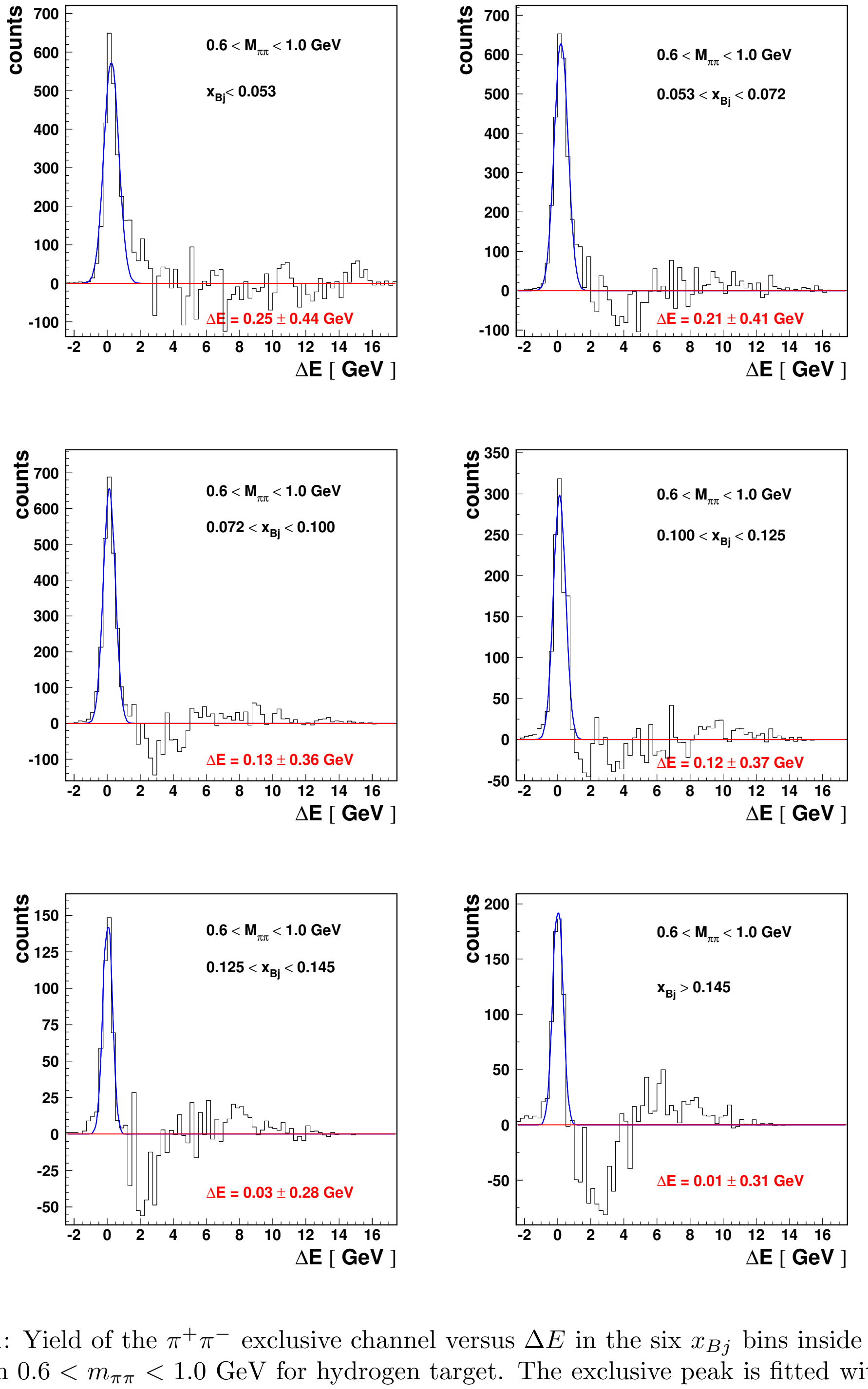

Figure 5.31: Yield of the $\pi^+\pi^-$ exclusive channel versus ΔE in the six x_{Bj} bins inside the invariant mass region $0.6 < m_{\pi\pi} < 1.0$ GeV for hydrogen target. The exclusive peak is fitted with a gaussian whose expectation value and width values are shown in the bottom left side of each plot.

$0.6 < m_{\pi\pi} < 1.0$ **GeV**
Deuterium target: extraction of the exclusive signal (Sg)

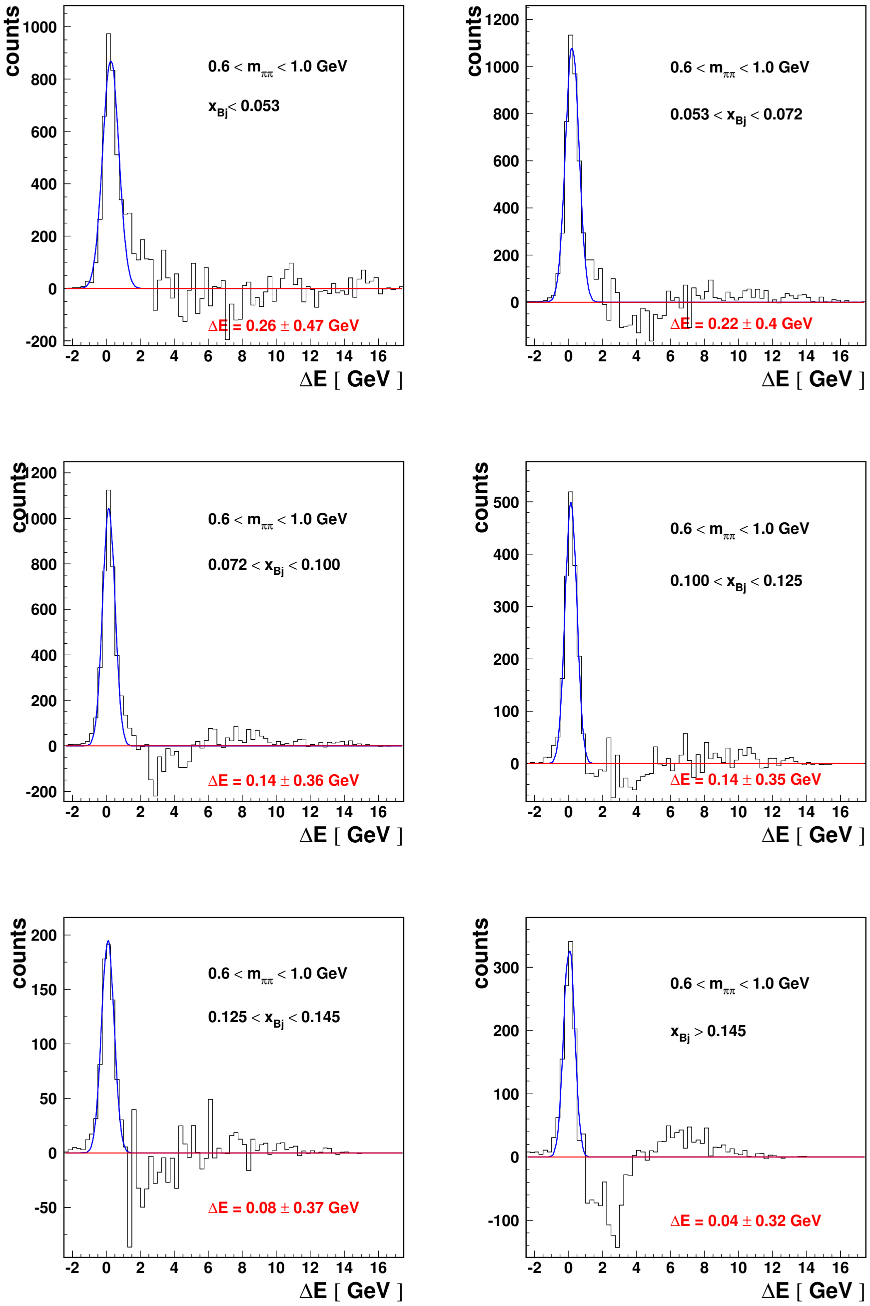

Figure 5.32: Yield of the $\pi^+\pi^-$ exclusive channel versus ΔE in the six x_{Bj} bins inside the invariant mass region $0.6 < m_{\pi\pi} < 1.0$ GeV for deuterium target. The exclusive peak is fitted with a gaussian whose expectation value and width values are shown in the bottom left side of each plot.

$0.6 < m_{\pi\pi} < 1.0$ **GeV**
Hydrogen target: ratio Sg/Bg versus ΔE

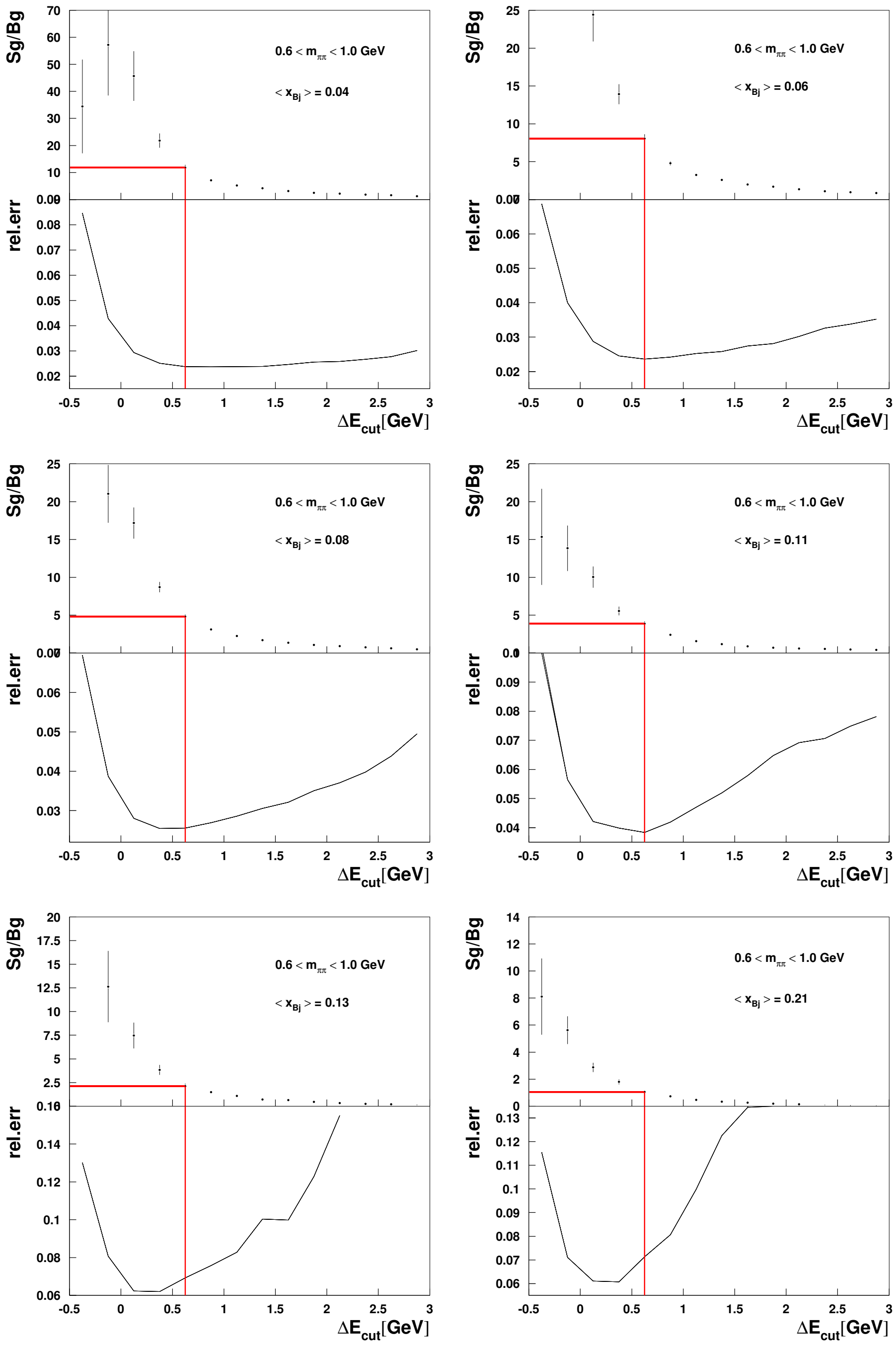

Figure 5.33: In each plot, the behavior of the ratio Sg/Bg (top panels) and its relative statistical error (bottom panels) versus ΔE in each of the six x_{Bj} bins inside the invariant mass region $0.6 < m_{\pi\pi} < 1.0$ GeV for hydrogen target, is shown. The vertical line shows the chosen ΔE_{cut} and the horizontal one shows the corresponding ratio Sg/Bg.

$0.6 < m_{\pi\pi} < 1.0$ **GeV**

Deuterium target: ratio Sg/Bg versus ΔE

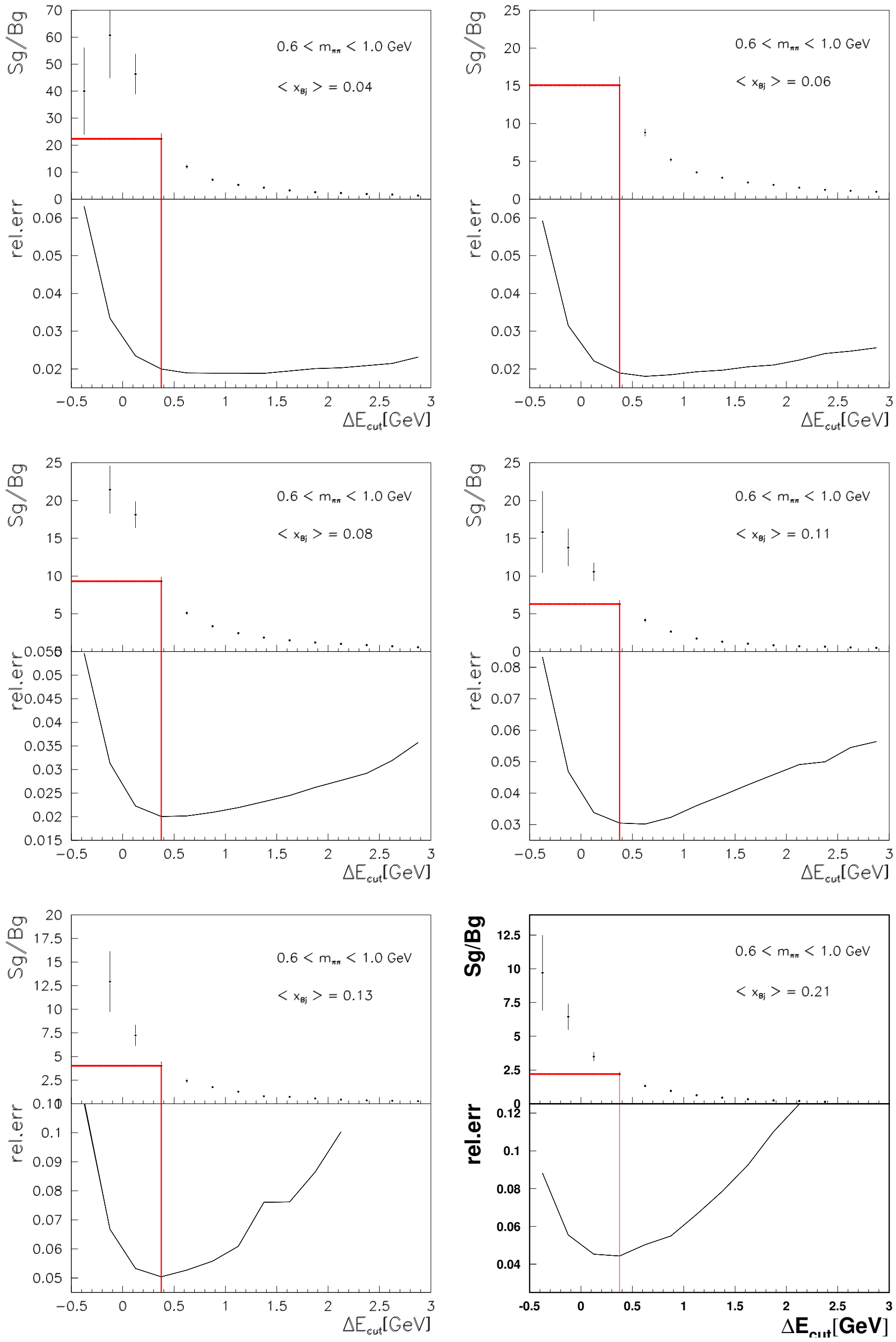

Figure 5.34: In each plot, the behavior of the ratio Sg/Bg (top panel) and its relative statistical error (bottom panel) versus ΔE in each of the six x_{Bj} bins inside the invariant mass region $0.6 < m_{\pi\pi} < 1.0$ GeV for deuterium target, is shown. The vertical line shows the chosen ΔE_{cut} and the horizontal one shows the corresponding ratio Sg/Bg.

target	Number of events for $0.6 < m_{\pi\pi} < 1.0$ GeV
H	$9.9 \cdot 10^3$ ($\Delta E < 0.625$ GeV)
D	$12.3 \cdot 10^3$ ($\Delta E < 0.375$ GeV)

Table 5.11: Total statistics of the data sample for hydrogen (deuterium) target in the exclusive chosen cut $\Delta E < 0.625$ GeV ($\Delta E < 0.375$ GeV) for the x_{Bj}-dependence of $\langle P_{1(3)}(cos\theta)\rangle$ in the invariant mass region $0.6 < m_{\pi\pi} < 1.0$ GeV.

Table 5.11 shows the total statistics of the data sample in the chosen exclusive cuts. Table 5.12 shows the ratio Sg/Bg corresponding to the selected ΔE_{cut} for each x_{Bj} bin in the invariant mass region $0.6 < m_{\pi\pi} < 1.0$ GeV with hydrogen and deuterium targets respectively. The values of Sg/Bg measured in different x_{Bj} bins decrease with increasing x_{Bj} showing that the contamination of *DIS* background increases sizably at large x_{Bj}.

For events in the chosen ΔE cuts the intensity densities $\langle P_{1(3)}(cos\theta)\rangle$ were evaluated for each target, Fig. 5.35. As in section 5.6.1, the intensity densities $\langle P_{1(3)}(cos\theta)\rangle$ of the *DIS* background were measured using data at $\Delta E > 2$ GeV, Fig. 5.36-5.37 left panels, and then subtracted weighting them by the ratio Sg/Bg corresponding to the selected exclusive cuts. In Fig. 5.36-5.37, right panels, the ΔE independence of $\langle P_{1(3)}(cos\theta)\rangle$ for the background was tested comparing the distributions in different ΔE regions.

$< x_{Bj} >$	Sg/Bg (H) $\Delta E < 0.625$ GeV $0.6 < m_{\pi\pi} < 1.0$ GeV	Sg/Bg (D) $\Delta E < 0.375$ GeV $0.6 < m_{\pi\pi} < 1.0$ GeV
0.04	11.81	22.31
0.06	8.05	15.08
0.08	4.82	9.30
0.11	3.86	6.29
0.13	2.12	4.02
0.21	1.05	2.20

Table 5.12: Ratio Sg/Bg corresponding to the chosen exclusive ΔE cuts for the different x_{Bj} bins in the invariant mass region $0.6 < m_{\pi\pi} < 1.0$ GeV for both hydrogen and deuterium targets.

Results confirm the assumption made.

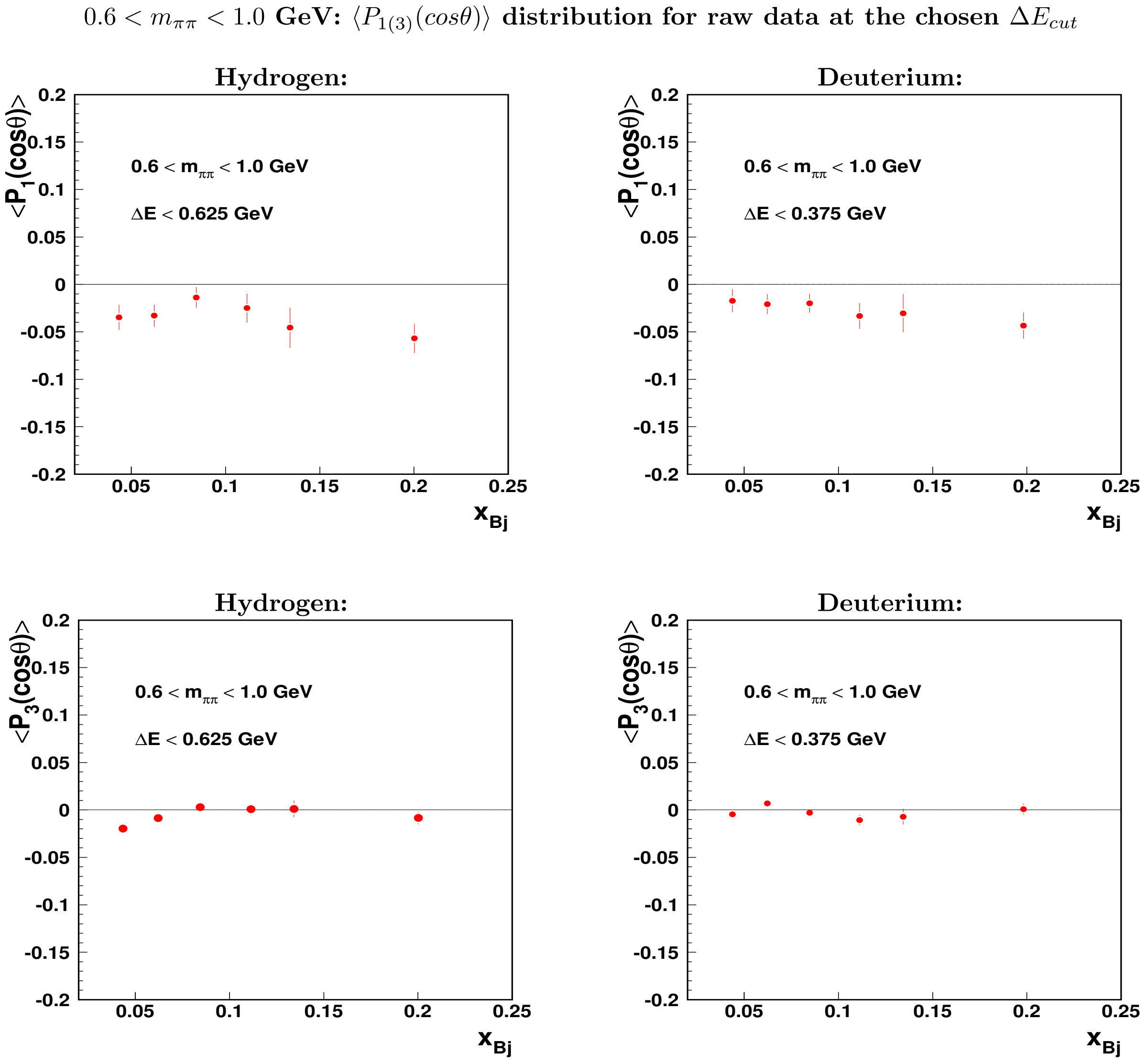

Figure 5.35: x_{Bj} dependence of $\langle P_1(cos\theta)\rangle$ (**upper panels**) and $\langle P_3(cos\theta)\rangle$ (**bottom panels**) distribution for raw data inside the invariant mass region $0.6 < m_{\pi\pi} < 1.0$ GeV at the chosen exclusive cut $\Delta E < 0.625$ GeV ($\Delta E < 0.375$ GeV) for hydrogen (deuterium) target. The DIS background contribution is not subtracted yet. The distributions has an average $< m_{\pi\pi} >= 0.78$ GeV.

$0.6 < m_{\pi\pi} < 1.0$ GeV: $\langle P_1(cos\theta)\rangle$ distributions for the DIS background

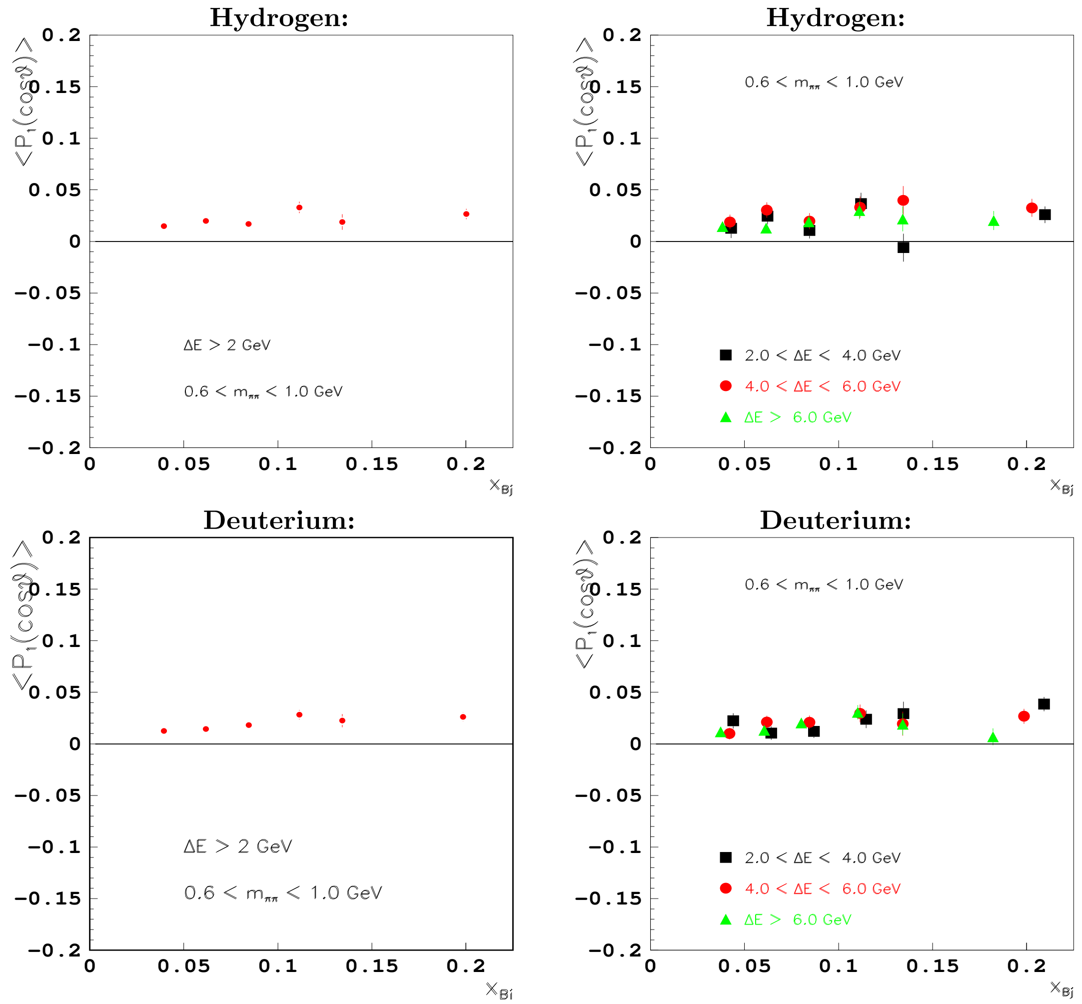

Figure 5.36: x_{Bj} dependence of the $\langle P_1(cos\theta)\rangle$ distribution of DIS background inside the invariant mass region $0.6 < m_{\pi\pi} < 1.0$ GeV for hydrogen and deuterium targets, **left panels**. The ΔE independence of the distributions has been tested measuring them in different ΔE bins, **right panels**.

$0.6 < m_{\pi\pi} < 1.0$ **GeV:** $\langle P_3(cos\theta)\rangle$ **distributions for the DIS background**

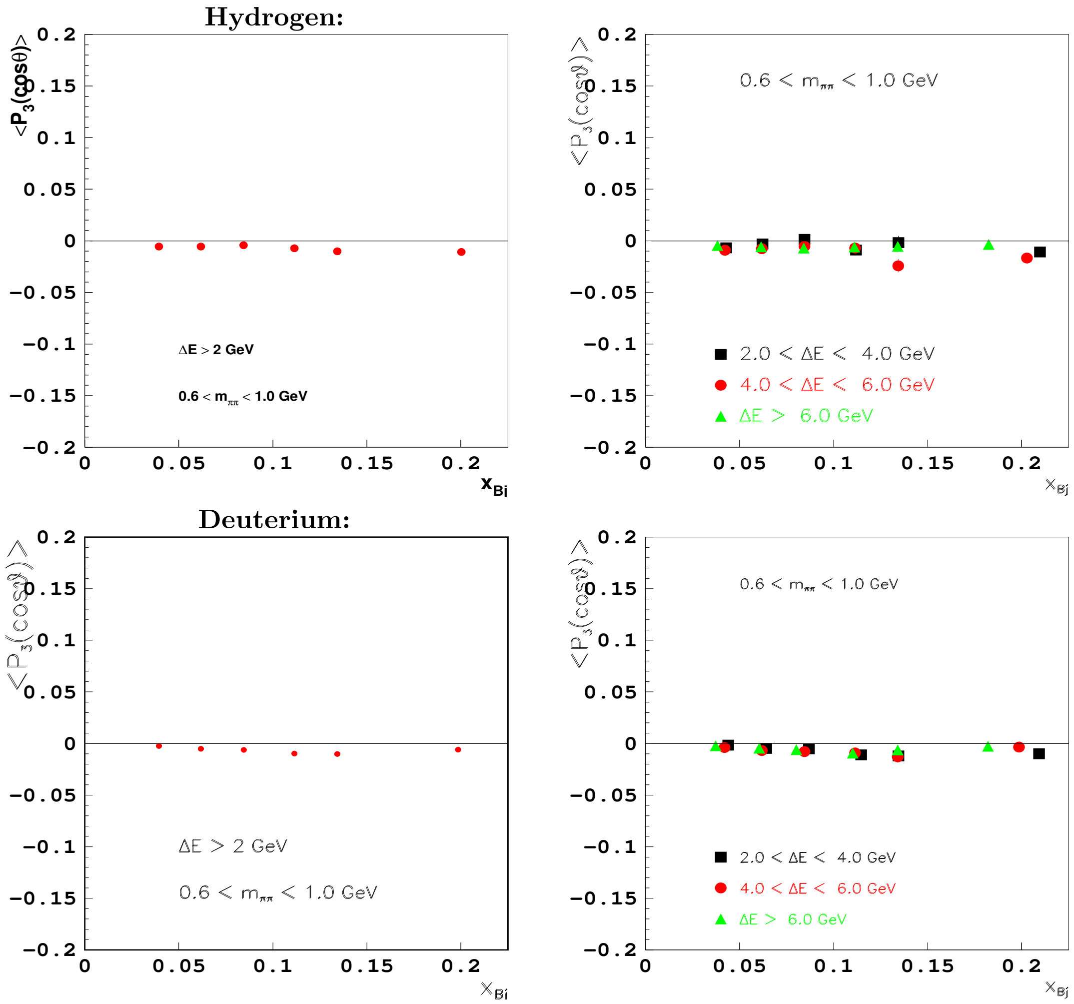

Figure 5.37: x_{Bj} dependence of the $\langle P_3(cos\theta)\rangle$ distribution of DIS background inside the invariant mass region $0.6 < m_{\pi\pi} < 1.0$ GeV for hydrogen and deuterium targets, **left panels**. The ΔE independence of the distributions has been tested measuring them in different ΔE bins, **right panels**.

Fig. 5.38 shows the distribution $\langle P_1(cos\theta)\rangle$ after background subtraction for hydrogen and deuterium target. The observed non zero *intensity density* $\langle P_1(cos\theta)\rangle$ may be interpreted as originating from the interference of the ρ^0 lower tail with the S-wave non-resonant $\pi^+\pi^-$ production. The asymmetry increases in size with x_{Bj}, and this behavior may be understood as to arise from the increased dominance of $q\bar{q}$ exchange at larger values of x_{Bj}, which leads to a sizable admixture of isoscalar and isovector pion pairs.

$0.6 < m_{\pi\pi} < 1.0$ **GeV:**
$\langle P_1(cos\theta)\rangle$ **distributions of** $\pi^+\pi^-$ **exclusive channel after DIS background subtraction:**

Hydrogen:

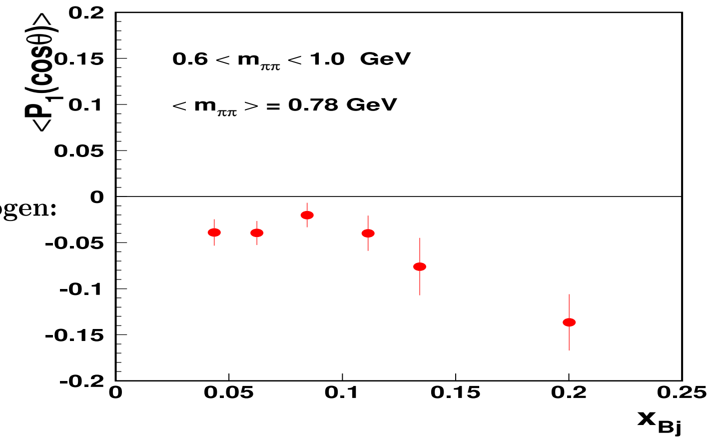

Deuterium:

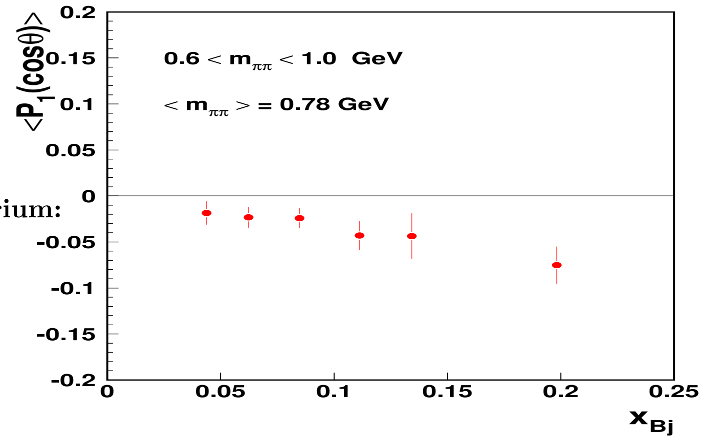

Figure 5.38: x_{Bj} dependence of the $\langle P_1(cos\theta)\rangle$ distribution inside the invariant mass region $0.6 < m_{\pi\pi} < 1.0$ GeV, after DIS background subtraction, for the exclusive channel $e^+p \to e^+p\ \pi^+\pi^-$ (**upper panel**) and $e^+d \to e^+d\ \pi^+\pi^-$ (**bottom panel**).

The distribution $\langle P_3(cos\theta)\rangle$ in the region $0.6 < m_{\pi\pi} < 1.0$ GeV is shown in Fig. 5.39 for both targets. Results are consistent with zero and confirm the expected absence of the $\pi^+\pi^-$ production in D-wave at $m_{\pi\pi} < 1$ GeV in the whole x_{Bj}-spectrum covered by the *HERMES* experiment.

$0.6 < m_{\pi\pi} < 1.0$ **GeV:**
$\langle P_3(cos\theta)\rangle$ **distributions of** $\pi^+\pi^-$ **exclusive channel after DIS background subtraction:**

Hydrogen:

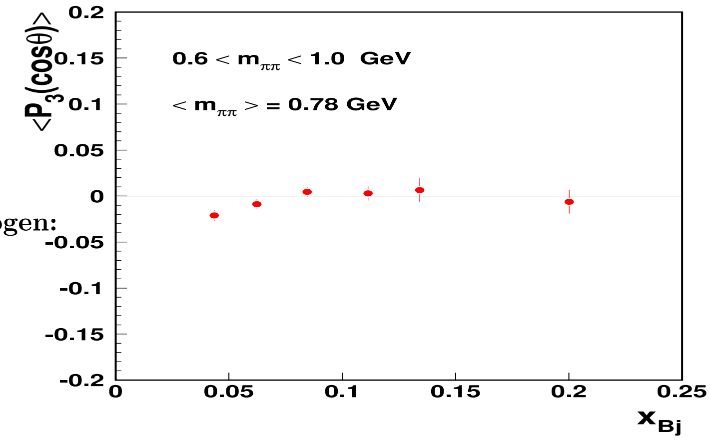

Deuterium:

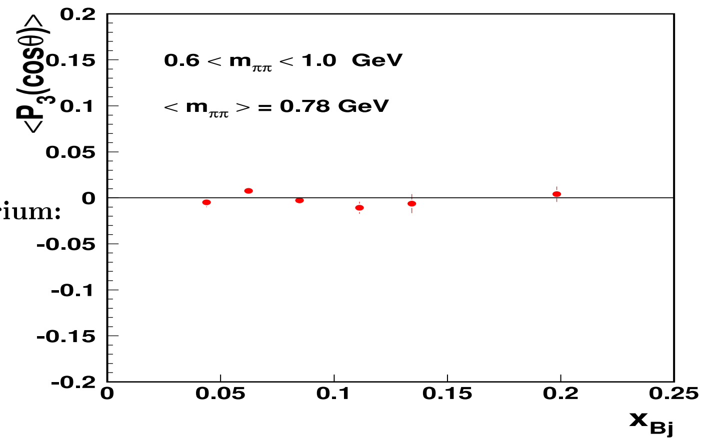

Figure 5.39: x_{Bj}-dependence of the $\langle P_3(cos\theta)\rangle$ distribution inside the invariant mass region $0.6 < m_{\pi\pi} < 1.0$ GeV, after DIS background subtraction, for the exclusive channel $e^+p \rightarrow e^+p\ \pi^+\pi^-$ (**upper panel**) and $e^+d \rightarrow e^+d\ \pi^+\pi^-$ (**bottom panel**).

target	Number of events for $0.3 < m_{\pi\pi} < 0.6$ GeV
H	$2.1 \cdot 10^3$ ($\Delta E < 0.625$ GeV)
D	$3.5 \cdot 10^3$ ($\Delta E < 0.625$ GeV)

Table 5.13: Total statistics of the data sample for hydrogen and deuterium targets within the chosen exclusive cut $\Delta E < 0.625$ GeV for the x_{Bj} dependence of $\langle P_{1(3)}(cos\theta)\rangle$ in the invariant mass region $0.3 < m_{\pi\pi} < 0.6$ GeV.

In the $0.3 < m_{\pi\pi} < 0.6$ GeV region, the ratio of the exclusive signal over the background was maximized, and its relative statistical error was minimized choosing the exclusive cuts $\Delta E < 0.625$ for both hydrogen and deuterium targets. Fig. 5.40-5.41 show that the Monte Carlo well reproduces the background shape at large ΔE, while at small ΔE there is an eccess of data due to the exclusive process $e^+p(d) \longrightarrow e^+p(d)\pi^+\pi^-$, not simulated in the Monte Carlo. This eccess of data is not so huge as in $0.6 < m_{\pi\pi} < 1.0$ GeV, due to the fact that there is no strong resonant decay in the considered $m_{\pi\pi}$ region. After the background normalization, the exclusive sample was extracted (Fig. 5.42-5.43) and the ratio *Sg/Bg* was measured (Fig. 5.44-5.45). Table 5.13 shows the total statistics of the data sample in the chosen exclusive cuts. Table 5.14 reports the ratio Sg/Bg corresponding to the selected ΔE_{cut} for each x_{Bj} bin in the region $0.3 < m_{\pi\pi} < 0.6$ GeV for hydrogen and deuterium targets, respectively.

$< x_{Bj} >$	Sg/Bg (H) $\Delta E < 0.625$ GeV $0.3 < m_{\pi\pi} < 0.6$ GeV	Sg/Bg (D) $\Delta E < 0.625$ GeV $0.3 < m_{\pi\pi} < 0.6$ GeV
0.04	3.12	3.34
0.06	3.65	3.70
0.08	1.74	2.25
0.11	1.62	1.87
0.13	0.77	1.02
0.21	0.50	0.70

Table 5.14: Ratio Sg/Bg chosen for the different x_{Bj} bins in the invariant mass region $0.3 < m_{\pi\pi} < 0.6$ GeV for both hydrogen and deuterium targets.

$0.3 < m_{\pi\pi} < 0.6$ **GeV**
Hydrogen target: MC **normalization to experimental data.**

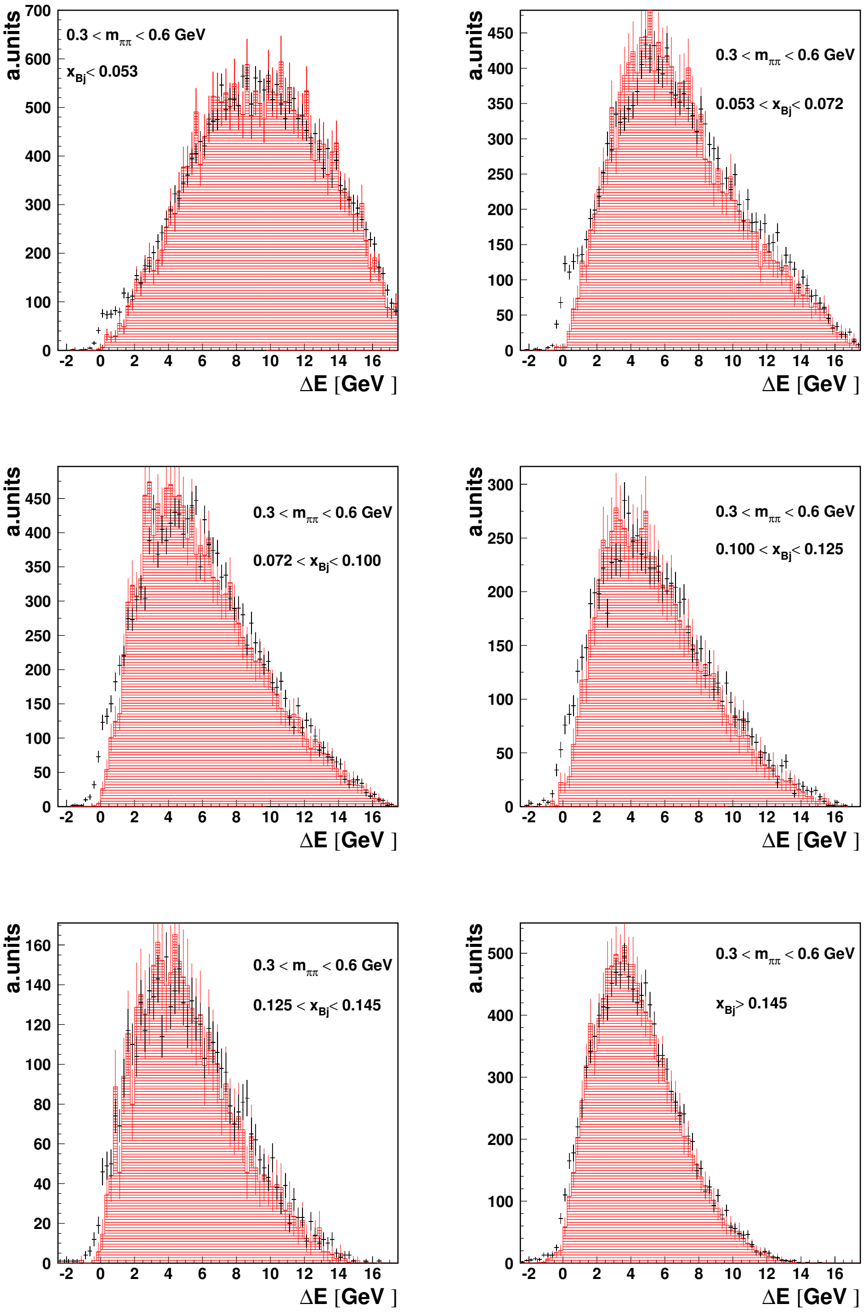

Figure 5.40: ΔE distribution in the six x_{Bj} bins inside the invariant mass region $0.3 < m_{\pi\pi} < 0.6$ GeV for hydrogen target. MC data (shadowed) are normalized to the experimental one (crosses) for $\Delta E > 2$ GeV.

$0.3 < m_{\pi\pi} < 0.6$ **GeV**
Deuterium target: *MC* **normalization to experimental data.**

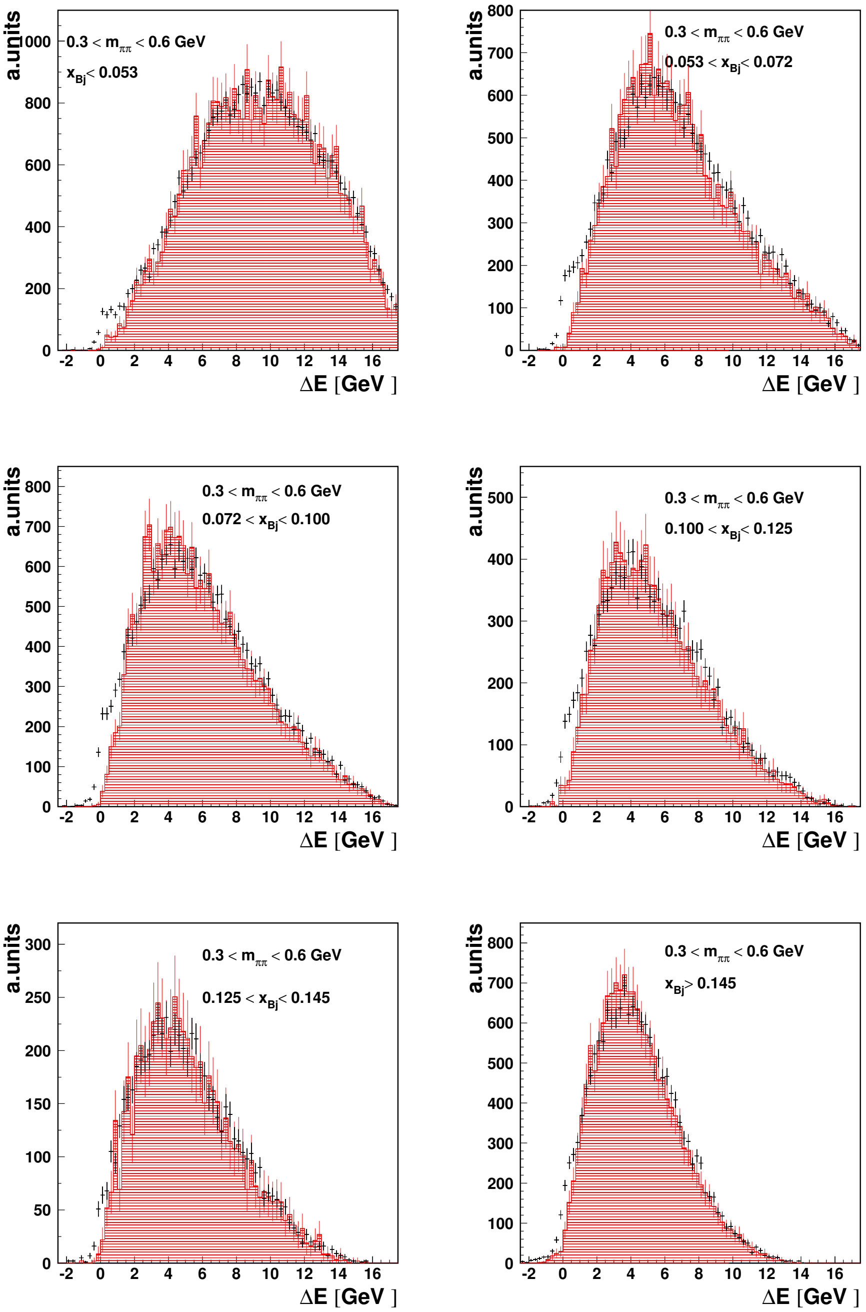

Figure 5.41: ΔE distribution in the six x_{Bj} bins inside the invariant mass region $0.3 < m_{\pi\pi} < 0.6$ GeV for deuterium target. *MC* data (shadowed) are normalized to the experimental one (crosses) for $\Delta E > 2$ GeV.

$0.3 < m_{\pi\pi} < 0.6$ **GeV**
Hydrogen target: extraction of the exclusive signal (Sg)

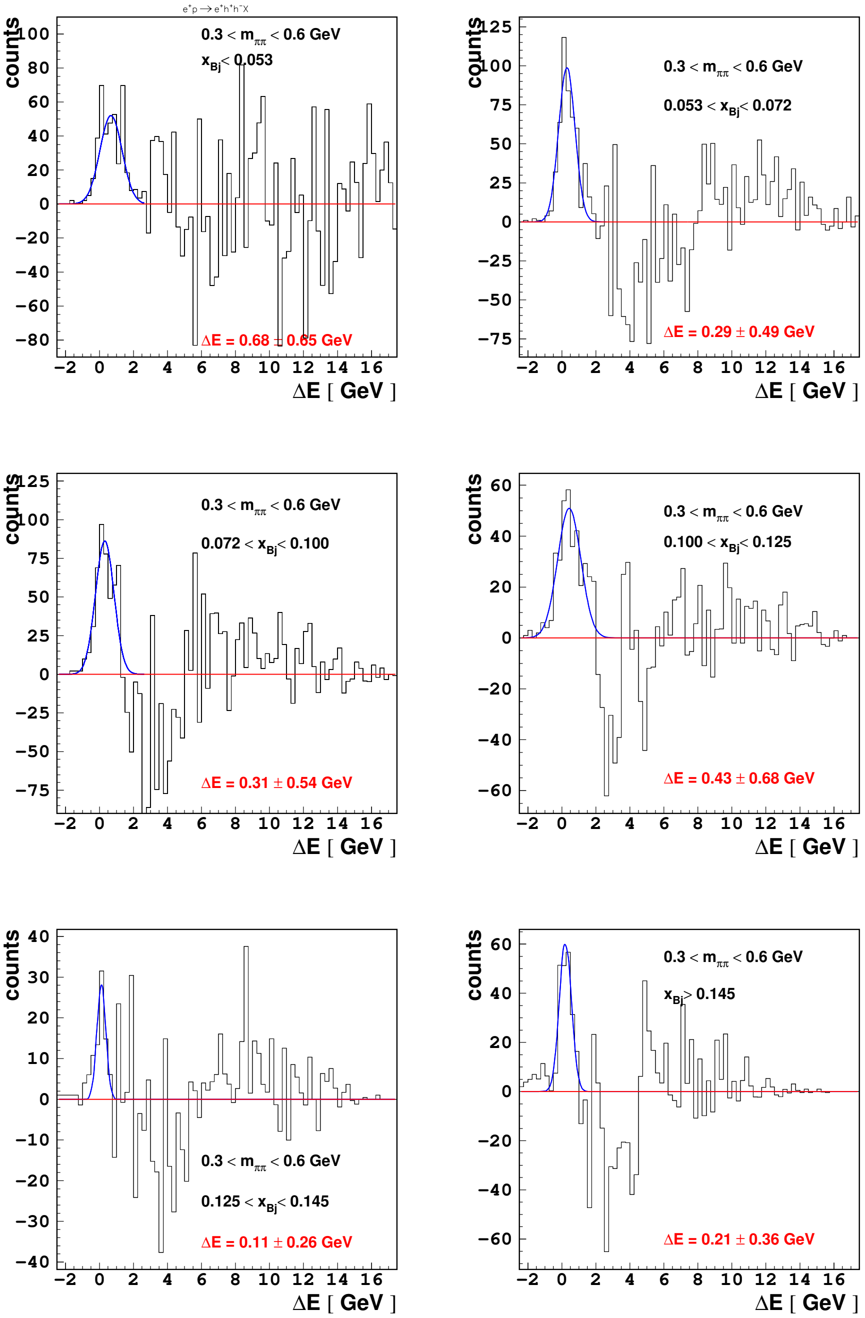

Figure 5.42: Yield of the $\pi^+\pi^-$ exclusive channel versus ΔE in the six x_{Bj} bins inside the invariant mass region $0.3 < m_{\pi\pi} < 0.6$ GeV for hydrogen target. The exclusive peak is fitted with a gaussian whose expectation value and width values are shown in the bottom left side of each plot.

$0.3 < m_{\pi\pi} < 0.6$ **GeV**
Deuterium target: extraction of the exclusive signal (Sg)

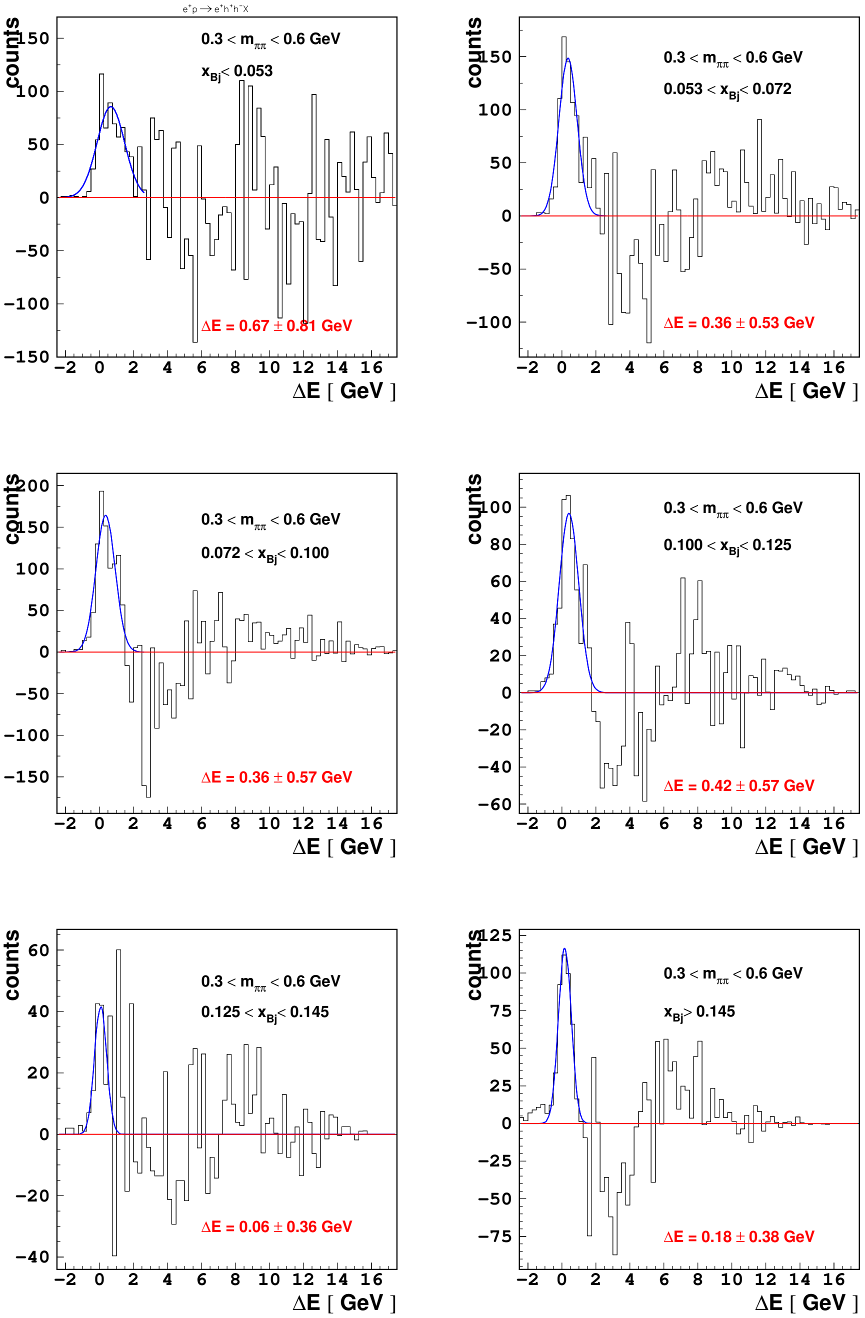

Figure 5.43: Yield of the $\pi^+\pi^-$ exclusive channel versus ΔE in the six x_{Bj} bins inside the invariant mass region $0.3 < m_{\pi\pi} < 0.6$ GeV with deuterium target. The exclusive peak is fitted with a gaussian whose expectation value and width values are shown in the bottom left side of each plot.

$0.3 < m_{\pi\pi} < 0.6$ GeV
Hydrogen target: ratio Sg/Bg versus ΔE

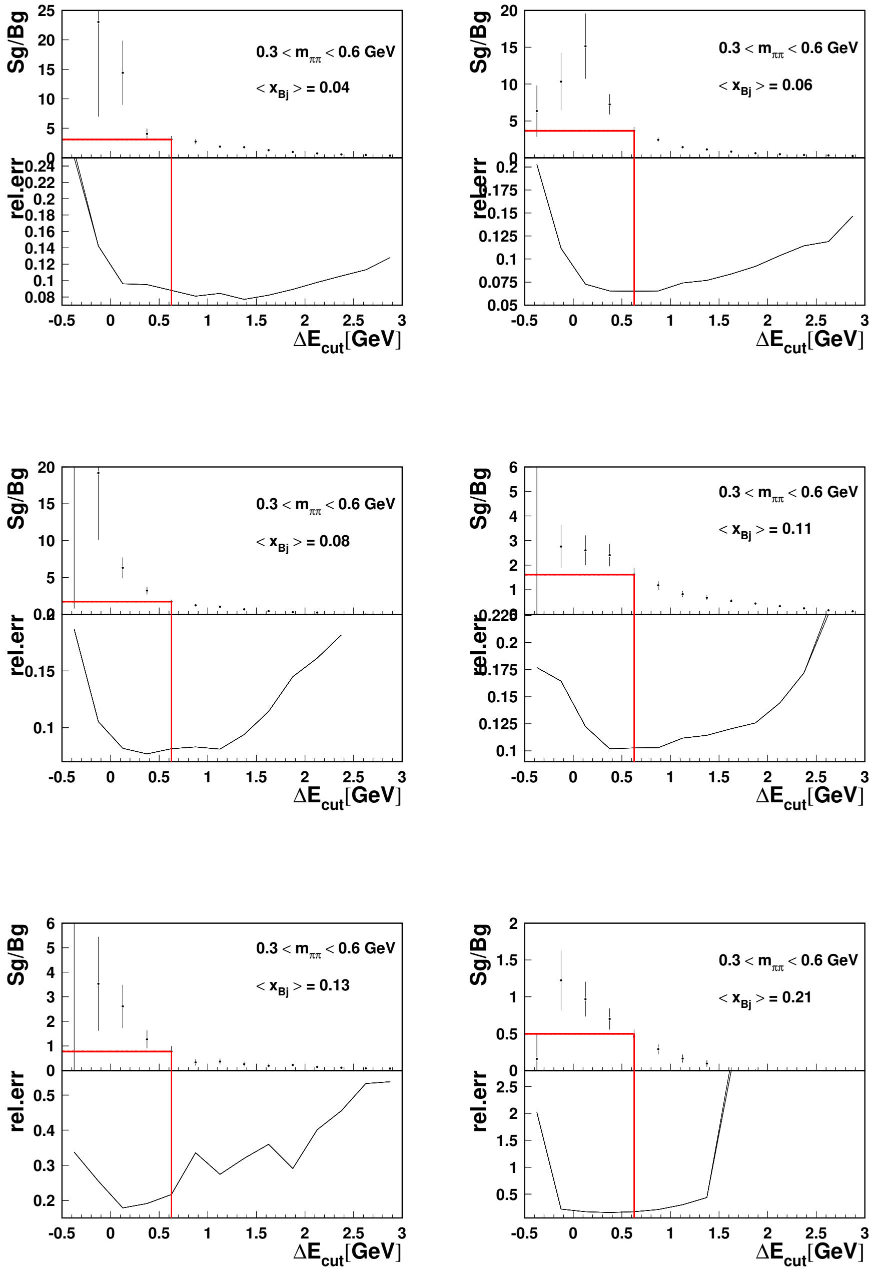

Figure 5.44: In each plot, the behavior of the ratio Sg/Bg (top panel) and its relative statistical error (bottom panel) versus ΔE in each of the six x_{Bj} bins inside the invariant mass region $0.3 < m_{\pi\pi} < 0.6$ GeV for hydrogen target is shown. The vertical line shows the chosen ΔE_{cut} and the horizontal one shows the corresponding ratio Sg/Bg.

$0.3 < m_{\pi\pi} < 0.6$ **GeV**
Deuterium target: ratio Sg/Bg versus ΔE

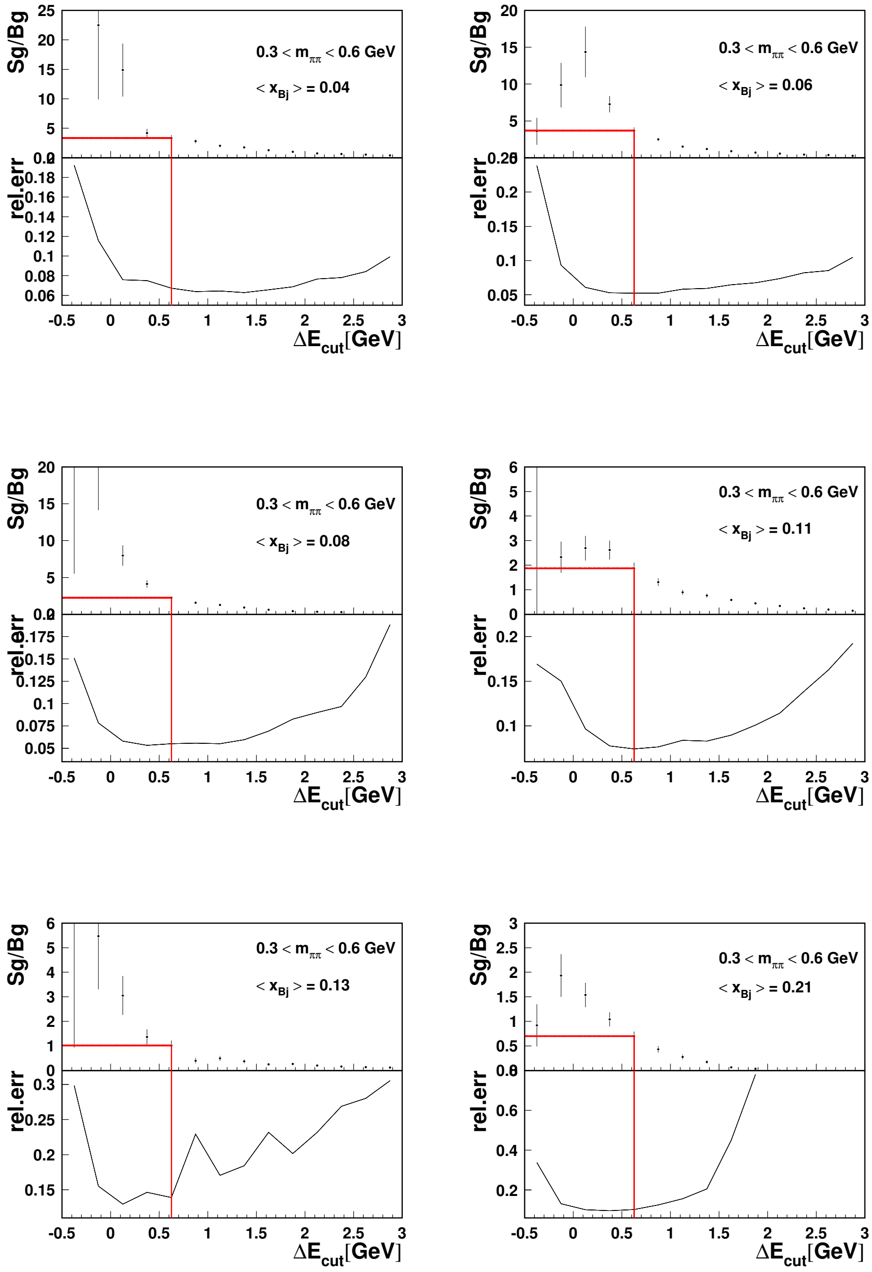

Figure 5.45: In each plot, the behavior of the ratio Sg/Bg (top panel) and its relative statistical error (bottom panel) versus ΔE in each of the six x_{Bj} bins inside the invariant mass region $0.3 < m_{\pi\pi} < 0.6$ GeV for deuterium target is shown. The vertical line shows the chosen ΔE_{cut} and the horizontal one shows the corresponding ratio Sg/Bg.

For events in the chosen ΔE cuts the intensity densities $\langle P_{1(3)}(cos\theta)\rangle$ were evaluated for each target, Fig. 5.46. The background contribution was measured using data at $\Delta E > 2$ GeV, Fig. 5.47- 5.48, left panels, and then subtracted following the procedure performed in the invariant mass region $0.6 < m_{\pi\pi} < 1.0$ GeV. In Fig. 5.47- 5.48, right panels, the ΔE independence of $\langle P_{1(3)}(cos\theta)\rangle$ for the background was tested and confirmed comparing the distributions in different ΔE regions.

$0.3 < m_{\pi\pi} < 0.6$ **GeV:** $\langle P_{1(3)}(cos\theta)\rangle$ **distribution for raw data at the chosen** ΔE_{cut}

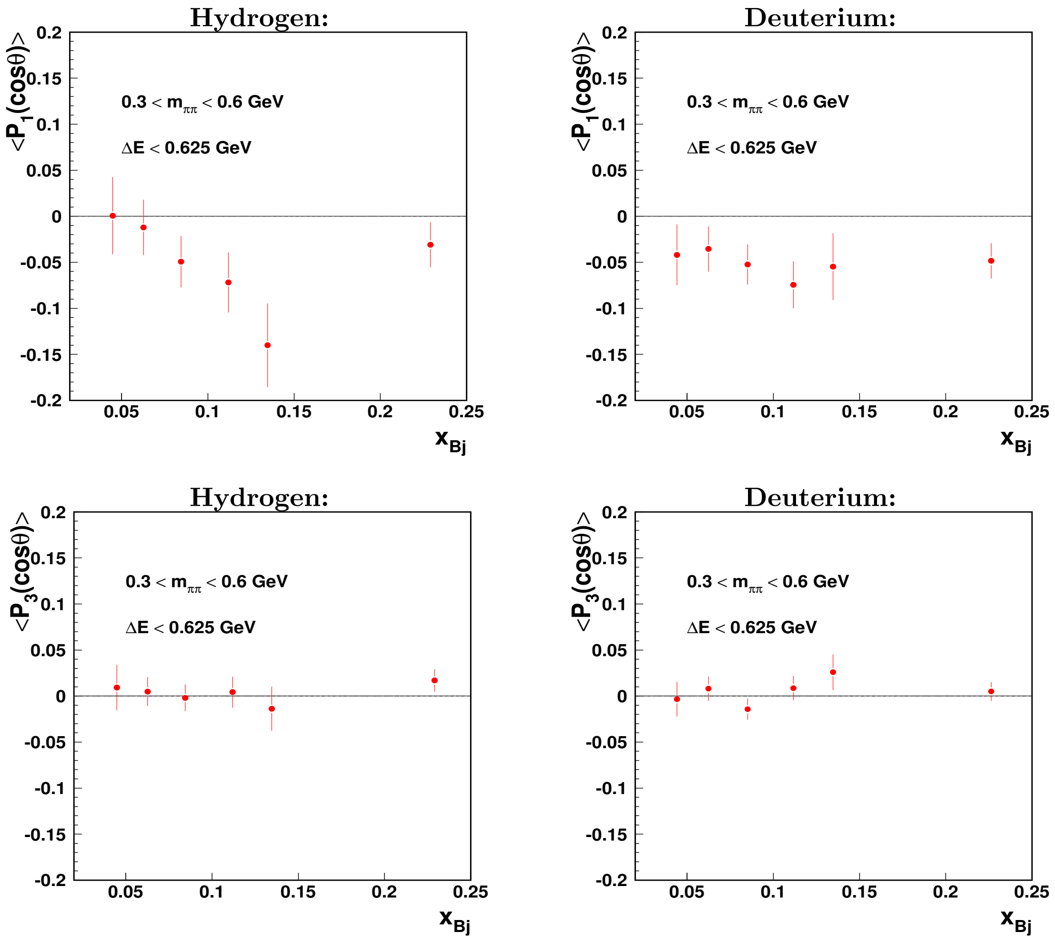

Figure 5.46: x_{Bj} dependence of $\langle P_1(cos\theta)\rangle$ (**upper panels**) and $\langle P_3(cos\theta)\rangle$ (**bottom panels**) distribution for raw data inside the invariant mass region $0.3 < m_{\pi\pi} < 0.6$ GeV at the chosen exclusive cut $\Delta E < 0.625$ GeV for hydrogen and deuterium targets respectively. The DIS background contribution is not subtracted yet. The distributions have $< m_{\pi\pi} >= 0.48$ GeV.

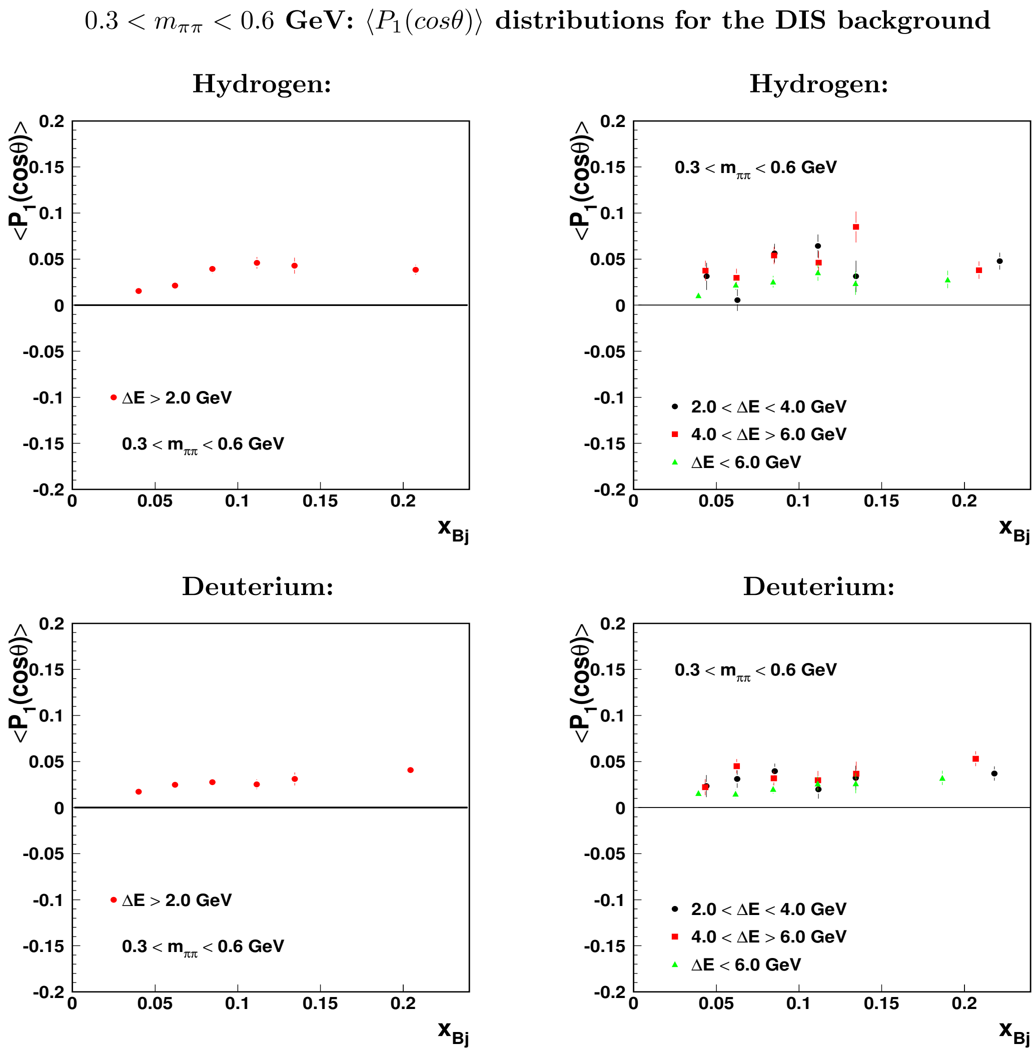

Figure 5.47: x_{Bj} dependence of the $\langle P_3(cos\theta)\rangle$ distribution of DIS background inside the invariant mass region $0.3 < m_{\pi\pi} < 0.6$ GeV for hydrogen and deuterium targets, **left panels**. The ΔE independence of the distributions has been tested measuring them in different ΔE bins, **right panels**.

$0.3 < m_{\pi\pi} < 0.6$ **GeV:** $\langle P_3(cos\theta)\rangle$ **distributions for the DIS background**

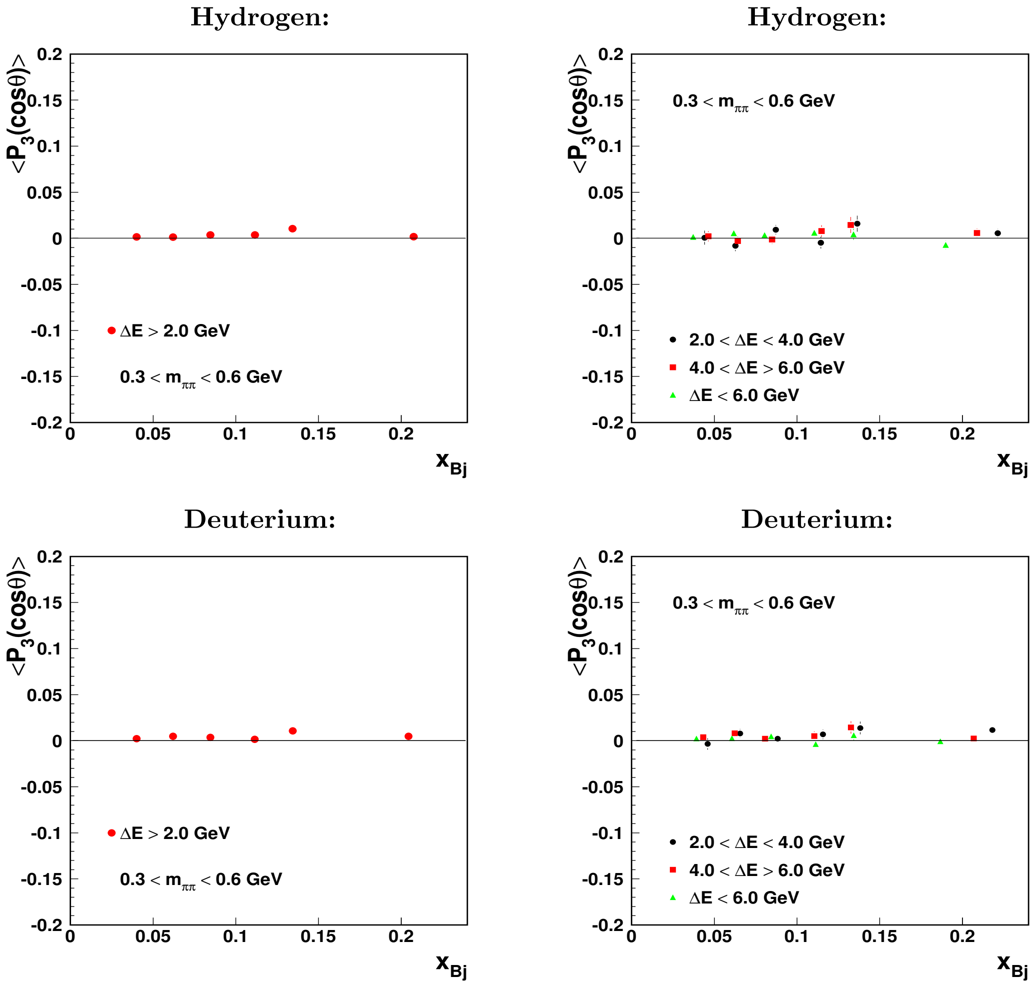

Figure 5.48: x_{Bj} dependence of the $\langle P_3(cos\theta)\rangle$ distribution of DIS background inside the invariant mass region $0.3 < m_{\pi\pi} < 0.6$ GeV for hydrogen and deuterium targets, **left panels**. The ΔE independence of the distributions has been tested measuring them in different ΔE bins, **right panels**.

Fig. 5.49, 5.50 show the distributions $\langle P_{1(3)}(cos\theta)\rangle$ after background subtraction for hydrogen and deuterium target. The observed non zero *intensity density* $\langle P_1(cos\theta)\rangle$ may be interpreted as originating from the interference of the ρ^0 lower tail with the S-wave non-resonant $\pi^+\pi^-$ production. The asymmetry increases in size with x_{Bj}, and this behavior may be understood as to arise from the increased dominance of $q\bar{q}$ exchange at larger values of x_{Bj}, which leads to a sizable admixture of isoscalar and isovector pion pairs.

$0.3 < m_{\pi\pi} < 0.6$ **GeV:**
$\langle P_1(cos\theta)\rangle$ **distributions of** $\pi^+\pi^-$ **exclusive channel after DIS background subtraction**

Hydrogen:

Deuterium:

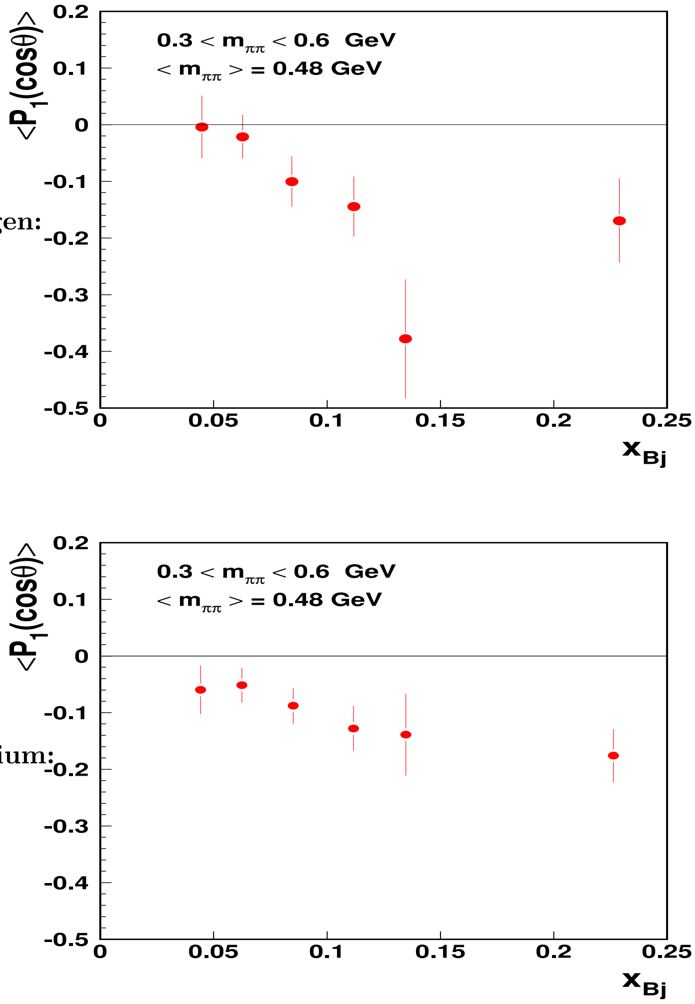

Figure 5.49: x_{Bj} dependence of the $\langle P_1(cos\theta)\rangle$ distribution inside the invariant mass region $0.3 < m_{\pi\pi} < 0.6$ GeV, after DIS background subtraction, for the exclusive channel $e^+p \rightarrow e^+p\ \pi^+\pi^-$ (**upper panel**) and $e^+d \rightarrow e^+d\ \pi^+\pi^-$ (**bottom panel**).

The distribution $\langle P_3(cos\theta)\rangle$ in the region $0.3 < m_{\pi\pi} < 0.6$ GeV is shown in Fig. 5.49 for both targets. Results are consistent with zero and confirm the expected absence of the $\pi^+\pi^-$ production in D-wave at $m_{\pi\pi} < 1$ GeV in the whole x_{Bj} spectrum covered by the *HERMES* experiment.

$0.3 < m_{\pi\pi} < 0.6$ **GeV:**
$\langle P_3(cos\theta)\rangle$ **distributions of** $\pi^+\pi^-$ **exclusive channel after DIS background subtraction**

Hydrogen:

Deuterium:

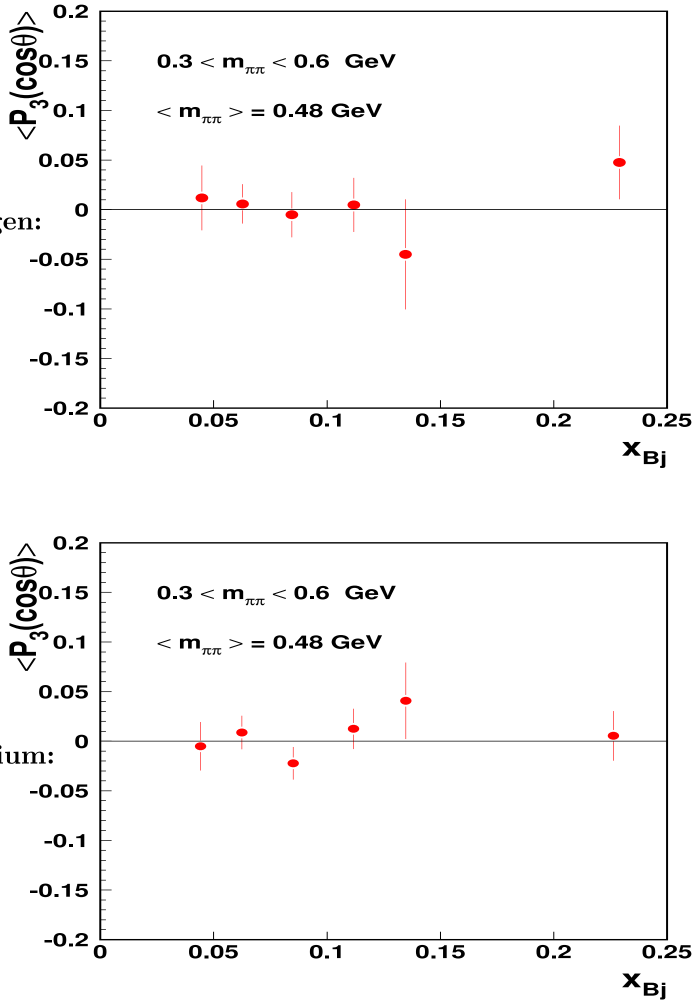

Figure 5.50: x_{Bj}-dependence of the $\langle P_3(cos\theta)\rangle$ distribution inside the invariant mass region $0.3 < m_{\pi\pi} < 0.6$ GeV, after DIS background subtraction, for the exclusive channel $e^+p \rightarrow e^+p\ \pi^+\pi^-$ (**upper panel**) and $e^+d \rightarrow e^+d\ \pi^+\pi^-$ (**bottom panel**).

5.7.2 Acceptance Effects and Radiative Corrections

Effects due to the forward geometrical acceptance and to the instrumental smearing have been evaluated following the same procedure applied in the analysis of $m_{\pi\pi}$ dependence of these distributions, described in section 5.6.2. Table 5.15 shows the total number of both the events generated in the solid angle 4π and the events reconstructed in the *HERMES* acceptance by the Monte Carlo *DIPSI* for hydrogen target, in the studied invariant mass regions $0.6 < m_{\pi\pi} < 1.0$ GeV and $0.3 < m_{\pi\pi} < 0.6$ GeV respectively. Fig. 5.51 shows the x_{Bj}-dependence of both the geometrical acceptance effects

target	$m_{\pi\pi}$ [GeV]	Generated events in the solid angle 4π	Reconstructed events in the *HERMES* acceptance
H	$0.6 - 1.0$	$100 \cdot 10^3$	$60 \cdot 10^3$
H	$0.3 - 0.6$	$13 \cdot 10^3$	$7.4 \cdot 10^3$

Table 5.15: The total statistics of the generated events and of the reconstructed events in the *HERMES* acceptance produced by the montecarlo *DIPSI* generator for hydrogen target in the invariant mass regions $0.6 < m_{\pi\pi} < 1.0$ GeV and $0.3 < m_{\pi\pi} < 0.6$ GeV respectively.

and smearing, for $\langle P_1(cos\theta)\rangle$ (upper panel) and $\langle P_3(cos\theta)\rangle$ (bottom panel) in the invariant mass region $0.6 < m_{\pi\pi} < 1.0$ GeV for the $\pi^+\pi^-$ exclusive electroproduction off protons. The same distributions in the invariant mass region $0.3 < m_{\pi\pi} < 0.6$ GeV are shown in Fig. 5.52. From the above results, the effects due to acceptance are clearly negligible.

The radiative corrections for the $\langle P_{1(3)}(cos\theta)\rangle$ distributions have been considered negligible following the same considerations in section 5.6.2.

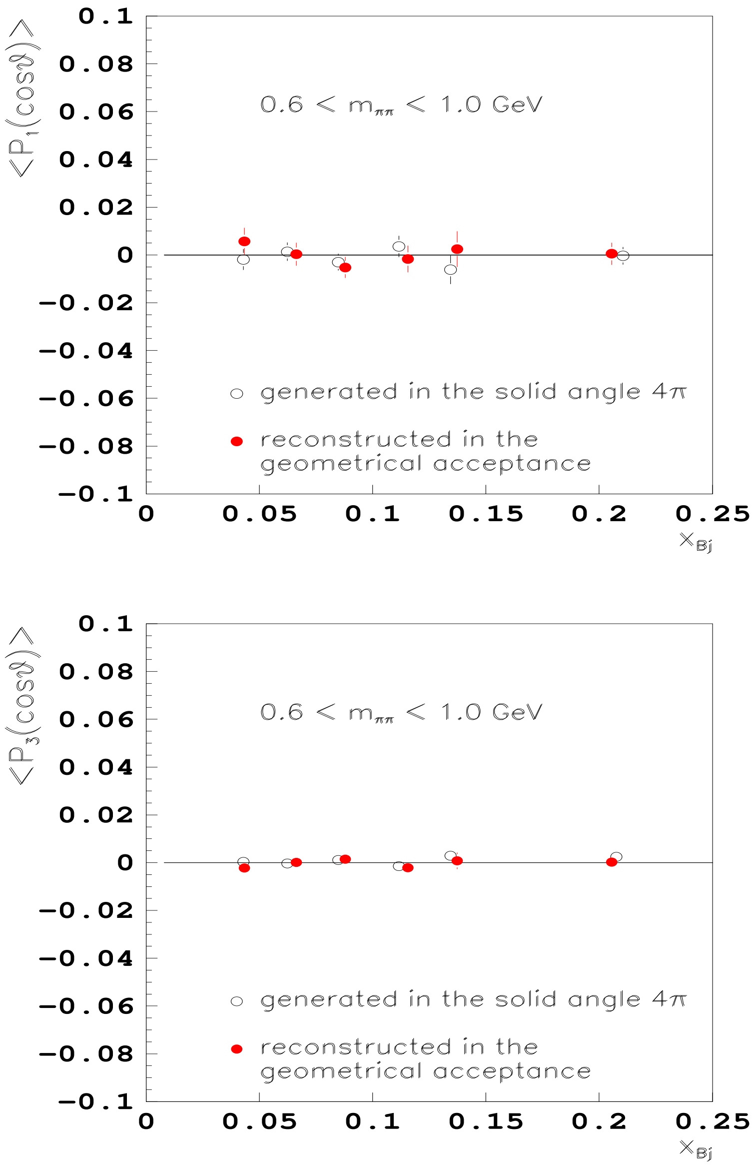

Figure 5.51: Instrumental smearing and geometrical acceptance effects evaluated for the x_{Bj} dependence of $\langle P_1(cos\theta)\rangle$, **upper panel**, and of $\langle P_3(cos\theta)\rangle$ **bottom panel**, for the $\pi^+\pi^-$ exclusive electroproduction off protons in the invariant mass region $0.6 < m_{\pi\pi} < 1.0$ GeV using the Monte Carlo *DIPSI*.

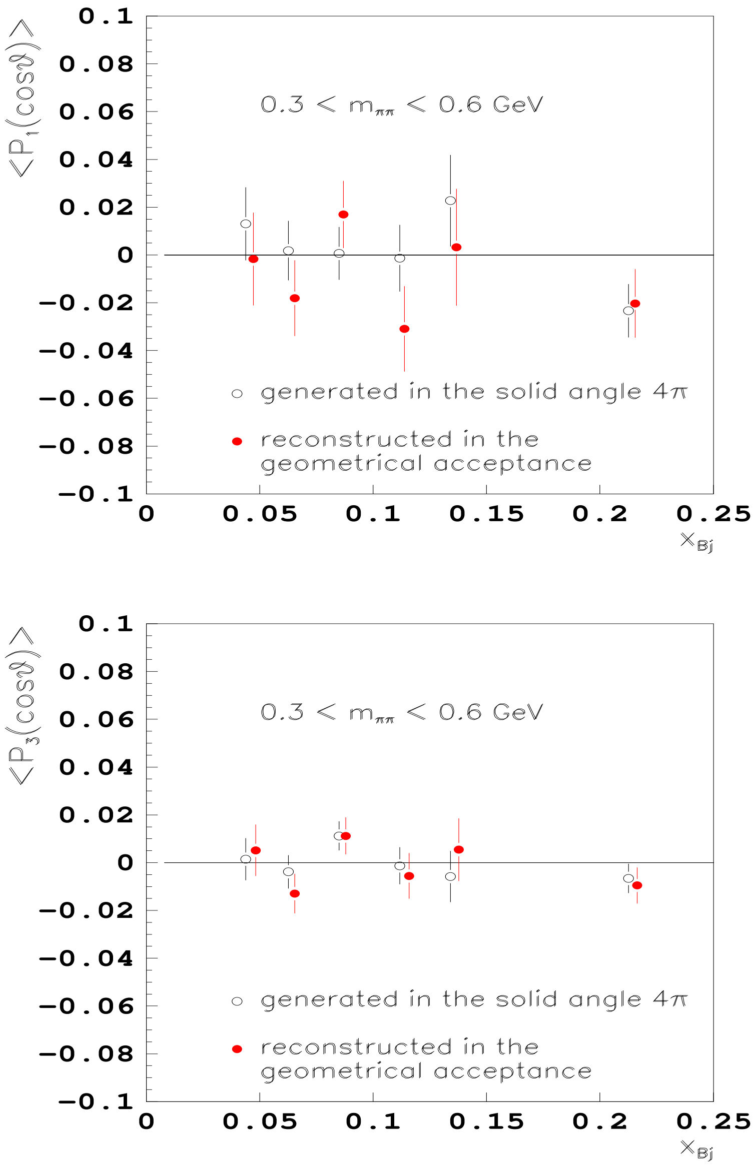

Figure 5.52: Instrumental smearing and geometrical acceptance effects evaluated for the x_{Bj} dependence of $\langle P_1(cos\theta)\rangle$, **upper panel**, and of $\langle P_3(cos\theta)\rangle$ **bottom panel**, for the $\pi^+\pi^-$ exclusive electroproduction off protons in the invariant mass region $0.3 < m_{\pi\pi} < 0.6$ GeV using the Monte Carlo *DIPSI*.

5.7.3 Systematic Uncertainties

As performed for the analysis of the $m_{\pi\pi}$ dependence of $\langle P_{1(3)}(cos\theta)\rangle$, the significativity of the results has been evaluated estimating the systematic uncertainties. The stability of the observables $\langle P_{1(3)}(cos\theta)\rangle$ applying different ΔE cut selections in the procedure performed in the analysis.

Fig. 5.53-5.54 show the x_{Bj} dependence of the $\langle P_{1(3)}(cos\theta)\rangle$ measured using different exclusive ΔE cuts for hydrogen and deuterium targets respectively. Table 5.16 reports the maximum factor change of the ratio Sg/Bg corresponding to these ΔE cuts in each x_{Bj} bin of the two $m_{\pi\pi}$ regions. Even though the ratio Sg/Bg changes up to a factor 7, the systematic uncertainties are less few percent in most of the bins, meaning that the *DIS* background subtraction was good and reliable. The maximum difference, bin by bin, of the measured distributions is considered the uncertainty given by the particular ΔE cut chosen in the analysis. Numerical results are reported in Tab. 5.17.

	Factor change of Sg/Bg	
	Hydrogen	**Deuterium**
x_{Bj}	$0.6 < m_{\pi\pi} < 1.0$ GeV:	$0.6 < m_{\pi\pi} < 1.0$ GeV:
≤ 0.053	6.43	6.44
$0.053 - 0.072$	5.10	5.09
$0.072 - 0.100$	5.47	5.39
$0.100 - 0.125$	4.18	4.00
$0.125 - 0.145$	5.01	4.14
≥ 0.145	3.93	3.68
x_{Bj}	$0.3 < m_{\pi\pi} < 0.6$ GeV:	$0.3 < m_{\pi\pi} < 0.6$ GeV:
≤ 0.053	5.28	5.31
$0.053 - 0.072$	6.20	5.79
$0.072 - 0.100$	5.12	5.05
$0.100 - 0.125$	2.20	2.05
$0.125 - 0.145$	7.90	7.63
≥ 0.145	3.34	3.58

Table 5.16: Maximum factor change of the ratio Sg/Bg due to the choice of different exclusive ΔE cuts for hydrogen and deuterium targets respectively in the invariant mass regions $0.6 < m_{\pi\pi} < 1.0$ GeV and $0.3 < m_{\pi\pi} < 0.6$ GeV.

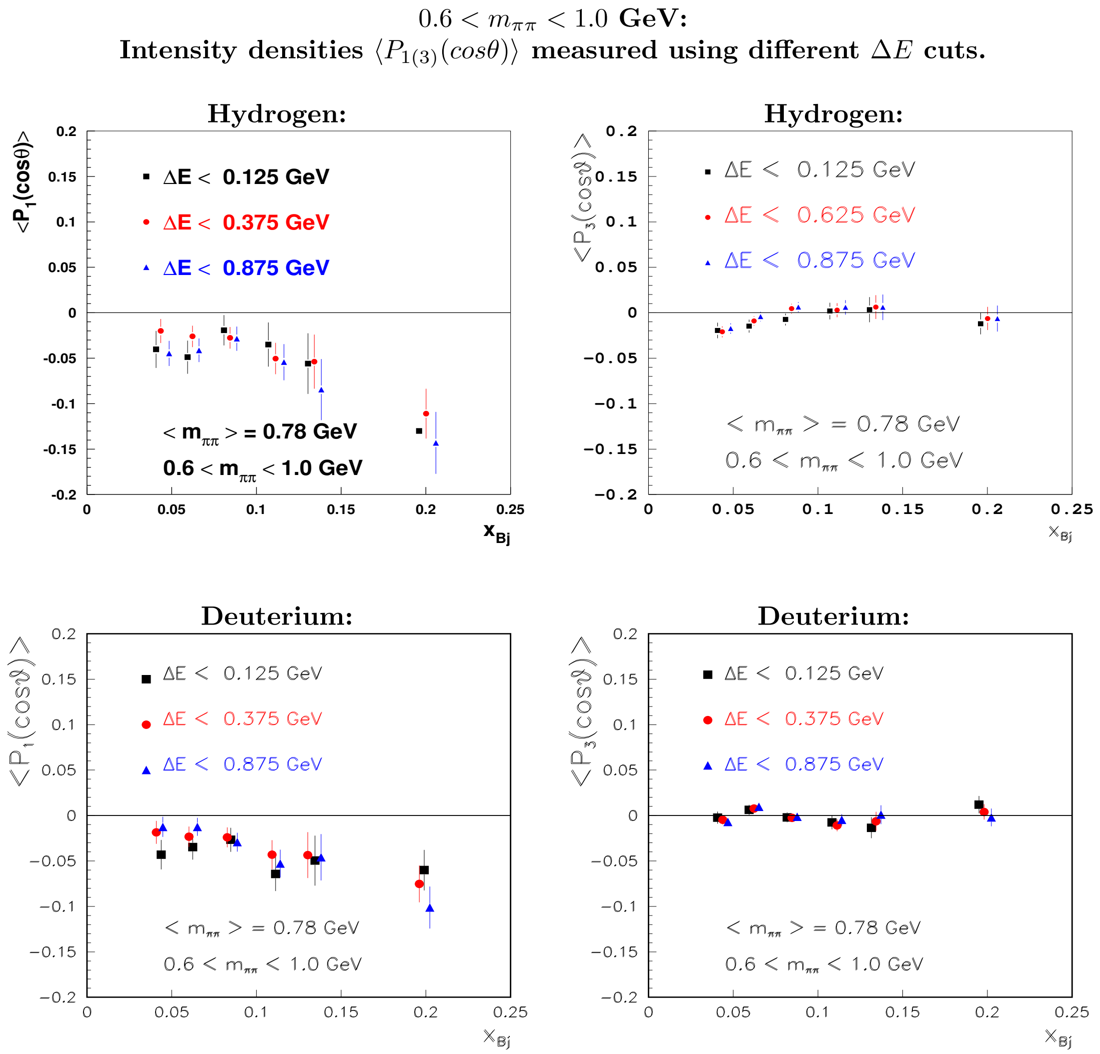

Figure 5.53: $\langle P_{1(3)}(cos\theta)\rangle$ distributions versus x_{Bj} in the invariant mass region $0.6 < m_{\pi\pi} < 1.0$ GeV, obtained using different exclusive ΔE cuts for hydrogen (**upper panels**) and deuterium (**bottom panels**) targets respectively.

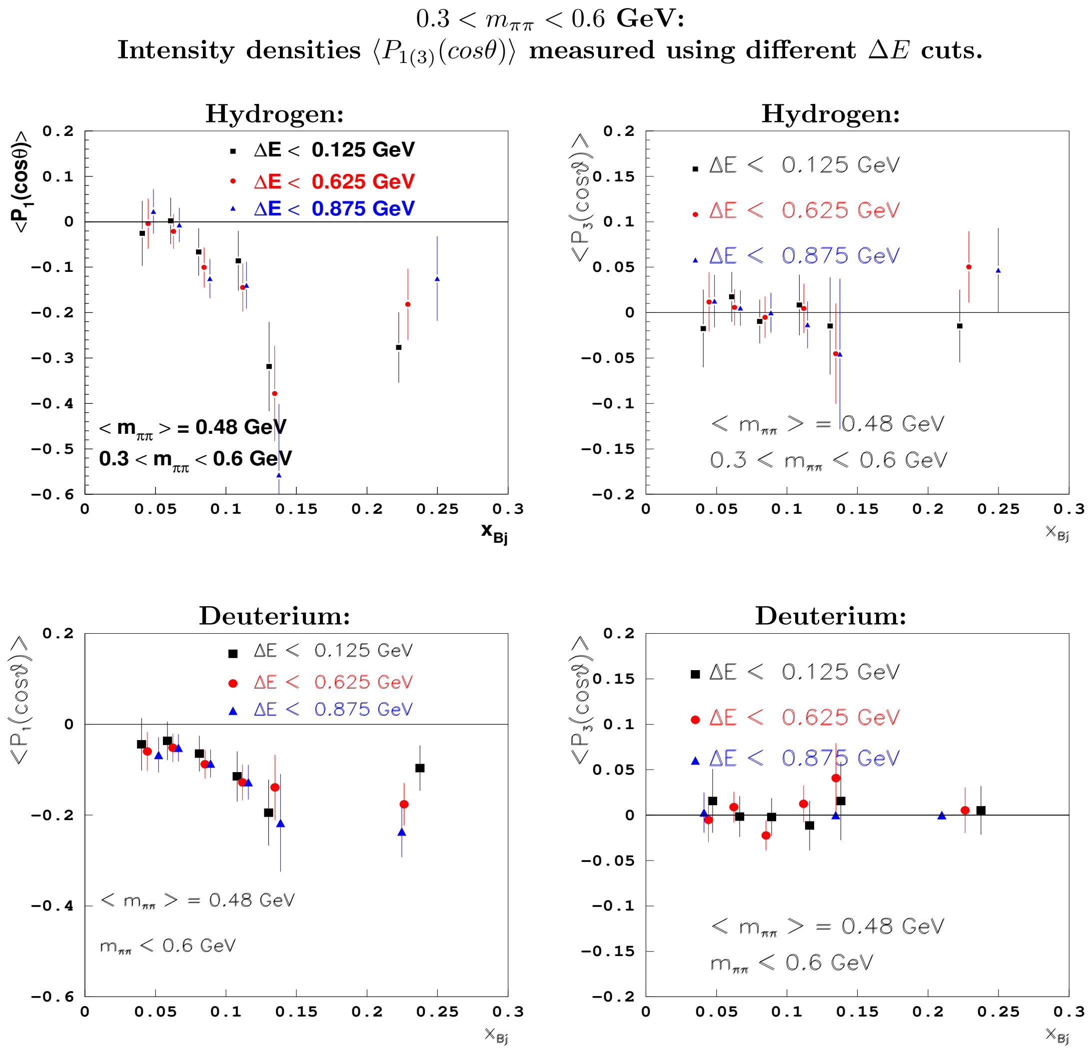

Figure 5.54: $\langle P_{1(3)}(cos\theta)\rangle$ distributions versus x_{Bj} in the invariant mass region $0.3 < m_{\pi\pi} < 0.6$ GeV, obtained using different exclusive ΔE cuts for hydrogen (**upper panels**) and deuterium (**bottom panels**) targets respectively.

Systematical Uncertainty due to different ΔE cuts				
	Hydrogen		**Deuterium**	
x_{Bj}	$\langle P_1(cos\theta)\rangle$	$\langle P_3(cos\theta)\rangle$	$\langle P_1(cos\theta)\rangle$	$\langle P_3(cos\theta)\rangle$
	$0.6 < m_{\pi\pi} < 1.0$ GeV		$0.6 < m_{\pi\pi} < 1.0$ GeV	
≤ 0.053	0.006	0.004	0.024	0.002
$0.053 - 0.072$	0.009	0.006	0.011	0.002
$0.072 - 0.100$	0.008	0.012	0.005	0.001
$0.100 - 0.125$	0.015	0.003	0.021	0.006
$0.125 - 0.145$	0.020	0.003	0.006	0.007
> 0.145	0.007	0.006	0.026	0.008
	$0.3 < m_{\pi\pi} < 0.6$ GeV		$0.3 < m_{\pi\pi} < 0.6$ GeV	
≤ 0.053	0.027	0.030	0.015	0.021
$0.053 - 0.072$	0.023	0.012	0.015	0.010
$0.072 - 0.100$	0.034	0.005	0.023	0.020
$0.100 - 0.125$	0.059	0.018	0.013	0.024
$0.125 - 0.145$	0.180	0.030	0.078	0.025
> 0.145	0.095	0.065	0.079	0.003

Table 5.17: Absolute systematic uncertainty in the determination of $\langle P_{1(3)}(cos\theta)\rangle$ versus x_{Bj} in the invariant mass region $0.6 < m_{\pi\pi} < 1.0$ GeV (**upper table**) and $0.3 < m_{\pi\pi} < 0.6$ GeV (**bottom table**) due to the choice of different ΔE cuts for hydrogen and deuterium targets respectively.

The systematic uncertainty due to the choice of the normalization procedure is estimated normalizing the Monte Carlo sample to data at $2.0 < \Delta E < 4.0$ GeV, i.e. in the ΔE region close to the exclusive peak for the studied process. This systematic uncertainty is evaluated as the difference of values bin by bin of $\langle P_{1(3)}(cos\theta)\rangle$, which are measured subtracting the background using the ratios Sg/Bg obtained with the normalization procedure and the ratios used in this analysis, respectively, Fig. 5.55, 5.56. Numerical results of this systematic uncertainty are reported in Tab. 5.18.

$0.6 < m_{\pi\pi} < 1.0$ GeV:
Intensity densities $\langle P_{1(3)}(cos\theta)\rangle$ measured using different MC normalization to data.

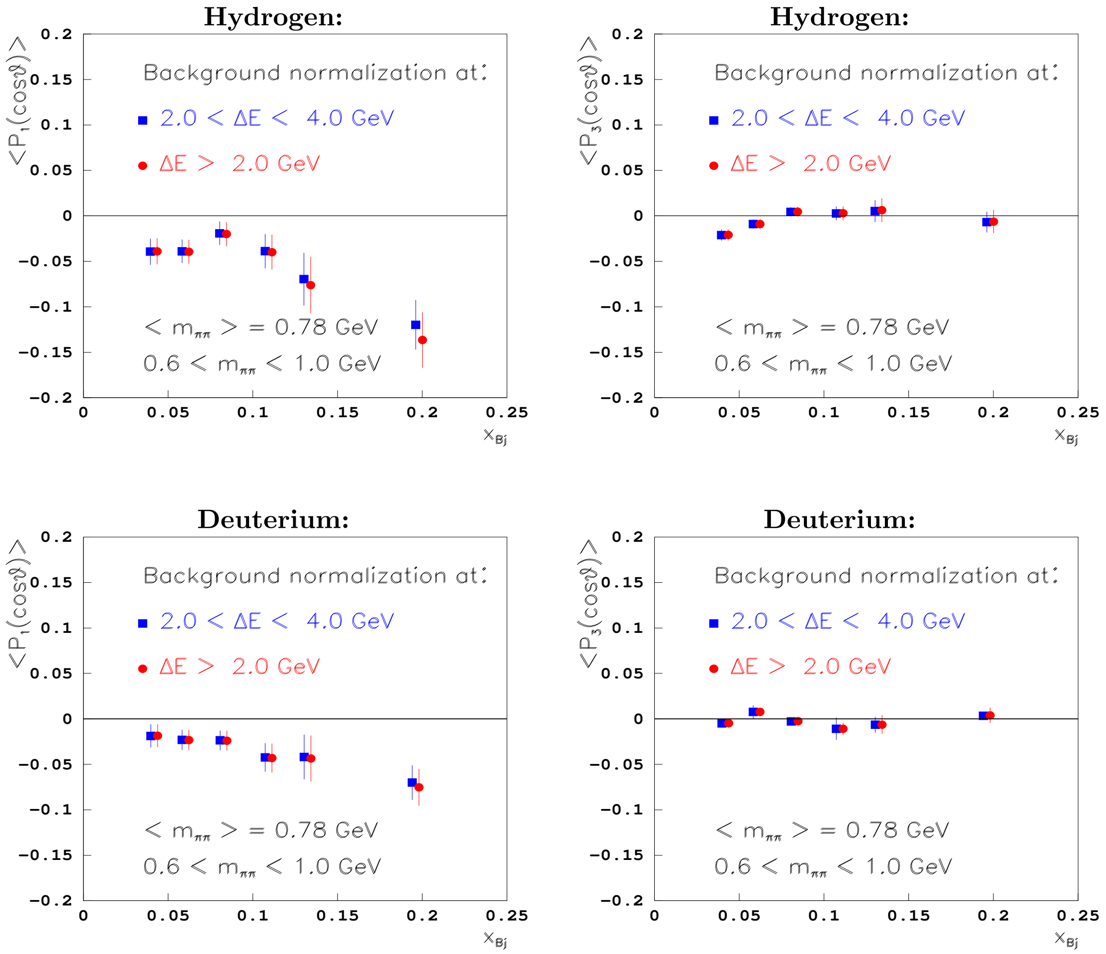

Figure 5.55: $\langle P_{1(3)}(cos\theta)\rangle$ distributions versus x_{Bj} in the invariant mass region $0.6 < m_{\pi\pi} < 1.0$ GeV, obtained using different procedures to normalize *DIS* background to data for hydrogen (**upper panels**) and deuterium (**bottom panels**) targets respectively.

$0.3 < m_{\pi\pi} < 0.6$ **GeV:**
Intensity densities $\langle P_{1(3)}(cos\theta)\rangle$ measured using different MC normalization to data.

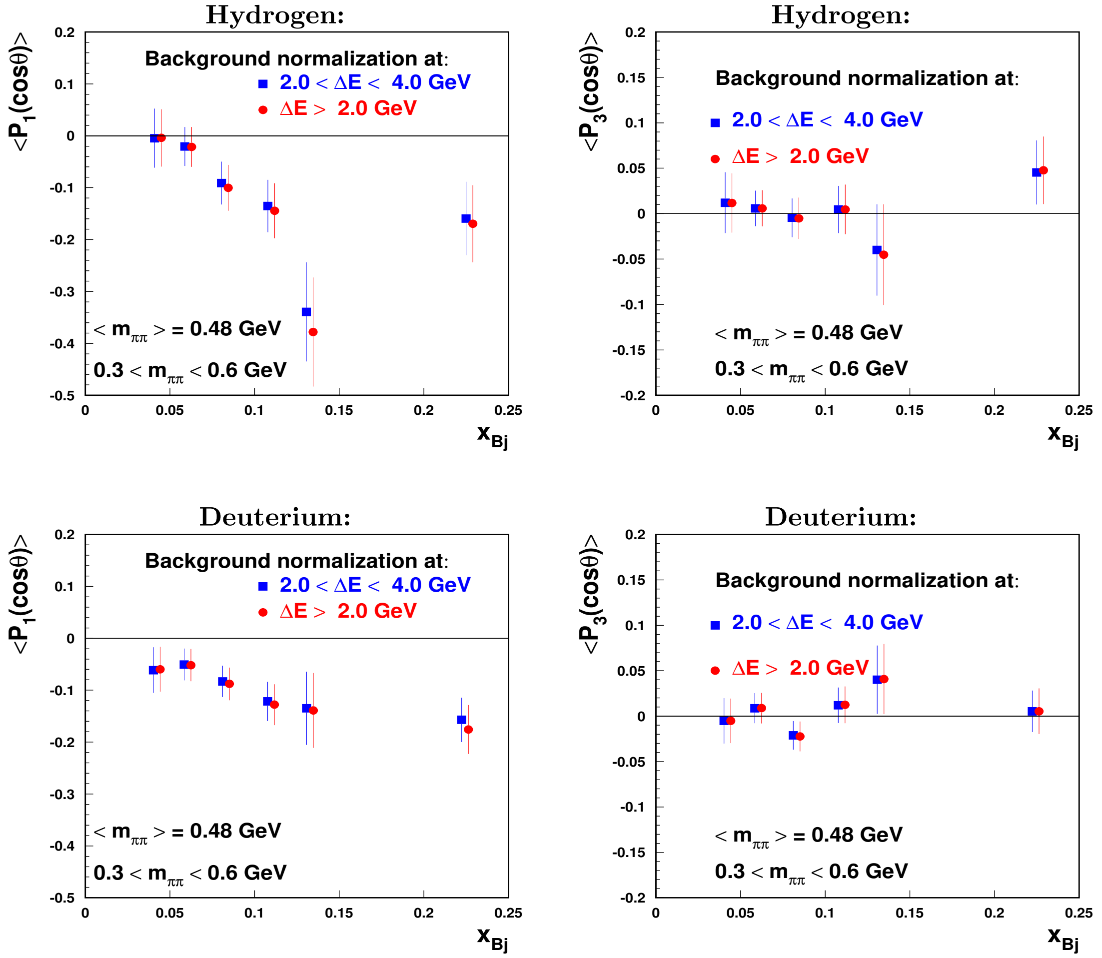

Figure 5.56: $\langle P_{1(3)}(cos\theta)\rangle$ distributions versus x_{Bj} in the invariant mass region $0.3 < m_{\pi\pi} < 0.6$ GeV, obtained using different procedures to normalize *DIS* background to data for hydrogen (**upper panels**) and deuterium (**bottom panels**) targets respectively.

Systematic uncertainty due to normalization procedure				
	Hydrogen		**Deuterium**	
x_{Bj}	$\langle P_1(cos\theta)\rangle$	$\langle P_3(cos\theta)\rangle$	$\langle P_1(cos\theta)\rangle$	$\langle P_3(cos\theta)\rangle$
	$0.6 < m_{\pi\pi} < 1.0$ GeV		$0.6 < m_{\pi\pi} < 1.0$ GeV	
≤ 0.053	0.000	0.000	0.000	0.000
$0.053 - 0.072$	0.001	0.000	0.000	0.000
$0.072 - 0.100$	0.001	0.000	0.000	0.000
$0.100 - 0.125$	0.001	0.000	0.001	0.000
$0.125 - 0.145$	0.007	0.001	0.002	0.000
> 0.145	0.017	0.000	0.005	0.001
	$0.3 < m_{\pi\pi} < 0.6$ GeV		$0.3 < m_{\pi\pi} < 0.6$ GeV	
≤ 0.053	0.001	0.000	0.002	0.000
$0.053 - 0.072$	0.001	0.000	0.001	0.000
$0.072 - 0.100$	0.009	0.001	0.005	0.000
$0.100 - 0.125$	0.009	0.000	0.006	0.000
$0.125 - 0.145$	0.039	0.001	0.004	0.001
> 0.145	0.010	0.002	0.019	0.000

Table 5.18: Absolute systematic uncertainty in the determination of $\langle P_{1(3)}(cos\theta)\rangle$ versus x_{Bj} in the invariant mass region $0.6 < m_{\pi\pi} < 1.0$ GeV (**upper table**) and $0.3 < m_{\pi\pi} < 0.6$ GeV (**bottom table**) due to the procedure to normalize *DIS* background to data for hydrogen and deuterium targets respectively.

The systematic uncertainty due to the assumption to consider all hadrons as pions, was evaluated as in the analysis of $m_{\pi\pi}$ dependence of the intensity densities. Pions have been identified and selected using the information from the RICH detector. For this sample the ratio Sg/Bg was measured at the exclusive ΔE cut used in this analysis, and the background contribution to $\langle P_{1(3)}(cos\theta)\rangle$ was subtracted. This systematic uncertainty is evaluated as the difference of values bin by bin of the intensity densities measured for hadron and pion pairs respectively, Fig. 5.57-5.58.

$0.6 < m_{\pi\pi(hh)} < 1.0$ **GeV:**
Comparison of intensity densities $\langle P_{1(3)}(cos\theta)\rangle$ measured using pions and hadrons at $2 < E < 15$ GeV, respectively

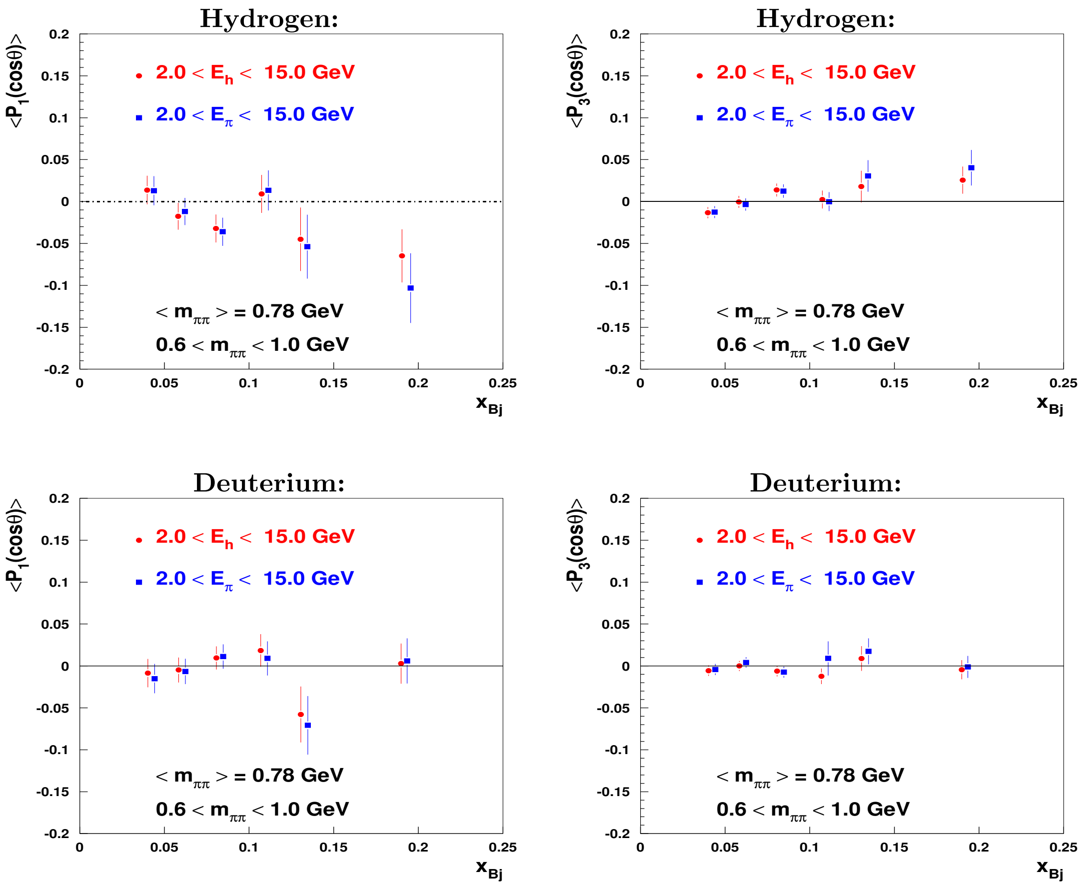

Figure 5.57: x_{Bj}-dependence of $\langle P_{1(3)}(cos\theta)\rangle$ in the invariant mass region $0.6 < m_{\pi\pi(hh)} < 1.0$ GeV, obtained using pion (squares) hadron (circles) pairs with particles having energy $2 < E < 15$ GeV, for hydrogen (**upper panels**) and deuterium (**bottom panels**) targets respectively.

$0.3 < m_{\pi\pi(hh)} < 0.6$ **GeV:**

Comparison of intensity densities $\langle P_{1(3)}(cos\theta)\rangle$ measured using pions and hadrons at $2 < E < 15$ GeV, respectively

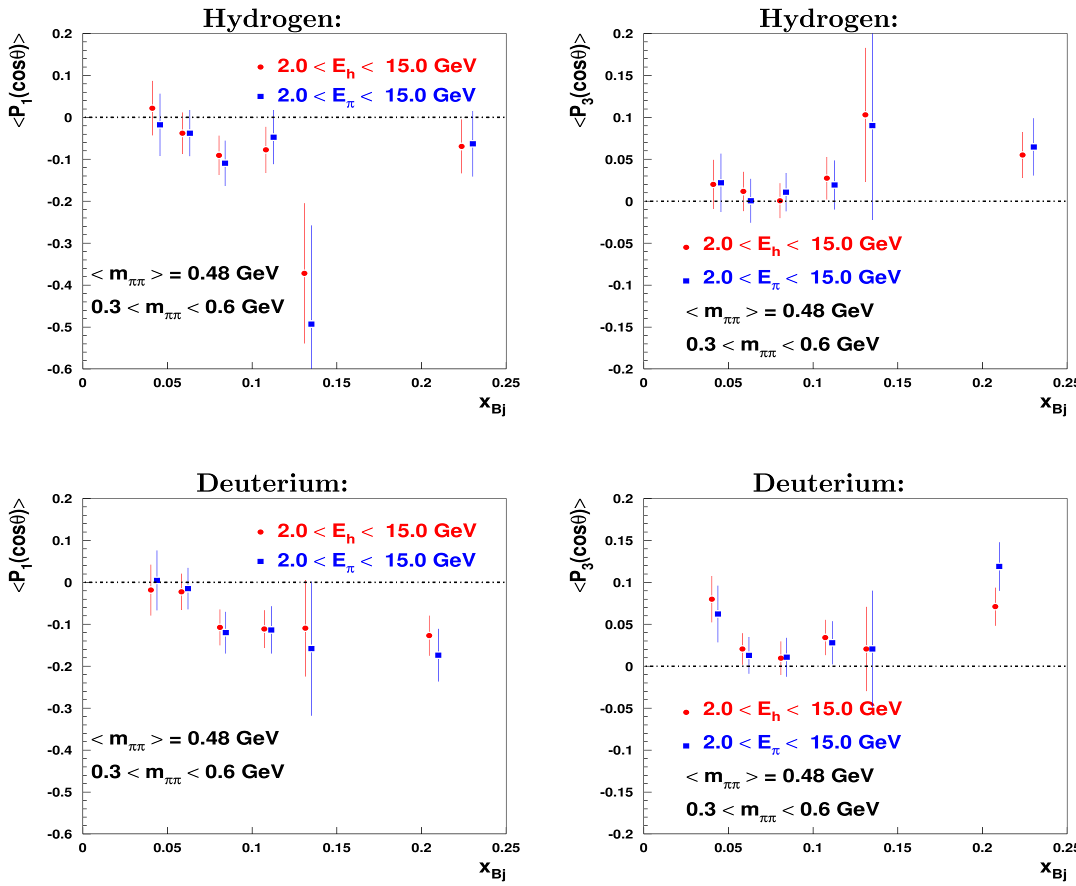

Figure 5.58: $\langle P_{1(3)}(cos\theta)\rangle$ distributions versus x_{Bj} in the invariant mass region $0.3 < m_{\pi\pi(hh)} < 0.6$ GeV, obtained using pion (squares) and hadron (circles) pairs with particles having energy $2 < E < 15$ GeV, for hydrogen (**upper panels**) and deuterium (**bottom panels**) targets respectively.

Systematic uncertainty due to assumption of considering all hadrons as pions				
	Hydrogen		**Deuterium**	
x_{Bj}	$\langle P_1(cos\theta)\rangle$	$\langle P_3(cos\theta)\rangle$	$\langle P_1(cos\theta)\rangle$	$\langle P_3(cos\theta)\rangle$
	$0.6 < m_{\pi\pi(hh)} < 1.0$ GeV		$0.6 < m_{\pi\pi(hh)} < 1.0$ GeV	
≤ 0.053	0.001	0.001	0.007	0.001
$0.053 - 0.072$	0.006	0.003	0.001	0.004
$0.072 - 0.100$	0.004	0.001	0.002	0.001
$0.100 - 0.125$	0.004	0.003	0.009	0.021
$0.125 - 0.145$	0.009	0.013	0.013	0.009
> 0.145	0.039	0.015	0.003	0.003
	$0.3 < m_{\pi\pi(hh)} < 0.6$ GeV		$0.3 < m_{\pi\pi(hh)} < 0.6$ GeV	
≤ 0.053	0.040	0.002	0.023	0.018
$0.053 - 0.072$	0.000	0.011	0.008	0.001
$0.072 - 0.100$	0.019	0.010	0.013	0.001
$0.100 - 0.125$	0.030	0.001	0.002	0.006
$0.125 - 0.145$	0.121	0.013	0.048	0.000
> 0.145	0.006	0.010	0.047	0.048

Table 5.19: Absolute systematic uncertainty in the determination of $\langle P_{1(3)}(cos\theta)\rangle$ versus x_{Bj} in the invariant mass region $0.6 < m_{\pi\pi} < 1.0$ GeV (**upper table**) and $0.3 < m_{\pi\pi} < 0.6$ GeV (**bottom table**) due to assumption to considering all hadrons as pions, for hydrogen and deuterium targets respectively.

In the two invariant mass regions, the total systematic uncertainty has been computed bin by bin, as follows:

$$\sigma_{syst\_tot} = \sqrt{\sum_{k=1,3} \sigma^2_{syst\_k}} \, , \tag{5.8}$$

considering the different uncertainties σ_{syst_k} as due to independent sources. From the comparison of all the uncertainties, the variation of the ΔE cut results to be the main source of systematic uncertainty.

Total systematic uncertainty				
	Hydrogen		**Deuterium**	
x_{Bj}	$\langle P_1(cos\theta)\rangle$	$\langle P_3(cos\theta)\rangle$	$\langle P_1(cos\theta)\rangle$	$\langle P_3(cos\theta)\rangle$
	$0.6 < m_{\pi\pi} < 1.0$ GeV		$0.6 < m_{\pi\pi} < 1.0$ GeV	
≤ 0.053	0.006	0.004	0.025	0.002
$0.053 - 0.072$	0.011	0.007	0.011	0.004
$0.072 - 0.100$	0.009	0.012	0.005	0.001
$0.100 - 0.125$	0.016	0.004	0.023	0.022
$0.125 - 0.145$	0.023	0.013	0.014	0.011
> 0.145	0.043	0.016	0.027	0.009
	$0.3 < m_{\pi\pi} < 0.6$ GeV		$0.3 < m_{\pi\pi} < 0.6$ GeV	
≤ 0.053	0.048	0.030	0.028	0.028
$0.053 - 0.072$	0.023	0.016	0.017	0.010
$0.072 - 0.100$	0.040	0.011	0.027	0.020
$0.100 - 0.125$	0.067	0.018	0.014	0.025
$0.125 - 0.145$	0.220	0.033	0.092	0.025
> 0.145	0.096	0.066	0.094	0.048

Table 5.20: Total absolute systematic uncertainty in the determination of $\langle P_{1(3)}(cos\theta)\rangle$ versus x_{Bj} in the invariant mass region $0.6 < m_{\pi\pi} < 1.0$ GeV (**upper table**) and $0.3 < m_{\pi\pi} < 0.6$ GeV (**bottom table**), for hydrogen and deuterium targets respectively.

5.7.4 Results

The x_{Bj} dependence of $\langle P_1(cos\theta)\rangle$ and $\langle P_3(cos\theta)\rangle$ have been measured for both processes $e^+p \longrightarrow e^+p\ \pi^+\pi^-$ and $e^+d \longrightarrow e^+d\ \pi^+\pi^-$, in the two regions $0.3 < m_{\pi\pi} < 0.6$ GeV and $0.6 < m_{\pi\pi} < 1.0$ GeV. The average values of the relevant variables $m_{\pi\pi}$, Q^2 and t are summarized in Tab. 5.21.

	Hydrogen		**Deuterium**	
$\langle m_{\pi\pi}\rangle$ $[GeV]$	$\langle Q^2\rangle$ $[GeV^2]$	$\langle -t\rangle$ $[GeV^2]$	$\langle Q^2\rangle$ $[GeV^2]$	$\langle -t\rangle$ $[GeV^2]$
0.78	2.1	0.27	2.1	0.22
0.48	2.3	0.42	2.3	0.39

Table 5.21: Average values of the relevant variables $m_{\pi\pi}$, Q^2 and t in the analysis of the x_{Bj}-dependence of $\langle P_1(cos\theta)\rangle$ and $\langle P_3(cos\theta)\rangle$.

Results on $\langle P_1(cos\theta)\rangle$ are shown in Fig. 5.59 for hydrogen and deuterium targets. In both the invariant regions and for both targets, data confirms the asymmetry of the angular production π^+ in the $\pi^+\pi^-$ rest frame, observed also in the analysis of $m_{\pi\pi}$ dependence of $\langle P_1(cos\theta)\rangle$. In the plots, the statistical uncertainty is reported as a band. The observed non zero *intensity density* may be interpreted as originating from the interference of the ρ^0 lower tail with the S-wave non-resonant $\pi^+\pi^-$ production. The asymmetry increases in size with x_{Bj}, and this behavior may be explained as to arise from the increased dominance of $q\bar{q}$ exchange at larger values of x_{Bj}, which leads to a sizable admixture of isoscalar and isovector pion pairs.

Results on $\langle P_3(cos\theta)\rangle$ in the two $m_{\pi\pi}$ regions are shown in in Fig. 5.60 for both targets, with the systematic uncertainty reported in the plots as a band. Results are consistent with zero and confirm the absence of the $\pi^+\pi^-$ production in D-wave at $m_{\pi\pi} < 1$ GeV in the whole x_{Bj}-spectrum covered by the *HERMES* experiment.

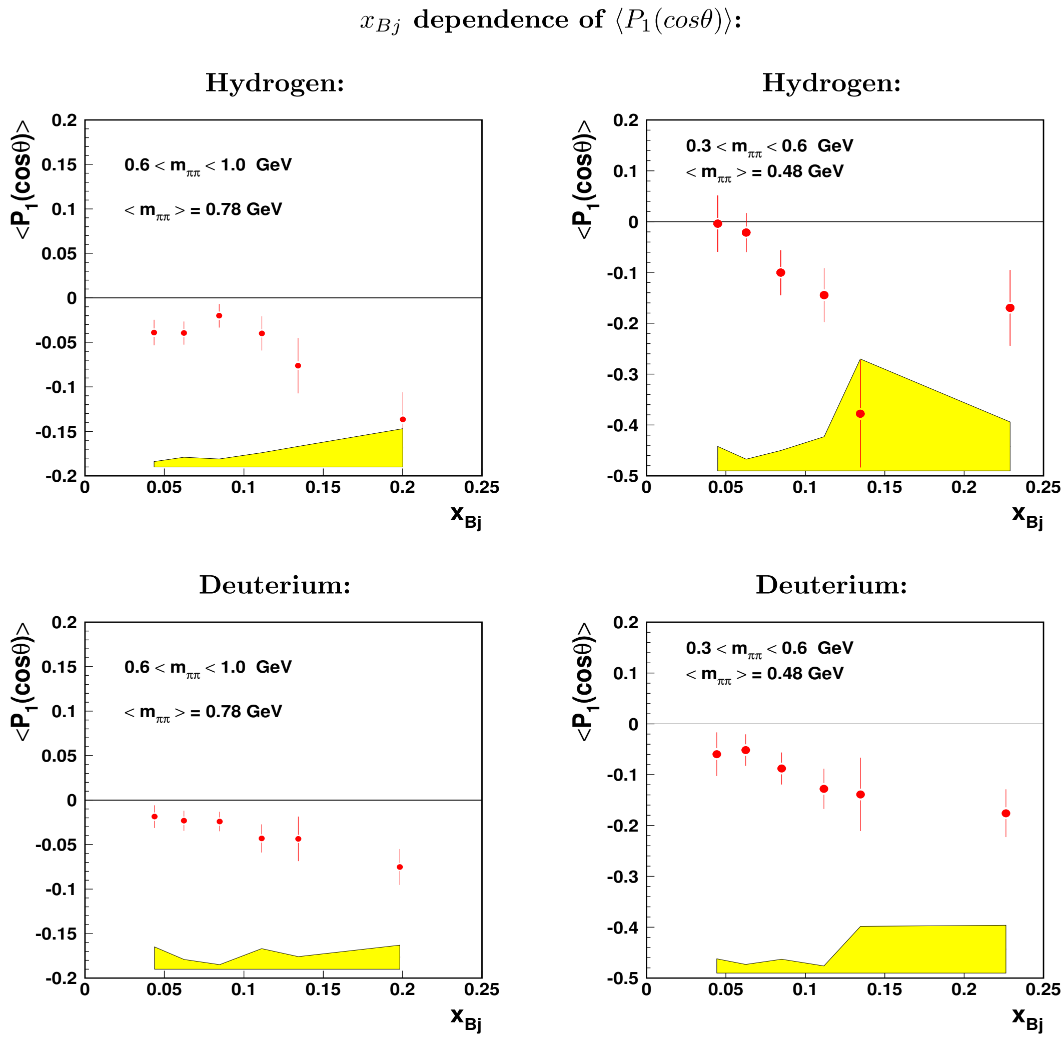

Figure 5.59: x_{Bj} dependence of the *intensity density* $\langle P_1(cos\theta)\rangle$ in the two invariant mass regions $0.6 < m_{\pi\pi} < 1.0$ GeV and $0.3 < m_{\pi\pi} < 0.6$ GeV for both hydrogen (**upper panels**) and deuterium (**bottom panels**) targets respectively.

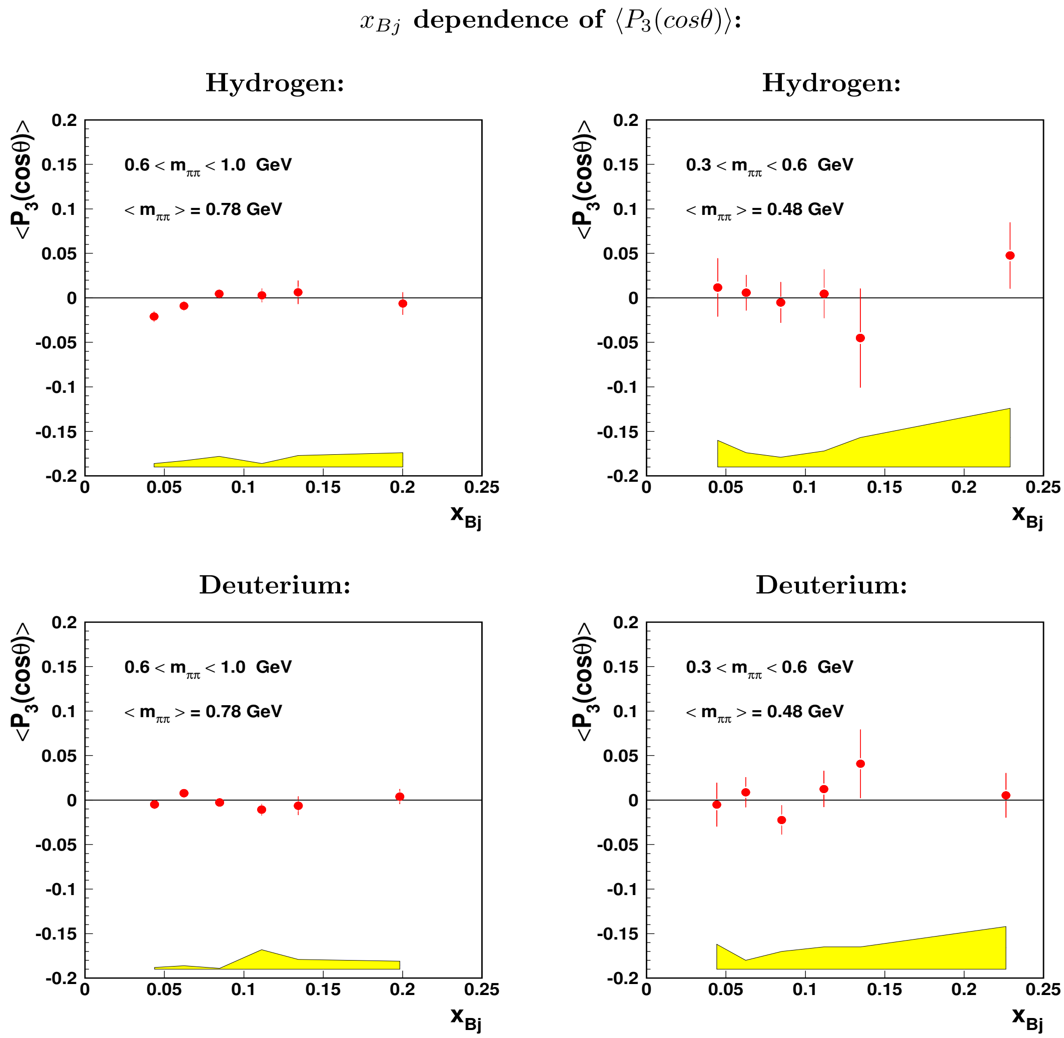

Figure 5.60: x_{Bj} dependence of the *intensity density* $\langle P_3(cos\theta)\rangle$ in the two invariant mass regions $0.6 < m_{\pi\pi} < 1.0$ GeV and $0.3 < m_{\pi\pi} < 0.6$ GeV for both hydrogen (**upper panels**) and deuterium (**bottom panels**) targets respectively.

5.8 Comparison with Theoretical Predictions

The experimental results on the $m_{\pi\pi}$ and x_{Bj} dependence of $\langle P_1(cos\theta)\rangle$ are compared with the available theoretical predictions. In the recent publications [48] [49] predictions have been reported for hydrogen, while no data have been calculated for deuterium target yet. Also, at the moment, no numerical predicted values are available for the $\langle P_3(cos\theta)\rangle$ distribution, for both hydrogen and deuterium targets. Results from the above references differ mainly by the following feature: in [49] all the leading-twist Feynman diagrams have been considered in the amplitude, while in [48] the *GPD* describing the two-gluon exchange (Fig. 3.1, panel *a*) has been neglected.

In Fig. 5.61 experimental values of the $m_{\pi\pi}$ dependence of $\langle P_1(cos\theta)\rangle$ are compared with predicted values in [48] (i.e. without gluon *GPD* in the nucleon), and in [49, 71] (i.e. with gluon *GPD*). In [71], predicted values have been computed at the same average x_{Bj} value of this analysis on the $m_{\pi\pi}$ dependence of $\langle P_{1(3)}(cos\theta)\rangle$. Using the same model of [71], in [49] the graphical behavior of the $m_{\pi\pi}$ dependence is shown in the region $x_{Bj} < 0.4$ for the whole invariant mass spectrum $0.4 < m_{\pi\pi} < 1.5$ GeV.

The shape of the theoretical distribution is nicely reproducing the data, in particular at the f_2 meson mass where there is an indication of change of sign for $\langle P_1(cos\theta)\rangle$. It is worth to point out that the behavior of data at the f_0 meson mass is not reproduced by theory, since the S-wave phase-shift used in the $2\pi DA$ (section 3.3) has been parameterized using only data from the $\pi^+\pi^-$ non-resonant channel, section 3.3.

By the comparison of the two theoretical predictions in the region of ρ^0 resonance

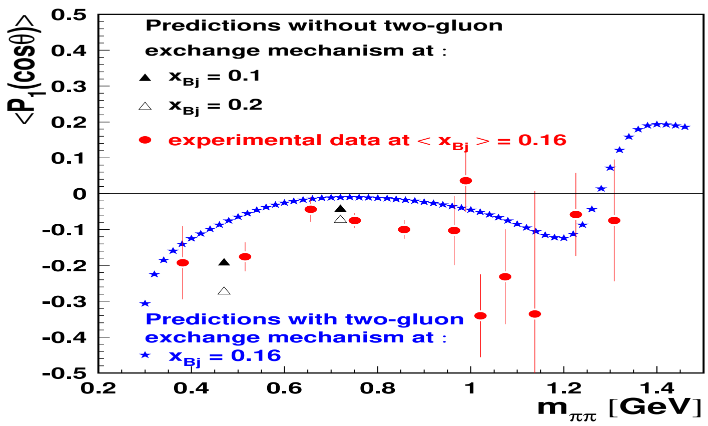

Figure 5.61: The experimental $\langle P_1(cos\theta)\rangle$ distribution versus the invariant mass for hydrogen target is compared with theoretical predictions including ([49, 71]) and not including ([48]) the contribution of the two-gluon exchange mechanism (gluon *GPD*) with the proton target to the amplitude.

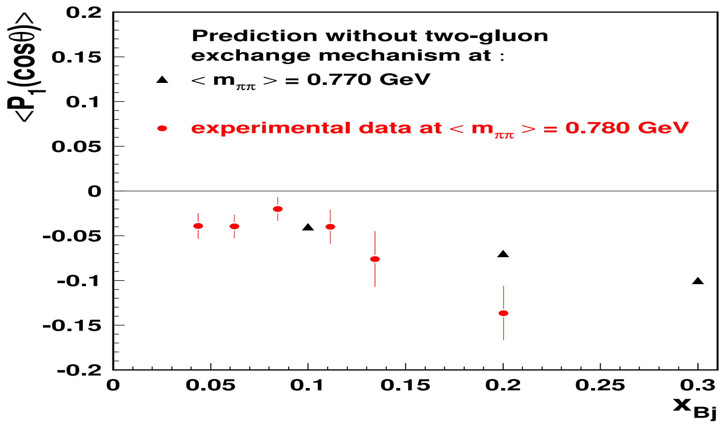

Figure 5.62: The experimental x_{Bj} dependence of $\langle P_1(cos\theta)\rangle$ in the invariant mass region $0.6 < m_{\pi\pi} <$ 1.0 GeV for hydrogen target is compared with the theoretical predictions at $m_{\pi\pi} = 0.770$ GeV [48], where the gluon *GPD* inside the proton has been neglected.

peak and of lower invariant mass, it is evident that the shape of $\langle P_1(cos\theta)\rangle$ is shifted upward when the nucleon gluon *GPD* is taken into account in the amplitude computation. In particular, the model used for the two-gluon exchange changes the size of the *intensity density* of one order of magnitude.

In Fig. 5.62 and Fig. 5.63 the x_{Bj} dependence of $\langle P_1(cos\theta)\rangle$ around the ρ^0 peak and in the region of lower invariant mass is compared to the theoretical predictions in [48] with the nucleon gluon *GPD* neglected, at $m_{\pi\pi} = 0.770$ GeV and $m_{\pi\pi} = 0.5$ GeV respectively. The few theoretical points are in fair agreement with data.

The reasonable agreement of the leading twist predictions on both $m_{\pi\pi}$ and x_{Bj} dependence of $\langle P_1(cos\theta)\rangle$ with data may be understood as to arise from the cancellation of higher twist effects in this kind of asymmetry analyzed [52]. It is worth mentioning that, tuning the theoretical GPDs distributions to the experimental results, may allow, in principle, to evaluate the contribution of gg and $q\bar{q}$ exchange mechanism.

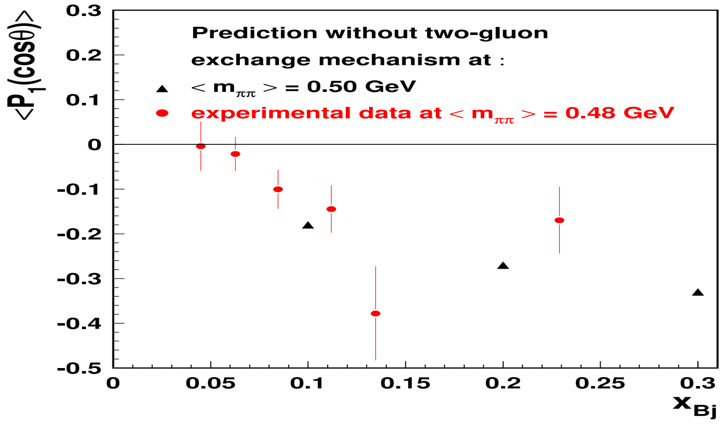

Figure 5.63: The experimental x_{Bj} dependence of $\langle P_1(cos\theta)\rangle$ in the invariant mass region $0.3 < m_{\pi\pi} < 0.6$ GeV for hydrogen target is compared with the theoretical predictions at $m_{\pi\pi} = 0.5$ GeV [48], where the gluon *GPD* inside the proton is neglected.

Chapter 6

Conclusions

In the physical debate to determine the inner spin structure of the nucleon, hard exclusive processes are supposed to access the total angular momentum of quarks and gluons. This is motivated since this kind of processes can be interpreted in terms of Generalized Parton Distributions (GPD) which have been demonstrated to be correlated to the total angular momentum carried by partons. In this work, the $\pi^+\pi^-$ hard exclusive electroproduction off both proton and deuteron from the reaction $e^+N \longrightarrow e^+N\pi^+\pi^-$, has been analyzed with the *HERMES* experiment. In particular for the first time, the intensity densities $\langle P_1(cos\theta)\rangle$ and $\langle P_3(cos\theta)\rangle$ have been measured.

The invariant mass dependence of the above quantities was analyzed in the region $0.3 < m_{\pi\pi} < 1.35$ GeV at $< x_{Bj} > = 0.16$ and at the scale $< Q^2 > = 3$ GeV^2. Results on $\langle P_1(cos\theta)\rangle$ report an angular production asymmetry of π^+ which depends on the invariant mass $m_{\pi^+\pi^-}$ of the $\pi^+\pi^-$ system at fixed x_{Bj}. At small invariant mass, i.e. close to the threshold $m^2_{\pi^+\pi^-} = 2m_\pi$, this non zero intensity density may be interpreted as originating from the interference of the ρ^0 lower tail with the S-wave non-resonant $\pi^+\pi^-$ production. At $m_{\pi^+\pi^-} = m_{\rho^0}$ the absolute value of this quantity shows a minimum. At larger invariant mass the size of the distribution increases due to the interference of the ρ^0 upper tail (P-wave) with the S-wave non-resonant $\pi^+\pi^-$ production. In the f_2 meson region, data indicates a change of sign interpreted as due to the interference of the ρ^0 upper tail with $\pi^+\pi^-$ production from the f_2 (D-wave). It is worth to mention that at $m_{\pi^+\pi^-} \sim 1$ GeV, the observed asymmetry suggests the interference with the ρ^0 tail and the $\pi^+\pi^-$ production from the f_0 (S-wave). This fact by itself is interesting due to the importance of the scalar meson physics.

Results on $\langle P_3(cos\theta)\rangle$ are sensitive only to the interference between the $\pi^+\pi^-$ production channels in P-wave and D-wave. Data clearly show that no pion pair in D-wave are produced in the region $m_{\pi^+\pi^-} \leq 1$ GeV. The distribution $\langle P_3(cos\theta)\rangle$ for deuterium target increases in size and changes sign in the f_2 meson region, as expected due to the interference of the P-wave and D-wave resonant $\pi^+\pi^-$ channels. On the contrary, inside the statistical and systematic uncertainty for hydrogen, results do not show evidence of the D-wave channel.

Consequences of the results on the $m_{\pi\pi}$ dependence of the studied intensity densities is that the angular distribution of the $\pi^+\pi^-$ pair is not the one of a pure P-wave. It is essential to know how important contributions from other partial waves are for the analysis of the helicity density matrix in ρ^0 production, which describes the transfer of virtual photon helicity to the vector meson. In fact the usual extraction methods for ρ^0 helicity density matrix assume a pure P-wave.

The x_{Bj} dependence of $\langle P_1(cos\theta)\rangle$ and $\langle P_3(cos\theta)\rangle$ have been measured in the two regions $0.3 < m_{\pi\pi} < 0.6$ GeV and $0.6 < m_{\pi\pi} < 1.0$ GeV, at the scale $< Q^2 > = 3$ GeV^2 for both hydrogen and deuterium targets. Results on $\langle P_1(cos\theta)\rangle$ report an angular production asymmetry which may be interpreted as originating from the interference of the ρ^0 lower tail with the S-wave non-resonant $\pi^+\pi^-$ production. The asymmetry increases in size with x_{Bj} and this behavior may be understood as to arise from the increased dominance of $q\bar{q}$ exchange at larger values of x_{Bj}, which leads to a sizable admixture of isoscalar and isovector pion pairs. Data on $\langle P_3(cos\theta)\rangle$ confirm the absence of the $\pi^+\pi^-$ production in D-wave at $m_{\pi\pi} < 1$ GeV in the whole x_{Bj}-spectrum covered by the *HERMES* experiment.

The reasonable agreement of the leading twist predictions on both $m_{\pi\pi}$ and x_{Bj} dependence of $\langle P_1(cos\theta)\rangle$ with data may be understood as to arise from the cancellation of higher twist effects in this kind of asymmetry analyzed [52].

Results of this work are a clear evidence of an $I = 0$ and $I = 1$ admixture in $\pi^+\pi^-$ exclusive electroproduction. In particular, the f_0 and f_2 mesons appear to be produced in the exclusive channel, and this fact by itself is interesting in view of the importance of the scalar and tensor meson physics.

Concluding, I want to point out that the interpretation of the results on $\pi^+\pi^-$ exclusive distributions in the framework of the Generalized Parton Distributions theory, in principle allows to evaluate the separate contributions of gg and $q\bar{q}$ exchange mechanisms.

Appendix A

The Spin Crisis

To investigate smaller and smaller objects, physicists use probes with decreasing wavelength. As an example, the observation of the nucleon internal structure may be performed when in a lepton-hadron scattering the exchanged virtual bosons have wavelength lower then the Fermi scale typical of hadrons size. The differential cross section of the elastic process, known as *Rosenbluth* formula, when protons are considered is found to be [96]:

$$\frac{d\sigma_{fi}}{d\Omega_f} = \frac{\alpha^2}{4E^2 sin^4\theta/2}\frac{E'}{E}\Big(\frac{G_E^2(Q^2)+\tau G_M^2(Q^2)}{1+\tau}cos^2\theta/2 + 2\tau G_M^2(Q^2)sin^2\theta/2\Big)\ , \quad \text{(A.1)}$$

where $\tau = -\frac{q^2}{4M_p^2}$, θ is the scattering angle of lepton with initial (final) energy $E(E')$, M_P is the proton mass, $Q^2 = -q_\mu^2$, q_μ being the four-momentum of the exchanged photon, and the electromagnetic and magnetic *Form Factors* G_E and G_M are introduced to parameterize our ignorance of the detailed structure of the proton represented in Fig. A.1 left panel. In the energy transfer limit $Q^2 \sim \vec{q}_\mu^{\,2}$. If proton were point-like, the cross section reduces to the elastic *Mott* cross section and experimentally people would get $G_E = G_M = 1$, $\forall\, q^2$. On the contrary, as shown in Fig. A.1 right panel, G_E has a clear q^2 dependence. This is an indication of a substructure inside the proton. In principle, studying the angular distributions after the scattering, and comparing them with results from the *Mott* cross section, information on the internal charge distribution may be determined, discriminating among different models [97]. The resolution of the probe can be enlarged using a probe of high virtuality Q^2, that can be reached with modern accelerators. At the *HERA* facility for example, the 27.6 GeV positron beam, when interacting with *HERMES* experiment target, exchanges virtual photons with average virtuality $Q^2 \sim 4EE'sin^2\theta/2$ of a few GeV. The order of energies involved implies also large energy transfer to the target. With hydrogen target, for smaller Q^2 the probability that the virtual photon just excites the proton into a Δ-state producing

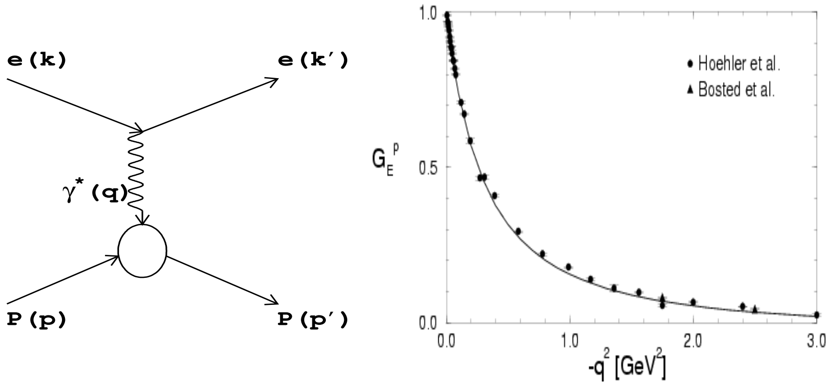

Figure A.1: **Left panel:** elastic scattering of a lepton off a proton. **Right panel:** the electric Form Factor of the proton; experimental data are taken from [98, 99].

an extra π-meson is large. These events correspond to $W \sim M_\Delta$, W being the invariant mass of the virtual-photon proton system, Fig. A.2. Increasing Q^2 and W, the target mainly breaks up into complicated multiparticle states, due to the large amount of energy transferred to the target. In this kinematic region exclusive processes with unbroken target, are still present even though they account for very few percent of the whole events.

A.1 Experimental evidences of quarks

The process $ep \to eX$ is the *inelastic* reaction when the target may fragment into a multiparticle system and only the scattered electron is detected. Its amplitude, in the lowest electromagnetic interaction order, is described in [100], and after a few algebra

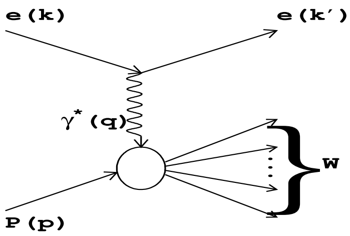

Figure A.2: Invariant mass W of the virtual-photon proton system in the process $ep \to eX$ when the target fragments into a multiparticle system and only the scattered electron is detected.

one finds

$$E' \frac{d\sigma}{d^3E'} \;=\; \frac{1}{k\cdot p}\Big(\frac{\alpha_{QED}}{q^2}\Big)^2 L^{\mu\nu} W_{\mu\nu} \;, \tag{A.2}$$

where

$$L^{\mu\nu} \;=\; k'^{\mu}k^{\nu} + k^{\nu}k'^{\mu} + \frac{q^2}{2} g^{\mu\nu} \tag{A.3}$$

is the leptonic tensor,

$$W_{\mu\nu} \;=\; \frac{1}{2\pi}\int d^4x e^{iq\cdot x}\frac{1}{2}\sum_{\lambda}\langle p\lambda \mid j_{\mu}(x) j_{\nu}(0) \mid p\lambda\rangle \tag{A.4}$$

is the hadronic tensor, λ is the proton target spin, $k(k'), p$ are the momenta of the incoming (scattered) electron and proton respectively, $j_{\mu}(x)$ is the electromagnetic hadronic current localized at x and $\mid p\lambda\rangle$ is the proton state. The hadronic tensor can be parameterized in the most general form constructed out of the metric tensor $g_{\mu\nu}$ and the independent momenta p_{μ} and q_{μ}. Considering the current conservation at the hadronic vertex, $W_{\mu\nu}$ is found to be parameterizable in

$$W_{\mu\nu} = W_1(-g_{\mu\nu} + \frac{q_{\mu}q_{\nu}}{q^2}) + W_2\frac{1}{M_P^2}(p_{\mu} - \frac{p\cdot q}{q^2}q_{\mu})(p_{\nu} - \frac{p\cdot q}{q^2}q_{\nu}) \;, \tag{A.5}$$

where W_i's are functions of the Lorentz scalar variables that can be constructed from the four-momenta at the hadronic vertex. Unlike the elastic scattering, there are two independent variables and Q^2, $x_{Bj} = \frac{Q^2}{2p\cdot q}$ are chosen. The cross section for $ep \to eX$ when the proton target is broken up by scattering electrons, is Instead of the W_i's it is more convenient to use the following structure functions:

$$F_1(x, Q^2) = M_P W_1(x, Q^2) \quad ; \quad F_2(x, Q^2) = \nu W_2(x, Q^2) \;. \tag{A.6}$$

It is interesting to compare this cross section with the formula of the elastic scattering of the electron off a point-like spin 1/2 particle with mass $M_\star$ and unit charge:

$$\frac{d\sigma_{fi}}{d\Omega_f} = \frac{Z^2\alpha^2 m^2}{4E^2 sin^4\theta/2}\frac{E'}{E}(cos^2\theta/2 - \frac{\mid q^2 \mid}{2M_\star^2}sin^2\theta/2)\delta(\nu + \frac{q^2}{2M_\star}) \;. \tag{A.7}$$

The delta distribution in the above equation reflects the elasticity of the considered process where the electroweak boson exchanged by the electron is absorbed by the other scattering particle with incoming (out-coming) momentum p (p'):

$$p' = p + q \;;\; M_\star^2 = M_\star^2 + q^2 + 2M_\star\nu \quad\to\quad \nu = -q^2/(2M_\star). \tag{A.8}$$

It may be expected that, in the limit of electron elastic scattering off point-like spin 1/2 particles, the inelastic cross section in eq. ?? should reduce to eq. A.7, with

$$\begin{aligned} F_1(x,Q^2) \underset{elastic}{\longrightarrow} F_1(Q^2) &= \frac{Q^2}{4M_\star^2}\delta(\nu - \frac{Q^2}{2M_\star}) \\ F_2(x,Q^2) \underset{elastic}{\longrightarrow} F_2(Q^2) &= \delta(\nu - \frac{Q^2}{2M_\star}) \ , \end{aligned} \tag{A.9}$$

where the structure functions depend once again on one variable only.

In the last decades, the structure functions F_1 and F_2 have been deeply studied at different kinematic regions. In Fig. A.3, top right panel, results on F_2 are shown. It is clear that at large Q^2, i.e. at large resolution of the probe, the structure function scales with one variable only; it depends on only one kinematic variable, x_{Bj}. This scaling is commonly named *Bjorken scaling*. The inelastic process, when scaling is observed is named Deep Inelastic Scattering (DIS). Actually, at very small x_{Bj} the scaling violation starts to appear, which is interpreted in the *QCD* framework as due to gluon radiation [101]. Therefore at the resolution scales of the order of ~ 1 GeV, the deep inelastic scattering behaves as the probe interacts elastically with some internal constituent of the target. This is an experimental evidence of the existence of point like particles inside nucleons.

A phenomenological interpretation in term of partons of the above results was given by Bjorken and Paschos in 1969 [102]. They discussed an intuitive but powerful model by Feynman in which the nucleon is built of fundamental point-like constituents. The basic idea in the model is to represent the inelastic scattering of the positron with a proton as a scattering off quasi free point-like constituents within the nucleon, when viewed from a frame in which the proton has infinite momentum. With lepton-proton scattering at high energies, the center of mass of the exchanged virtual-photon and the proton is found to be a good approximation of such a frame. The proton is considered as consisting of a certain number N of free partons with negligible transverse momentum of the parton before the collision with the lepton, and each of them carrying a longitudinal momentum fraction x of the total momentum of the nucleon. Within the model, the incoming lepton interacts elastically with one of the partons with fraction x of the total nucleon momentum, while the rest remains undisturbed during the interaction. For a general distribution of partons in the proton, summing over the individual contributions from partons weighted by their electrical charge e_i, and integrated in all the x spectrum $F_2(x,Q^2) = \sum_i e_i^2 x q_i(x)$, where the Parton Distribution Function $q_i(x)$, that is the probability of finding a parton i_type with longitudinal fraction x of the proton momentum, was phenomenologically introduced. Following the same procedure used to determine $F_2(x)$ in the Bjorken regime, and assuming the hypothesis of partons as spin 1/2 particles, the *Callan-Gross* relation is obtained:

$$F_1(x) \quad = \quad \frac{1}{2x} F_2(x) \; . \tag{A.10}$$

The above relation between the structure functions $F_1(x)$ and $F_2(x)$ is valid within *DIS* regime, when the inner structure of the studied hadron does not depend on the probing scale. The experimental observation of this relation is a confirmation of the spinorial nature of the charged constituents of hadrons. In Fig.A.3, top left panel, results on the ratio $\frac{2xF_1(x)}{F_2(x)}$ are presented at different scales Q^2, confirming the validity of the Callan-Gross relation. In the first models of hadrons, as the flavor $SU(3)$ model by Gell-Mann, barions and mesons were assumed to be formed of three quarks and a $q\bar{q}$ pair respectively. These quarks, are historically named as *valence quarks* because they are responsible of many of the macroscopic properties of hadrons which they build up. For barions, expecting each of the three quarks to have effective mass $m \sim \frac{1}{3}M_b$, M_b being the barion mass, one should find the structure function F_2 peaked at $x \sim \frac{1}{3}$, null at $x = 0$ and $x = 1$, with a spreading $\frac{\Delta x}{x} \sim \frac{p_F}{mc} \sim 1$ due to quarks confined within a volume of dimensions of the nucleon radius R, and therefore having a Fermi momentum $p_F \sim \frac{\hbar}{R} \sim 150 MeV/c$ [103]. Instead, what is shown in Fig.A.3 top left panel, clearly puts in evidence that at low x there is a strong contribution which cannot be referred to valence quarks. Instead, in the QCD framework quarks in the nucleon are surrounded by a cloud of gluons and quark-antiquark pairs (sea quarks) and we expect them to have a bremsstrahlung-like behavior, so that the number of sea quarks grows logarithmically as $x \to 0$ and may give reason of the results in Fig.A.3. Furthermore the cloud becomes more and more detailed as the resolution scale Q^2 is increased. If a quark is probed at a certain value of Q^2, at some higher scale this parton will carry a lower momentum fraction then before, since at higher resolution its radiation can be resolved from the cloud. Consequently, the parton distributions must still depend on Q^2.

By scattering electrons off a deuterium target, F_2 for neutrons is determined, one finds

$$\begin{aligned}
\frac{1}{x} F_2^{en}(x) \quad &= \quad \left(\frac{2}{3}\right)^2 [u^n(x) + \bar{u}^{\;n}(x)] + \left(\frac{1}{3}\right)^2 [d^n(x) + \bar{d}^{\;n}(x)] + \left(\frac{1}{3}\right)^2 [s^n(x) + \bar{s}^{\;n}(x)] \\
\frac{1}{x} F_2^{ep}(x) \quad &= \quad \left(\frac{2}{3}\right)^2 [u^p(x) + \bar{u}^{\;p}(x)] + \left(\frac{1}{3}\right)^2 [d^p(x) + \bar{d}^{\;p}(x)] + \left(\frac{1}{3}\right)^2 [s^p(x) + \bar{s}^{\;p}(x)] \; ,
\end{aligned} \tag{A.11}$$

with heavier flavors c, b, t neglected. As the proton and the neutron are members of an isospin doublet, their quark content is related: there are as many u quarks in a proton as d quarks in a neutron, and so on,

$$u^p(x) = d^n(x) \equiv u(x), \;\; d^p(x) = u^n(x) \equiv d(x), \;\; s^p(x) = s^n(x) \equiv s(x) \; . \tag{A.12}$$

For each flavor, valence and sea quark distributions are defined as:

$$u(x) = u_v(x) + u_s(x) \quad , \quad u_v(x) = u(x) + \bar{u}(x) \ , \tag{A.13}$$

and in a very first approximation we may assume that the three lightest quarks u, d, s occur in the sea S with roughly the same frequency and momentum distribution. Combining all these informations one obtains

$$\frac{F_2^{en}}{F_2^{ep}} = \frac{u_v + 4d_v + 12S}{4u_v + d_v + 12S}, \quad \frac{F_2^{en}}{F_2^{ep}} \xrightarrow[x\to 0]{} 1, \quad \frac{F_2^{en}}{F_2^{ep}} \xrightarrow[x\to 1]{} \frac{u_v + 4d_v}{4u_v + d_v} \ . \tag{A.14}$$

Moreover, for the proton it can be argued that $u_v \gg d_v$ and that the ratio should tend to 1/4. Experimental data in Fig.A.3, bottom left panel, confirm the $q\bar{q}$ sea pairs contribute mostly at low x while valence quarks dominate at large x with the u_v dominance over d_v.

If one considers *DIS* of neutrino off nuclear targets containing approximately equal number of protons and neutrons, neglecting s, c, b, t quark contribution, and comparing results with electron-nucleon scattering one, the following expressions are obtained:

$$F_2^{\nu N} \sim \frac{1}{2}(\ F_2^{\nu p} + F_2^{\nu n}) \ = 2x(u(x) + \bar{u}(x) + d(x) + \bar{d}(x)) \sim \frac{2}{e_u^2 + e_d^2} F_2^{eN} \ , \tag{A.15}$$

where e_u and e_d are the electric charges of quarks u and d respectively. The equivalence $F_2^{\nu N} = F_2^{eN}$ would mean that quarks u and d have charge 1. Instead what is experimentally measured, is shown in Fig.A.3, bottom right panel, where data on neutrino-nucleon scattering from *Gargamelle* at *CERN* are compared with data on electron-nucleon scattering from *SLAC*. Results clearly show that quarks have fractional charge, and are in agreement with $e_u = \frac{2}{3}$ and $e_d = -\frac{1}{3}$. From the same data it was also obtained:

$$\int F_2^{\nu N}(x)dx \sim \int [u(x) + \bar{u}(x) + d(x) + \bar{d}(x)]xdx = 0.50 \pm 0.05 \ , \tag{A.16}$$

for values of Q^2 in the range $1 - 10$ GeV^2. The total momentum summed over all constituents is not unity, meaning that partons inside nucleons account for only half the nucleon momentum. Half of it must be inferred to different constituents besides quarks, which are inert to electromagnetic and weak interactions, and were subsequently identified with gluons.

A.2 The Spin Content of Hadrons and the Spin Crisis

In order to access the spin properties of nucleons in inclusive DIS of leptons off hadrons, both the scattering particles must be polarized. In this case, the most general decomposition of the leptonic and hadronic tensor is $L_{\mu\nu} = L_{\mu\nu}^{[S]} + L_{\mu\nu}^{[A]}$, $W_{\mu\nu} = W_{\mu\nu}^{[S]} + W_{\mu\nu}^{[A]}$,

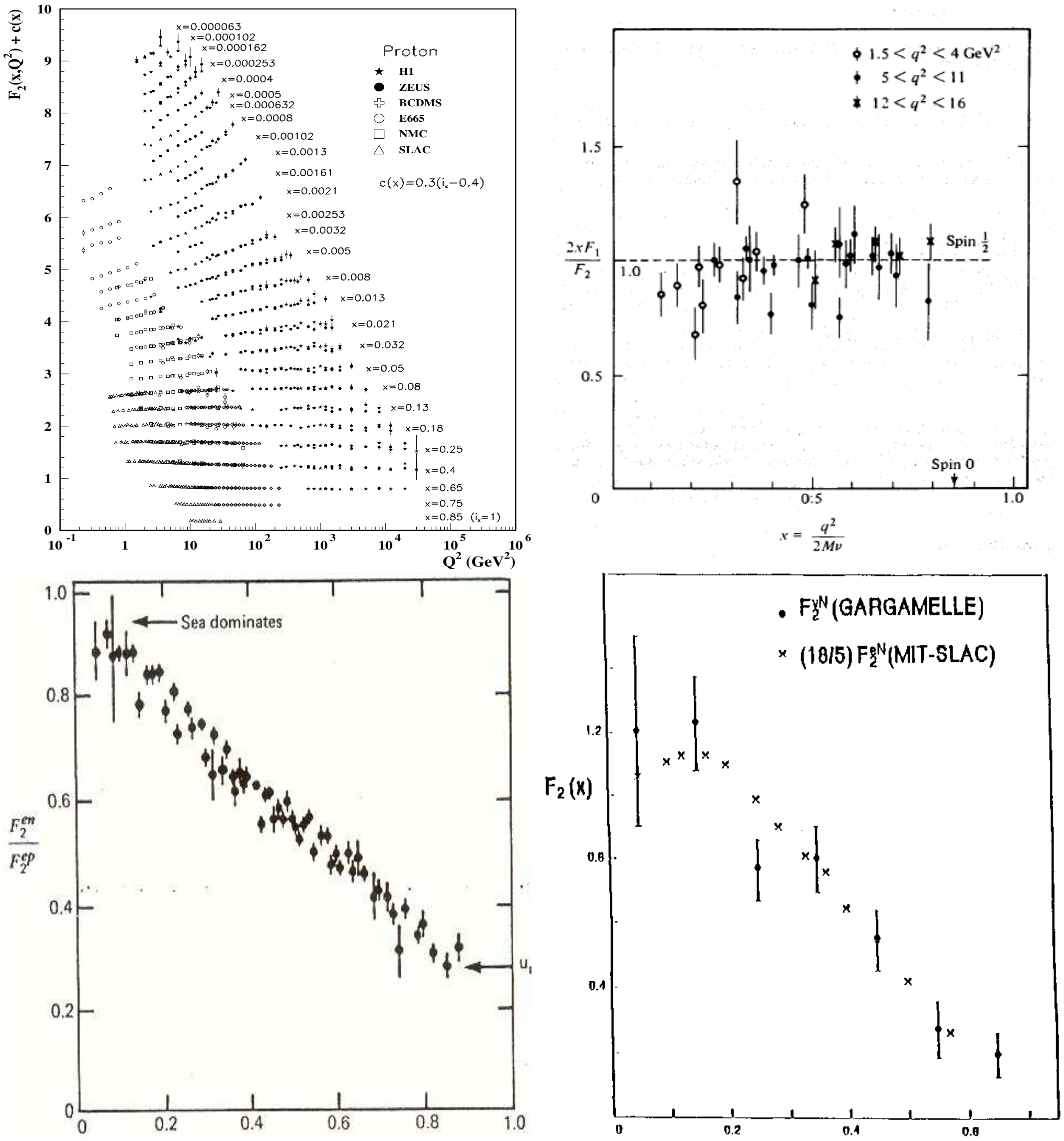

Figure A.3: **Top left panel:** Q^2 dependence of $F_2(x)$ at different x_{Bj} values. For most of the x_{BJ} spectrum data scales on Q^2 only. **Top right panel:** experimental data on $\frac{2xF_1(x)}{F_2(x)}$ at different scales Q^2 are in agreement with quarks having spin 1/2. **Bottom left panel:** x_{Bj} dependence of F_2^{en}/F_2^{ep} confirms that $q\bar{q}$ sea pairs contribute mostly at low x, while valence quarks contribution dominate at large x. **Bottom right panel:** The comparison of $F_2^{\nu p}$ from *Gargamelle* with $18/5 \cdot F_2^{ep}$ from SLAC confirms the fractional charge of quarks.

namely the symmetric part ($[S]$) describing the unpolarized sector of the cross section, and the antisymmetric part ($[A]$) describing the spin sector:

$$\begin{aligned} L_{\mu\nu}^{[A]} &= 2i\epsilon_{\mu\nu\alpha\beta}k^\alpha q^\beta \ , \\ W_{\mu\nu}^{[A]} &= i\epsilon_{\mu\nu\lambda\sigma}q^\lambda \left[\frac{S^\sigma}{\nu M_P} g_1(x,Q^2) + [(P\cdot q)S^\sigma) - (q\cdot S)P^\sigma] \frac{g_2(x,Q^2)}{\nu M_P^2} \right] \ , \end{aligned} \tag{A.17}$$

where $\epsilon_{\mu\nu\alpha\beta}$ is the totally antisymmetric *Levi-Civita* tensor, $S^\mu(\vec{p})$ is the four-vector spin direction [104], with the properties $S^2 = -1, \quad S\cdot p = 0$, and two extra structure functions g_1 and g_2 have been introduced.

In the framework of parton model, the structure functions g_1 and g_2 can be related to parton distributions. Defining $q_f(x) = q_f^{\overrightarrow{\Rightarrow}} + q_f^{\overleftarrow{\Rightarrow}}$ where $q_f^{\overrightarrow{\Rightarrow}}$ ($q_f^{\overleftarrow{\Rightarrow}}$) denotes the probability to find a quark of type f with momentum fraction (x) and spin parallel (antiparallel) to the nucleon spin, therefore, for the polarized structure functions one has

$$g_1(x) = \frac{1}{2}\sum_f e_f^2 \Delta q_f(x) \quad ; \quad g_2(x) = 0 \ , \tag{A.18}$$

where $\Delta q_f(x) = q_f^{\overrightarrow{\Rightarrow}} - q_f^{\overleftarrow{\Rightarrow}}$ defines the polarized distribution and represents the difference of the momentum distributions of partons with different helicity states within the nucleon. The polarized structure functions can be extracted from *DIS* experiments. Experimental data on the Q^2 dependence of g_1 for proton target are shown in Fig.A.4, left panel, at different x bins. The Bjorken scaling is well established at medium and large x, while it is broken at small x, as found with F_2. In Fig.A.4, right panel, the x dependence of the product $x\cdot g_1$ for different targets is shown. Data have been collected from experiments at different Q^2 regimes.

When the scattering particles energy is larger then some GeV, the light quark masses can be considered null, e.g. at the hadronic scale $m_\rho^0 = 0.770$ GeV: $m_u/m_\rho^0 \sim 10^{-3}$, $m_d/m_\rho^0 \sim 10^{-2}$, $m_s/m_\rho^0 \sim 0.23$. Therefore, the global flavor symmetry $SU_A(3)$ and the symmetry $U_A(1)$ induced by γ^5 can be considered good symmetries in QCD. The currents associated to $SU_A(3)$ and $U_A(1)$ are found to be $\vec{A}_\mu^{(i)} = \frac{1}{2}\bar{\psi}\gamma_\mu\gamma_5\vec{\lambda}^{(i)}\psi$ and $J_\mu^5 = \frac{1}{2}\bar{\psi}\gamma_\mu\gamma^5\psi$ respectively, $\lambda_{i=1\div 8}$ being the Gell-Mann matrices, are the eight independent generators of $SU_A(3)$. These conserved currents are defined as axial currents. The forward matrix element of J_μ^5 and $\vec{A}_\mu^{(i)}$ on proton states are parameterized as [104]

$$\langle P,S \mid J_\mu^5 \mid P,S\rangle = 2M_P a_0 S_\mu \quad ; \quad \langle P,S \mid A_\mu^{(i)} \mid P,S\rangle = M_P a_i S_\mu \ , \tag{A.19}$$

respectively, while in the parton model framework, the matrix element of the free quark

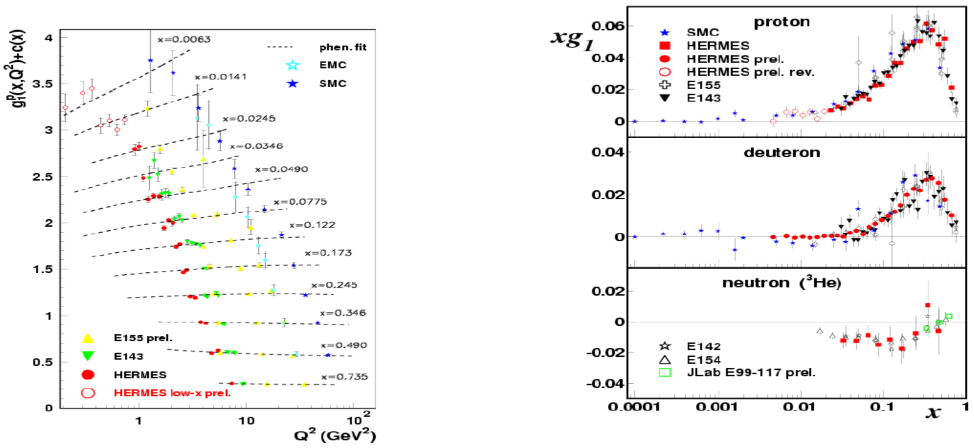

Figure A.4: **Left panel:** function structure $g_1(x, Q^2)$ versus lnQ^2. Data from experiments in different kinematic regimes $\langle Q^2 \rangle$ are compared. As for the unpolarized structure function $F_1(x, Q^2)$, the Bjorken scaling is broken at very low x_{Bj}. **Right panel:** x dependence of the product $x{\cdot}g_1$ for different targets. Data are collected from experiments at different Q^2 regimes.

axial current $J^{(i)}_{\mu 5}$ on proton states can be expressed in terms of polarized distributions:

$$\langle P, S \mid \bar{\psi}_f(0)\gamma_\mu\gamma_5\psi_f(0) \mid P, S\rangle = 2M_P S_\mu \int_0^1 dx[\ \Delta q_f(x) + \Delta\bar{q}_f(x)]\ . \qquad \text{(A.20)}$$

It follows that

$$\begin{aligned} a_0 = \Sigma &= \int_0^1 dx[\ \Delta q_f(x) + \Delta\bar{q}_f(x)] \\ a_3 &= \int_0^1 dx[\ \Delta u(x) + \Delta\bar{u}(x) - \Delta d(x) - \Delta\bar{d}(x)] \\ a_8 &= \int_0^1 dx[\ \Delta u(x) + \Delta\bar{u}(x) + \Delta d(x) + \Delta\bar{d}(x) - 2\Delta s(x) - 2\Delta\bar{s}(x)]\ , \end{aligned} \qquad \text{(A.21)}$$

where Σ is the total quark spin. In hyperon β-decays that same axial currents $\vec{A}^{(i)}_\mu$ are involved [105]. All these decays are described in terms of two constants F and D that are therefore related to unknown parameters a_i: $a_3 = F + D$, $a_8 = \frac{1}{\sqrt{3}}(3F - D)$. An analysis in 1983 of hyperon decay data [106] led to the values $F = 0.477 \pm 0.012$,

$D = 0.756 \pm 0.011$. Introducing the *Ellis-Jaffe* sum rule $\Gamma^P = \int_0^1 dx\, g_1^P(x)$, one obtains $\Gamma^P = \frac{1}{12}(a_3 + \frac{1}{\sqrt{3}}a_8 + \frac{4}{3}a_0)$.

In 1988 the *EMC* Collaboration at *CERN* from its data on $xg_1^P(x)$, with data on a_3 and a_8 from hyperon decays, extrapolated the result $a_0 = 2\Sigma \sim 0.040 \pm 0.117 \pm 0.171$, [107]. This highly unexpected result was lately named the 'spin crisis in the parton model'. No more in contradiction with an eventually small experimental value of Σ is found, if one can generalize the angular momentum sum rule

$$J_z^{proton} = \frac{1}{2} = S_z^{quarks} + S_z^{gluons} + L_z^{quarks} + L_z^{gluons} \ , \tag{A.22}$$

allowing for the existence of any orbital momentum is perpendicular to the proton momentum and for polarized gluons.

The surprising small value of a_0 can be explained within the QCD framework as a consequence of the axial anomaly [105,108]. Anomalies occur in a theory if symmetries present at the classical level are destroyed by quantum effects [109,110]. They typically involve contributions to a current, classically conserved, that are not present at the classical level. Due to the axial anomaly it is found that, when extracting a_0 from Γ_1 measurement, this axial charge does not coincide with the total quark spin $\Delta\Sigma$ at all, but mixes quark and gluon contributions in a factorization scheme dependent way. In particular, in the Adler-Bardeen (AB) scheme a_0 is decomposed as [111] $a_0(Q^2) = \Delta\Sigma - N_f \frac{\alpha_s(Q^2)}{2\pi}\Delta G(Q^2)$. In this picture, a_0 is modified by an anomalous contribution which is proportional to $\Delta G(Q^2) = \int dx g(x)$. Thus the smallness of the measured value of a_0 could be explained by a positive value for $\Delta G(Q^2)$, without requiring a small helicity contribution from quarks. To get a correct answer on the quark spin content, it is therefore necessary the knowledge of $\Delta G(Q^2)$. In principle, the polarized quark and gluon distributions can be probed by fitting studies on g_1 data from *DIS* experiments, taking into account the evolution equation for $\Delta\Sigma$ and ΔG, [112, 113]. However, the presently available data on polarized inclusive DIS only poorly constrain $\Delta G(Q^2)$. It is clear that a more direct measurement of $\Delta G(Q^2)$, based on the investigation of semi-inclusive processes is needed. Here one or more hadrons in coincidence with the scattered lepton are detected. In 2000, the *HERMES* Collaboration published the first result in this direction, [114]. The value of $\Delta g(x)/g(x)$ at one average x point, at the scale $Q^2 = 2.1$ GeV^2, and obtained at LO QCD, is

$$\frac{\Delta g(x)}{g(x)} = 0.41 \pm 0.18\ (stat.) \pm 0.03\ (syst.) \quad at \quad \langle x \rangle = 0.17 \ , \tag{A.23}$$

where the systematic uncertainty represents the experimental contribution only.

The result hints to a positive total gluon spin contribution ΔG. This could help and discriminate models which predicts opposite sign for ΔG, [111, 115]. Anyway, it is clear that more data are needed and in order to achieve this goal, dedicated experiments were set up. Spin physics at *RHIC* and at *CERN*, complementary to data from *HERMES* at *DESY* are expected to give a more detailed description of quark and gluon helicity distributions.

Semi-inclusive scattering can additionally provide a more direct information on the individual contributions of u, d, and s quarks as well as the separate contributions of valence and sea quarks. Within the QPM, the cross section for leptoproduction of a hadron (semi-inclusive scattering) can be expressed as

$$\frac{d\sigma^h}{dz} = \sigma_{DIS}(x, Q^2) \left[\frac{\sum_i e_i^2 q_i(x, Q^2) D_i^h(z, Q^2)}{\sum_i e_i^2 q_i(x, Q^2)} \right] , \tag{A.24}$$

where σ_{DIS} is the inclusive DIS cross section, the fragmentation function, $D_i^h(z, Q^2)$, is the probability that the hadron h originated from the struck quark of flavor i, $z = E_h/\nu$ is the hadron momentum fraction and the sums are over quark and antiquark flavors $u, d, s, \bar{u}, \bar{d}, \bar{s}$. Assuming factorization of the cross section as given in Eq. A.24, one can write the following semi-inclusive asymmetry for leptoproduction of a hadron:

$$A_1^h(x, Q^2) = \frac{\sum_i e_i^2 \Delta q_i(x, Q^2) \int_z D_q^h(z, Q^2) dz}{\sum_i e_i^2 q_i(x, Q^2) \int_z D_i^h(z, Q^2) dz} . \tag{A.25}$$

By making measurements with H, D and ^{3}He targets for different final-state hadrons and assuming isospin symmetry of the quark distributions and fragmentation functions a system of linear equations can be constructed:

$$\begin{pmatrix} A^p_{\pi^+} \\ A^p_{\pi^-} \\ A^n_{K^+} \\ A^n_{K^+} \\ \vdots \end{pmatrix} = f[q_i(x), D_i^h] \begin{pmatrix} \Delta u \\ \Delta d \\ \Delta s \\ \Delta \bar{u} \\ \vdots \end{pmatrix} \tag{A.26}$$

and solved for the Δq_i, once a parameterization for the unpolarized quark distributions and for the fragmentation functions is chosen. SMC and HERMES have made measurements of semi-inclusive asymmetries [116–118], and valence and quark helicity distributions were extracted through a Leading Order (LO) analysis.

Appendix B

Quark Distribution Functions

The optical theorem relates the hard elastic scattering off quarks to the imaginary part of the forward virtual Compton scattering, Fig. 2.1. The hadronic blob that describes the transition of the nucleon between equal states is represented in Fig. B.1 (i and j are Dirac indices) and is referred to as quark-quark correlation matrix Φ. The most general decomposition of Φ in a basis of Dirac matrices [104],

$$\Gamma = \left\{ \mathbb{1},\ \gamma^\mu,\ \gamma^\mu\gamma^5,\ \mathrm{i}\gamma^5,\ \mathrm{i}\sigma^{\mu\nu}\gamma^5 \right\}, \tag{B.1}$$

is

$$\Phi(k,P,S) = \frac{1}{2}\left\{ \mathcal{S}\ \mathbb{1} + \mathcal{V}_\mu\,\gamma^\mu + \mathcal{A}_\mu\gamma^5\gamma^\mu + i\ \mathcal{P}_5\gamma^5 + \frac{1}{2}i\ \ \mathcal{T}_{\mu\nu}\,\sigma^{\mu\nu}\gamma^5 \right\}. \tag{B.2}$$

The quantities $\mathcal{S}$, $\mathcal{V}^\mu$, $\mathcal{A}^\mu$, $\mathcal{P}_5$ and $\mathcal{T}^{\mu\nu}$ are constructed with the vectors k^μ, P^μ and the pseudovector S^μ, and have the following formal expression:

$$Tr(\Gamma_i\Phi) = \int d^4\xi\, e^{i\ k\cdot\xi}\,\langle PS|\bar{\psi}(0)\,\Gamma_i\,\psi(\xi)|PS\rangle\,, \tag{B.3}$$

where Γ_i is the corresponding element of the Dirac matrix basis in Eq. B.2. The Φ matrix satisfies certain relations arising from hermiticity, parity invariance and time-

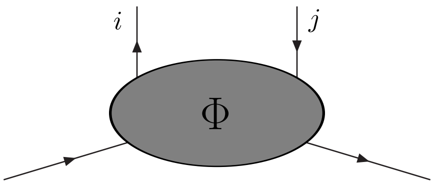

Figure B.1: The quark-quark correlation matrix Φ.

reversal invariance:

$$\Phi^\dagger(k,P,S) = \gamma^0\,\Phi(k,P,S)\,\gamma^0 \qquad \text{(hermiticity)}, \tag{B.4a}$$
$$\Phi(k,P,S) = \gamma^0\,\Phi(\tilde{k},\tilde{P},-\tilde{S})\,\gamma^0 \qquad \text{(parity)}, \tag{B.4b}$$
$$\Phi^*(k,P,S) = \gamma^5 C\,\Phi(\tilde{k},\tilde{P},\tilde{S})\,C^\dagger\gamma^5 \qquad \text{(time-reversal)}, \tag{B.4c}$$

where $C = i\,\gamma^2\gamma^0$ and the tilde four-vectors are defined as $\tilde{k}^\mu = (k^0, -\boldsymbol{k})$. Imposing the constraints (B.4a–B.4c), the general parameterization is found:

$$\mathcal{S} = \tfrac{1}{2}\,\mathrm{Tr}(\Phi) = C_1\,, \tag{B.5a}$$
$$\mathcal{V}^\mu = \tfrac{1}{2}\,\mathrm{Tr}(\gamma^\mu\Phi) = C_2\,P^\mu + C_3\,k^\mu\,, \tag{B.5b}$$
$$\mathcal{A}^\mu = \tfrac{1}{2}\,\mathrm{Tr}(\gamma^\mu\gamma_5\Phi) = C_4\,S^\mu + C_5\,k{\cdot}S\,P^\mu + C_6\,k{\cdot}S\,k^\mu\,, \tag{B.5c}$$
$$\mathcal{P}_5 = \tfrac{1}{2\mathrm{i}}\,\mathrm{Tr}(\gamma_5\Phi) = 0\,, \tag{B.5d}$$
$$\mathcal{T}^{\mu\nu} = \tfrac{1}{2\mathrm{i}}\,\mathrm{Tr}(\sigma^{\mu\nu}\gamma_5\Phi) = C_7\,P^{[\mu}S^{\nu]} + C_8\,k^{[\mu}S^{\nu]} + C_9\,k{\cdot}S\,P^{[\mu}k^{\nu]}\,, \tag{B.5e}$$

where the coefficients $C_i = C_i(k^2, k{\cdot}P)$ are real functions, owing to hermiticity.

In QCD, in order to make Φ gauge invariant, a path-dependent link operator

$$\mathcal{L}(0,\xi) = \mathcal{P}\,e^{\left(-i\ g\int_0^\xi d\ s_\mu\,A^\mu(s)\right)}, \tag{B.6}$$

where $\mathcal{P}$ denotes path-ordering, must be inserted between the quark fields. Thus, by working in the axial gauge $A^+ = 0$ and choosing an appropriate path, $\mathcal{L}$ can be reduced to unity. Hereafter we shall the link operator is assumed to be unity, and is omitted.

When only leading-twist contributions are considered, i.e. the terms in Eqs. (B.5a–e) which are of order $\mathcal{O}(P^+)$ in the infinite momentum frame, the available vectors for the Φ parameterization are P^μ, $k^\mu \simeq xP^\mu$, and $S^\mu \simeq \lambda_N P^\mu/M + S_\perp^\mu$, where the approximate equality signs indicate that we are neglecting terms suppressed by $(P^+)^{-2}$; the transverse spin vector $S_\perp^\mu$ is of order $(P^+)^0$.

At leading order (LO) in P^+ only the vector, axial, and tensor terms in (B.2) survive and eqs. (B.5b, c, e) become

$$\mathcal{V}^\mu = \tfrac{1}{2}\int d^4\xi\,e^{i\ k\cdot\xi}\,\langle PS|\bar\psi(0)\gamma^\mu\psi(\xi)|PS\rangle = A_1\,P^\mu\,, \tag{B.7a}$$
$$\mathcal{A}^\mu = \tfrac{1}{2}\int d^4\xi\,e^{i\ k\cdot\xi}\,\langle PS|\bar\psi(0)\gamma^\mu\gamma^5\psi(\xi)|PS\rangle = \lambda_N\,A_2\,P^\mu\,, \tag{B.7b}$$
$$\mathcal{T}^{\mu\nu} = \tfrac{1}{2\mathrm{i}}\int d^4\xi\,e^{i\ k\cdot\xi}\,\langle PS|\bar\psi(0)\sigma^{\mu\nu}\gamma^5\psi(\xi)|PS\rangle = A_3\,P^{[\mu}S_\perp^{\nu]}\,, \tag{B.7c}$$

where the new real functions $A_i(k^2, k{\cdot}P)$ have been introduced. The leading-twist quark correlation matrix (B.2) is then (with $P^{[\mu}S_\perp^{\nu]}\sigma_{\mu\nu} = 2\mathrm{i}\,\not{P}\,\not{S}_\perp$)

$$\Phi(k, P, S) = \frac{1}{2}\left\{A_1\,\not{P} + A_2\,\lambda_N\,\gamma^5\,\not{P} + A_3\,\not{P}\,\gamma_5\,\not{S}_\perp\right\}. \tag{B.8}$$

From (B.7a–c) one obtains

$$A_1 = \frac{1}{2P^+}\,\mathrm{Tr}(\gamma^+\Phi)\,, \tag{B.9a}$$

$$\lambda_N\,A_2 = \frac{1}{2P^+}\,\mathrm{Tr}(\gamma^+\gamma_5\Phi)\,, \tag{B.9b}$$

$$S_\perp^i\,A_3 = \frac{1}{2P^+}\,\mathrm{Tr}(i\,\sigma^{i+}\gamma_5\Phi) = \frac{1}{2P^+}\,\mathrm{Tr}(\gamma^+\gamma^i\gamma^5\Phi)\,. \tag{B.9c}$$

The leading-twist distribution functions $f(x)$, $\Delta f(x)$ and $\Delta_T f(x)$ are obtained by integration over k of A_1, A_2 and A_3, respectively, with the constraint $x = k^+/P^+$:

$$\left\{\begin{array}{c} f(x) \\ \Delta f(x) \\ \Delta_T f(x) \end{array}\right\} = \int \frac{d^4k}{(2\pi)^4}\left\{\begin{array}{c} A_1(k^2, k{\cdot}P) \\ A_2(k^2, k{\cdot}P) \\ A_3(k^2, k{\cdot}P) \end{array}\right\}\delta\!\left(x - \frac{k^+}{P^+}\right), \tag{B.10}$$

and using (B.9a–c), and setting for definiteness $\lambda_N = +1$ and $S_\perp^i = (1, 0)$,

$$f(x) = \frac{1}{2}\int \frac{d^4k}{(2\pi)^4}\,\mathrm{Tr}(\gamma^+\Phi)\,\delta(k^+ - xP^+)\,, \tag{B.11a}$$

$$\Delta f(x) = \frac{1}{2}\int \frac{d^4k}{(2\pi)^4}\,\mathrm{Tr}(\gamma^+\gamma_5\Phi)\,\delta(k^+ - xP^+)\,, \tag{B.11b}$$

$$\Delta_T f(x) = \frac{1}{2}\int \frac{d^4k}{(2\pi)^4}\,\mathrm{Tr}(\gamma^+\gamma^1\gamma_5\Phi)\,\delta(k^+ - xP^+)\,. \tag{B.11c}$$

Inserting the definition (B.2) of Φ in (B.11a–c), the three leading-twist distribution functions as light-cone Fourier transforms of expectation values of quark-field bilinears are obtained:

$$f(x) = \int \frac{d\xi^-}{4\pi} e^{i\;xP^+\xi^-}\,\langle PS|\bar{\psi}(0)\gamma^+\psi(0, \xi^-, 0_\perp)|PS\rangle\,, \tag{B.12a}$$

$$\Delta f(x) = \int \frac{d\xi^-}{4\pi} e^{i\;xP^+\xi^-}\,\langle PS|\bar{\psi}(0)\gamma^+\gamma_5\psi(0, \xi^-, 0_\perp)|PS\rangle\,, \tag{B.12b}$$

$$\Delta_T f(x) = \int \frac{d\xi^-}{4\pi} e^{i\;xP^+\xi^-}\,\langle PS|\bar{\psi}(0)\gamma^+\gamma^1\gamma_5\psi(0, \xi^-, 0_\perp)|PS\rangle\,. \tag{B.12c}$$

In terms of the three leading-twist distribution functions, the quark-quark correlation matrix Φ reads

$$\Phi(x) = \frac{1}{2}\left\{f(x)\,\not{P} + \lambda_N\,\Delta f(x)\,\gamma_5\,\not{P} + \Delta_T f(x)\,\not{P}\,\gamma_5\,\not{S}_\perp\right\}. \tag{B.13}$$

Applying the same procedure with antiquarks, their distribution functions are found to be:

$$\begin{aligned}\bar{f}(x) &= \frac{1}{2}\int \frac{d^4k}{(2\pi)^4}\ \mathrm{Tr}(\gamma^+\overline{\Phi})\,\delta(k^+ - xP^+) \\ &= \int \frac{d\xi^-}{4\pi} e^{i\ xP^+\xi^-} \langle PS|\,\mathrm{Tr}\left[\gamma^+\psi(0)\bar{\psi}(0,\xi^-,0_\perp)\right]|PS\rangle\,, \end{aligned} \tag{B.14}$$

$$\begin{aligned}\Delta\bar{f}(x) &= -\frac{1}{2}\int \frac{d^4k}{(2\pi)^4}\ \mathrm{Tr}\left(\gamma^+\gamma^5\overline{\Phi}\right)\delta(k^+ - xP^+) \\ &= \int \frac{d\xi^-}{4\pi} e^{i\ xP^+\xi^-} \langle PS|\,\mathrm{Tr}\left[\gamma^+\gamma_5\psi(0)\bar{\psi}(0,\xi^-,0_\perp)\right]|PS\rangle\,, \end{aligned} \tag{B.15}$$

$$\begin{aligned}\Delta_T\bar{f}(x) &= \frac{1}{2}\int \frac{d^4k}{(2\pi)^4}\ \mathrm{Tr}\left(\gamma^+\gamma^1\gamma_5\overline{\Phi}\right)\delta(k^+ - xP^+) \\ &= \int \frac{d\xi^-}{4\pi} e^{i\ xP^+\xi^-} \langle PS|\,\mathrm{Tr}\left[\gamma^+\gamma^1\gamma_5\psi(0)\bar{\psi}(0,\xi^-,0_\perp)\right]|PS\rangle\,. \end{aligned} \tag{B.16}$$

The variable $x \equiv k^+/P^+$ is not *a priori* constrained to be positive and to range from 0 to 1. It turns out that there is a set of symmetry relations connecting quark and antiquark distribution functions, which are obtained by continuing x to negative values. Using anticommutation relations for the fermion fields in the connected matrix elements

$$\langle PS|\bar{\psi}(\xi)\psi(0)|PS\rangle_c = -\langle PS|\psi(0)\bar{\psi}(\xi)|PS\rangle_c\,, \tag{B.17}$$

one obtains the following relations for the three distribution functions

$$\bar{f}(x) = -f(-x)\,, \tag{B.18a}$$

$$\Delta\bar{f}(x) = \Delta f(-x)\,, \tag{B.18b}$$

$$\Delta_T\bar{f}(x) = -\Delta_T f(-x)\,. \tag{B.18c}$$

Therefore, antiquark distributions are given by the continuation of the corresponding quark distributions into the negative x region.

B.1 Probabilistic Interpretation of Distribution Functions

Distribution functions are essentially the probability densities for finding partons with a given momentum fraction x and a given polarization inside a hadron. This interpretation comes about from the field-theoretical definitions of quark and antiquark distribution functions. The quark fields can be decomposed into "good" and "bad" components:

$$\psi = \psi_{(+)} + \psi_{(-)} \,, \tag{B.19}$$

where

$$\psi_{(\pm)} = \frac{1}{2}\,\gamma^{\mp}\,\gamma^{\pm}\,\psi \,. \tag{B.20}$$

The usefulness of this procedure lies in the fact that "bad" components are not dynamically independent: using the equations of motion, they can be eliminated in favor of "good" components and terms containing quark masses and gluon fields. In the $P^+ \to \infty$ limit $\psi_{(+)}$ dominates over $\psi_{(-)}$, therefore the presence of "bad" components in a parton distribution function signals higher twists. Using the relations

$$\begin{aligned}
\bar{\psi}\,\gamma^+\,\psi &= \sqrt{2}\,\psi^\dagger_{(+)}\,\psi_{(+)} \,, &\text{(B.21a)}\\
\bar{\psi}\,\gamma^+\gamma_5\,\psi &= \sqrt{2}\,\psi^\dagger_{(+)}\,\gamma_5\,\psi_{(+)} \,, &\text{(B.21b)}\\
\bar{\psi}\,\mathrm{i}\sigma^{i+}\gamma_5\,\psi &= \sqrt{2}\,\psi^\dagger_{(+)}\,\gamma^i\gamma_5\,\psi_{(+)} \,, &\text{(B.21c)}
\end{aligned}$$

the leading-twist distributions (B.12a–c) can be re-expressed as

$$\begin{aligned}
f(x) &= \int \frac{d\xi^-}{2\sqrt{2}\,\pi} e^{i\;xP^+\xi^-} \langle PS|\psi^\dagger_{(+)}(0)\gamma^+\psi_{(+)}(0,\xi^-,0)|PS\rangle \,, &\text{(B.22a)}\\
\Delta f(x) &= \int \frac{d\xi^-}{2\sqrt{2}\,\pi} e^{i\;xP^+\xi^-} \langle PS|\psi^\dagger_{(+)}(0)\gamma_5\psi_{(+)}(0,\xi^-,0)|PS\rangle \,, &\text{(B.22b)}\\
\Delta_T f(x) &= \int \frac{d\xi^-}{2\sqrt{2}\,\pi} e^{i\;xP^+\xi^-} \langle PS|\psi^\dagger_{(+)}(0)\gamma^1\gamma_5\psi_{(+)}(0,\xi^-,0)|PS\rangle \,, &\text{(B.22c)}
\end{aligned}$$

where only "good" components appear. It is the peculiar structure of the quark-field bilinears in eqs. (B.22a–c) that allows one to put the distributions in a form that renders their probabilistic nature transparent. The correct support in x of the distributions emerges, along with their probabilistic content, if one inserts into (B.22a–c) a complete set of intermediate states $\{|n\rangle\}$. Considering, for instance, the unpolarised distribution one obtains from (B.22a)

$$f(x) = \tfrac{1}{\sqrt{2}} \sum_n \delta\big((1-x)P^+ - P^+_n\big)\,|\langle PS|\psi_{(+)}(0)|n\rangle|^2 \,, \tag{B.23}$$

where $\sum_n$ incorporates the integration over the phase space of the intermediate states. Eq. (B.23) gives the probability of finding inside the nucleon a quark with longitudinal

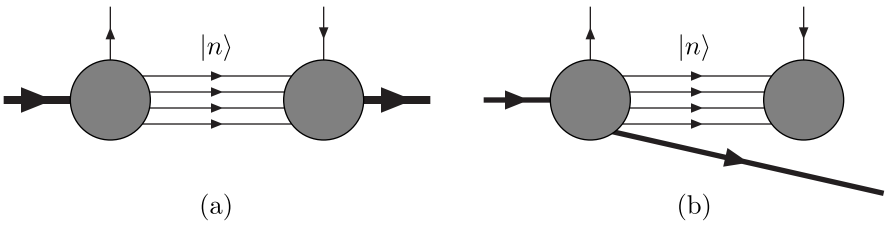

Figure B.2: **(a)** A connected matrix element with the insertion of a complete set of intermediate states and **(b)** a semi-connected matrix element.

momentum k^+/P^+, irrespective of its polarization. Since the states $|n\rangle$ are physical one must have $P_n^+ \geq 0$, that is $E_n \geq |\boldsymbol{P}_n|$, and therefore $x \leq 1$. Moreover, if exclude semiconnected diagrams like that in Fig. B.1b are excluded, that correspond to $x < 0$, one is left with the connected diagram of Fig. B.1a and with the correct support $0 \leq x \leq 1$. A similar reasoning applies to antiquarks.

Using the Pauli-Lubanski projectors $\mathcal{P}_\pm = \frac{1}{2}(1 \pm \gamma^5)$ (for helicity) and $\mathcal{P}_{\uparrow\downarrow} = \frac{1}{2}(1 \pm \gamma^1\gamma^5)$ (for transverse polarization), one obtains

$$\begin{aligned} \Delta f(x) &= \frac{1}{\sqrt{2}} \sum_n \delta\left((1-x)P^+ - P_n^+\right) \\ &\quad \times \left\{ \left|\langle PS|\mathcal{P}_+\psi_{(+)}(0)|n\rangle\right|^2 - \left|\langle PS|\mathcal{P}_-\psi_{(+)}(0)|n\rangle\right|^2 \right\} , \\ \Delta_T f(x) &= \frac{1}{\sqrt{2}} \sum_n \delta\left((1-x)P^+ - P_n^+\right) \\ &\quad \times \left\{ \left|\langle PS|\mathcal{P}_\uparrow\psi_{(+)}(0)|n\rangle\right|^2 - \left|\langle PS|\mathcal{P}_\downarrow\psi_{(+)}(0)|n\rangle\right|^2 \right\} . \end{aligned} \tag{B.24}$$

These expressions exhibit the probabilistic content of the leading-twist polarized distributions $\Delta f(x)$ and $\Delta_T f(x)$: $\Delta f(x)$ is the number density of quarks with helicity $+$ minus the number density of quarks with helicity $-$ (assuming the parent nucleon to have helicity $+$); $\Delta_T f(x)$ is the number density of quarks with transverse polarization $\uparrow$ minus the number density of quarks with transverse polarization $\downarrow$ (assuming the parent nucleon to have transverse polarization $\uparrow$). The distribution $\Delta_T f$ admits an interpretation in terms of probability densities only in the transverse polarization basis.

If the correlation matrix $\Phi(k, P, S)$ is integrated over k, or equivalently $\Phi(x)$ over x, one obtains a local matrix element Φ (defined with no arguments)

$$\Phi = \int d^4k\, \Phi(k, P, S) = \int dx\, \Phi_{ij}(x) \tag{B.25}$$

which, in view of (B.8), can be parameterized as

$$\Phi = \frac{1}{2}\left[g_V \not{P} + g_A\,\lambda_N\,\gamma^5 \not{P} + g_T \not{P}\,\gamma_5 \not{S}_\perp\right] \;, \tag{B.26}$$

where g_V, g_A and g_T are the vector, axial and tensor charge, respectively. They are given by the following matrix elements (recall (B.7a–c)):

$$\begin{aligned} \langle PS|\bar{\psi}(0)\gamma^\mu\psi_i(0)|PS\rangle &= 2g_V\,P^\mu \;, \\ \langle PS|\bar{\psi}(0)\gamma^\mu\gamma^5\psi_i(0)|PS\rangle &= 2g_A\,MS^\mu \;, \\ \langle PS|\bar{\psi}(0)\mathrm{i}\sigma^{\mu\nu}\gamma^5\psi_i(0)|PS\rangle &= 2g_T\,(S^\mu P^\nu - S^\nu P^\mu)\,. \end{aligned} \tag{B.27}$$

Integrating Eqs. (B.12a–c) and using the symmetry relations (B.18a–c) yields

$$\begin{aligned} \int_{-1}^{+1} dx\, f(x) &= \int_0^1 dx\left[f(x) - \bar{f}(x)\right] = g_V \;, \\ \int_{-1}^{+1} dx\, \Delta f(x) &= \int_0^1 dx\left[\Delta f(x) + \Delta\bar{f}(x)\right] = g_A \;, \\ \int_{-1}^{+1} dx\, \Delta_T f(x) &= \int_0^1 dx\left[\Delta_T f(x) - \Delta_T\bar{f}(x)\right] = g_T \;, \end{aligned} \tag{B.28}$$

where g_V is simply the valence number. As a consequence of the charge conjugation properties of the field bilinears $\bar{\psi}\gamma^\mu\psi$, $\bar{\psi}\gamma^\mu\gamma^5\psi$ and $\bar{\psi}\mathrm{i}\sigma^{\mu\nu}\gamma^5\psi$, the vector and tensor charges are the first moments of flavor non-singlet combinations (quarks minus anti-quarks) whereas the axial charge is the first moment of a flavor singlet combination (quarks plus antiquarks).

Appendix C

Parameters Tuning of DIS Monte Carlo Production

On summer 2001 $2.3 \cdot 10^6$ DIS events were generated in the *HERMES* acceptance using the *HERMES* Monte Carlo simulation program *GMC*.

The simulation of DIS events processes is driven by input tunable parameters mainly from experimental data. As an example, the quark fragmentation functions $D_q^h(z)$, express the probability to form from quark-jet q a hadron carrying a fraction between z and $z+dz$ of W. They play a key role in the hadronization of partons and the model can be tuned with their knowledge from experiments. Further parameters may also be tuned, e.g. the string tension, the strangeness suppression factors, describing the probability to create $s\bar{s}$ pairs compared to the $u\bar{u}$, $d\bar{d}$ production,

$$\gamma_s \equiv \frac{N(s\bar{s})}{N(u\bar{u}) + N(d\bar{d}) + N(s\bar{s})} \ , \tag{C.1}$$

the vector versus pseudoscalar meson production factor,

$$\alpha_V \equiv \frac{N(vectors)}{N(vectors) + N(pseudoscalars)} \ , \tag{C.2}$$

and the postulated gaussian transverse momentum distribution of quarks relative to the string axis and the postulated gaussian transverse momentum distribution of quarks relative to the string axis

$$\frac{dP}{dp_T^2} = dp_T^2 \ e^{-p_T^2/2\sigma_q^2} \tag{C.3}$$

where σ_q is known as *smearing* parameter.

A set of tuned parameters were given as input to the *JETSET* and *LEPTO* packages, and the chosen setting is shown in the following tables. A detailed explanation of the meaning of *JETSET* parameters *PARJ*, *MSTJ* and *MSTU* can be found [119]. Instead, the *LEPTO* parameters *LST* and *PARL* are discussed in [87].

JETSET PARAMETERS	
nominal number of flavors assumed in α_s expression	MSTU 112=3
minimum number of flavors that may be assumed in α_s expression	MSTU 113=3
maximum number of flavors that may be assumed in α_s expression	MSTU 114=3
treatment of α_s singularity for $Q^2 \to 0$	MSTU 115=0
diquark suppression P(qq)/P(q)	PARJ 1=0.03
s quark suppression P(s)/P(u)	PARJ 2=0.2
suppression of BMBbar to BBbar in popcorn model	PARJ 5=0.001
minimum allowable energy for color-singlet jet system	PARJ 32=1.0
minimum energy used to stop fragmenting a jet (D: 0.8)	PARJ 33=0.8
width for px, py transverse momentum distributions for primary hadrons	PARJ 21= 0.336
a parameter for symmetric LUND fragmentation function	PARJ 41=1.02
b parameter for symmetric LUND fragmentation function	PARJ 42=0.370
choose string fragmentation	MSTJ 1=1
conserve flavor and momentum	MSTJ 3=0
use std LUND fragmentation function	MSTJ 11=1
baryon production model: popcorn (D: 2)	MSTJ 12=2
parton showers OFF (D:2)	MSTJ 41=0

LEPTO CONTROL SWITCHES	
simulation of QCD effects in hadronic final state (D: 12)	LST 8=0
scale in parton showers	LST 9=5
numerical integration of cross section in LINIT	LST 10=1
inclusion of F_L, target mass, and higher twist (D: 0)	LST 11=1
maximum number of sea quark flavors (D: 4)	LST 12=3
heaviest quark flavor allowed in boson-gluon fusion (D: 5)	LST 13=3
treatment of target remnant	LST 14=4
energy variation of initial particles from event to event	LST 17=0
running of EM coupling alpha, and choice of W,Z masses	LST 18=2
scheme for cutoffs against divergences (D: 5)	LST 20=1
switch for soft color interaction (D: 1)	LST 34=1
turn on/off new sea quark treatment	LST 35=1
Gaussian width of primordial k_t	PARL 3=0.44
probability that a ud-diquark in remnant has I=S=0	PARL 4=0.75
sin (theta_W) (D: 0.2319)	PARL 5=0.2294
probability for soft color interaction between parton pairs	PARL 7=0.5
width of Gaussian distribution for the virtuality of sea quarks (when LST(35)=2) required relative accuracy for 1d-integrations (ME and longitudinal SF)	PARL 10=0.44 PARL 11=0.01
probability for an intrinsic charm quark-antiquark pair in proton (D: 0.01)	PARL 12=0.
internal parameter for adjustment of y_cut for integration of QCD ME	PARL 13=0.1
width of Gaussian distribution in transverse momentum when a non-trivial target remnant is split into 2 particles (D: 0.35)	PARL 14=0.52
required relative accuracy for 2d integration of cross section	PARL 15=0.01

Acknowledgments

I think that this experience would not have been so amazing without the contribution given by most of the people I met during these last years.

Well, a sincere thanks to my fantastic group in Ferrara which gave me the possibility to do physics:
THANKS Paola, Peppone, Michelle, el matador Contalb, Paolo, Davide, Marco Jr.

I want to thank 'Saint Pasquale': since the very first step of this analysis he supported and helped me with his suggestions. Thanks also for all the time dedicated to our collaboration.
Special thanks are devoted to the INFN-Frascati staff, who suggested this kind of analysis and, most important, gave me the possibility to 'feel myself at home' each time I was at the Laboratories in Frascati:
THANKS Nicola, Enzo, Valeria, Alessandra, Delia, Karo, Gianpaolo and Donatella.

I did not forget whom was able to organize the weekly appointment with soccer, ...I re-discovered the 'Platini' inside me, thanks Gigi. And I cannot miss all the guys at INFN in Ferrara, with whom I drank beer, at least once!!!! ....and, also the only person in Ferrara who gave me the possibility to drive his own car, ...when his wife was absent of course, thanks Cesco.

Big thanks to the "Cesenatico forever crew", which was a constant lighthouse for me, please do not change!!!

....and last, but not least for importance, thanks to my family which strongly supported me during my PhD studies, ...and during my life.

Bibliography

[1] K. Goeke, M.V. Polyakov, M. Vanderhaeghen Prog. Part. Nucl. Phys. **47** (2001) 401.

[2] A.G.Sitenko, P.J.Shepard, Lectures in Scattering Theory, Pergamon Press.

[3] A. V. Radyushkin, Phys. Rev. D **56** (1997) 5524.

[4] J. Collins, L. Frankfurt and M. Strickman, Phys. Rev. D **56** (1997) 2982.

[5] X. Ji, J. Phys. G **24** (1998) 1181.

[6] P. Hoodbhoy and X. Ji, Phys. Rev. D **58** (1998) 054006.

[7] M. Diehl, Eur. Phys. J. C bf 19 (2001) 485.

[8] J. H. Ely, Measurement of the single spin azimuthal asymmetry in the predominantly exclusive electroproduction of photons from the proton, PhD Thesis 2002, HERMES-02-014.

[9] X. Ji, Phys. Rev. Lett. **78** (1997) 610.

[10] X. Ji, Phys. Rev. D **55** (1997) 7114.

[11] M. Diehl et al., Nucl. Phys. **B596** (2001) 33.

[12] M. Burkardt, hep-ph/0105324.

[13] M. Diehl, Eur. Phys. Jour. C **25** (2002) 223.

[14] J. P. Ralston and B. Pire, hep-ph/0110075

[15] S. J. Brodsky et al., Nucl. Phys. **B596** (2001) 99.

[16] X. Ji, J. Tang, and P. Hoodbhoy, Phys. Rev. Lett. **76** (1996) 740.

[17] X. Ji, Phys. Rev. Lett **74** (1995) 1071; Phys. Rev. D **52** (1995) 271.

[18] R. L. Jaffe and A. Manohar, Nucl. Phys. **B337** (1990) 509.

[19] G. Altarelli and G. Parisi, Nucl. Phys. **B126** (1977) 298.

[20] S.V. Bashinsky and R.L. Jaffe, Nucl. Phys. **B536** (1998) 303.

[21] A. Harindranath and R. Kundu, Phys. Rev. D **59** (1999) 116013.

[22] P. Hagler and A. Schafer, Phys. Lett. B **430** (1998) 179.

[23] HERMES Collaboration, Phys. Rev. Lett. **87** (2001) 182001.

[24] CLAS Collaboration, Phys. Rev. Lett. **87** (2001) 182002.

[25] HERMES Collaboration, Phys. Lett. B **535** (2002) 85.

[26] X. Ji, W. Melnitchouk and X. Song, Phys. Rev. D **56** (1997) 5511.

[27] A. Chodos et al., Phys. Rev. D **9** (1974) 3471.

[28] X. Song and J. S. McCarthy, Phys. Rev. C **46** (1992) 1077.

[29] M. Betz and R. Goldflam, Phys. Rev. D **28** (1983) 2848.

[30] R. L. Jaffe and X. Ji, Phys. Rev. Lett. **67** (1991) 552.

[31] R. C. Walker et al., Phys. Rev. D **49** (1994) 5671.

[32] L. Andivahis et al., Phys. Rev. D **50** (1994) 5491.

[33] D. Diakonov et al., Nucl. Phys. **B480** (1996) 34.

[34] D. I. Diakonov, Yu. V. Petrov and P. V. Pobylitsa, Nucl. Phys. **B306** (1988) 809.

[35] E. Witten, Nucl. Phys. **B223** (1983) 433.

[36] G. Adkins, C. Nappi and E. Witten, Nucl. Phys. **B228** (1983) 552.

[37] D. Diakonov, hep-ph/9802298, NORDITA-98/14.

[38] K. Goeke et al., Acta Phys. Polon. B32 (2001) 1201.

[39] M. Glück et al., Phys. Rev. **53** (1996) 4775.

[40] V. Yu. Petrov et al., Phys. Rev. D **57** (1998) 4325.

[41] M. Vanderhaegen et al., Phys. Rev. D **60** (1999) 094017.

[42] E. Leader, A.V. Sidorov and D.B. Stamenov, Phys. Rev. D **58** (1998) 114028.

[43] HERMES Collaboration, Phys. Lett. B **464** (1999) 123.

[44] A. V. Radyushkin, Phys. Lett. B **380** (1996) 417.

[45] A. V. Radyushkin, Phys. Rev. D **59** (1999) 014030.

[46] A.D. Martin at al., Eur. Phys. J. C **4** (1998) 463.

[47] M. V. Polyakov and C. Weiss, Phys. Rev. D **60** (1999) 114017.

[48] B. Lehmann-Dronke et al, Phys. Lett. B **475** (2000) 147.

[49] B. Lehmann-Dronke et al., Phys. Rev. D **63** (2001) 114001.

[50] Particle Data Group, Eur. Phys. J. **C 3** 1-4 (1998) 1.

[51] Proceedings of Workshop on Exclusive and Semiexclusive Processes at High Momentum Transfer, Jefferson Lab, May 1999, hep-ph/9909445.

[52] M. Garcon, hep-ph/0210068, to be published in Eur. Phys. Jour. A.

[53] M. Polyakov, Nucl. Phys. **B555** (1999) 231.

[54] G. P. Lepage and S. J. Brodsky, Phys. Lett. B **87** (1979) 359.

[55] A. V. Efremov and A. V. Radyushkin, Phys. Lett. B **94** (1980) 245.

[56] W. O. U. Romero, Boletín de la Asociaciòn Matemática Venezolana Vol.V, No. 2 (1998) 143.

[57] N. Kivel, L. Mankiewicz, and M. V. Polyakov, Phys. Lett. B **467** (1999) 263.

[58] K. M. Watson, Phys. Rev. **95** (1954) 228.

[59] R. Omnès, Nuovo Cimento **8** (1958) 316.

[60] A. D. Martin, R. G. Roberts, and W. J. Stirling, Phys. Lett. B **354** 155 (1995).

[61] L. Mankiewicz, G. Piller, and T. Weigl, Eur. Phys. J. C **5** (1998) 119.

[62] M. Vanderhaeghen, P. A. M. Guichon, and M. Guidal, Phys. Rev. Lett. **80** (1998) 5064.

[63] T. Ericson and W. Weise, *Pions and Nuclei*, Oxford University Press, (1988).

[64] V. M. Braun et al., Phys. Lett. B **302** (1993) 291.

[65] F. Guerrero and A. Pich, Phys. Lett. B **412** (1997) 382.

[66] J. F. Donoghue and B. R. Holstein, Phys. Rev. D **48** (1993) 137.

[67] HERMES Collaboration, Eur. Phys. Jour. C **17** (2000) 389.

[68] M. Vanderhaeghen et al., Phys. Rev. D **60** (1999) 094017.

[69] Ph. Hagler et al., Nucl. Phys. A **711** (2002) 232.

[70] Ph. Hagler et al., Eur. Phys. J. C **26** (2002) 261.

[71] B. Lehmann-Dronke, Private Communications.

[72] M. Duren, The *HERMES* Experiment: From the Design to the First Results, DESY-HERMES-95-02.

[73] A. A. Sokolov and I. M. Ternov, Sov. Phys. Dokladi **8** (1968) 1203.

[74] L. Thomas, Philos. Mag. **3** (1927) 1.

[75] V. Bargmann, L. Michel and V. L. Telegdi, Phys. Rev. Lett. **2** (1959) 435.

[76] Ya. S. Derbenev et al., Part. Accel. **8** (1978) 115.

[77] K. Steffen, DESY-PET-78/11

[78] C. Cohen-Tannoudji, B. Diu and F. Laloe, Quantum Mechanics Vol.II (1977).

[79] F. Stock et al., Nucl. Inst. and Methods **A 343** (1994) 334.

[80] C. Baumgarten, Studies of Spin Relaxation and Recombination at the *HERMES* Hydrogen/Deuterium Gas Target, PhD Thesis 2000, HERMES-00-03.

[81] A. Abragam and J. M. Winter, Phys. Rev. Lett. Vol.1 No.10 (1958) 374.

[82] C. Baumgarten et al., The Storage Cell of the Polarized H/D Internal Gas Target of the *HERMES* Experiment at *HERA* , submitted to Elsevier Science.

[83] T. Walker and L. W. Anderson, Nucl. Inst. and Methods **A 334** (1993) 313.

[84] *HERMES* Collaboration, Nucl. Inst. and Methods **A 417** (1998) 230.

[85] *HERMES* Collaboration, Nucl. Inst. and Method, **A 378** (1996) 13.

[86] J. D. Jackson. Classical Electrodynamics, Wiley, New York, 1999.

[87] G. Ingelman, A. Edin and J. Rathsman, Phys. Comp. Comm. **101** 108.

[88] B. Andersson et al. Phys. Rep. **97** 1983.

[89] http://wwwinfo.cern.ch/asd/geant/

[90] M. Arneodo, L. Lamberti and M. Ryskin, Phys. Comp. Comm. **100** 195.

[91] M. G. Ryskin, Z. Phys. **C 57** (1993) 89.

[92] M. Tytgat, Diffractive Production of ρ^0 and ω Vector Mesons at HERMES, DESY-THESIS-2001-018.

[93] http://durpdg.dur.ac.uk/HEPDATA/

[94] S. Brandt, Statistical and computational methods in data analysis, North-Holland Publishing Company, 1970.

[95] I.Akushevich and P.Kuzhir, Phys. Lett. B **474** (2000) 411.

[96] C. Itzykson, J. Zuber, Quantum Field Theory, McGraw-Hill.

[97] F. Halzen, A. Martin, Quarks and Leptons, John Wiley & sons.

[98] G. Hoeler et al, Nucl. Phys. **B114** 505 (1976).

[99] P. E. Bosted et al., Phys. Rev. Lett. **68** 3841 (1992).

[100] T. Muta, Foundations of QCD, World Scientific, 2000.

[101] R. K. Ellis, W. J. Stirling, B. R. Webber, QCD and Collider Physics, Cambridge (1996).

[102] J. D. Bjorken, E. A. Paschos, Phys. Rev. Vol.185, N.**5** 1975 (1969).

[103] D. H. Perkins, Introduction to High Energy Physics, Addison Wesley.

[104] V. Barone, A. Drago, P. G. Ratcliffe, Phys. Rept. **359** (2002) 1.

[105] M. Anselmino, A. Efremov, E. Leader Phys. Rept. **261** (1995).

[106] WA2 Group, Z. Phys., **C21** (1983) 27.

[107] J. Ashman et al., Phys. Lett **B 206** (1988) 364.

[108] R. G. Roberts, The Structure of the Proton, Cambridge (1990).

[109] S. L. Adler, Phys. Rev. **182** (1969) 2426.

[110] J. S. Bell and R. Jakiw, Nuovo Cimento A **60** (1969) 47.

[111] V.Barone, A.Drago, Proceeding of 'Perspective in Hadronic Physics' Trieste, World Scientific, 1999.

[112] G. Altarelli, G. G. Ross, Phys. Lett. B **212** (1988) 391.

[113] L. De Nardo, Measurements of the Structure Function g_1^d at *HERMES* and Extraction of Polarized Parton Distributions, PhD Thesis 2002, HERMES-02-038.

[114] HERMES Collaboration, Phys. Rev. Lett. **84** (2000) 2584.

[115] R. L. Jaffe, Phys. Lett. B **365** (1996) 359.

[116] J. Ashman et al., Phys. Lett. **206** (1988) 364.

[117] HERMES Collaboration, Phys. Lett. B **464** (1999) 123.

[118] A. Miller, Proceedins of 15th International Spin Physics Symposium (SPIN2002), BNL, Sept. 2002.

[119] T. Sjöstrand et al., hep-ph/0108264